UNIVERSITÀ
DEGLI STUDI
DI TRIESTE

Università degli Studi di Trieste

XXXVI CICLO DEL DOTTORATO DI RICERCA IN
FISICA

Cold gas and dust in QSO's host galaxies at $z > 6$

SETTORE SCIENTIFICO-DISCIPLINARE: ASTRONOMIA E ASTROFISICA

DOTTORANDA:
Roberta Tripodi

COORDINATORE:
Prof. Francesco Longo
Francesco Longo

SUPERVISORE:
Prof. Fabrizio Fiore

CO-SUPERVISORE:
Dr. Chiara Feruglio
Chiara Feruglio

Anno Accademico 2022-2023

Università degli Studi di Trieste

XXXVI CICLO DEL DOTTORATO DI RICERCA IN
FISICA

Cold gas and dust in QSO's host galaxies at $z > 6$

SETTORE SCIENTIFICO-DISCIPLINARE: ASTRONOMIA E ASTROFISICA

DOTTORANDA:
Roberta Tripodi

COORDINATORE:
Prof. Francesco Longo

SUPERVISORE:
Prof. Fabrizio Fiore

CO-SUPERVISORE:
Dr. Chiara Feruglio

Anno Accademico 2022-2023

Abstract

Luminous quasi-stellar objects (QSOs), fueled by accretion onto supermassive black holes (SMBHs), were already in place during the Epoch of Reionisation (EoR), when the Universe was only 0.5-1 Gyr old. In recent decades, *Herschel*, the Northern Extended Millimeter Array (NOEMA), the Very Large Array (VLA), and, notably, the Atacama Large Millimeter/sub-millimeter Array (ALMA) have enabled us to delve into the properties of the gas and dust inside the inter stellar medium (ISM) of the QSO's host galaxies. These properties are pivotal in unraveling the assembly and nature of these early QSOs. In particular, the [CII] $\lambda 158 \mu$m and carbon monoxide (CO) emission lines serve as bright tracers of the gas content in distant galaxies. Detailed examinations of these emission lines, including measurements of the line widths, profiles and velocity maps unveil important information about gas kinematics and dynamics. For instance, the study of the velocity rotation curve allows us to determine the mass budgets of the components of the host galaxy and the total mass of the galaxy, called dynamical mass ($M_{\rm dyn}$). Moreover, a reliable and accurate determination of the dust properties, through the analysis of the continuum emission, enables us to determine the star formation rate (SFR) of the QSO's host galaxy.

Up to now, observations using the instruments on *Herschel*, NOEMA, and ALMA have successfully detected the dust continuum in the host galaxies of many $z \sim 6$ QSOs, revealing far-infrared (FIR) luminosities of 10^{11-13} $L_\odot$ and dust masses of about 10^{7-9} $M_\odot$ (Decarli et al., 2018; Carniani et al., 2019; Shao et al., 2019). However, it is often hard to determine the temperature and mass of the dust precisely, since they are both highly degenerate and the FIR spectral energy distribution (SED) is sparsely probed, often relying on single-frequency continuum detection.

The cold molecular phase is the least explored up to now at $z > 6$. A few tens of quasars at redshift up to $z \sim 6.8$ have been detected in CO, indicating massive molecular reservoirs of dense gas feeding both star formation and nuclear accretion (e.g., Carniani et al., 2019; Decarli et al., 2022). The [CII] line is, instead, the preferred tracer for studying the cold, warm neutral and mildly ionised ISM (Cormier et al., 2015; Olsen et al., 2018) and, thanks to its brightness, for analysing the gas kinematics and dynamics. Through kinematical studies of [CII], dynamical masses have been derived of $< 10^{11}$ $M_\odot$ (e.g., Shao et al., 2017; Neeleman et al., 2021), which place most of the $z \sim 6$ QSOs above the $M_{\rm BH} - M_{\rm dyn}$ local relation by a factor of $\sim 3 - 10$. The questions that naturally arise are if and how high-z QSOs evolve towards the observed local $M_{\rm BH} - M_{\rm dyn}$ relation, and therefore if massive high-z QSO's host galaxies are the progenitor of local massive galaxies.

The goal of this Thesis is to perform a comprehensive analysis of the cold gas and dust in the host galaxies of QSOs at the EoR, shedding light on the properties of these objects and on their formation and evolution, addressing the aforementioned questions. I will present results on a sample of 12 QSOs at $6 \lesssim z \lesssim 7.5$, partially drawn from the HYperluminous QSOs at the Epoch of ReionizatION (HYPERION) survey. HYPERION is a 2.4 Ms XMM-Newton Multi-Year Heritage Programme targeting the titans among $z > 6$ QSOs (Zappacosta et al., 2023), powered by the fastest growing and most massive SMBH at their epoch, and likely assembled from the largest BH seeds, or experienced peculiar, possibly supercritical, mass accretion histories. I will show analyses of NOEMA and ALMA (sub) kpc-resolution observations that allowed us to perform detailed study of the kinematics and dynamics of the gas in the host galaxies of our sample, revealing signatures of mergers, H_2O disks, powerful outflows, and provided the first CO detections at $z > 7$ (Tripodi et al., 2022; Tripodi et al., 2023b; Tripodi et al., 2023a; Tripodi et al., 2023c; Feruglio et al., 2023). We also performed a dynamical decomposition of the rotation curve of QSO J2310+1855 at $z = 6.0031$, based on high-resolution ALMA observations, and we found that the SMBH mass of 5×10^9 $M_\odot$ is not sufficient to explain the high velocities in the central regions. Our dynamical model suggests the presence of a stellar bulge with a mass of $M_{\rm bulge} \sim 10^{10}$ $M_\odot$ in this object, when the Universe was less than 1 Gyr old. Moreover, thanks to unprecedented ALMA observations at very high frequency (670 GHz, Band 9), we accurately modelled the cold dust SED of the QSOs in our sample, and we obtained a reliable and precise determination of the dust properties, such as dust temperature, dust mass and dust emissivity index, and a precise estimate for the SFR of the QSO's host galaxies. We will discuss the importance of high frequency observations in deriving the dust properties and SFR, and the systematics introduced by the presence of the central AGN as an additional source of dust heating.

I will also focus on the properties of 10 quasars in our sample, and discuss the evolutionary scenario of these objects. Indeed, the outstanding mass growth of SMBHs at the EoR and its relation to the concurrent growth of their host galaxies poses challenges to theoretical models aimed at explaining how these systems formed on short timescales (< 1 Gyr). To trace the average evolutionary paths of QSOs and their host galaxies in the plane of BH mass to host mass ($M_{\rm dyn}$), we compare the SFR, derived from the accurate estimate of the dust temperature and the dust mass based on infrared and sub-millimeter (sub-mm) SED, with the BH accretion rate, derived from $L_{\rm bol}$ based on X-ray, optical and ultraviolet SED. Consequently, I will present the study of the evolutionary path of SMBHs and their host galaxies within our sample, with the ultimate goal of gaining a broader understanding of the properties of high-z QSOs.

Alice laughed. ‘There’s no use trying,’ she said. ‘One can’t believe impossible things.’
‘I daresay you haven’t had much practice,’ said the Queen. ‘When I was your age,
I always did it for half-an-hour a day. Why, sometimes
I’ve believed as many as six impossible things before breakfast [...].’

Lewis Carroll, Through the Looking Glass.

CONTENTS

ACKNOWLEDGEMENTS

At the end of every remarkable adventure, one inevitably reflects on the people who have made that adventure worthwhile. In my case, the foremost people who come to mind are my mentors, Fabrizio and Chiara. Words, in truth, cannot adequately express the gratitude I hold for sharing this experience with both of them. For the first time in my still relatively brief academic career, they welcomed me into their large scientific group dedicated to unraveling the puzzling nature of galaxies. I thank them for their thoughtful advice, for their constant support, for always encouraging me to strive for excellence and to share my own ideas. They also 'allowed' me to learn from my mistakes without being judged, or scolded [1]. Each challenge we encountered became a fresh starting point, leading to new questions and new methods, ultimately yielding unexpected results. And a special mention is due to Chiara, who stood by my side during each step of the way, exemplifying kindness, patience, passion about our work, while demonstrating a necessary degree of rigor when circumstances demanded it. I wholeheartedly believe that none of this would have been possible without her support.

Moving forward, a great thank goes to the members of our team in Trieste and abroad whose invaluable contributions enriched my work and shaped my PhD journey: Enrico, Luca, Manuela and Francesco S.

I would like to extend my sincere gratitude to Roberto Maiolino, and all his exceptional research team at the Kavli Institute for Cosmology in Cambridge, where I have spent 4 months. The time and guidance generously provided by Roberto did not go unnoticed. I am truly grateful for the opportunity of living a professionally intense and really enriching experience. Within this context, I would like to acknowledge Jan and Francesco D. for their exceptional mentorship, unwavering openness, and genuine care. As I once mentioned, I aspire to become a postdoc as exemplary as both of you, particularly in mentoring future students. I reserve a special expression of gratitude for Carlotta, Filippo, and Giuseppe, who were, without a doubt, the most wonderful flatmates. Our time together was truly memorable.

I wish to express my deep appreciation to Federico Lelli, who initiated me into the enchanting world of galaxy dynamics. He generously shared his knowledge without anticipating

---

[1] Maybe, I was scolded just a couple of times, well deserved.

anything in return, even though it was not officially his duty. Our shared experiences have significantly enriched both my professional and personal growth.

Returning to the Trieste chapter of my journey, I would like to thank all my colleagues for making this journey vibrant and dynamic, with a special recognition to Jasbir, Francesco G., Vieri, Jacopo, Giova and, last but certainly not the least, Arianna.

Marta, my friend, thank you for sharing this intense experience by my side. I believe I saw you more than my boyfriend, and all of this would not have been the same without you. Thanks for all the endless laughter and whining in our office. Thanks for being inspirational as a strong and independent woman. Thanks Paolo for the funny and interesting discussions about books, board games and movies, and for being supportive. Thank you MaVi for always sharing both the joy and tribulations of the PhD journey. I am also particularly thankful for my closest friends who have always stood by me: Vale, Anto, Mari, Andrea, Cri and Fra.

Finally, I wish to express my deepest gratitude to my family. Thank you Ale, my love, for being my rock. You never let me fall (metaphorically and literally). Thanks mom, dad and bro for supporting my dreams unconditionally. And to my beloved grannies, your constant reminder that I am engaged in the most ‘incredible job on earth’ warms my heart.

To the reader, thanks for investing your precious time in exploring this work. Each of the people I have mentioned has left their unique imprint on its creation. I sincerely hope that you will enjoy this journey too.

ACRONYMS

AGN	Active Galactic Nucleus
ALMA	Atacama Large Millimeter/sub-millimeter Array
BH	Black hole
BLR	Broad line region
BLRG	Broad line radio galaxies
CGM	Circumgalactic medium
CNM	Cold neutral medium
EoR	Epoch of Reionization
FIR	Far Infrared
FUV	Far ultraviolet
GDR	Gas-to-dust ratio
HIM	Hot ionized medium
HSC	Hyper Suprime-Cam
HST	Hubble Space Telescope
HYPERION	HYPerluminous QSOs at the Epoch of ReionizatION
ISM	Interstellar medium
JWST	James Webb Space Telescope

los	Line of sight
LSST	Legacy Survey of Space and Time
MBB	Modified black body
MCMC	Markov chain Monte Carlo
NIR	Near Infrared
NLR	Narrow line region
NLRG	Narrow line radio galaxies
NOEMA	Northern Extended Millimeter Array
OVV	Optically Violently Variable
PAH	Polycyclic aromatic hydrocarbon
PDR	Photo-dissociation region
PLCO	Power law with exponential cut-off
PV	Position velocity
QSO	Quasi-stellar object
SAM	Semi-analytic model
SDSS	Sloan Digital Sky Survey
SED	Spectral Energy distribution
SF	Star formation
SFR	Star formation rate
SLED	Spectral line energy distribution
SMBH	Super massive black hole
SOI	Sphere of influence
SPT	South Pole Telescope
SSP	Subaru Strategic Program
TIR	Total infrared
ULIRG	Ultra-luminous infrared galaxy
VLA	Very Large Array
WIM	Warm ionized medium
WISSH	WISE-SDSS Selected Hyper-luminous

WNM	Warm neutral medium
XDR	Xray-dissociation region

LIST OF FIGURES

LIST OF TABLES

CHAPTER 1

INTRODUCTORY VIEW OF HIGH-REDSHIFT QSOS

The light of normal galaxies in the optical and near infrared (NIR) part of the spectrum is dominated by stars, with small contributions by gas and dust. This is thermal radiation since the emitting plasma in stellar atmospheres is in thermodynamical equilibrium. The spectrum of a galaxy is basically confined to a range between ~ 4000 to ~ 20000 Å, and if the galaxy is actively forming stars, young hot stars extent this frequency range to higher frequency, and the thermal radiation from dust, heated by these new-born stars, extends the emission to far-IR (FIR). However, there are galaxies that show significant emission in the full range from radio wavelengths to the X-ray, and even gamma range. This emission originated mainly from a very small region of such an active galaxy which is called active galactic nucleus (AGN). The energy source of an AGN originates in accretion of matter onto a supermassive black hole (SMBH). This small emission region is structured and consists of multiple components with different physical properties, including a wide range of ratios of radio-to-optical emission strength, their total luminosities and their ratio of nuclear luminosity to that of the stellar light. Some classes of AGNs, in particular the quasars (or QSOs), belong to the most luminous sources in the Universe, and they have been observed out to the highest redshifts (z~11). In this chapter, I will introduce the main characteristics of AGNs, their discovery, their classifications. In particular, I will focus on the properties of quasars and their host galaxies at the highest redshifts, and on the importance of millimeter/sub-millimeter observations for these studies. Then, I will discuss the open question about the co-evolution between the SMBHs and their host galaxies. Finally, I will present the main goals of this Thesis and the sample of quasars that has been studied to fulfill those goals.

1.1 Brief history of discovery and general properties

Once upon a time, in 1908, strong emission lines were discovered in the galaxy NGC 1068 (see Fig. 1.1), which showed a line width of up to ~ 3000 km s^{-1}. However, only the systematic analysis by Carl Seyfert in 1943 drew the focus to this new class of galaxies. The cores of these Seyfert galaxies have an extremely high surface brightness, and the spectrum of their central region is dominated by emission lines of very high excitation. Some of these lines are extremely broad and, when interpreted as Doppler broadening, $\Delta\lambda/\lambda = \Delta v/c$, yields values of up to $\Delta v \sim 8500$ km s^{-1} for the full line width (see Fig. 1.2). The high excitation energy of some of the line-emitting atoms shows that they must have been excited by photons that are more energetic than photons from young stars that are responsible for the ionization of HII-regions, given that the hydrogen lines are often broader than other spectral lines. In 1959, Lodewijk Woltjer argued that the extent of the core of Seyfert galaxies cannot be larger than $r \leq$ 100 pc because they appear point-like on optical images, i.e., they are not spatially resolved. If the line-emitting gas is gravitationally bound, the relation $\mathrm{G}M/r \simeq v^2$ between the central mass $M(< r)$, the separation r of the gas from the center, and the typical velocity v must be satisfied. The latter is obtained from the line width: typically $v \sim 1000$ km s^{-1}. Therefore, with $r \leq 100$ pc, a mass estimate gives

$$M > 10^{10}\left(\frac{r}{100\mathrm{pc}}\right)\mathrm{M}_{\odot}. \tag{1.1}$$

Thus either $r \sim 100$ pc, which implies an enormous mass concentration in the center of these galaxies, or r is much smaller that the estimated upper limit, which then implies an enormous energy density inside AGNs.

An important milestone in the history of AGNs was made with the 3C and 3CR radio catalogs which were completed around 1960. These are surveys of the northern ($\delta > -22°$) sky at 158 and 178 MHz, width a flux limit of $S_{\mathrm{min}} = 9$ Jy[1]. In 1963, Thomas Matthews and Allan Sandage showed that 3C48 is a point-like ('stellar like') source of apparent magnitude $m = 16$ mag. It has a complex optical spectrum consisting of a blue continuum and strong, broad emission lines which could not be assigned to any atomic transition, and thus could not be identified. In the same year, Maarten Schmidt succeeded in identifying the radio source 3C273 with a point-like optical source which also showed strong and broad emission lines at unusual wavelengths. Schmidt could identify the emission lines of the source with those of the Balmer series of hydrogen but at, for that time, an extremely high redshift of $z = 0.158$. Interpreting the redshift as cosmological redshift, the implied absolute magnitude was ~ 100 brighter than normal (spiral) galaxies. Since the optical source had not been resolved but appeared point-like, this enormous luminosity must originate from a small spatial region. With the improving determination of radio source positions, many such quasi-stellar objects (QSOs or quasars) were identified in quick succession, the redshifts of some being significantly higher than that of 3C273.

---

[1] A Jansky is the flux unit commonly used by radio astronomers, where 1 Jy = 10^{-23} erg s^{-1} cm^{-2} Hz^{-1}.

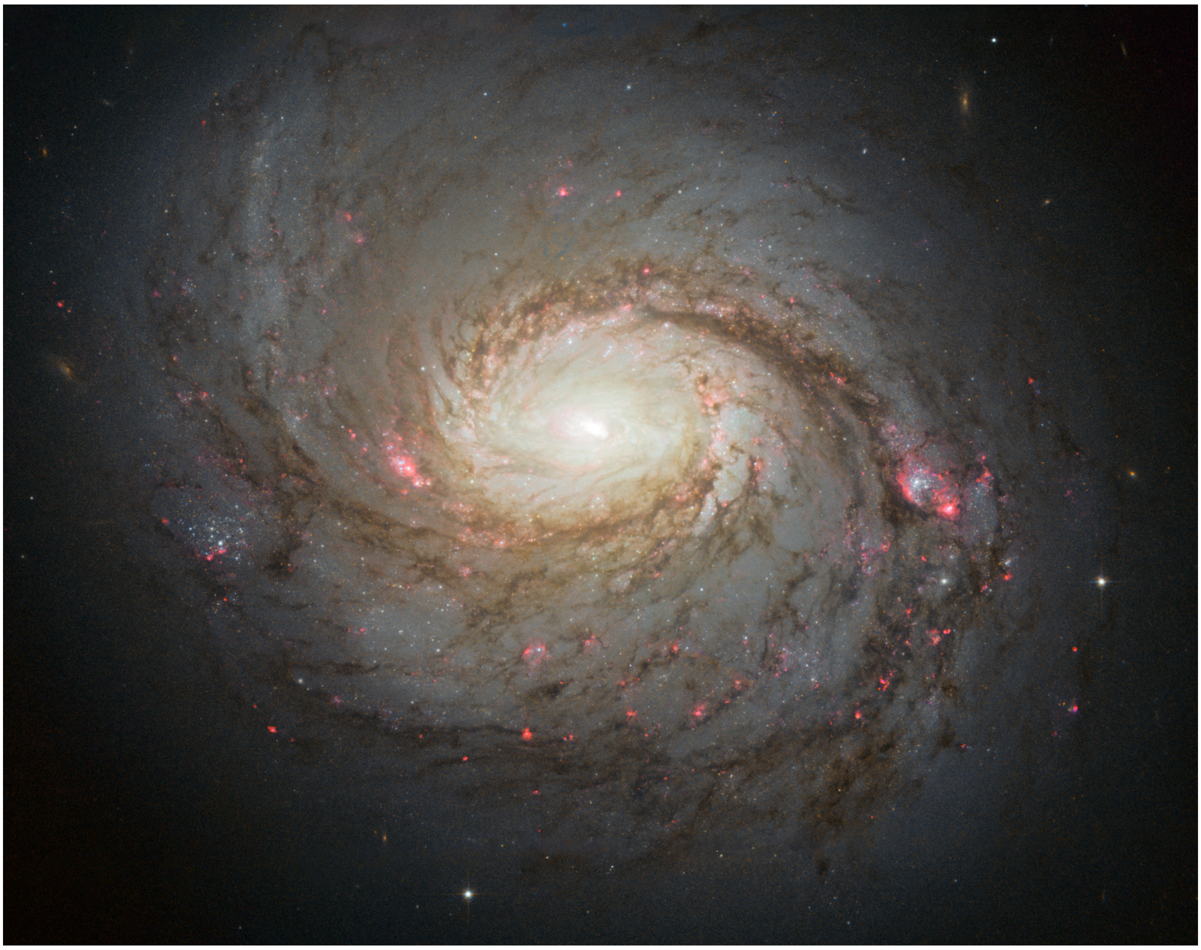

Figure 1.1: *Optical image of the Seyfert galaxy NGC 1068, obtained with the Hubble Space Telescope (HST). Its active nucleus is seen as the intense, high surface brightness center; it is powered by accretion onto a central SMBH with mass* $\sim 15 \times 10^6$ $M_\odot$. *Credit: NASA, ESA & A. van der Hoeven*

1.1.1 The unified model

Quasars are the most luminous members of the class of AGNs and Seyfert galaxies, previously mentioned, are another type of AGNs too. In fact, a wide range of objects are subsumed under the name AGN, all of which have in common strong non-thermal emission in the core of a galaxy (host galaxy). The large variety of appearances of AGNs can be understood, at least to a first approximation, by geometric considerations (Urry and Padovani, 1995). Fig. 1.3 presents the geometric picture of an AGN. Surrounding the central engine, the SMBH, is an accretion disk that emits the bulk part of the optical and UV continuum emission. The central region around the accretion disk is the source of most of the X-ray radiation. Gas clouds above and below the accretion disk are responsible for the broad emission lines. In the plane of the disk, a distribution of gas and dust is present, which can absorb radiation from the inner region of the AGN; this obscuring material is sometimes depicted as a torus, though its geometry is probably more complex. The appearance of the AGN depends on whether the observer is located near the plane of the disk - where the radiation is partly absorbed by the material in

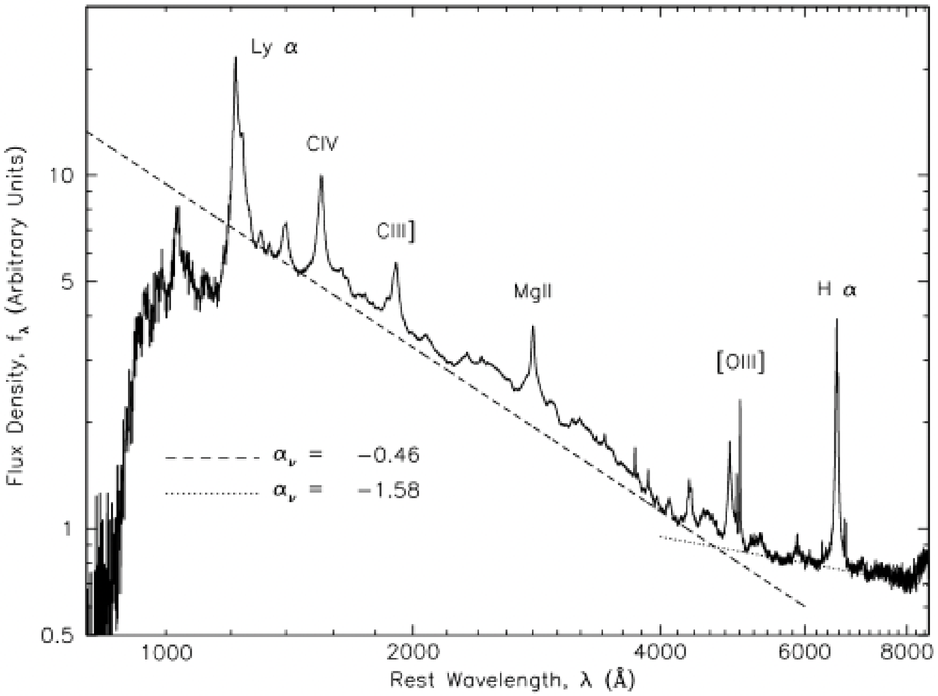

Figure 1.2: *The combined optical spectrum of more than 2200 QSOs from SDSS. The most prominent lines are marked. Here both broad and narrow emission lines are visible. The dashed and dotted lines show the power-law fits of the estimated underlying continuum emission of the QSOs. Taken from Vanden Berk et al. (2001).*

the torus - or placed in a direction closer to the axis of the disk. This concerns in particular the broad line emission, which may be fully obscured for an observer in the plane of the disk. In contrast, the gas responsible for the narrow emission lines is located at much larger distances from the BH, so that it cannot be fully hidden by the obscuring tours. The radio jets are launched very close to the central BH along the direction of the disk axis. The emission of these jets is strongly beamed in the direction of the jet motion, since the velocity in the inner part of these jets is close to the speed of light. This implies that the appearance of the jet depends on how close the line-of-sight (los) of an observer is to the jet axis. If the jet points almost directly at the observer, the jet emission can outshine all the other radiation from the AGN.

In Fig. 1.3, the different green arrows indicate different LOS to observers, and they are labeled with the characteristic AGN class the corresponding observer will see. In the upper half of the figure, it is assumed that the AGN produces strong jet, whereas in the lower part, weaker jets (or none) are assumed. The different classes of AGN are summarized as follows, with a particular focus on the QSOs that are the subject of this Thesis:

- **QSOs**. As already mentioned, QSOs were discovered by identifying radio sources with point-like sources. They emits at all wavelengths, from the radio to the X-ray, or even gamma ray domain of the spectrum (see Fig. 1.4 for a sketch of the broad band energy distribution of the quasar 3C273). The radiation in the different frequencies comes from

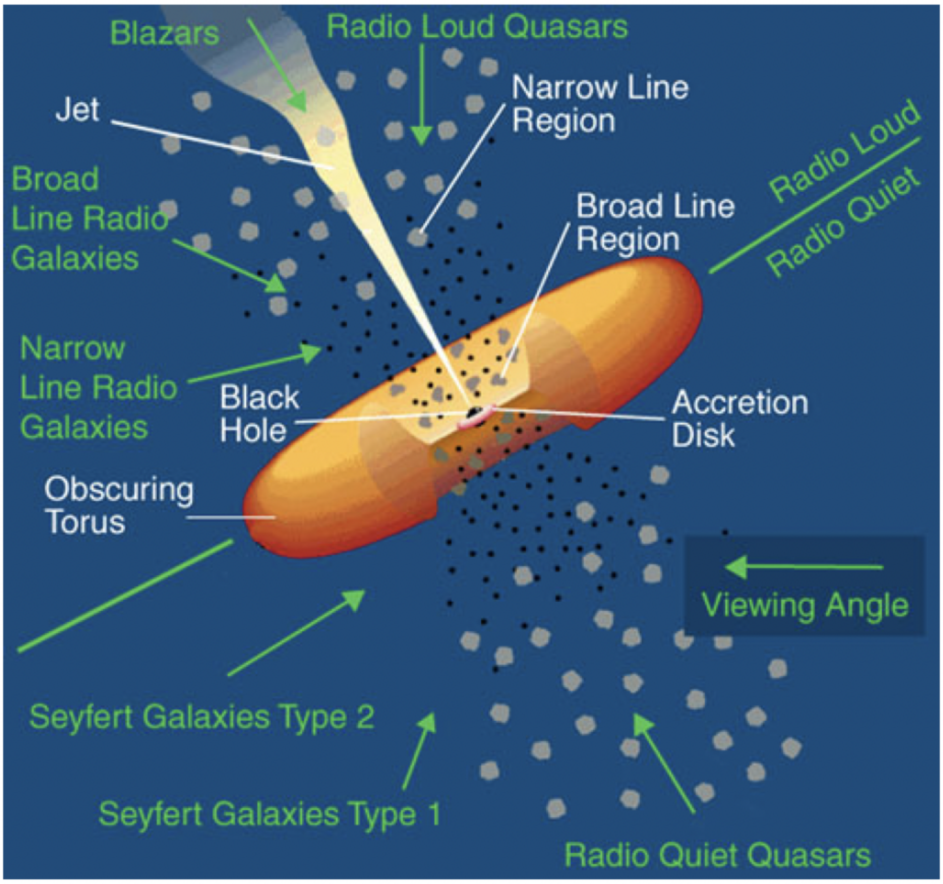

Figure 1.3: *Sketch of our current understanding of the unification of AGN types. Taken from P. Schneider (2015).*

various components. The optical spectrum is very blue; most of the quasars at redshifts $z \leq 2$ have $U - B < -0.3$. Besides this blue continuum, broad emission lines are characteristic of the optical and UV spectrum (see Fig. 1.2). The unusually blue color of quasars made the photometric surveys for point-like sources with a blue $U - B$ color index very successful. Most of these sources were nearly invisible in the radio domain of the spectrum, and therefore are called radio-quiet. Apart from their radio properties, these source appeared to be like quasars. Therefore they were called radio-quiet quasars, or quasi-stellar objects, QSOs. Today this terminology is not considered valid anymore, since radio-quiet quasars also show radio emission if they are observed at sufficiently high sensitivity. Now, the expression QSO encompasses both the quasars and the radio-quiet QSOs. QSOs are the most luminous AGNs. Their core luminosity can be as high as thousand times that of a normal galaxy, therefore they can outshine their host galaxy and appear as point-like on optical images. Hereafter, the terms quasar and QSO are used interchangeably.

- **Seyfert galaxies**. These are the AGNs that were detected first, and their nuclear luminosity is considerably lower than that of QSOs. On optical images they are identified as spiral galaxies which have an extraordinarily bright core whose spectrum shows strong emission lines which are broader than typical velocities in galaxies. We distinguish between Type 1 and Type 2 Seyfert galaxies: the former have both very broad and very narrow emission lines, and the latter only narrow emission lines. The optical spectrum of a Type 1 is similar to that of a QSO and indeed a smooth transition exists between (radio-quiet) QSOs and Seyfert 1. Often both classes are combined under the name Type 1 AGNs.

- **LINERs**. The least luminous and most common type of AGNs are the LINERs, low-ionization nuclear emission-line region. Almost one third of all nearby galaxies contain a LINER in their core, characterized by emission lines from neutral atoms or ions with rather low ionization energies, and the width of emission lines is typically smaller than the narrow emission lines in Seyfert galaxies. It is sometimes questioned whether the LINER emission from the center of spirals is indeed a signature of an AGN, or whether LINERs can be powered by star-formation activity, namely post-AGB stars.

- **Radio galaxies**. These are elliptical galaxies with an active nucleus, and we distinguish between those with and without broad emission lines: broad-line radio galaxies (BLRG) and narrow-line radio galaxies (NLRG), respectively. They are also distinguished according to their radio morphology: Fanaroff-Riley Type I (FR I) sources are brightest close to the core, and the surface brightness decreases outwards; Fanaroff-Riley Type II (FR II) sources have the surface brightness increasing outwards, their luminosity is generally higher than that of FR I sources, and they often have jets.

- **OVVs**. The Optically Violently Variables (OVVs) are one subclass of QSOs that is characterized by the strong and rapid variability of its optical radiation, and their relatively high polarization of optical light. OVVs are usually strong radio emitters, and their radiation also varies in other wavelength regions besides the optical.

- **BL Lac objects**. The class of AGNs called BL Lac objects (on short: BL Lacs) is named after its prototypical source BL Lacertae. They are AGNs with strongly varying radiation and with highly polarized optical radiation, like the OVVs, but without strong emission and absorption lines. This lack of emission lines clearly makes the determination of the redshifts of these sources challenging. The optical luminosity of some BL Lacs varies by several magnitudes if observed over a sufficiently long time period and, in epochs of low luminosity, emission lines are sometimes observed and then BL Lacs appears like an OVV. For this reason, OVVs and BL Lacs are collectively called blazars. All known blazars are radio sources.

In the literature, a more general classification is often found where AGNs are divided in just two classes: type 1 AGNs are those sources with unobscured LOS to their centers, showing both broad and narrow emission lines; type 2 AGNs have heavily obscuration along the LOS

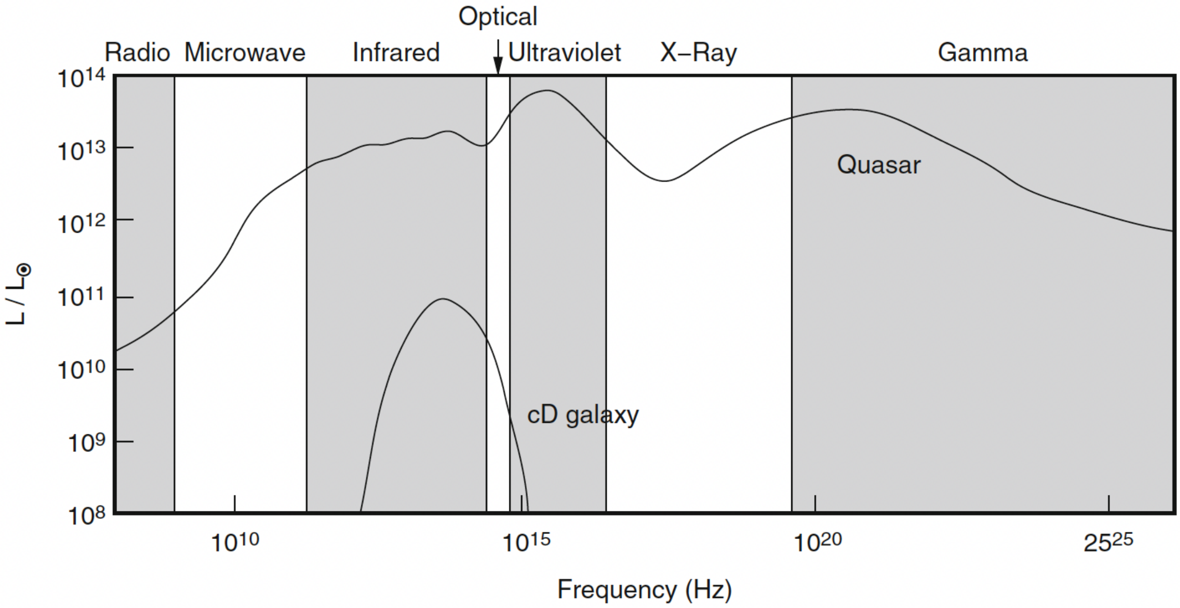

Figure 1.4: *The spectrum of a quasar (3C273) in comparison to that of an elliptical galaxy, in terms of the ratio* $\nu L_\nu / \mathrm{L}_\odot$. *While the radiation from an elliptical is concentrated in a narrow range, the emission of the quasar is observed over a full range of the electromagnetic spectrum, and the energy per logarithmic frequency interval is roughly constant. This demonstrates that the light from the quasar cannot be interpreted as a superposition of stellar spectra, but instead has to be generated by completely different sources and radiation mechanisms. Taken from (P. Schneider, 2015).*

that extincts basically all the optical-UV radiation from the inner parsec (pc), showing narrow emission lines only. We summarize here some of the relevant observational facts for AGNs.

1. The extent of some radio sources in AGNs may reach ≥ 1 Mpc. From this length-scale a minimum lifetime for activity in the nucleus of these objects can be derived, since even if the radio source expands outwards from the core with the speed of light, the age of such a source would be $\tau \geq 10^7$ yr.

2. Luminous QSOs have a luminosity of up to $L_{\mathrm{bol}} \sim 10^{47}$ erg s^{-1}. Assuming that the luminosity does not change substantially over the lifetime of the source (this is not always justified), a total energy can be estimated from the luminosity and the minimum age,

$$E \geq 10^{47}\ \mathrm{erg\ s^{-1}} \times 10^{7}\ \mathrm{yr} \sim 3 \times 10^{61}\ \mathrm{erg}. \tag{1.2}$$

3. The luminosity of some AGNs varies by more than 50% on time-scales of a day. From this variability time-scale, an upper limit for the spatial extent of the source can be determined, because the source luminosity can change substantially only on such time-scales where the source as a whole is in causal contact. This yields a characteristic extent of the central source of $R \leq 1$ lightday $\sim 3 \times 10^{15}$ cm.

1.1.2 The structure of an AGN

Fig. 1.3 also shows the physical structure of an AGN with its components, as given by the currently accepted model. All these components are concentrated in the nucleus of the host galaxy i.e., in a very small volume. Due to observational limitations, it has been quite hard to investigate the innermost region, on ~ parsec scales, directly. For instance, just a couple of years ago, we obtained the first direct image of the region immediately surrounding the SMBH with interferometric techniques, using the Event Horizon Telescope. It is of fundamental importance to observe and study all the components of an AGN, in order to understand the mechanisms that drive their emissions and that generate their properties. In the following paragraphs, I will briefly present all the components of the AGN, summarizing the most important characteristics that the scientific community have discovered so far.

The central engine. The SMBH is the central engine of the AGN, having mass in the interval $\sim 10^6 - 10^{10}$ M$_\odot$. The other two properties defining a BH are its angular momentum and its charge, the latter usually assumed to be zero for neutral BHs. The angular momentum is described by the adimensional parameter per unit mass, the spin, that can assume values between $+1$ and -1. Given that this component is highly involved in the results of this Thesis, Sect. 1.1.3 is devoted to explain the reason for the presence of a SMBH and its most important properties.

Accretion disk. Accretion disks in galactic centers are naturally formed by infalling gas that sinks into the central plane of the galaxy while retaining most of its angular momentum. The assumption is that the viscosity in the disk is sufficient to provide the necessary mechanism to transfer outward the angular momentum of the gas and to allow it to spiral into the center, losing a considerable fraction of its gravitational energy on the way. The energy lost during accretion can be converted into electromagnetic radiation with high efficiency (6%-42%), and thus large luminosities can be produced for a modest amount of accretion, making AGN the most powerful non-explosive objects in the Universe. AGN disks can be optically thick or thin, depending on the column density, the level of ionization of the gas and the mass accretion rate (see e.g., Netzer, 2013). The overall emission can be explained as the sum of different temperature black body spectra and the total spectrum takes the shape of a power law with a spectral index equal to 1/3. In particular, for a disk surrounding a 10^8 M$_\odot$ - BH accreting at the Eddington rate, the maximum temperature is roughly T $\sim 10^5$ K and most of the emission is in the range 30-300 nm, which is the UV-optical part of the spectrum.

Hot corona. In the outer layers of the accretion disk, above the optically thick part, in analogy to stars, a hot layer of gas forms, named a corona. The gas in the corona is thin and cannot cool efficiently, implying higher temperatures than in the disk, reaching $T \sim 10^8 - 10^9$ K. It has been proposed as a mechanism to explain the energetic X-ray emission of AGN. The soft thermal photons produced by the disk are up-scattered to their observed X-ray energy by the hot electrons in the corona. This is still an open problem.

The broad line region. One of the most surprising characteristics of type 1 AGNs are the presence of very broad emission lines. Interpreted as Doppler velocities, the corresponding width of the velocity distribution of the components in the emitting region is of order $\Delta v \leq$ 10000 km s^{-1}. These lines cannot be due to thermal line broadening because that would imply temperatures of $T \sim 10^{10}$ K and therefore atoms would be fully ionized, not producing any emission lines. Therefore, the observed line width is interpreted as Doppler broadening, and the high velocities are indicators of the presence of a strong gravitational field, as would occur in the vicinity of a SMBH. The region in which these broad emission lines are produced is called broad line region (BLR). This is formed by gas clouds with large column density ($\sim 10^{23}$ cm^{-2}) and high-density ($\sim 10^{10}$ cm^{-3}), situated around an accreting SMBH. In these conditions we find allowed and semi-forbidden transitions, such as HeII-III, OIV-VI, CIII-IV, MgII, Hα, Lyα. The density is high enough to suppress all optical forbidden lines. The absence of forbidden lines is then used to derive a lower limit for the gas density, and the occurrence of semi-forbidden lines yields an upper bound for the density.

Broad emission lines are also extremely important for the derivation of the mass of the accreting SMBH (see also Sect. 1.1.3). For instance, Fig. 1.5 shows 10 faint broad-line AGNs observed for the first time with James Webb Space Telescope (JWST)/NIRSpec deep spectroscopy (Harikane et al., 2023). Among the 185 galaxies at $z_{\rm spec} = 3.8 - 8.9$ confirmed with NIRSpec, they revealed 10 type 1 AGNs at $z = 4.015 - 6.936$ whose broad component is only seen in the permitted Hα line and not in the forbidden [OIII]λ5007 line, which is detected with greater significance than Hα. The broad Hα line widths of FWHM $\simeq$ 1000 - 6000 km s^{-1} suggest that the AGNs have black holes with $M_{\rm BH} \sim 10^6 - 10^7$ M$_\odot$, remarkably lower than those of low-luminosity quasars previously identified at $z > 4$ with ground-based telescopes. A high fraction of the broad-line AGNs ($\sim$ 5%), higher than $z \sim 0$, indicates that a number density of such faint AGNs is higher than an extrapolation of the quasar luminosity function, implying a large population of AGNs including type 1 and type 2 in the early universe.

The narrow line region. Most AGNs show narrow emission lines, with typical width of $\sim$ 400 km s^{-1}. The region were these line are produced is called narrow line region (NLR). It has a size of $r \sim 100$ pc, and has a biconical shape, as if the ionization of the NLR by the AGN is not isotropic but is confined largely to a cone-shaped region, called ‘ionization cone’. The strongest line from the NLR is, besides Lyα and CIV, the forbidden [OIII] line at $\lambda = 5007$ Å. The existence of forbidden lines implies that the gas density in the NLR is significantly lower than in the BLR. The gas is assumed to be ionized by UV-radiation from the central continuum source. The line ratios of allowed and forbidden lines yield $n_e \sim 10^4$ cm^{-3} and $T \sim 15000$ K for the typical density and temperature of the gas. Like the BLR, the properties of the NLR are not homogeneous but vary with the radius.

Obscuring torus. A basic concept of the unified scheme centers on the presence of a geometrically and optically thick gas cloud, often referred to as the torus, enveloping the broad-line regions along the equatorial plane in an AGN. This obscuring torus plays a pivotal role in our

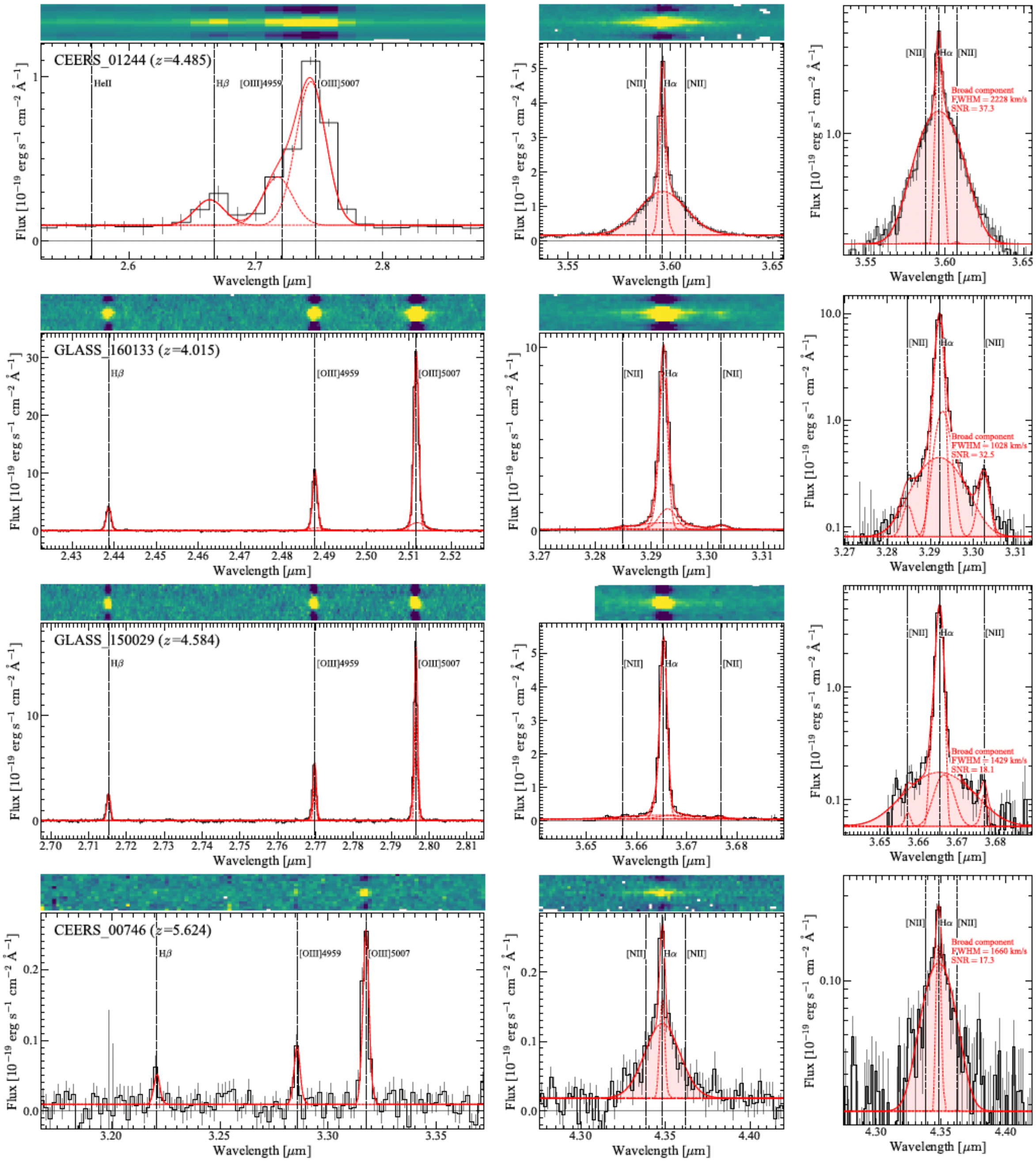

Figure 1.5: *NIRSpec spectra of 4 AGNs taken from Harikane et al. (2023). For each object, the left and middle panel show the spectra around Hβ+[OIII] and Hα+[NII], respectively. The 2D and 1D spectra are shown in the top and bottom panels, respectively. The red dashed line with the shaded region shows the best-fit broad-line component and the other red dashed lines show the best-fit narrow components. The right panels show the spectra around Hα+[NII] with the logarithmic scale. The broad-line components only seen in Hα, which are detected with higher S/N ratio than [OIII], indicates that these objects are type 1 AGNs.*

understanding of AGN, acting as a barrier to broad-line emissions when our line of sight aligns with the equatorial plane, resulting in the classification of type 2 objects. Conversely, when viewed pole-on, both the narrow and broad emission line regions become directly observable, leading to a type 1 classification. The torus also elucidates the observed ionization cones in AGN, where the ionizing radiation is shadowed by the torus, manifesting as biconical shapes in emission lines and polarized flux. Moreover, the torus contributes to X-ray variations, partially absorbing soft X-rays as they traverse this optically and geometrically dense structure (Maiolino and Risaliti, 2007). Comprising dust and gas, the torus extends from approximately 0.1 to 10 parsecs from the central SMBH. The dusty component consists of carbonaceous and amorphous silicate grains, while the gaseous component spans a wide range of states, from fully ionized to neutral and molecular. Typical gas densities range from 10^4 to 10^7 cm^{-3}, with velocities around 1000 km s^{-1}. Its inner boundary is determined by the dust sublimation radius, where the medium is ionized by the central source, while the outer edge is influenced by the SMBH's gravitational sphere of influence, approximately 10 parsecs for nearby systems. Although the torus' expected geometry is toroidal, ongoing research suggests a clumpy distribution of dust within it (e.g., Jaffe et al., 2004; Burtscher et al., 2013; F. Combes et al., 2019).

Jets. Jets are extended, collimated and relativistic linear structures, shown by ~10% of powerful AGN. These enigmatic astrophysical phenomena exert a significant influence on the energy balance and evolutionary trajectory of AGN. AGN jets primarily consist of electrons and positrons that are accelerated to velocities near the speed of light, giving rise to synchrotron and inverse Compton radiation spanning the entire electromagnetic spectrum, ranging from radio to gamma-rays. The mechanisms responsible for initiating and confining these jets are subjects of ongoing investigation, with magnetic fields and interactions with accretion disks being prominent considerations. The most robust AGN jets propagate into the interstellar and intergalactic medium, extending up to Mpc scales, far surpassing the dimensions of the stellar component by tens of kpc. Interactions between these jets and the surrounding environment result in the formation of prominent features such as hot spots and large-scale radio lobes.

1.1.3 The reason for a SMBH and its properties

We have previously mentioned that the energy production in AGNs must be related to a SMBH in its center. Indeed, if considering that the energy is produced by nuclear fusion, its maximum efficiency[2] is too low to generate the energy derived in Eq. 1.2. The only known mechanism yielding to larger efficiencies is gravitational energy production. Through the infall of matter onto a central BH, potential energy is converted into kinetic energy. If it is possible to convert part of this inward-directed kinetic energy into internal energy and subsequently to emit this in the form of radiation, ϵ can be larger than that of thermonuclear processes. From the theory

---

[2] The maximum efficiency of a nuclear fusion, by burning hydrogen into iron, is $\epsilon \leq 0.8\%$, where ϵ is defined as the mass fraction of fuel that is converted into energy, according to $E = \epsilon\, mc^2$.

of accretion onto BHs, a maximum efficiency of $\epsilon \sim 6\%$ for accretion onto a non-rotating BH (also called a Schwarzshild hole) is derived. A BH with the maximum allowed angular momentum can have an efficiency of $\epsilon \sim 29\%$.

Accretion onto BHs and the associated release of the binding gravitational energy are important sources of radiation. Two fundamental quantities that are related to such processes are the Eddington luminosity and the Eddington accretion rate. Assuming a central point source with mass $M_{\rm BH}$, total luminosity $L_{\rm BH}$, and a fully ionized gas at a distance r from the source, the radiation pressure force acting on a gas particle is

$$F_{\rm rad} = \frac{N_e \sigma_{\rm T} L}{4\pi r^2 c}, \tag{1.3}$$

where N_e is the electron density and $\sigma_{\rm T}$ is the Thomson cross section. The gravitational force per particle is

$$F_{\rm grav} = \frac{G M_{\rm BH} \mu m_p N_e}{r^2}, \tag{1.4}$$

where μ is the mean molecular weight. Spherical accretion of fully ionized gas onto the central object can proceed as long as $F_{\rm grav} > F_{\rm rad}$ therefore, for a pure hydrogen gas, we have

$$L < \frac{4\pi G c \mu m_p}{\sigma_{\rm T}} M_{\rm BH} =: L_{\rm Edd} \approx 1.26 \times 10^{38} \left(\frac{M_{\rm BH}}{\rm M_\odot}\right) \rm erg\ s^{-1}, \tag{1.5}$$

where we defined the Eddington luminosity as the limiting requirement for accretion (i.e., $F_{\rm grav} = F_{\rm rad}$) onto a BH of mass $M_{\rm BH}$.

We can invert this argument, having that if a luminosity L is observed, we conclude $L_{\rm Edd} > L$ or

$$M_{\rm BH} > M_{\rm Edd} := \frac{\sigma_{\rm T}}{4\pi G c m_p} L \approx 8 \times 10^7 \left(\frac{L}{10^{46}\ \rm erg\ s^{-1}}\right) \rm M_\odot. \tag{1.6}$$

Therefore, a lower limit for the mass of the SMBH can be derived from the luminosity. For QSOs typical masses are $M_{\rm BH} \geq 10^8$ $\rm M_\odot$. In the above definition of Eddington luminosity, we have implicitly assumed that the emission of radiation is isotropic. In principle, if the emission is highly anisotropic, the luminosity can exceed the Eddington luminosity. A geometrical concept for this would be, for instance, accretion through a disk in the equatorial plane and the emission of a major part of the radiation along the polar axes.

If the conversion of infalling mass into energy takes place with an efficiency ϵ, the accretion rate can be determined,

$$\dot{M}_{\rm BH} = \frac{L}{\epsilon c^2} \approx 0.18 \frac{1}{\epsilon} \left(\frac{L}{10^{46}\ \rm erg\ s^{-1}}\right) \rm M_\odot\ yr^{-1}. \tag{1.7}$$

If L is measured in units of the Eddington luminosity, we obtain $\dot{M}_{\rm BH} = L/L_{\rm Edd} \times \dot{M}_{\rm Edd}$, where the Eddington accretion rate as been defined as

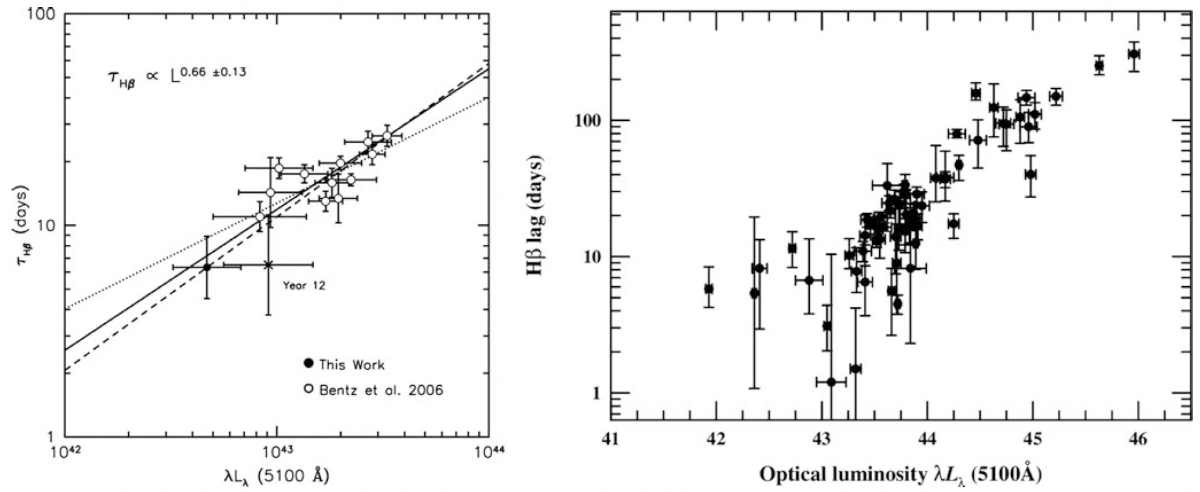

Figure 1.6: *Left panel: for the source NGC5548, the time lag between line- and continuum variations are shown for the Hβ line, as a function of the optical continuum luminosity of the source. The data were obtained by monitoring this galaxy for almost two decades. Right panel: measured time lags of the Hβ line as a function of optical luminosity, for a sample of 35 AGNs with reverberation mapping. The slope of the best-fitting power law is again 0.6 ± 0.1 as for the case of NGC5548. Taken from (P. Schneider, 2015).*

$$\dot{M}_{\rm Edd} = \frac{L_{\rm Edd}}{\epsilon c^2} \approx \frac{1}{\epsilon}\, 2 \times 10^{-9} \left(\frac{M_{\rm BH}}{\rm M_\odot} \right) {\rm M_\odot\ yr^{-1}}. \tag{1.8}$$

The Eddington accretion rate is the maximum accretion rate if isotropic emission is assumed, and it depends on the assumed efficiency ϵ. Estimating a characteristic time in which the mass of the SMBH will significantly increase,

$$t_{\rm Edd} := \frac{M_{\rm BH}}{\dot{M}_{\rm BH}} \approx \epsilon \left(\frac{L}{L_{\rm Edd}} \right)^{-1} 5 \times 10^8 \;\; yr^{-1}, \tag{1.9}$$

i.e., even with efficient energy production ($\epsilon \sim 0.1$), the mass of a SMBH can increase greatly on cosmologically short time-scales by accretion. The various mechanisms of SMBH formation will be extensively discussed in Sect. 1.3.

BH mass estimates. We just derived a lower limit for the BH mass however, given the importance of this quantity for this work (see Sect. 1.3 and Sect. 5.1), I will briefly illustrate some methods used to determine the BH mass.

One of the most accurate methods for estimating the BH mass in AGNs comes from reverberation mapping, which directly examine the extent of the BLR. This observational technique utilizes the fact that heating and ionization of the gas in BLR are both caused by the central continuum source of the AGN. Since the UV radiation varies, we expect corresponding variations of the physical conditions in the BLR. Due to the finite extent of the BLR, the observed variability in the lines will be delayed in time compared to the ionizing continuum. This delay Δt can be identified with the light travel time across the BLR, $\Delta t \sim r_{\rm BLR}/c$. From the observed correlated variabilities of continuum and line emission, Δt can be determined for different line transitions, and so the corresponding values of r_{BLR} can be estimated. Furthermore, the relative line width $\Delta\lambda/\lambda$ can be measured, and can be related to the characteristic velocity dispersion, σ. Assuming that the gas is virialized, or moving approximately on Keplerian orbits around the BH, the BH mass can be estimated to be $M_{\mathrm{BH}} = f(r_{\mathrm{BLR}})r_{\mathrm{BLR}}\sigma^2/G$, where $f \sim 1$ for circular orbits and for the observer being located in the plane of the orbit. However, reverberation mapping is a fairly expensive observing technique, and the effort required increases with AGN luminosity. Moreover, there is not enough information to determine $f(r_{\mathrm{BLR}})$ from the line profile of individual objects. That is why another method is used, based on the well-established correlation between the BH mass and the width of stellar absorption lines σ_* in the bulge of the galaxy, and on an empirical relationship between the size of the BLR determined from reverberation studies, r_{BLR}, and the continuum luminosity.

From the $M_{\mathrm{BH}} - \sigma_*$ correlation, one can obtain an empirical estimate of $f(r_{\mathrm{BLR}})$. The use of $f(r_{\mathrm{BLR}})$ to estimate M_{BH} in sources where σ_* is not known is based on the assumption that the value is typical of all AGNs, of low and high luminosity, of small and large r_{BLR}, and of all inclinations to the los. This is a major source of uncertainty and scatter in the entire M_{BH} determination process. From reverberation studies, a scaling relation between the size of the BLR for a given transition and the optical continuum luminosity has been found of the form $r_{\mathrm{BLR}} \propto L^{\gamma}$. Fig. 1.6 shows how this γ is computed for the case of NGC5548, obtaining $\gamma \sim 0.6$ for the Hβ emission line. Since r_{BLR} cannot be determined from reverberation studies for every sources, especially the more luminous and high-redshift ones, the continuum luminosity is often used as a proxy of r_{BLR}. Therefore, we can estimate the BH mass using the full width at half maximum (FWHM) of broad emission lines, which gives an estimate for the velocity of the gas clouds in the BLR, and the continuum luminosity as follows

$$\frac{M_{\mathrm{BH}}}{\mathrm{M}_{\odot}} = 10^{\alpha}\left(\frac{\mathrm{FWHM}_{\mathrm{line}}}{1000\ \mathrm{km\ s}^{-1}}\right)^{\beta}\left(\frac{\lambda L_{\lambda}}{10^{44}\mathrm{erg\ s}^{-1}}\right)^{\gamma}, \tag{1.10}$$

where the best fit values for the scaling parameters α, β, γ depend on the respective emission lines and monochromatic luminosity L_{λ}. For instance, in high-z QSOs, considering the Hβ line one has $\alpha = 6.91, \beta = 2, \gamma = 0.50$ at $\lambda = 5100$Å or, considering the MgII line, it is found $\alpha = 6.86, \beta = 2, \gamma = 0.50$ at $\lambda = 3000$Å or, for the CIV line, $\alpha = 6.71, \beta = 2, \gamma = 0.53$ at $\lambda = 1350$Å (Eilers et al., 2022; Coatman et al., 2017; Vestergaard and Peterson, 2006; Vestergaard and Osmer, 2009a). Equations of this form are used to obtain the so-called single-epoch virial mass estimates of M_{BH} with a single continuum point to obtain L and a single line width to obtain FWHM. These relationships are calibrated to the most recently updated and robust mass determinations from reverberation mapping. The majority of reverberation mapping studies have been conducted using Hβ on low redshift AGN (e.g., Bentz et al., 2013; Barth et al., 2015; Grier et al., 2017; Malik et al., 2023). For high-z sources, the MgII or CIV line is often utilised. However, this involves applying additional scaling from the Hβ line to formulate the virial mass based on other lines (e.g., Shen et al., 2011). There have been efforts to establish the $r_{\mathrm{BLR}} - L$ relation for high redshift AGN (e.g., Shen et al., 2019; Homayouni et al., 2020; Yu et al., 2023), though it is still debatable whether the single-epoch mass from these lines are reliable or will need further correction (e.g., Shen et al., 2008; Shen and Kelly, 2012; Shen and X. Liu, 2012) since they might be affected by non-virial component due to the stratified BLR of the different lines (Murray et al., 1995; Shen et al., 2008; Yong, Webster, and A. L. King, 2016; Yong et al., 2017). These relations have been used to measure BH masses for thousands of sources with an estimated uncertainty of about factor 2-3 (i.e. dex=0.3-0.5, Shen et al., 2013), when using either Hβ or MgII. Estimates based on the high ionization CIV line are very uncertain (> 0.5 dex), as this line shows large velocity offsets, implying significant non-virialized motions (Mejıéa-Restrepo et al., 2018; Park et al., 2017). Moreover, there is mounting evidence that large CIV blueshifts (> 2000 km s^{-1}) are more common at $z > 6$ than at lower redshifts (e.g., Meyer, Bosman, and Ellis, 2019; Schindler et al., 2020; Matthews et al., 2023).

Determining the BH mass from broad MgII, Hβ, or CIV emission lines is feasible only for not heavily obscured type 1 AGNs, i.e., when lines coming from the BLR can be observed. This is the case for the sample of QSOs investigated in this Thesis. However, it is worth mentioning methods for estimating the BH mass in case of either type 2 AGNs or obscured and low-luminosity type 1 AGNs. Notably, type 2 AGNs represent the majority of the AGN population (F. La Franca et al., 2005). In order to measure the BH masses of type 2 AGNs, virial relations have been calibrated based on the hard X-ray luminosity and on the width of the most relevant NIR (0.8–2.5 μm) and optical emission lines (F. La Franca et al., 2015; Fabio La Franca et al., 2016; Onori et al., 2017; Ricci et al., 2017). In particular, Ricci et al. (2017) calibrated relations between the FWHM$_{\rm NIR}$ of the most relevant NIR emission lines (Paα, Paβ, HeI $\lambda 1.083 \mu$m) and the intrinsic hard X-ray luminosity, L_X, of the type $M_{\rm BH} \propto \mathrm{FWHM}^2_{\rm NIR} L^0_X.5$. Using those relations, Onori et al. (2017) derived virial measurements of the BH mass of a sample of 17 type 2 AGNs. They found that at fixed X-ray luminosity type 2 AGN have 0.5 dex smaller BH masses than type 1 AGN. This disagrees with the standard AGN unification scenarios, in which type 1 and type 2 AGN are the same objects observed along different viewing angles with respect to a toroidal absorbing material. Their findings instead suggests an alternative scenario (see e.g., Hopkins et al., 2005) in which type 2 AGNs represents the preceding stage of a type 1 AGN.

1.1.4 The new high-z frontier

In the last decade, the quasar redshift frontier is increasingly expanding as a result of new sky surveys and with the recent advent of JWST. The first discoveries of QSOs at $z > 4$ were dated back in the 1980s, thanks to the implementation of the drop-out selection techniques (e.g., Warren et al., 1987). Nowadays, about 1000 QSOs have been discovered at $z > 5$, and more than 200 at $z > 6$ using the Sloan Digital Sky Survey (SDSS) and other wide-field near-infrared sky surveys such as UKIDSS (e.g., Fan et al., 1999; Fan et al., 2001; Mortlock et al., 2011). The quasar redshift frontier currently stands at $z = 10.1$ (Bogdán et al., 2023), more discoveries

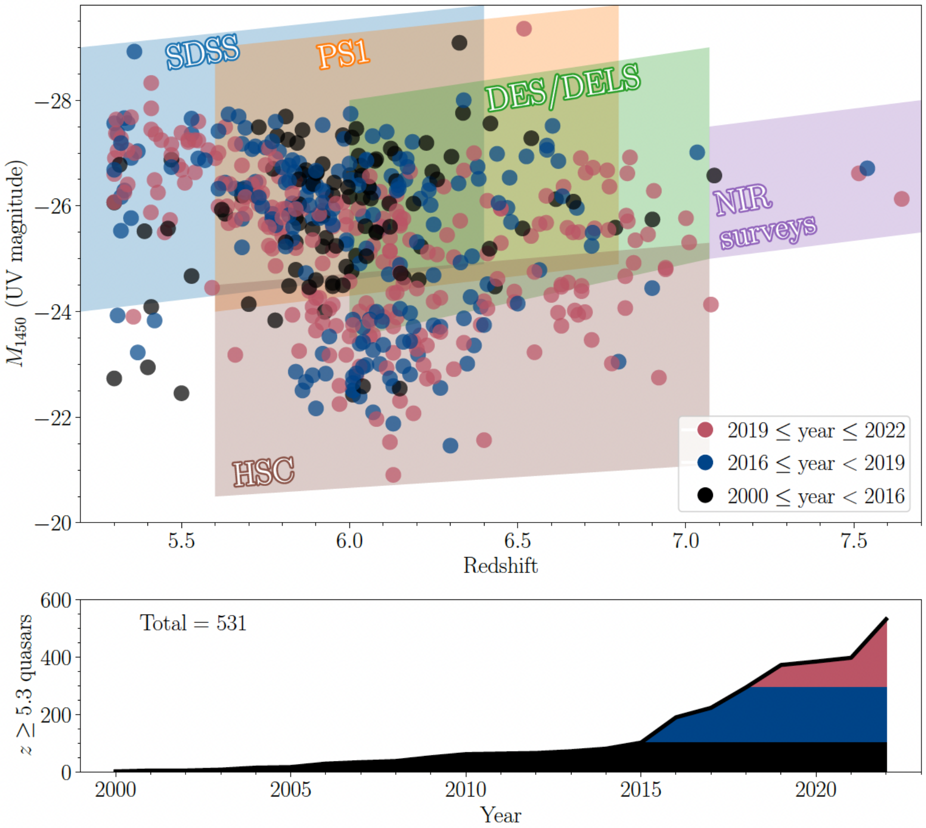

Figure 1.7: *Distribution of all known $z \geq 5.3$ QSOs in the absolute magnitude-redshift plane (top panel). The shaded areas are the parameter space probed by selected large QSO survey programs. The bottom panel shows the cumulative number of QSOs known at $z \geq 5.3$ as a function of year of publication. Taken from Fan, Banados, and Simcoe (2022).*

at higher redshifts are expected from JWST observations. For instance, an extensive analysis of the JWST-NIRSpec spectrum (from the JADES survey) of GN-z11, which is an exceptionally luminous galaxy at $z = 10.6$ (Oesch et al., 2016), revealed the detection of the high ionization [NeIV]λ2423 transition and semi-forbidden nebular lines tracing gas densities higher than 10^{10} cm^{-3}, typical of the BLR of an AGN (Maiolino et al., 2023). This can potentially shift the frontier to $z \sim 11$. Also ESA's Euclid mission will soon provide deep NIR photometry that has been not possible with ground based observations.

Surveys of quasars at the highest redshift are extremely challenging. Quasars at and near the Epoch of Reionization (EoR) are among the rarest objects in the Universe. Indeed, the SDSS $z \sim 6$ sample covers more than 11000 deg^2, but contains only 52 quasars (Jiang et al., 2016). Most high-z quasar survey are based on Lyman break dropout selection using optical and NIR photometric survey data. However, other population of objects, such as compact early-type intermediate-redshift galaxies, have similar optical and NIR colors, and these contaminant populations outnumber high-z QSOs by 2-4 orders of magnitude in deep photometric surveys (Euclid Collaboration et al., 2019). Therefore, effective quasar surveys require a balance between selection efficiency and completeness. Fig. 1.7 presents the distribution of all published $z \geq 5.3$ QSOs, as of December 2022, on the absolute magnitude-redshift plane,

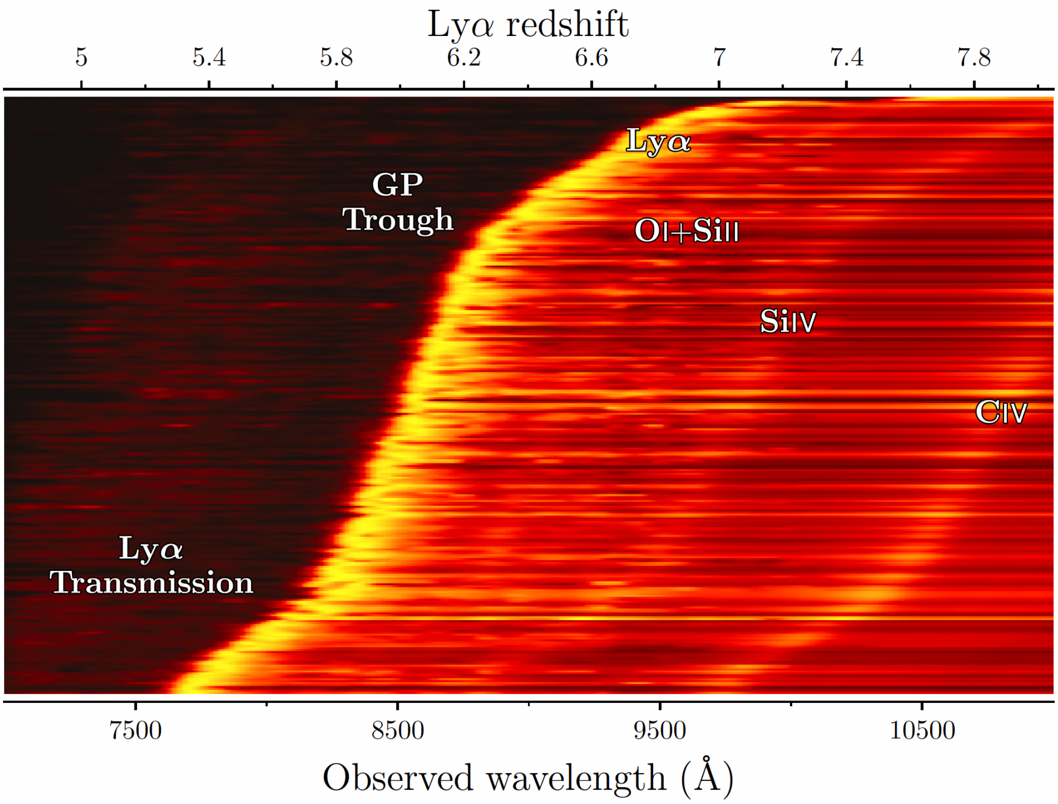

Figure 1.8: *2D image representation of 527/531 of all published spectra of $z \geq 5.3$ QSOs. Traces of major emission lines are labeled. Taken from Fan, Banados, and Simcoe (2022).*

highlighting the major survey programs from which most of these quasars are selected (Fan, Banados, and Simcoe, 2022). Given the difficulties in the search for high-z QSOs, up to now quasars surveys are generally biased towards higher luminosities. Selection of fainter QSOs requires photometric observations on large aperture telescopes: the SHELLQs project (Matsuoka et al., 2022) is based on the Hyper Suprime-Cam (HSC) survey on the 8.2m Subaru Telescope and discovered only 69 quasars at $5.8 < z < 7.0$ in the low luminosity regime, down to $M_{1450} \sim -21$ mag. Now, with JWST the intermediate and low-luminosity populations of QSOs will be fully and properly explored for the first time.

Fig. 1.8 shows a 2D image representation of all spectra of QSOs at $z \geq 5.3$ known up to Dec. 2022 (Fan, Banados, and Simcoe, 2022). Each row is the 1D spectrum of a QSO, ordered in ascending redshift. The flux level of each column is normalized by its Lyα flux. The image shows how the QSO Lyα emission line moves to NIR wavelengths as the redshift increases from $z \sim 5$ to $z > 7$. On the blue side of the Lyα emission, the spectra show the extent of the highly ionized QSO proximity zone, where the flux does not immediately drop to zero. At higher redshift the Gunn-Peterson absorptions get increasingly stronger and this effect is complete at $z > 6$. On the red side of Lyα emission, broad emission lines such as OI+SiII, SiIV+OIV] and CIV are clearly visible.

The current quasar redshift forntier is represented by the three luminous QSOs known at $z > 7.5$, selected using a combination of NIR, optical, and MIR (WISE) surveys: J1342+0928 at $z = 7.54$ (Bañados et al., 2018); J1007+2115 at $z = 7.52$ (J. Yang et al., 2020); and J0313-1806 at z=7.64 (F. Wang et al., 2021). This frontier will be expanded with the advent of the Legacy Survey of Space and Time (LSST) by the Vera C. Rubin Observatory, which will cover the southern sky at optical wavelengths to unprecedented depths, and of the NASA's Nancy Grace Roman Space Telescope, which will cover a smaller area in its High Latitude Survey but reaching two magnitude deeper.

1.2 Properties of the ISM of high-z QSO's host galaxies

AGNs are considered the central engine of otherwise quite normal galaxies. This nuclear activity is nourished by accretion of matter onto a SMBH. For long time, however, it was not clear as to whether QSOs are also hosted in a galaxy. Their high luminosity made the surrounding or host galaxy difficult to identify on images taken from the ground, with their resolution limited to ~ 1 arcsec. In the 1980s, the host galaxies of some QSOs were detailed imaged for the first time with the HST (see Fig. 1.9), pushing these studies even at $z = 2 - 3$. In these investigations, it was also found that the host galaxies of QSOs are often heavily disturbed, e.g., by tidal interactions with other galaxies or even by merging processes. These mechanisms are essential for the gas to flow towards the center of the galaxy, and also seem to increase the star formation rate (SFR), likewise in starburst galaxies. Some of the information was detailed enough to enable systematic studies of the morphology, color, and even stellar population of the hosts. Nowadays, these properties are known for numerous low-z AGNs, also thanks to the vast improvement in the performance of adaptive optics systems on giant ground-based telescopes. The picture that emerged suggests that the morphology of most AGN host galaxies are similar and even indistinguishable from those of inactive galaxies at the same redshifts, as well as for the color and stellar populations (Netzer, 2013). On the other hand, accurate information about higher-z host is difficult to obtain and more uncertain. The detection of starlight from the host galaxies of quasars during the EoR ($z > 6$) has been elusive, even with deep HST observations. The current highest redshift quasar host detected, at $z = 4.5$ (Peng et al., 2006), required the magnifying effect of a foreground lensing galaxy. Low-luminosity quasars from the HSC Subaru Strategic Program (HSC-SSP, Aihara et al., 2018) mitigate the challenge of detecting their underlying, previously-undetected host galaxies. Recently, Ding et al. (2022) reported rest- frame optical images and spectroscopy of two HSC-SSP quasars, J2236+0032 and J2255+0251, at $z > 6$ with JWST. Using NIRCam imaging at 3.6μm and 1.5μm and subtracting the light from the unresolved quasars, they found that the host galaxies are massive (stellar masses of $13\times$ and 3.4×10^{10} $M_\odot$, respectively), compact, and disk-like. As shown in Fig. 1.10, they detected the host galaxies for both targets, which are visible after subtracting the quasar point-source model (third column). For J2236+0032, the quasar host is significantly detected in both filters ($m_{\rm F356W} = 23.12 \pm 0.20$ mag; $m_{\rm F150W} = 25.12 \pm 0.29$ mag), and the light distribution is elongated in the same direction (i.e., NE–SW) in the two

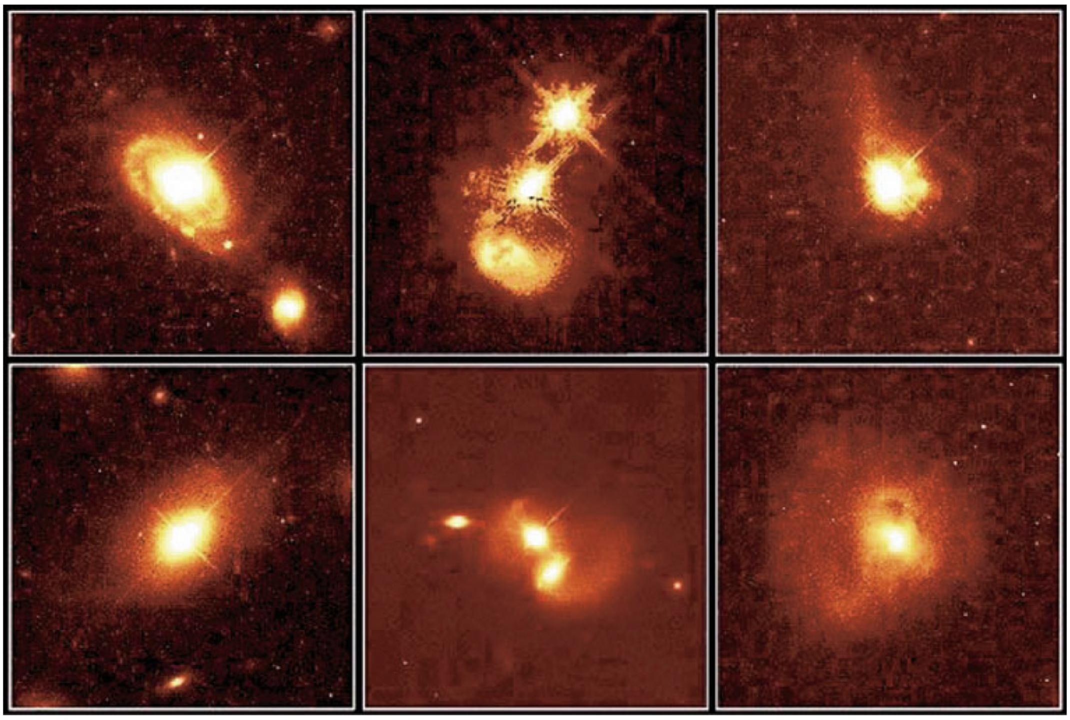

Figure 1.9: *HST images of QSOs in the local universe. In all cases the host galaxy can be easily identified, with the QSO itself being visible as a (central) point source in these images. Taken from P. Schneider (2015).*

filters, suggesting a mildly inclined disk-like host. For J2255+0251, the host galaxy is clearly detected in the F356W band (m_{F356W} = 24.58 ± 0.30 mag) with a host-to-total flux ratio of 9.8 ± 2.6%. The host emission extends southeast (left) of the quasar's location. This is the first step towards a systematic analysis of the properties of the host galaxies at the highest redshifts with JWST.

Even if high-z host galaxies have been proven difficult to detect in the optical/NIR wavelengths, telescopes observing in other wavelength regimes as, for instance, *Herschel*, the Northern Extended Millimeter Array (NOEMA), the Very Large Array (VLA), and the Atacama Large Millimeter/sub-millimeter Array (ALMA), shed light into the properties of the gas and dust inside the QSO's host galaxies, giving us a picture of the composition and the properties of the interstellar medium (ISM) in these objects.

The ISM is formed by the gas and dust that exist between stars, and fills most of the volume of the galaxy. It plays a crucial role in the process of SF throughout a galaxy's lifetime. The local properties of ISM indeed affect the efficiency of SF, and in turn, feedback via stellar winds and supernova explosions regulate the mechanism for the ongoing process of the buildup of galaxies throughout cosmic time. Hydrogen gas is the most abundant species (in both number and mass) in the ISM, and the mass of dust material is generally of order 0.01 times the mass in hydrogen. Dust particles usually range in size from the molecular domain to sizes of order 0.3 μm, and are composed largely of amorphous carbon or graphite, aromatic hydrocarbons, silicates, ices, silicon carbide, and possibly iron particles, metallic oxides, and

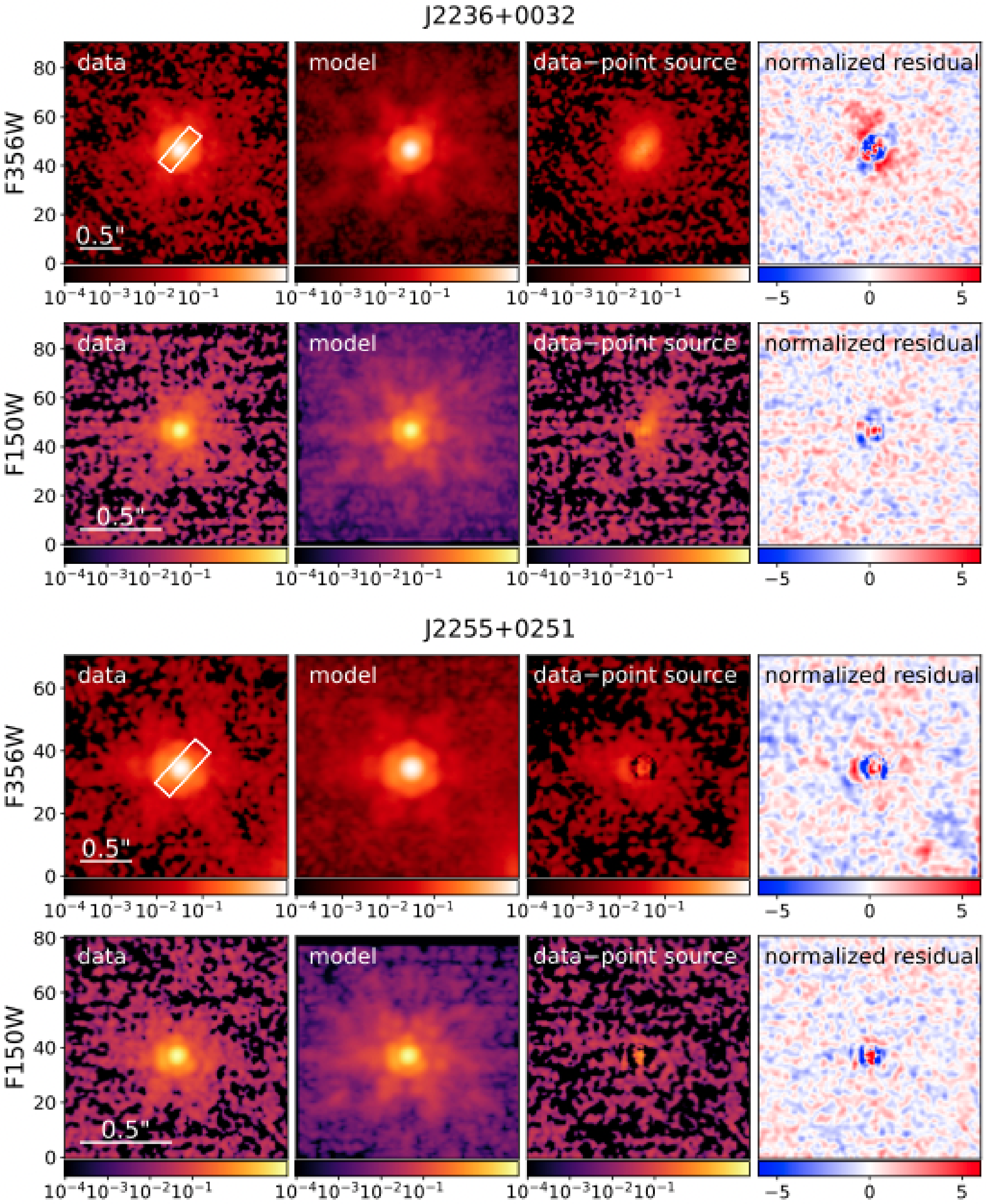

Figure 1.10: *2D decomposition into quasar and host-galaxy emission. Panels are as follows from left to right: quasar image (data), best-fit model (quasar + host galaxy), host galaxy only (data - model quasar point-source component), and normalized residual image, i.e., (data - model)/ σ , where σ is the flux uncertainty of each pixel. The target name is above each row of panels and the filter is indicated on the left. The alignment of the NIRSpec slit (0.2 × 0.6 arcsec^2) is shown in the left panel of the F356W image for each target. Pixel units are Mega-Janskys per steradian. A scale bar of 0.5 arcsec corresponds to 2.8 kpc at $z \sim 6.4$. Taken from* Ding et al. (2022).

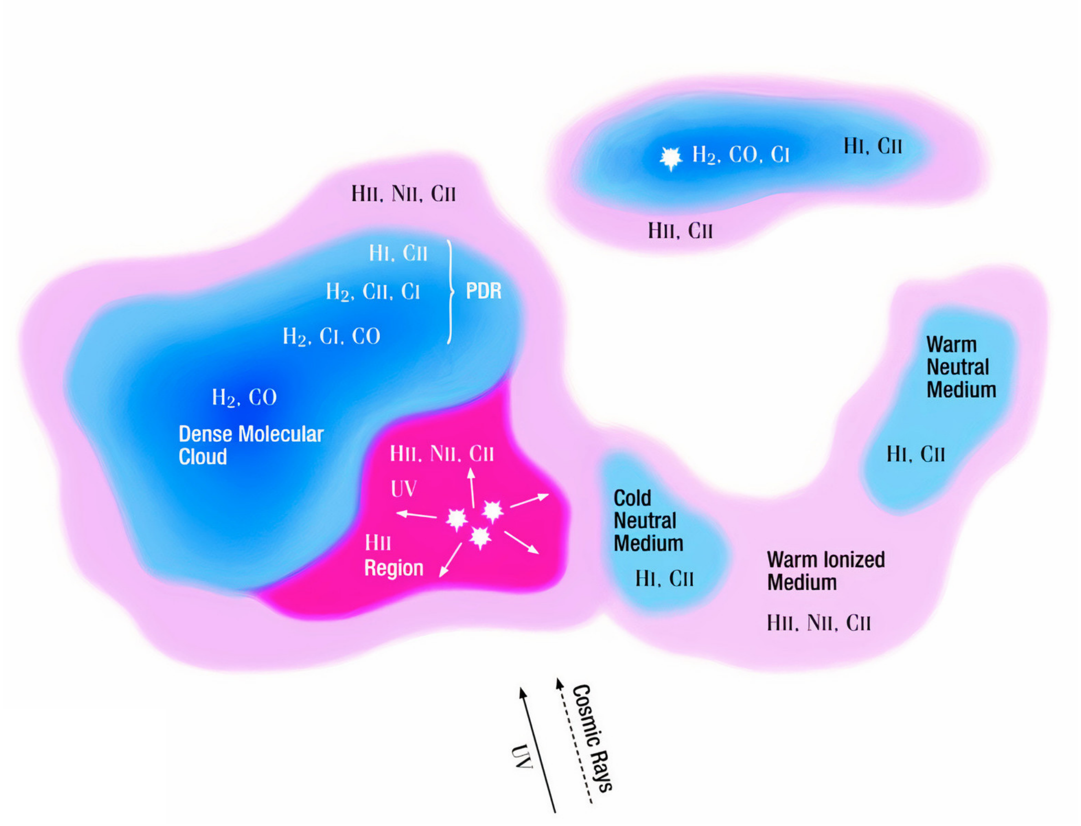

Figure 1.11: *Sketch of the composition of the ISM in a galaxy. Taken from publicly available slides of a talk by Jorge L. Pineda (link).*

sulfides (D. J. Hollenbach and Tielens, 1999). At the small end of the size regime lie polycyclic aromatic hydrocarbons (PAHs), which are really large, planar molecules rather than 'solid' dust particles. The ISM is composed by three phases, which exist in thermal equilibrium pressure: a hot phase formed by hot ionized medium (HIM) with hydrogen nucleus density $n \sim 3 \times 10^{-3}$ cm^{-3} and $T \sim 10^6$ K; a warm phase formed by the warm neutral medium (WNM) with $n \sim 0.3 \times 10^{-3}$ cm^{-3} and $T \sim 8000$ K and by the warm ionized medium (WIM) with similar n and T but with the hydrogen nearly completely ionized; a cold phase of neutral clouds formed by a cold neutral medium (CNM) with $n \sim 30$ cm^{-3} and $T \sim 100$ K. The majority of the volume of the ISM is filled by the lower-density media. There are also dense clouds, small in volume filling factor, with much higher thermal pressures than the average ISM thermal pressure. Their cores are cold ($T \sim 1 - 30$ K), opaque to optical or ultraviolet photons, and molecular (H_2). They are either collapsing to form stars (HII regions) or are expanding due to the interaction of radiation or winds from embedded or nearby stars (e.g., the extreme ultraviolet photons from massive stars near molecular clouds produce the bulk of the fully ionized gas in the galaxy). The regions in which the stellar far-ultraviolet (FUV) photons affect the structure, chemistry, thermal balance, and evolution of the neutral ISM of galaxies are called photodissociaton regions (PDRs). The structure of a PDR is well established (D. J. Hollenbach and Tielens, 1999). The outermost layer, which is exposed to the ambient radiation is ionized, and its thickness determined by the ionization parameter. This is followed by a neutral layer, and yet deeper lies a molecular layer. The study of PDRs are linked to the study of the SF in galaxies, since the ultraviolet photons not only illuminate the star forming regions but also regulate the SF processes. A sketch of the composition of the ISM is shown in Fig. 1.11.

1.2.1 The multi-phase cold gas in high-z QSO's hosts

At high redshifts, the examination of the ionized ISM can be accomplished by employing a combination of optical emission lines, such as Lyα and Hα, alongside FIR atomic fine structure lines like [CII], [NII], and [OIII]. The investigation of the neutral medium can also be conducted using FIR atomic fine structure lines, including [OI], [CI], and [CII]. Regrettably, it is not feasible to analyze HI 21cm emission from galaxies at $z > 0.5$ due to limited sensitivity; this endeavor awaits the full deployment of the square kilometer array, as detailed by (Carilli, Ivison, and Frail, 2003). The atomic phase within high redshift systems can be further scrutinized through absorption measurements along individual LOS (Wolfe, Gawiser, and Prochaska, 2005).

In the molecular medium, the elevated gas densities serve as protection against UV photodissociation for molecules, thanks to the shielding effect of dust and HII self-shielding (Dyson and Williams, 1980; Tielens, Waters, and Bernatowicz, 2005; Lequeux, 2005). The molecular gas phase is believed to precede star formation directly, a point emphasized by studies such as Leroy et al. (2008); Schruba et al. (2011). This phase holds particular significance in assessing a galaxy's potential to generate new stars. In the outermost layers of PDRs, carbon monoxide (CO) undergoes dissociation due to UV radiation, resulting in dominant emissions originating from atomic fine structure lines, H_2 roto-vibrational lines, dust continuum, and PAH emissions. As one moves deeper into this region, dust shielding and self-shielding facilitate the persistence of CO, with gas primarily heated by electrons released from dust grain surfaces following UV absorption. Several lines have ionization potentials higher than that of hydrogen and exclusively serve as cooling lines for the ionized medium (e.g., [NII], [OIII]), while others with lower ionization potentials trace both the neutral ISM and ionized regions (e.g., [CII], [OI], [CI]). A significant portion of the FUV energy generated by star formation in galaxies, up to a few percent, contributes to gas heating through the emission of photoelectrons, which is subsequently re-emitted via fine structure lines, notably the [CII] 158μm line (and occasionally [OI]). The majority of stellar radiation is dedicated to heating dust, with the balance achieved through FIR emission or direct radiation into the universe, with proportions roughly equal, contingent upon factors such as geometry and dust content (Elbaz et al., 2002).

The main H_2 molecule is symmetric and lacks of dipolar transition. In the extremely cold environment of the ISM ($\sim$ 20K), another type of transition, known as quadrupolar transitions, does not occur due to the low temperatures and their inherently weak Einstein coefficient. For investigating and characterizing molecular gas in space, CO serves as a valuable tool. It

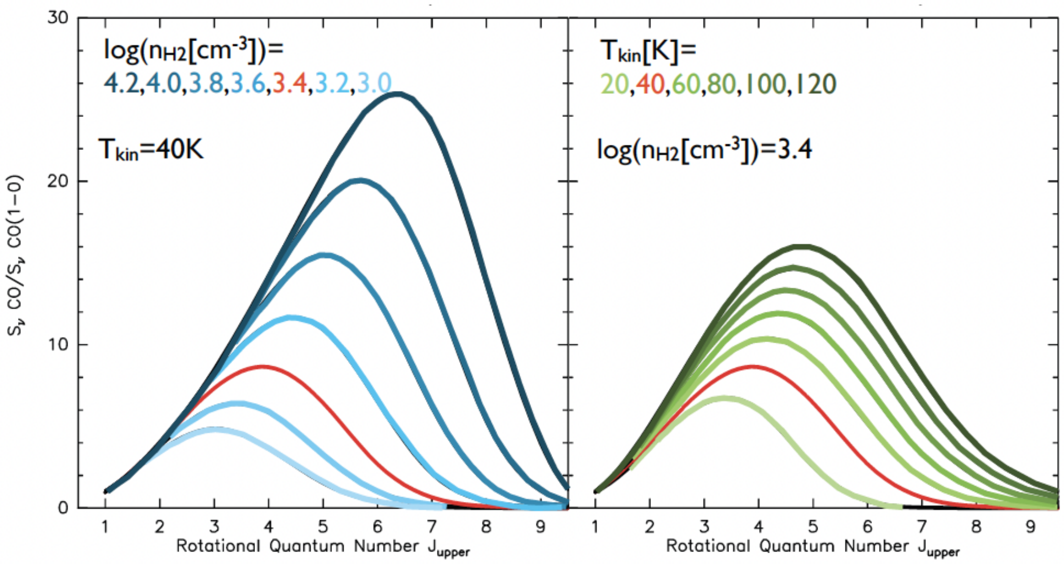

Figure 1.12: *CO emission ladder at fixed temperatures and varying density (left panel) and viceversa (right panel). Both panels have been normalized to the CO(1-0) transition. Taken from Carilli and Walter (2013).*

is considered a reliable tracer with its solar abundance of CO/H_2 $\sim 10^{-4}$ and it can provide wealth of information about the interstellar gas. At higher redshifts, the utility of CO as a tracer becomes even more pronounced owing to the high probability of encountering rotational ladder lines of any J level. This arises from the contraction of ladder spacings, scaling inversely with $(1 + z)$. Furthermore, when the gas undergoes excitation, the line strengths of J levels exhibit a nearly quadratic frequency dependence. This is illustrated in Fig. 1.12 where the expected CO excitation is shown as a function of density and temperature (Carilli and Walter, 2013).

At high redshift, galaxies have a higher gas fraction (e.g., Tacconi et al., 2010), where the gas fraction can be defined by the gas to stellar mass ratio, or the gas to baryonic mass ratio. In addition to being more abundant, the gas is characterized by higher densities, resulting in elevated average rates of star formation. Consequently, the CO lines tend to exhibit greater excitation, thereby enhancing the prospects of detecting molecular gas.

The CO line luminosity can be expressed in several ways (Solomon and Vanden Bout, 2005; Carilli and Walter, 2013). From energy conservation, the monochromatic luminosity, observed flux density, and luminosity distance are related by $\nu_{\rm rest}L(\nu_{\rm rest}) = 4\pi D_{\rm L}^2 \nu_{\rm obs}S(\nu_{\rm obs})$, yielding

$$L_{\rm CO} = 1.04 \times 10^{-3} S_{\rm CO}\Delta v\ \nu_{\rm rest}(1+z)^{-1}D_{\rm L}^2, \tag{1.11}$$

where the CO line luminosity, $L_{\rm CO}$, is measured in $L_\odot$; the velocity integrated flux, $S_{\rm CO}\Delta v$, in Jy km s^{-1}; the rest frequency, $\nu_{\rm rest} = \nu_{\rm obs}(1 + z)$, in GHz; and the luminosity distance, $D_{\rm L}$, in Mpc.

Alternatively the line luminosity, $L'_{\rm CO}$, can also be expressed for a source of any size in terms of the total line flux, in units of K km s^{-1} pc^2 as follows

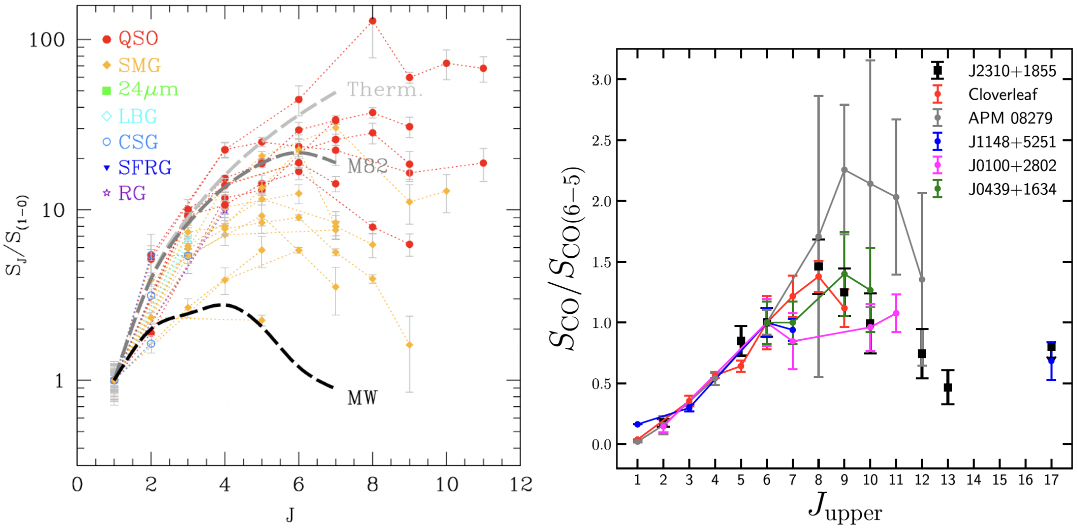

Figure 1.13: *Left panel: CO SLED of all sources where CO(1-0) line has been measured. The line fluxes have been normalized to the CO(1-0) line. The QSOs are the most excited systems found. The dashed light grey line shows constant brightness temperature on the Rayleigh-Jeans scale, i.e.* $S \sim \nu^2$*, for low-J. Taken from Carilli and Walter (2013). Right panel: CO SLED normalized to CO(6-5) of high-z QSOs. J0439+1634 at* $z = 6.511$ *in green (J. Yang et al., 2019); J1148+5251 at* $z = 6.419$ *in blue (Riechers et al., 2009; S. Gallerani et al., 2014); J0100+2802 at* $z = 6.327$ *in magenta (F. Wang et al., 2019); J2310+1855 at* $z = 6.003$ *in black (Li et al., 2020); APM08279+5255 at* $z = 3.911$ *in grey (P. Papadopoulos et al., 2001; Weiß et al., 2007); Cloverleaf at* $z = 2.560$ *in red (Bradford et al., 2009; Uzgil et al., 2016).Taken from Li et al. (2022).*

$$L'_{\rm CO} = 3.25 \times 10^{7} S_{\rm CO} \Delta v \, \nu_{\rm obs}^{-2} D_{\rm L}^{2} (1+z)^{-3}. \tag{1.12}$$

Comparing the two equations we have $L_{\rm CO} = 3 \times 10^{-11} \nu_{\rm rest}^{3} L'_{\rm CO}$. Note that L' line is directly proportional to the surface brightness temperature, i.e. the L' line ratio of two lines give the ratio of their intrinsic, source-average surface brightness temperatures. If the molecular gas emission were to come from thermalized, optically thick regions, L' line is constant for all J levels.

The distribution of radiating energy among the various J-lines of the CO ladder called the SLED (Spectral Line Energy Distribution), is a very useful diagnostic of the physics of the emitting ISM, in particular its density and temperature. It has been shown that the CO SLED can effectively discriminate between quiescent galaxies akin to the Milky Way, where emission peaks at J=3, and densely populated, vigorously star-forming starbursts, where the peak may reach J=8 (Weiß et al., 2007). Such excitations predominantly arise from star formation processes, such as PDRs. However, in proximity to an AGN, higher excitations become plausible, notably through the influence of hard X-rays, referred to as X-Ray Dominated Regions (XDRs, see P. P. van der Werf et al., 2010). In certain instances of highly concentrated starbursts, perturbations in the SLED can also arise from the opacities associated with dust (P. P. Papadopoulos et al., 2010).

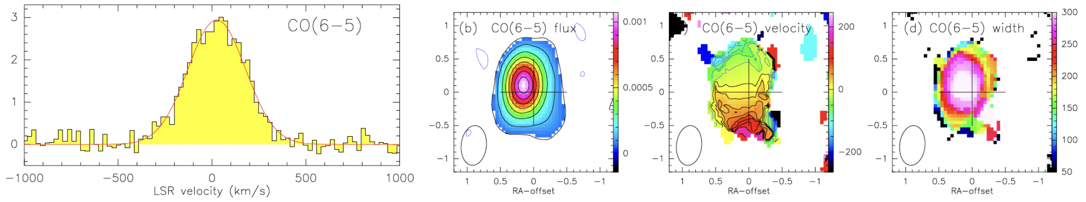

Figure 1.14: *Left panel: Continuum-subtracted CO(6-5) spectrum of QSO J2310+1855 at z = 6.003. The red line shows a fit with a Gaussian profile. Other three panels from left to right: moment-0, moment-1, moment-2 maps of the CO(6-5) emission line of QSO J2310+1855. The cross indicates the phase center. The synthesized beam is indicated in the lower-left corner. RA- and DEC- offset are in arcsec. Taken from* Feruglio et al. (2018).

Different source populations at high-z show different excitation, as can be seen in the left panel of Fig. 1.13 (Carilli and Walter, 2013). The CO excitation of QSO's host galaxies can generally be described by a simple model with one temperature and density out to the highest–J CO transition with a typical gas density of $\log(n(\mathrm{H_2})[\mathrm{cm^{-3}}]) = 3.6 - 4.3$, and temperatures of $T_{\mathrm{kin}} = 40 - 60$ K. A prominent example is the highly excited quasar host APM08279+5255 (Weiß et al., 2007). Right panel of Fig. 1.13 shows a compilation of CO SLEDs for high-z QSOs. This comparison suggest that a highly excited molecular gas component is common in the nuclear region of the quasar hosts. While for low-J ($J < 6$) the trend of the CO SLED seems to be quite similar, for high-J transitions the shape of the CO SLED of these systems is different from object to object.

The estimation of molecular content based on CO lines relies on the CO-to-H2 conversion factor, which has been well calibrated at lower redshifts, particularly within the Milky Way. At lower redshifts, clouds are individually detected, and their virial masses are subsequently estimated. Nevertheless, this factor remains intricately dependent on gas metallicity (Bolatto, M. Wolfire, and Leroy, 2013). With its low energy and critical density, CO is easily excited even in cold molecular clouds. At a wavelength of 2.6 mm, the $J = 1 - 0$ transition of CO lies in a fairly transparent atmospheric window. It has thus become the preferred tracer of the bulk distribution of $\mathrm{H_2}$ in our Galaxy and beyond. There is a direct link between the molecular gas mass and the CO(1-0) line luminosity,

$$M_{\mathrm{H_2}} = \alpha_{\mathrm{CO}} L_{\mathrm{CO(1-0)}}, \tag{1.13}$$

where α_{CO} is the so called CO-to-H2 conversion factor, simply a mass-to-light ratio, and it is expressed in units of $\mathrm{M_\odot}(\mathrm{K\ km\ s^{-1}\ pc^2})^{-1}$. The conversion factor typical for ULIRG and QSOs is found to be $\alpha_{\mathrm{CO}} = 0.8\ \mathrm{M_\odot}(\mathrm{K\ km\ s^{-1}\ pc^2})^{-1}$ (Bolatto, M. Wolfire, and Leroy, 2013; Carilli and Walter, 2013). However, in $z > 6$ QSOs it is challenging to detect the CO(1-0) and, up to now, the lowest transition reached is the (2-1) (see QSO J0100+2802 in Fig. 1.13). Therefore, we use the CO SLED to re-scale the lowest detected transition to the (1-0) one, and then we estimate the molecular gas mass. This approach clearly introduces big uncertainties to the estimate of $M_{\mathrm{H_2}}$.

Fig. 1.14 shows the spectrum and momenta of the CO(6-5) emission line in a QSO at $z \sim 6$ (Feruglio et al., 2018). The emission is spatially resolved thanks to the high resolution and sensitivity provided by ALMA. There is a gradient in the velocity map that may indicate the presence of a rotating disk. Feruglio et al. (2018) found a molecular gas mass of $\sim 3 \times 10^{10}$ $M_{\odot}$ and a size of the molecular disk of $\sim 2.9 \pm 0.5$ kpc. Recently, Decarli et al. (2022) presented a survey of CO(7-6) and CO(6-5) in a sample of 10 QSO's host galaxies at $z \sim 6$. They derived a molecular gas masses of the order of $10^{10} - 10^{11}$ $M_{\odot}$. This confirmed previous results suggesting the large gaseous reservoirs in the first QSO's host galaxies (e.g., R. Wang et al., 2013; Carniani et al., 2019; B. P. Venemans et al., 2017).

The single [CII] 158 μm fine structure transition is a very important coolant of the atomic ISM and of PDRs, wherein carbon is partially or completely in ionized form. Since carbon has an ionization potential lower than that of the hydrogen, this line emission can originate from a variety of phases of the ISM: cold atomic clouds (CNM), diffuse WNM and WIM, and HII regions. Excitation of the [CII] fine structure transition can be via collisions with hydrogen molecules, atoms, and electrons. Observationally, it is a challenging task to disentangle the contribution of [CII] emission from all different components. Analysis of [CII] observations is also complicated by the fact that it is difficult to determine the optical depth of the line (e.g., Neri et al., 2014). For metallicities corresponding to the bulk of our galaxies at high redshift, the fraction of [CII] emission originating in the neutral phase approaches 90%. At higher redshift, in the interacting system BR1202-0725 at z = 4.7, while [CII] emission arises primarily in the neutral gas for the sub-millimetre galaxy and the quasar, [CII] emission seems to be associated with the ionized medium (HII regions) for one Lyman-α emitter of the system (Decarli et al., 2014). Studying 20 dusty star-forming galaxies from the South Pole Telescope (SPT) sample at $2.1 < z < 5.7$, Gullberg et al. (2015) found that [CII] emission is consistent with PDRs. Similarly, Stacey et al. (2010) found that the bulk of the [CII] emission line (70%) is originating from PDRs in twelve z ~ 1-2 galaxies. The [CII] line is a powerful diagnostics to assess the morphology and kinematics of primeval galaxies, given that it is generally the strongest emission lines observed in the spectra of high-z galaxies. Since its first detection at high redshift (Maiolino et al., 2005), this transition has then been detected in large samples of distant galaxies.

B. P. Venemans et al. (2020) studied the [CII] emission line in a sample of 27 QSO's host galaxies at $z \sim 6$ observed with ALMA at a spatial resolution of ~ 1 kpc. They found that the [CII] emission in the quasar hosts has sizes between 1.0 and 4.8 kpc, and that 13 quasars (48%) have companion [CII]-emitting galaxies in the field, with distances between 3 and 88 kpc. Using the same sample, Neeleman et al. (2021) explored the kinematics of these objects, revealing that one-third of the hosts have disturbed [CII] emission profiles, another third shows a smooth velocity gradient consistent with emission arising from a rotating disk, and the last third shows a velocity profile consistent with emission arising from a dispersion-dominated system. Fig. 1.15 presents the momenta for one of the QSOs with kinematics showing ordered

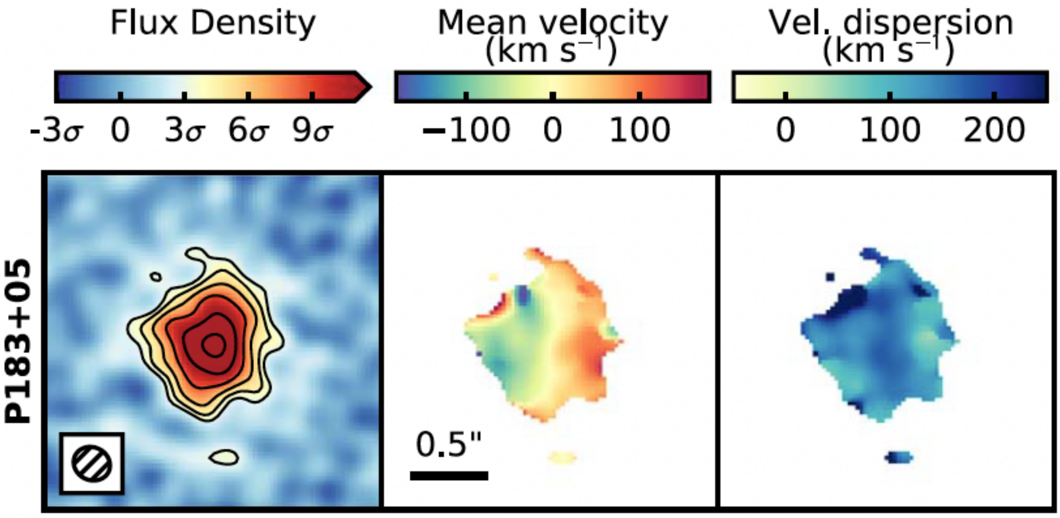

Figure 1.15: *From left to right: moment-0, moment-1 and moment-2 of QSO P183+05. The ALMA synthesized beam is shown in the inset in the lower left corner. Taken from Neeleman et al. (2021).*

motions. The mean velocity dispersion of the sample is ~ 129 km s^{-1}. The analysis of the host kinematics provides an essential information regarding the properties of the hosts, that is an estimate of the dynamical mass. The dynamical mass enclosed within a radius R is expressed as:

$$M_{\rm dyn}[{\rm M}_\odot] = \frac{v_{\rm circ}^2}{\rm G} R, \tag{1.14}$$

where G is the gravitational constant and $v_{\rm circ}$ is the maximum circular velocity of the gas disk. The latter is estimated from the rotation curve of the hosts derived from the analysis of [CII] emission line. However, the determination of $v_{\rm circ}$ requires the knowledge of the inclination angle of the galaxy, which is very difficult to estimate for high-z sources even if using high resolution and sensitivity observations. Thus, this becomes the major factor of uncertainty in deriving dynamical masses through kinematical studies. When studies of the velocity rotation curve are unfeasible due to limitation on the sensitivity and resolution of the [CII] observations, the dynamical mass can be alternatively derived from the following relation:

$$M_{\rm dyn}[{\rm M}_\odot] = 1.16 \times 10^5 v_{\rm circ}^2 {\rm D}, \tag{1.15}$$

where D is the disk diameter in kpc, and $v_{\rm circ} = 0.75{\rm FWHM}_{\rm [CII]}/\sin(i)$. Even in this case, a substantial factor of uncertainty is given by the inclination angle. Estimates of dynamical masses combined with robust BH masses make it feasible to push BH/galaxy co-evolution studies to the highest accessible redshifts (for a detailed discussion see Sect. 1.3). Measuring the dynamical masses for all the undisturbed galaxies, Neeleman et al. (2021) found a mean dynamical mass of $\sim 5 \times 10^{10}$ M$_\odot$.

A tight relation between the [CII] luminosity and the global SFR is seen in local galaxy observations, at least when excluding extreme (ULIRG-like) cases (De Looze et al., 2014; Kapala et al., 2015; Herrera-Camus et al., 2015). This makes [CII] a promising tool to investigate the properties of early galaxies and to trace their star formation. Carniani et al. (2017) revealed that the [CII] emission breaks into multiple subcomponents in 9 out of the studied 21 galaxies having [CII] detections. Taking into account the presence of these subcomponents and the proper associations between [CII] and UV components, they found that the distribution of $z > 5$ galaxies on the L[CII]-SFR diagram follows the local relation, but the dispersion is 1.8 times larger than that observed in nearby galaxies.

Water is thought to be one of the most abundant molecules in galaxies, present predominantly in icy mantels of dust grains in cold environments (Tielens et al., 1991; D. Hollenbach et al., 2009). In warmer environments, water in the gas phase is thought to play an important role in cooling (Neufeld and Kaufman, 1993; Neufeld, Lepp, and Melnick, 1995). The rotational transitions of water have high critical densities ($> 10^8$ cm^{-3}), i.e. collisional excitiation can only happen in the very centres of dense cloud cores and other excitation mechanisms, in particular infrared pumping, are typically invoked. Indeed, Pensabene et al. (2021) detected $H_2O(3_{21} - 3_{12})$ transition in QSOs PJ231-20 at $z > 6$, and found that it lies on the $L_{H_2O} \propto L_{TIR}^{1.1-1.2}$ relation found for low-z sources (C. Yang et al., 2013; C. Yang et al., 2016), where L_{TIR} is the total infrared (TIR) luminosity, suggesting that the H_2O line is predominantly excited by pumping of IR photons of the dust UV-reprocessed radiation field.

1.2.2 The cold dust in high-z QSO's hosts

Dust grains play a key role in the physics and chemistry of the ISM, which is a complex and dynamic environment. They heat the gas through the photo-electric effect, and therefore influence the thermal structure of the ISM. Inter stellar dust is a primary coolant of the ISM and facilitates the gravitational collapse and fragmentation of gas clouds from which stars form, while altering the emission spectrum of galaxies from UV to FIR wavelengths through the reprocessing of starlight. All these processes depend on the dust population, chemical composition (carbonaceous, silicates etc.) and size distribution. Multiple dust population models have been proposed (Mathis, Rumpl, and Nordsieck, 1977; Zubko, Dwek, and Arendt, 2004; Draine et al., 2007; Compiègne et al., 2011; A. P. Jones et al., 2013) with a various range of grain compositions and size distributions.

The chief advantage for galaxies at high redshifts resides in the fact that the peak of dust emission, typically centered around 100 microns in the case of star-forming objects, is redshifted to the sub-mm and mm domain, covered by the ALMA telescope.

The study of the cold dust SED of the QSO's hosts provides essential information about the dust properties of the ISM in this objects, since the modelling of the cold dust SED directly depends on the dust temperature, T_{dust}, dust mass, M_{dust}, and dust emissivity index, β. Once the SED is modelled, and therefore the dust properties are precisely constrained, the TIR

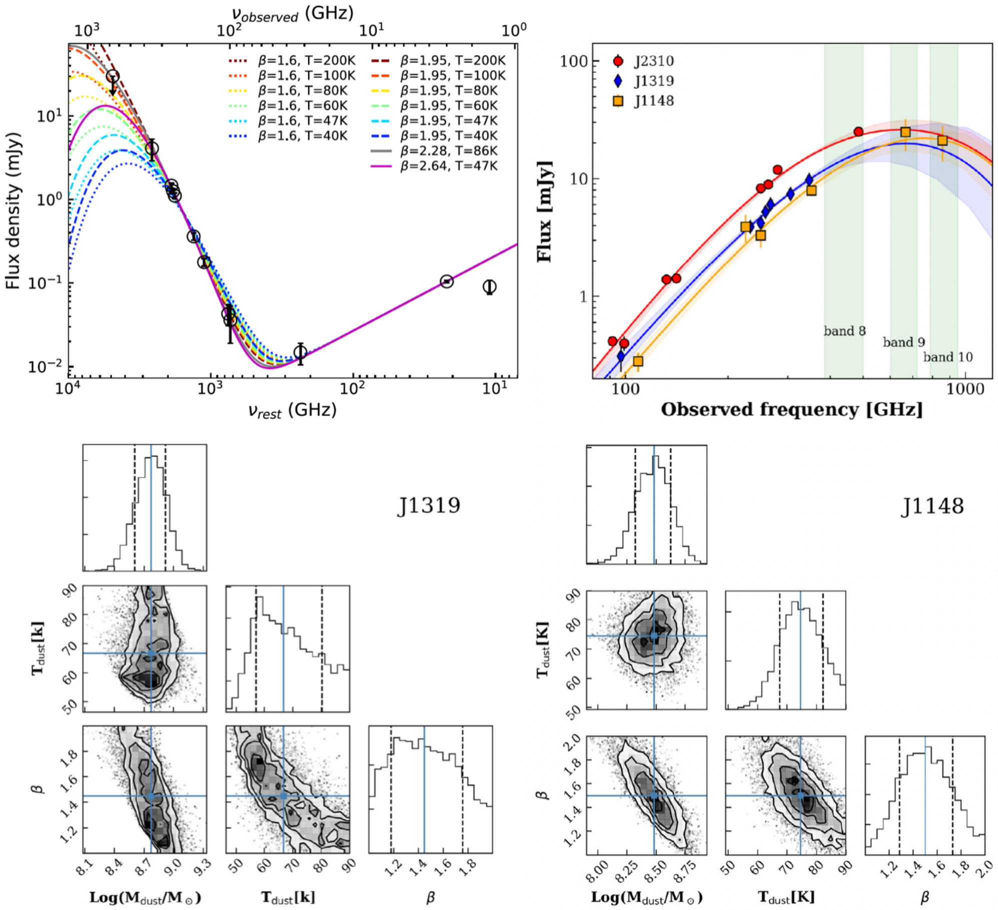

Figure 1.16: *Top left panel: FIR dust continuum and radio emissions of the J0100+2802 host. The dashed lines are graybody model fits with the emissivity index fixed at β =1.95, and the dotted lines are models with fixed β =1.6. The magenta solid line denotes a graybody model fit with $T_{\rm dust}$ fixed at 47 K. The gray solid line denotes a graybody model fit with both β and $T_{\rm dust}$ as free parameters, which yields* $\beta = 2.28 \pm 0.26$ *and* $T_{\rm dust} = 86 \pm 54$ *K. Top right panel: observed SED of J2310+1855 (red), J1319+0950 (blue), and J1148+5251 (orange) with best-fitting curves (solid lines). The vertical shaded green region shows the range of frequency covered by ALMA Bands 8, 9, and 10, which are fundamental to constrain dust properties in high-z sources (see text). Bottom left panel: corner plots showing the three-dimensional posterior probability distributions of $M_{\rm dust}$, $T_{\rm dust}$, and β for J1319+0950. Blue lines indicate the best-fitting parameter, while the dashed lines show the 16 and 84 per cent percentiles for each parameter. Bottom right panel: same as bottom left but for J1148+5251.*

luminosity and the SFR can be derived with high accuracy (for more details see Sect. 4.2).

However, most high-redshift quasars lack full FIR SED measurements, and $L_{\rm FIR}$ and $M_{\rm dust}$ are commonly determined with single or two photometric measurements by assuming an optically thin graybody model with a dust temperature of $T_{\rm dust} = 47$ K and an emissivity index of β=1.6 (e.g., F. Wang et al., 2016; B. P. Venemans et al., 2018). This temperature and emissivity index are measured from fitting a combined SED of a sample of high-redshift quasars with two or more rest-frame FIR photometric measurements by (Beelen et al., 2006). This clearly introduces major uncertainties in the determination of the dust properties and the SFR.

Up to now, only a bunch of objects at $z \gtrsim 6$ have a well sampled SED in the mm/sub-mm

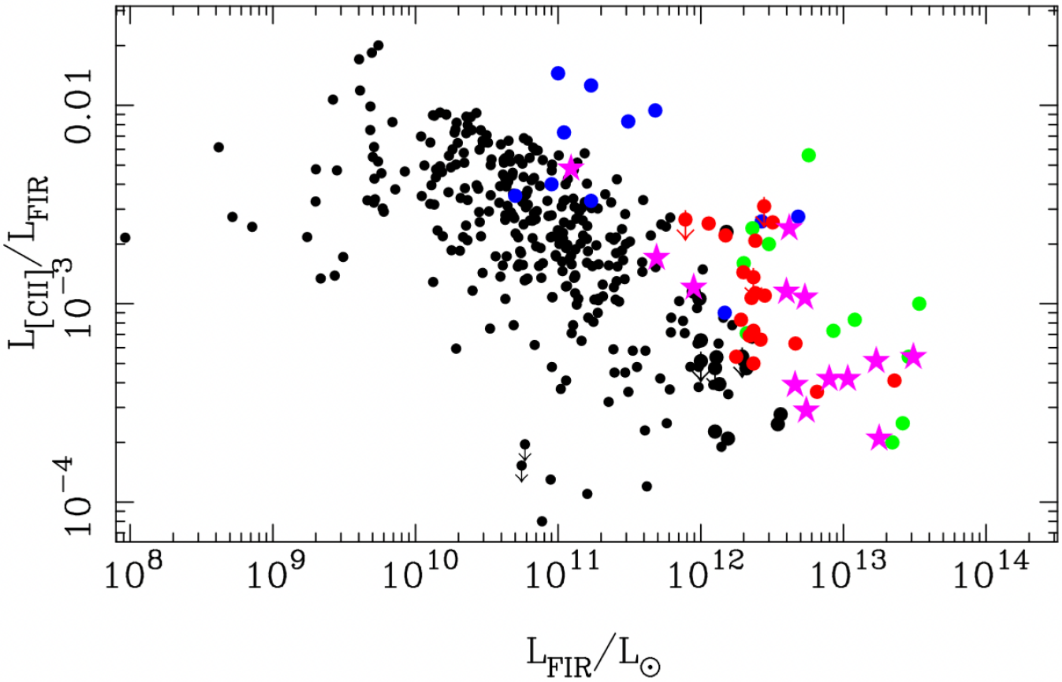

Figure 1.17: *The [CII] to FIR luminosity ratio versus the FIR luminosity. The low-z galaxies are plotted as black circles, ULIRGs at high-z* ($1 < z < 6$) *as green circles, the Hello sources* ($z = 1 - 3$) *as blue circles, the high-z SPT sources as red circles, and the QSOs at* $z > 4$ *as magenta stars. Taken from Françoise Combes (2018).*

regime. Fig. 1.16 shows the SEDs of some high-z QSOs (Carniani et al., 2019; F. Wang et al., 2019).

J1148+5251 and J2310+1855 are the only QSOs for which the cold dust SED is probed both in the Rayleigh-Jeans regime and near the peak, yielding a precise estimates of the dust parameters and the SFR. This can be seen in the corner plots of Fig. 1.16, where the $T_{\rm dust}$ of J1319+0950 results largely unconstrained with respect to the one of J1148+5251. Even though the Rayleigh-Jeans regime of the SED is finely sampled, uncertainties on the dust parameters are still significant, especially for the dust temperature, as seen for the case of J0100+2802 (top left panel of Fig. 1.16). Given the data available, the $T_{\rm dust}$ of J0100+2802 can be any between 47 K and 100 K, strongly affecting the estimate of the SFR that ranges from few hundreds to few thousands of $M_{\odot}$ yr^{-1}. This emphasizes the critical role played by ALMA Bands 8, 9, and 10 in providing indispensable insights towards the constraint of dust properties and the determination of SFR with high accuracy.

A reliable and precise estimation of dust mass can additionally serve as a means to determine the gas-to-dust ratio (GDR) for QSO's hosts with an already well-established gas mass measurement. By investigating the GDR within a sample of high-redshift QSOs, an average GDR can be derived and subsequently applied to infer the gas mass for objects, particularly those lacking information on lower CO transitions where gas mass remains highly uncertain or undetermined. To calculate gas mass, the GDR has frequently been assumed, introducing a notable level of uncertainty in its estimation. Recent investigations of hyper-luminous QSOs

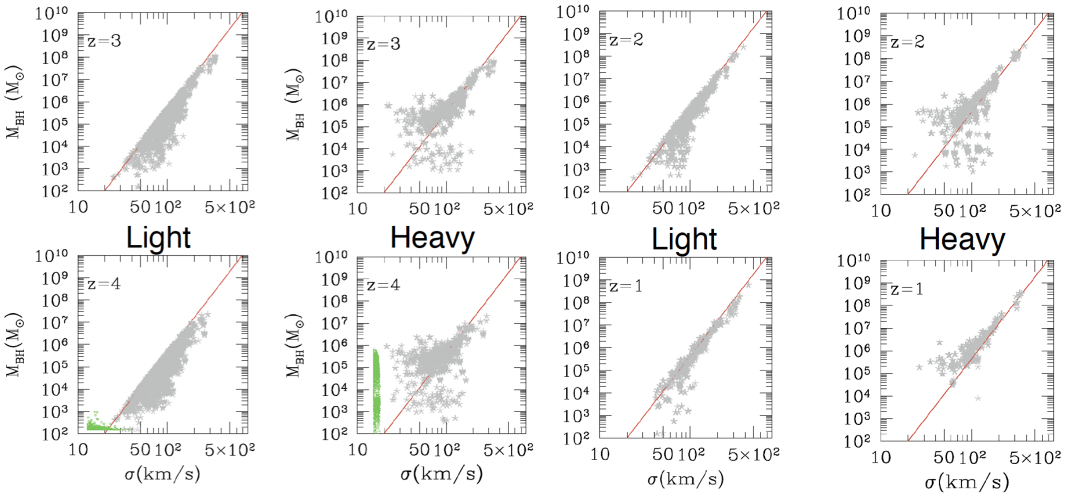

Figure 1.18: *The $M_{\rm BH} - \sigma$ relation for BH masses at different redshifts for light and heavy seeds. The lack of an initial $M_{\rm BH} - \sigma$ correlation for these seeds is also evident here and is shown at the bottom of the z = 4 panels (green points). Adapted from M. Volonteri (2010).*

at redshifts approximately $z \sim 2.4 - 4.7$ have revealed a wide range of GDR values, spanning from 100 to 300, with an average GDR of approximately 180 (Bischetti et al., 2021). These findings align with earlier results obtained for sub-millimeter galaxies up to redshifts of $z \sim 3 - 5$, where GDR values typically range from 150 to 250 (e.g., Saintonge et al. 2013; Miettinen et al. 2017). In contrast, lower-redshift galaxies tend to exhibit a GDR around 100 (Draine et al., 2007; Leroy et al., 2011), suggesting an increase in the GDR with redshift.

When studying the photoelectric heating efficiency of the dust, measured by the ratio $L_{\rm [CII]}/L_{\rm FIR}$, varies by about 2 orders of magnitude, and is decreasing at high $L_{\rm FIR}$, for strong starbursts. The main factor reducing this efficiency has been shown to be the dust temperature, and the strong UV field (Malhotra et al., 2017): indeed, the $L_{\rm [CII]}/L_{\rm FIR}$ ratio is well anticorrelated to the dust temperature, whatever the redshift. Fig. 1.17 gathers a large fraction of the [CII] studies so far, and shows that the [CII]/FIR ratio is higher at high redshift, although still declining with $L_{\rm FIR}$. The high-z quasars detected reveal a wide range of properties, sometimes behaving like starbursts, while sometimes the quasar excitation may prevail (e.g., B. P. Venemans et al., 2016).

1.3 The co-evolution between supermassive black holes and their host galaxies: an open question

In the previous sections, I presented some general properties of high-z QSOs, focusing in particular on the cold gas and dust in the ISM of the host galaxies. I have also discussed the need for a SMBH in the center of an AGN and its most important properties. This laid the groundwork for a proper comparison between the SMBH and its host galaxy, in order to examine the problem of the existence of these SMBHs and the co-evolution with their host-

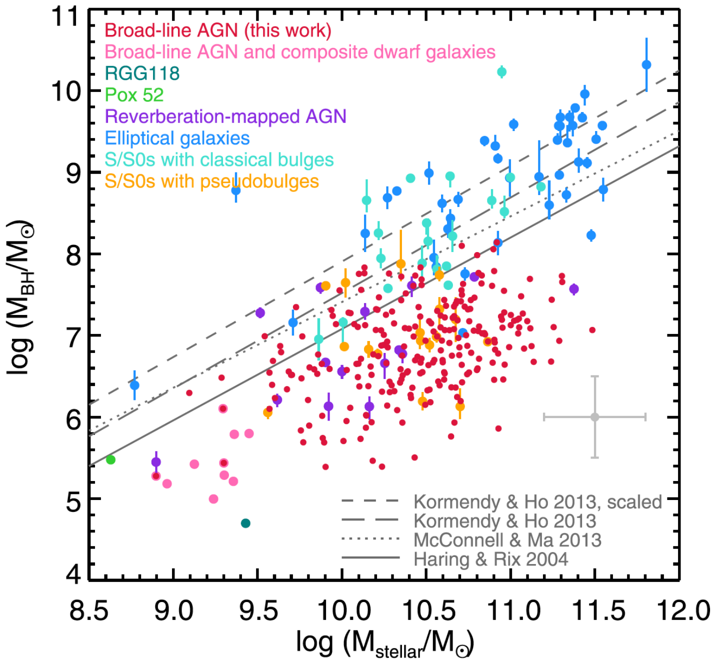

Figure 1.19: *BH mass vs. total host galaxy stellar mass. The sample of 244 broad-line AGNs are shown as red points. The 10 broad-line AGNs and composite dwarf galaxies are shown as pink points. The dwarf galaxy RGG 118 is the dark green point and Pox 52 is the light green point. Fifteen reverberation-mapped AGNs are shown as purple points. Elliptical, S/S0 with classical bulges, S/S0 with pseudo bulges are shown as blue, turquoise, and orange points, respectively. The gray error bar indicates uncertainties in stellar masses for all points, and single epoch spectroscopic BH masses. The gray lines show various $M_{\rm BH}$ vs. $M_{\rm bulge}$ relations based on ellipticals and spiral bulges with dynamical BH mass measurements. Taken from (Reines and M. Volonteri, 2015).*

galaxies. The latter will be done tracing the relation between the BH mass and the dynamical mass of high-z QSOs.

The outstanding mass growth of SMBHs at the EoR and its relation to the concurrent growth of their host galaxies pose challenges to theoretical models aimed at explaining how these systems formed on short timescales (< 1 Gyr). The time $t(M_{\rm BH})$ required for a BH of initial mass $m_{\rm seed}$ to reach a mass $M_{\rm BH}$, assuming Eddington-limited and continuous accretion, is given by (Meyer, Bosman, and Ellis, 2019):

$$t(M_{\rm BH}) = \frac{t_{\rm Edd}}{f_{\rm Edd}} \frac{\epsilon_r}{(1-\eta)} \ln\left(\frac{M_{\rm BH}}{m_{\rm seed}}\right), \qquad (1.16)$$

where $t_{\rm Edd}$ is the Eddington time[3] (see Eq. 1.9), $f_{\rm Edd}$ expresses at which fraction of the Eddington limit the BH is accreting, and ϵ_r and η are, respectively, the radiative efficiency and accretion efficiency[4]. For a radiatively-efficient accretion event, we assume $\epsilon_r = \eta = 0.1$, a

---

[3] $t_{\rm Edd} \sim 0.45$ Gyr for a pure hydrogen gas, with $\mu = 1$. Assuming μ for a plasma at zero metallicity with cosmic abundance of hydrogen ($X = 0.75$) and helium ($Y = 0.25$), and therefore $\mu = 1.14$, the Eddington time is $t_{\rm Edd} \sim 0.39$ Gyr.

[4] The accretion efficiency η directly depends on the spin of the BH, and reaches the maximum value of $\eta \sim 0.42$ for maximally rotating Kerr BHs. The radiative efficiency ϵ_r depends both on the type of accretion and on

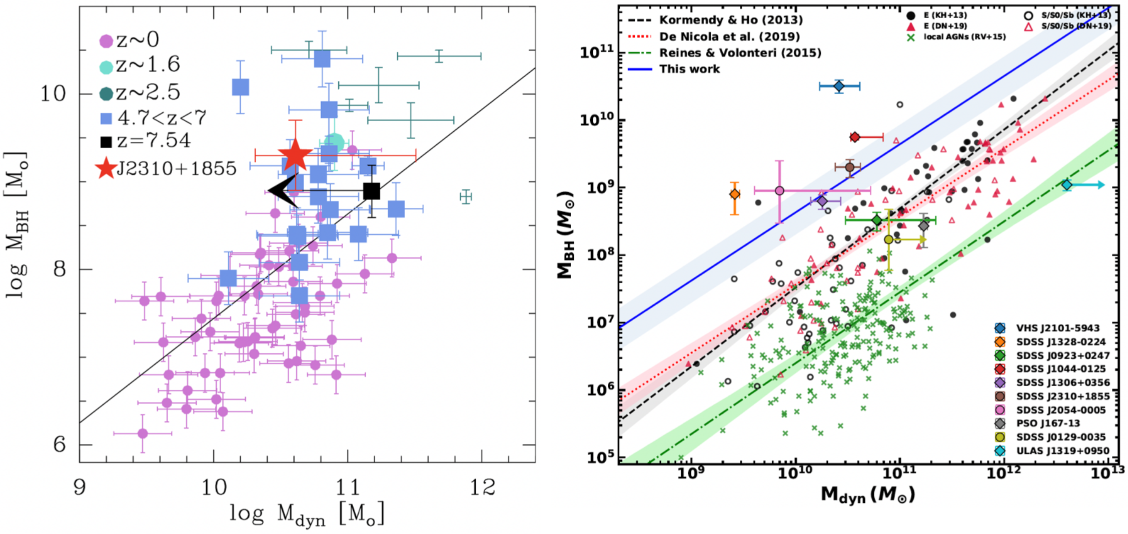

Figure 1.20: *Left panel: $M_{\rm BH}$ vs. $M_{\rm dyn}$ for QSO J2310+1855 (red star) and a compilation of AGNs at different redshifts. The solid line is the local relation (Kormendy and Ho, 2013). Taken from (Feruglio et al., 2018). Right panel: $M_{\rm BH}$ vs. $M_{\rm dyn}$ for high-z QSOs (legend in the lower right corner), and for local galaxies and AGNs. Dashed black red dotted lines are the local relation by Kormendy and Ho (2013) and de Nicola, Marconi, and Longo (2019), respectively. The green line is the local relation for AGNs (Reines and M. Volonteri, 2015), and the blue line is the relation found by Pensabene et al. (2020) for high-z QSOs. It should be noted that the local relations of Kormendy and Ho (2013) and de Nicola, Marconi, and Longo (2019) are obtained using bulge stellar masses, and the one by Reines and M. Volonteri (2015) from total stellar masses of AGN hosts. Taken from (Pensabene et al., 2020).*

typical average value for Shakura–Sunyaev thin disks (Shakura and Sunyaev, 1973). Observations of high-z QSOs revealed the presence of BHs with $M_{\rm BH} \sim 10^9$ M$_\odot$ already at $z \sim 7$, that is $\sim$ 0.7 Gyr from the beginning of the Universe (e.g., Zappacosta et al., 2023; Mazzucchelli et al., 2023; Eilers et al., 2022). To reproduce such high BH mass at $z \sim 7$ (i.e., $t(M_{\rm BH}) = 0.7$ Gyr) using Eq. 1.16, one has to assume continuous accretion at Eddington limit, $f_{\rm Edd} = 1$, with a seed BH of mass $m_{\rm seed} \sim 10^2$ M$_\odot$, which is the average value for light seeds produced by Pop III stars. It is clearly unreasonable that a whole population of objects is able accrete for hundred of Myrs continuously at Eddington rate. Different prescription of accretion and BH seeding are currently under investigation. For instance, the correlation that exists between the BH mass and the velocity dispersion in galaxies enables to discriminate between light and heavy seeds ($M_{\rm BH} \sim 10^5$ M$_\odot$).

The $M_{\rm BH} - \sigma$ relation has been established more than 20 yrs ago in all type of local galaxies (Tremaine et al., 2002; Ferrarese and Ford, 2005), and it has been proven to be valid also at higher redshifts. From a theoretical point of view, Marta Volonteri and Natarajan (2009) explored the establishment and evolution of the empirical correlation between BH mass and velocity dispersion with redshift for two seeding models: ‘light seeds’, derived from Population III remnants, and ‘heavy seeds’, derived from direct gas collapse. As shown in Fig. 1.18,

---

the accretion efficiency: for radiatively efficient accretion events, one can assume $\epsilon_r = \eta$.

the massive end of the $M_{\rm BH} - \sigma$ relation is established early, and lower mass BHs migrate onto it as hierarchical merging proceeds. How BHs migrate toward the relation depends critically on the seeding prescription: light seeds initially lie well below the $M_{\rm BH} - \sigma$ relation, and BH masses can grow via steady accretion episodes unhindered by self-regulation; for the heavy seeding model, BHs are initially over-massive compared to the empirical correlation, and the host haloes assemble prior to kick-starting the growth of the $M_{\rm BH}$. If $m_{\rm seeds}$ are massive, $\sim 10^5 M_\odot$, the low-mass end of the $M_{\rm BH} - \sigma$ flattens towards an asymptotic value, creating a characteristic 'plume' consisting of ungrown seeds at $\sigma < 50$ km s^{-1}, that merely continue to track the peak of the seed mass function down to late times (M. Volonteri, 2010). Here lies the importance of study the population of low-massive BHs, which enable us to discriminate between different formation models. This will also be the focus of future/ongoing campaign with JWST.

Analogously there is also a relation between $M_{\rm BH}$ and the stellar mass in the galaxy. Reines and M. Volonteri (2015) studied this relation differentiating between galaxies with active and inactive BHs in the local Universe ($z < 0.055$). Inclusion of the latter sources allowed them to extend their sample to low BH masses. As can be seen in Fig. 1.19, a single linear fit to the whole population of galaxies was disfavored. Rather, the AGN host galaxies define a relation that has a similar slope ($M_{\rm BH} \propto M_*$) to early-type galaxies with quiescent BHs, but a normalization that is more than an order of magnitude lower.

However, before the advent of JWST, it was difficult to obtain reliable ad accurate estimates of the stellar mass in QSO's hosts at high-z, even with deep HST observations (Mechtley et al., 2012; M. A. Marshall et al., 2020). Difficulties mainly arose from the nuclear emission dominating over the host emission in the optical-UV range. The QSOs for which stellar masses could be roughly determined were the dust-reddened and type-2 ones (Glikman et al., 2015; Banerji et al., 2018). Therefore for the majority of QSOs, instead of the stellar mass, the dynamical mass has been used at high-z, exploring the $M_{\rm BH} - M_{\rm dyn}$ relation. For instance, Feruglio et al. (2018) and Pensabene et al. (2020) studied the $M_{\rm BH} - M_{\rm dyn}$ relation in luminous high-z QSO's hosts, finding that this relation evolves with redshift and that high-z QSOs lie above the local relations (see Fig. 1.20). This implies that the SMBHs formed significantly earlier than their hosts. In this context, Izumi et al. (2018); Izumi et al. (2019) studied the $M_{\rm BH} - M_{\rm dyn}$ using a sample of seven $z > 6$ low-luminosity quasars, and found that while the luminous quasars typically lie above the local relation (Kormendy and Ho, 2013) with BHs overmassive compared to local AGNs, the discrepancy becomes less evident for low-luminosity ones. In order to avoid being biased by the properties of higher luminosity sources, it is essential to study the whole population of QSOs and galaxies at high-z, including the low-luminosity ones. This is now possible thanks to JWST (see e.g. Santini et al., 2023; Harikane et al., 2023), that enable us to determine the stellar mass especially in low-luminosity sources, thanks to a sharper PSF (especially in the short-wavelength bands) and longer-wavelength coverage out to 5 micron compared to HST, being less affected by dust attenuation. Recently,

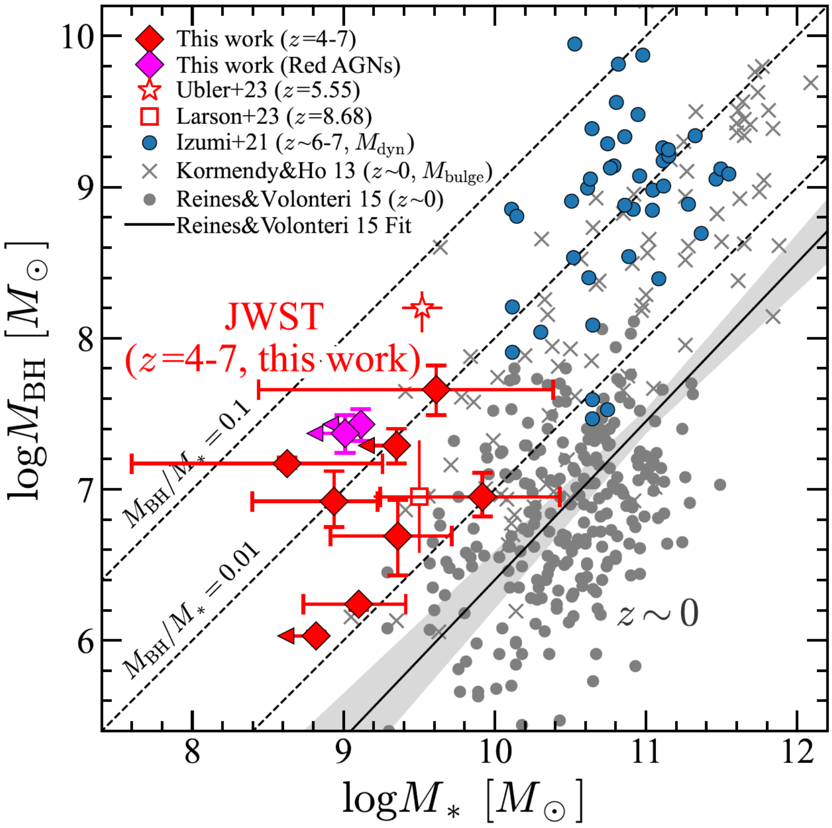

Figure 1.21: *Relation between the BH mass and host's stellar mass. The red and magenta diamonds are AGNs at z = 4 - 7 from (Harikane et al., 2023). The red open star and square are AGNs at z = 5.55 and 8.78 identified with JWST/NIRSpec observations in Übler et al. (2023) and Larson et al. (2023), respectively. The blue circles show* $z > 6$ *quasar samples compiled in Izumi et al. (2021b) (see also Izumi et al., 2018; Izumi et al., 2019). The gray crosses and circles are z ∼ 0 AGNs in Kormendy and Ho (2013) and Reines and M. Volonteri (2015), respectively. The black solid line with the shaded region is the relation at* $z \sim 0$ *in Reines and M. Volonteri (2015), and the dashed lines correspond to* $M_{\mathrm{BH}} = M_{*} = 0.1, 0.01,$ *and 0.001. Taken from Harikane et al. (2023).*

Harikane et al. (2023) performed a first statistical sample of faint type-1 AGNs at $z > 4$ identified by JWST/NIRSpec deep spectroscopy. Fig. 1.21 shows the $M_{\mathrm{BH}} - M_{*}$ relation for their AGNs compared to the AGNs at $z \sim 0$ (Reines and M. Volonteri, 2015), and high-z QSOs. Their AGNs have similar BH masses but systematically lower stellar masses than the local ones. Similar results are obtained in previous studies with a smaller number of AGNs (Kocevski et al., 2023; Übler et al., 2023), but they confirmed this trend of lower M_{*} (higher M_{BH}). This indicates that the BH grows faster than its host galaxy at high redshift. The fast BH growth is also suggested by previous studies at $z \sim 2$ (e.g., Y. Zhang et al., 2023). Such over-massive black holes compared to their host stellar masses are indeed predicted in some theoretical simulations (e.g., Toyouchi et al., 2021; Trinca et al., 2022; Inayoshi et al., 2022; Hu et al., 2022; H. Zhang et al., 2023).

1.4 Thesis goals

In the previous sections, I have elucidated the key features of AGNs, with a specific focus on QSOs at high-z. In the following, I will outline the main goals of my PhD project.

As already discussed, QSOs at $z \gtrsim 6$ appear to lie above the local $M_{\mathrm{BH}} - M_*$ correlation, and thus the BH growth seems to precede that of its host galaxy (M. Volonteri, 2012). At the same time, the host galaxies are already massive, thus likely undergoing rapid growths through sustained star formation rates. Therefore, targeting QSO's host galaxies at these redshifts provides a unique opportunity to characterize both the formation and the concurrent build-up of SMBHs and their host galaxies, and the physical properties of the ISM in the first Gyr of the Universe (e.g., Decarli et al., 2018; B. P. Venemans et al., 2020; Neeleman et al., 2021). The primary objective of my PhD project can be encapsulated in the following questions:

- *Is the SMBHs growth coupled to the evolution of their host galaxies, and how?*
- *Are QSO's hosts at high-z the progenitors of the massive galaxies observed in the local Universe?*

These questions are pivotal to the study of galaxy evolution and are tightly interconnected. They can be addressed only through the attainment of a reliable and precise understanding of the properties of QSOs and their massive hosts.

Indeed, in the last few decades, many advances have been made in unveiling the properties of the first QSO's host galaxies both from theory and observations. In the latter, ALMA, and recently JWST, played a major role. Presently, as outlined in Sect. 1.2, we have assessed that QSOs live in an overdense and complex environment, and they host massive host galaxies, which are gas and dust rich, and highly star-forming. Also, their evolution is regulated by powerful mechanisms such as SMBH accretion and feedback. However, significant uncertainties affect the estimation of the properties of QSOs i.e., BH mass, the total mass of galaxy and of its components, the SFR. These limitations are mainly due to the combination of different factors, e.g. the poor sampling of the cold dust SED and the simplistic treatment of the dust heating by the AGN. In this context, the gas and cold dust in the ISM are key elements to understand the assembly and nature of the first QSOs.

Within the scope of my research project, I performed a comprehensive analysis of the properties of the gas and dust in a statistically sound sample of 12 high-z QSOs (see Chap. 2, and Tab. 2.1). We aimed at deriving the molecular gas mass and SFR with the smallest statistical and systematic uncertainty. Additionally, we conducted an in-depth examination of the gas's kinematics and dynamics, thereby facilitating the determination of the mass budgets of the host galaxy's components. The final goal was to explore the $M_{\mathrm{BH}} - M_{\mathrm{dyn}}$ relation in the sample to quantify the evolutionary paths of high-z QSOs. To reach these goals, we exploited both proprietary and archival data from ALMA and NOEMA telescopes.

1.5 Structure of the thesis

Specifics on the sample, analysis and the results achieved are deferred to the following chapters. Here, I briefly summarize their content.

In Chap. 2, I introduce the sample employed to fulfill this thesis' goals. Moreover, I summarize the properties of the observations used for the analysis of the continuum and line emissions, and I present the QSOs in our sample individually.

In Chap. 3, I present the analysis of the CO(6-5) and/or CO(7-6) emission lines aimed at deriving the molecular gas mass and study the CO SLED. Additionally, I discuss the analysis of the [CII] emission line, which was undertaken to probe the gas's kinematics and dynamics and to perform dynamical modeling of the galaxy's rotation curve. These investigations were conducted on QSOs for which we had access to proprietary or archival ALMA observations in Bands 3 and 6. Notably, these datasets had not been subject to prior analysis.

In Chap. 4, I present an in-depth examination of the SED of cold dust, utilizing data from both ALMA and Herschel observations, where available. The objective of this analysis is to extract key dust properties and estimate the SFR for all QSOs within the sample. This investigation was carried out consistently across the entire sample, yielding high precision in dust property determination for 10 out of the 12 QSOs. It's worth noting that two of the QSOs lacked high-frequency ALMA or Herschel data essential for probing the peak of the cold dust SED. In the final section of Chap. 4, I provide a contextualization of our findings, drawing comparisons with results obtained for QSOs and standard galaxies at various redshifts.

In Chap. 5, I discuss the evolutionary path of the 10 QSOs in our sample for which the dust properties have been accurately determined. I will draw comparisons with results from literature and discuss possible answers to the aforementioned inquiries.

In Chap. 6, I draw our main conclusions and present some future perspectives.

CHAPTER 2

SAMPLE AND OBSERVATIONS

In Chap. 1, I have elucidated the key features of QSOs at high-z, and I have outlined the main goals of this Thesis. In this chapter, I will introduce the sample I have employed to fulfill the goals. I will summarize the observations employed for the analysis presented in Chaps. 3 and 4. Finally, I will briefly present the QSOs individually.

2.1 Presentation of the studied sample

We selected all the QSOs at $z > 6$ for which we were able to derive or retrieve accurate estimates of the dust properties, SFR and gas mass. In other words, all these QSOs have state-of-the-art ALMA and/or NOEMA observations targeting the continuum emission from low to high frequencies, i.e. probing both the Rayleigh-Jeans and peak region of the cold dust SED, and targeting the CO and [CII] line emissions. This first selection consisted of 10 QSOs. Additionally, we included two other QSOs (J1007+2115 and J0129-0035) for which we had new ALMA and/or NOEMA observations able to constrain the gas mass, even though they lacked of observations targeting the continuum emission at the peak region of the SED. Thus, this prevented us to derive the SFR for these two QSOs precisely.

This sample is biased by construction towards high luminosities ($L_{\rm bol} > 10^{47}$erg s^{-1}) and high BH masses ($M_{\rm BH} \gtrsim 10^9\ M_\odot$). Consequently, our findings are not directly applicable to the entire population of AGNs at $z > 6$; instead, they specifically pertain to high-luminosity sources. Nevertheless, this luminosity bias aligns with our objectives, as we are particularly interested in investigating the role of AGN feedback in influencing the SMBH-galaxy evolution and, notably, high-luminosity QSOs exhibit compelling evidence of powerful outflows (see e.g., Bischetti et al., 2022; Shao et al., 2022; Tripodi et al., 2023c; Salak et al., 2023).

We divided the sample in two sub-samples of 7 and 5 QSOs each, hereafter named 'HYPERION QSOs' and '$z > 6$ QSOs', respectively (see Tab. 2.1).

The first sub-sample is composed of the 7 QSOs belonging to the HYPerluminous QSOs

Table 2.1: General properties of QSOs in our sample

QSO	z	$\log(M_{\rm BH}/M_\odot)$	$\log(L_{\rm bol}/{\rm erg\ s^{-1}})$	Refs	Results
J0100+2802	6.327	10.04 ± 0.27	48.24 ± 0.04	[1],[2]	[CII], SED
J036+03	6.540	9.49 ± 0.12	47.33 ± 0.05	[1],[2]	$M_{\rm H_2}$, SED
J0224-4711	6.522	9.36 ± 0.08	47.53 ± 0.01	[1]	$M_{\rm H_2}$, SED
J231-20	6.587	9.50 ± 0.09	47.31 ± 0.01	[1],[2]	$M_{\rm H_2}$, SED
J1342+0928	7.540	8.90 ± 0.14	47.19 ± 0.01	[1],[2]	SED
J1148+5251	6.419	9.74 ± 0.03	47.57 ± 0.01	[1]	–
J1007+2115	7.494	9.18 ± 0.05	47.30 ± 0.02	[1]	$M_{\rm H_2}$, SED
J2310+1855	6.003	$9.67^{+0.06}_{-0.08}$	$47.49^{+0.10}_{-0.13}$	[3],[4]	[CII], SED
J2054-0005$^{(*)}$	6.390	9.17	47.03	[2],[5]	$M_{\rm H_2}$, SED
J1319+0950	6.133	$9.53^{+0.05}_{-0.11}$	$47.30^{+0.07}_{-0.08}$	[3],[2]	$M_{\rm H_2}$
J183+05	6.439	$9.41^{+0.21}_{-0.41}$	$47.20^{+0.16}_{-0.25}$	[3],[2]	SED
J0129-0035	5.778	8.23	46.3	[5]	$M_{\rm H_2}$

Notes. Columns: QSO name; redshift from [CII] emission line; BH mass; bolometric luminosity; references for z, $M_{\rm BH}$, and $L_{\rm bol}$; results presented in this work: gas mass from CO(6-5) or CO(7-6) emission lines ($M_{\rm H_2}$, in Chap. 3), [CII] kinematics and/or dynamics ([CII], in Chap. 3), cold dust SED along with dust properties and SFR (SED, in Chap. 4). $^{(*)}$ The error on BH mass for J2054-0005 and J0129-0035 was not provided in the reference works, so I considered the average systematic error on BH mass of 0.3 dex. QSOs above the double black line belong to the HYPERION sample. Errors for BH masses and bolometric luminosities of the HYPERION QSOs are taken from Tortosa et al. in prep. Refs: [1] Zappacosta et al. (2023); [2] Neeleman et al. (2021); [3] Mazzucchelli et al. (2023); [4] Tripodi et al. (2022); [5] R. Wang et al. (2013).

at the Epoch of ReionizatION (HYPERION) sample. HYPERION comprises the titans among $z > 6$ QSOs Zappacosta et al. (2023), i.e. those whose SMBH experienced the fastest mass growth history. In particular, these QSOs have been selected so that the SMBHs powering them required to form at least a 1000 $M_\odot$ BH seed (at $z = 20$) under the hypothesis on a continuous exponential accretion at the Eddington rate. These SMBHs likely assembled from the largest BH seeds, or alternatively experienced peculiar, possibly super-Eddington, mass accretion histories. Among the $\sim$ 300 QSOs known at the Epoch of Reionization (EoR), the HYPERION QSOs comprise 18 QSOs with a mean redshift $z \approx 6.7$, average $\log({\rm L_{bol}/erg/s}) \approx 47.3$, and BH mass in the range $10^9 - 10^{10}$ $\rm M_\odot$. HYPERION is based on a 2.4 Ms XMM-Newton Multi-Year Heritage Programme (PI: Zappacosta) to provide, for the first time for such a large sample of $z > 6$ QSOs, a uniform high quality X-ray spectral characterization for a detailed investigation of the nuclear properties and accretion and ejection processes tied to the fast build up experienced by their SMBH. The first results suggest a genuine redshift evolution of their X-ray spectral slopes which appear to be steeper than reported in $z < 6$ QSOs with similar luminosity and accretion rate. This supports a different regime for the X-ray nuclear properties of the first quasars possibly linked to the presence of fast disc-driven winds (Zappacosta et al., 2023). While the nuclear properties of HYPERION QSOs are well constrained, as are the dynamical masses of most QSOs based on archival [CII] observations, their dust properties and SFR are still mostly unconstrained.

The '$z > 6$ QSOs' sub-sample comprises the QSOs that did not satisfy the criteria for belonging to the HYPERION sample (see Sect. 2 of Zappacosta et al., 2023), i.e., they did not experience rapid SMBH mass growth.

We divided our final sample based on the HYPERION survey's selection criteria in order to assess whether the BH accretion history has strong implications on the properties of the host galaxy.

Seven QSOs in our sample[1] are also part of the XQR-30 ESO Large Program (Valentina D'Odorico et al., 2023). Therefore they have high-S/N X-Shooter spectra, from which Mazzucchelli et al. (2023) derived BH masses using both C IV and Mg II emission lines. The Mg II BH masses derived for J0100+2802, J036+03, J0224-4711, J231-20 are in good agreement with those in Zappacosta et al. (2023).

The properties of QSOs in our sample are summarised in Tab. 2.1. Hereafter, even when not explicitly written, one should remember that the uncertainties on BH masses are a factor of 0.1-0.3 dex. Moreover, the uncertainties associated to the quantities derived in this Thesis are given at 68% of confidence (i.e., 1 σ).

2.2 Observations

In the following, I describe the observations used for the analysis of the line and/or continuum emission of the QSOs in our sample and the data reduction.

2.2.1 Line emission

Regarding J1007+2115, observations were taken with the NOEMA interferometer under project W21ED in March 2022. The receivers were tuned at 81.2 GHz in the Lower Side Band (LSB). The CO(6-5) emission line from the quasar host galaxy is redshifted to the Lower Side Band (LSB), while the CO(7-6) line lies in the Upper Side Band (USB), so the bandwidth covered by the correlator PolyFiX enables detection of both lines in a single frequency tuning. Amplitude and phase calibration were done on the quasars J1012+232 and J0953+254, and LkHa101 (0.2 Jy) was used as flux calibrator. Calibration and imaging was performed using `CLIC` and `MAPPING` within the `GILDAS` software [2]. The continuum visibility tables at two representative frequencies in LSB and USB were derived using the task `uv_filter` within `MAPPING` to filter out a spectral region 400 MHz wide around the emission lines, and `uv_continuum`. Deconvolution using natural weighting leads to a synthesized beam of 3.1 × 2.2 arcsec^2 (PA=30°) in LSB and 2.5 × 1.8 arcsec^2 (PA=30°) in USB. Cleaning of the image cube was done using the `Hogbom` algorithm without applying any mask. The CO(6-5) and (7-6) line profiles and velocity-integrated maps were produced by subtracting the continuum in each sideband using `uv_subtract`. We produced an averaged uv table across the line width for both lines, using the `uv_average` task within `MAPPING`, and analyzed the line visibilities.

---

[1] These QSOs are J0100+2802, J036+03, J0224-4711, J231-20, J2310+1855, J1319+0950, J183+05.

[2] www.iram.fr/IRAMFR/GILDAS

Table 2.2: Details of the observations used for the analysis of line emissions

QSO	Obs freq (GHz)	Beam cont [arcsec^2]	r.m.s. cont [mJy/beam]	line (spw:chans)	Beam line [arcsec^2]	r.m.s line [mJy/beam]	chan width [km s^{-1}]	Project ID
J0224-4711	95.33	3.95 × 2.32	0.016	CO(7-6) (0/1:56-76)(a) [CI] (0/1:88-100)(a)	3.53 × 2.07	0.14	43.7	2017.1.01472.S
J2310+1855	264.69	0.26×0.21(b)	0.0088	[CII] (1:72-168)	0.30×0.24(b)	0.23	8.5	2019.1.00661.S
				H$_2$O (0:107-185)	0.34×0.24(b)	0.14		
		0.17×0.15(c)	0.0091	[CII] (1:72-168)	0.17×0.16(c)	0.23		
J0100+2802	252.87	1.03×0.78	0.01	[CII] (0/1:90-265)(d)	1.08×0.82	0.2	9	2021.1.00211.S
J1319+0950	103.51	0.3 × 0.3	0.054	CO(6-5) (0/1:100-141)(a)	0.32 × 0.31	0.1	24	2018.1.01289.S
J2054-0005	92.26	0.42 × 0.32	0.006	CO(6-5) (0/1:106-130)(a)	0.39 × 0.30	0.1	24	2018.1.01289.S
J0129-0035	95.72	0.44 × 0.35	0.006	CO(6-5) (0/1:106-133)(a)	0.45 × 0.34	0.07	23	2018.1.01289.S
J1007+2115	81.2	3.1 × 2.2	0.015	CO(6-5)	3.1 × 2.2	0.28	74	W21ED
	94	2.5 × 1.8	0.014	CO(7-6)	2.5 × 1.8	0.26	63	W21ED

Notes. Columns: (1) Target QSO; (2) observed frequency of the observation; (3) clean beam of the continuum map; (4) r.m.s of the continuum map; (5) spw and channels of the detected emission lines; (6) clean beam of the continuum-subtracted cube; (7) r.m.s of the continuum-subtracted cube; (8) channel width of the continuum-subtracted cube; (9) project ID of the observation. (a): spw 0 and spw 1 were combined since they covered almost the same spectral range and in order to maximize the S/N of the emission lines. (b): natural weighting. (c): briggs weighting with robust=0.5. (d): since the [CII] of J0110+2802 showed emission up to high-velocities (∼ 1000 km s^{-1}), we combined the two spectral windows in the upper side band to ensure a reliable continuum subtraction.

For the ALMA observations of the other QSOs, calibration and imaging were performed as outlined in the following. The visibility calibration of the observations was executed by the ALMA science archive. The imaging was performed through the Common Astronomy Software Applications (CASA; McMullin et al. 2007), version 5.1.1-5. We applied `tclean` using natural weighting and a 3σ cleaning threshold. Briggs weighting with a robust parameter equal to 0.5 has been used for imaging the [CII] emission of J2310+1855 in order to maximise the angular resolution, with 3σ cleaning threshold. We imaged the continuum using the multi-frequency synthesis (MFS) mode in all line-free channels. To image the line emissions, we used the CASA task `uvcontsub` to fit the continuum visibilities in the line-free channels with a first-order polynomial for QSOs J0224-4711, J2310+1855, since the continuum showed a non-negligible slope, and zeroth-order polynomial for the other QSOs. We then obtained continuum-subtracted cubes to be used in our analyses. We produced line maps using the MFS mode in the channels where the emission lines were detected.

Note that the observation in Band 6 of J2310+1855 was primarily designed to detect [CII] emission towards Serenity-18 (V. D'Odorico et al., 2018), a DLA located on the QSO sight-line at $z = 5.938646$. The primary beam of the observation includes QSO J2310+1855, the frequency setup covers the [CII] ${}^2P_{3/2} -^2 P_{1/2}$ emission line from the QSO and the underlying continuum, allowing high-resolution imaging of the QSO. This is the reason why the x- and y-axes of the continuum and line maps of J2301+1855 are displayed in WCS coordinates, differently from the other objects that have RA- and DEC-offset in arcsec from the central pointing of the observation.

Information about the project ID, synthesized beam, lines detected, line channels, and r.m.s noise of the continuum map and of the continuum-subtracted cube for each observation is reported in Tab. 2.2. Analysis of these observations, results and discussion are presented in Chap. 3.

2.2.2 Continuum emission

Regarding J1007+2115, the continuum visibility tables at two representative frequencies in LSB and USB were derived using the task `uv_filter` within `MAPPING` to filter out a spectral region 400 MHz wide around the emission lines, and `uv_continuum`. Deconvolution using natural weighting leads to a synthesized beam of 3.1×2.2 arcsec^2 (PA=30°) in LSB and 2.5×1.8 arcsec^2 (PA=30°) in USB. Cleaning of the image cube was done using the `Hogbom` algorithm without applying any mask.

For the ALMA observations of the other QSOs, calibration and imaging were performed as outlined in the following. We always considered observations centered on the position of the QSO to avoid primary beam correction, which has to be applied if scientifically relevant emission is off the phase center. The visibility calibration and the imaging of the observations was executed as in Sect. 2.2.1 i.e., applying `tclean` using natural weighting and a 3σ cleaning threshold. We imaged the continuum using the multi-frequency synthesis (MFS) mode in all

Table 2.3: Details of the observations used for the analysis of the continuum emission

QSO	Obs freq (GHz)	Beam cont [arcsec^2]	r.m.s. cont [mJy/beam]	Refs	Project ID
J0100+2802	670.9	1.97×1.17	0.8	TP	2021.2.00151.S
J036+03	106.97	6.1×3.5	0.038	[1]	S17CD (NOEMA)
	243.11	0.12×0.08	0.007	TP	2019.1.01633.S
	260.53	0.18×0.17	0.01	TP, [2]	2015.1.00399.S
	338.71	0.77×0.54	0.03	TP	2018.1.01790.S
	404.99	2.10×1.43	0.60	TP	2021.2.00151.S
	670.92	1.12×0.97	0.50	TP	2021.2.00151.S
J0224-4711	95.33	3.95×2.32	0.016	TP	2017.1.01472.S
	245.67	0.56×0.56	0.024	TP	2018.1.01188.S
	260.51	0.13×0.11	0.013	TP	2021.1.00934.S
	405.19	3.87×2.79	0.88	TP	2021.2.00151.S
	670.96	1.08×0.95	1.3	TP	2021.2.00151.S
J231-20	406.848	4.35×2.90	0.50	TP	2021.2.00064.S
J2054-0005	92.26	0.42×0.32	0.006	TP	2018.1.01289.S
	262.6	0.33×0.29	0.019	TP	2019.1.00672.S
	263.93	1.23×1.12	0.010	TP	2017.1.01088.S
	488.31	0.43×0.37	0.064	TP	2017.1.01195.S
	674.97	0.65×0.57	0.50	TP	2016.1.01063.S
J2310+1855	91.500	0.71×0.43	0.0053	TP, [3]	2015.1.00584.S
	136.627	0.74×0.71	0.015	TP, [4], [5], [6]	2015.1.01265.S
	140.995	0.79×0.65	0.015	TP, [4], [5], [6]	2015.1.01265.S
	153.070	0.21×0.17	0.0091	TP	2018.1.00597.S
	263.315	0.14×0.11	0.016	TP	2018.1.00597.S
	265.369	1.62×1.3	0.056	TP	2019.1.01721.S
	284.988	0.51×0.39	0.073	TP, [5]	2013.1.00462.S
	289.180	0.58×0.47	0.025	TP, [4], [5], [6]	2015.1.01265.S
	344.185	0.53×0.43	0.051	TP, [4], [5], [6]	2015.1.01265.S
	490.787	0.7×0.6	0.10	TP, [7]	2017.1.01195.S
	599.584	...	...	[4]	*Herschel*/SPIRE
	856.549	...	...	[4]	*Herschel*/SPIRE
	1199.169	...	...	[4]	*Herschel*/SPIRE
	1873.703	...	...	[4]	*Herschel*/PACS
	2997.924	...	...	[4]	*Herschel*/PACS

Notes. Columns: (1) Target QSO; (2) observed frequency of the continuum emission; (3) clean beam of the continuum map; (4) r.m.s of the continuum map; (5) References: This paper (TP); [1] Decarli et al. (2022); [2] B. P. Venemans et al. (2020); [3] Feruglio et al. (2018); [4] Shao et al. (2019); [5] Carniani et al. (2019); [6] Li et al. (2020); [7] Hashimoto et al. (2019). (6) project ID of the observation. $^{(a)}$: flux corrected for the contribution of the companion to the QSO emission.

line-free channels.

Observations in B9[3] for J0100+2802, and in B8 and B9 for J036+03 and J0224-4711 belong to our approved ALMA 7m program 2021.2.00151.S (PI: C. Feruglio), as well as, an high resolution observation in B6 for J2310+1885, which belongs to our approved ALMA program 2019.1.00661.S (PI: C. Feruglio). Therefore, we discuss the results of these observations in detail in Sect. 4.1.1.

Regarding the analysis of the SED of J0100+2802, we used the results from F. Wang et al. (2019) on continuum emissions at frequencies lower than our B9 observation. To study the SED of the J0100+2802's companion (hereafter J0100+2802-C), we analysed the dataset 2021.1.00211.S (PI: R. Maiolino) from the ALMA 12m array, designed to detect the [CII] (see Sect. 3.3) and CO(6-5) emission lines of J0100+2802 and their underlying continuum emission at 252.8 GHz (Band 6) and 99.5 GHz (Band 3). Properties of these two observations are described in detail in Sect. 4.3.3, since they required a specific study.

Regarding J2310+1855, Carniani et al. (2019) performed an analysis of its cold dust SED, but we decided to re-analyse the ALMA archival observations for this source since some of them were not available at the time of their analysis. This ensured a consistent analysis of all the observations. Moreover, we also considered Herschel observations in the FIR in order to model the dusty torus contribution to the cold dust SED. Specifics on the observations and on the results are reported in Sect. 4.3.1.

Regarding J036+03 and J0224-4711, we analysed all archival observations available for these sources since they are still not published. We also used the results on the continuum emission at $\sim$ 107 GHz of J036+03, obtained from a NOEMA observation (project ID: S17CD, Decarli et al., 2022).

Regarding J2054-0005, since many ALMA observations are available for this source especially in B6, we considered only archival observations with continuum sensitivity and resolution suited for the analysis of the SED. That is: when multiple observations per band were available, we considered the one with the highest continuum sensitivity and with resolution that allowed to spatially resolve the source and/or as close as possible to the resolution of B9 observation, in order to ensure a reliable and consistent analysis of the cold dust SED (for more details see Sect. 4.1.1). We tapered the higher resolution observations at 92.26 GHz, 262.6 GHz, and 488.31 GHz using `uvtaper`=[0.7 arcsec], in order to account for the more extended and fainter emission. We achieved a resolution of 1.0×0.89 arcsec^2, 0.88×0.82 arcsec^2, and 0.88×0.81 arcsec^2 for the 92.26 GHz, 262.6 GHz and 488.31 GHz observation, respectively. We did not found any further emission for the lowest frequency observation, while we gained $\sim$ 5% of the flux in the other two observations.

Regarding J231-20, we used the results presented in Pensabene et al. (2021), who analysed all the ALMA observations from Band 3 to Band 6 available for this QSO, and we independently analysed a new Band 8 ALMA observation targeting this QSO (ID: 2021.2.00064.S,

---

[3] Hereafter, the word band will be sometimes abbreviated to B.

PI: R. Decarli). Since J231-20 was found to have a close companion (at distance < 10 kpc), we discuss the analysis of the Band 8 observation in more detail in Sect. 4.1.1.

Information about the properties of the ALMA observations and the results on the continuum emissions analysis are reported in Tab. 2.3. Analysis of these observations, results and discussion are presented in Chap. 4.

2.3 Individual QSO's properties

In the following, I briefly describe the QSOs in our sample individually.

SDSS J010013.02+280225.8 (HYPERION)

For QSO SDSS J010013.02+280225.8 (hereafter J0100+2802) at $z_{\rm [CII]} = 6.327$ (F. Wang et al., 2019), Wu et al. (2015) estimated a bolometric luminosity of $L_{\rm bol} = 4.29 \times 10^{14}$ $L_\odot$ and a BH mass of $M_{\rm BH} = 1.24 \times 10^{10}$ $M_\odot$, making it the most optically luminous QSO with the most massive SMBH known at $z > 6$. Both measurements have been recently confirmed by JWST (Eilers et al., 2022). F. Wang et al. (2019) performed a multi-frequency analysis of the dust SED, but they could not obtain a precise determination of the dust properties, concluding that J0100+28 has either a high dust emissivity ($\beta \gtrsim 2$) or a high dust temperature ($T_{\rm dust} \gtrsim 60$ K), or a combination of thereof.

PSO J036.5078+03.0498 (HYPERION)

PSO J036.5078+03.0498 (hereafter J036+03, B. P. Venemans et al., 2015) at $z = 6.5405$ was observed for the first time in the Pan-STARRS1 survey (B. P. Venemans et al., 2015), and it has a BH mass of $M_{\rm BH,MgII} = (2.69 - 3.09) \times 10^9$ $M_\odot$ from the analysis of MgII emission line and a bolometric luminosity of $L_{\rm bol} = (2.13 - 3.16) \times 10^{47}$ erg s^{-1} (Zappacosta et al., 2023; Mazzucchelli et al., 2023). Decarli et al. (2022) studied the CO(6-5), CO(7-6) and $\rm [CI]_{2-1}$ emission lines of this QSO's host with NOEMA observations, and they found $L_{\rm CO(6-5)} = 12.7 \times 10^9$ K km s^{-1} pc^2, $L_{\rm CO(7-6)} = 10.7 \times 10^9$ K km s^{-1} pc^2 and $L_{\rm [CI]} = 5.7 \times 10^9$ K km s^{-1} pc^2, implying a molecular gas mass of $M_{\rm H2,CO} = 5.0^{+0.5}_{-0.6} \times 10^{10}$ $M_\odot$ and $M_{\rm H2,[CI]} = 7.1^{+1.6}_{-1.4} \times 10^{10}$ $M_\odot$. The [CII] emission shows ordered motion, with a clear and regular velocity gradient in the moment-1 map and $v_{\rm rot}/\sigma > 3$, and it has a $L_{\rm [CII]} = 3.38 \times 10^9$ $L_\odot$ and a size of $\sim 2.4 \times 1.6$ kpc^2 (B. P. Venemans et al., 2020; Neeleman et al., 2021). Form the modelling of the velocity rotation they estimated a dynamical mass of $M_{\rm dyn} = 2.9^{+1.1}_{-0.7} \times 10^{10}$ $M_\odot$, and from the [CII] underlying continuum emission they derived a gas mass of $M_{\rm H2,cont} = 2.8^{+15}_{-1.1} \times 10^{10}$ $M_\odot$, assuming a gas-to-dust ratio of 100 and a molecular-to-total gas mass fraction of 0.75. Greiner et al. (2021) did not find any companion brighter than $M_{1450}(AB) < -26$ mag within 0.1-3.3h^{-1} comoving Mpc search radius, using the simultaneous seven-channel Gamma-ray Burst Optical/Near-infrared Detector, confirming the results of B. P. Venemans et al. (2020), who did not detect any companion for this source using ALMA observation of [CII] emission.

VDES J022426.54-471129.4 (HYPERION)

VDESJ022426.54-471129.4 (hereafter J0224-4711, Reed et al., 2017) at $z = 6.5222$, firstly discovered by Reed et al. (2017), is one of the most X-ray luminous QSOs at $z > 5.5$ and the most X-ray luminous QSO at $z > 6.5$ (Pons et al., 2020; Zappacosta et al., 2023). It belongs to the HYPERION sample, the XQR-30 sample and the ASPIRE survey (J. Yang et al., 2023), and has a bolometric luminosity of $L_{\rm bol} = 3.47 \times 10^{47}$ erg s^{-1}, and BH mass of $M_{\rm BH,MgII} = (1.30 - 2.29) \times 10^9$ M$_\odot$ from the analysis of MgII emission line (Reed et al., 2019; F. Wang et al., 2021; Zappacosta et al., 2023; Mazzucchelli et al., 2023) and $M_{\rm BH,H\beta} = 2.15 \times 10^9$ M$_\odot$, from the analysis of Hβ emission line (J. Yang et al., 2023). It has the most extreme broad and blueshifted [OIII] lines observed to date, even compared to observations of lower-redshift QSOs, with a velocity shift of -1690 km s^{-1} relative to the narrow [OIII], suggesting powerful ionized outflows (J. Yang et al., 2023).

PSO J231.6576-20.8335 (HYPERION)

PSO J231.6576-20.8335 (hereafter J231-20) at $z = 6.587$ has been discovered using the Pan-STARRS1 survey (Mazzucchelli et al., 2017), and it is one of the brightest objects at $z > 6.5$. Decarli et al. (2017) detected a [CII]-bright nearby companion at <10 kpc separation. Pensabene et al. (2021) performed an extensive study of both the QSO and its companion, detecting [NII], CO(7-6), CO(10-9) emission lines, two OH transitions and their underlying continuum in both of them. Additionally, the CO(15-14), CO(16-15) and three transitions of H_2O emission line have been detected for the central QSO. Analysing the cold dust SED of both the QSO and its companion, they derived $T_{\rm dust} = 54$ K, $M_{\rm dust} = 5.1 \times 10^8$ M$_\odot$ and $T_{\rm dust} = 35 - 46$ K, $M_{\rm dust} = (2.3 - 3.4) \times 10^8$ M$_\odot$, respectively. The estimates on the dust temperature suffer of high uncertainties given that they lack of high-frequency observations to probe the peak of the SED. Neeleman et al. (2021) found a dynamical mass $M_{\rm dyn} = 1.4 \times 10^{10}$ M$_\odot$ from the modelling of the velocity rotation curve, and reported a BH mass of $M_{\rm BH} = 4.1 \times 10^9$ M$_\odot$. Finally, Bischetti et al. (2022) classified this as a broad absorption line (BAL) QSO, indicating that J231-20 may be caught in a phase of strong BH feedback.

ULAS J134208.10+092838.35 (HYPERION)

ULAS J134208.10+092838.35 (hereafter J1342+0928) at $z = 7.54$, the most distant QSO known to date, was discovered by Bañados et al. (2018) who reported an absolute AB magnitude $M_{1450} = -26.8$, bolometric luminosity of $L_{\rm bol} = 10^{13}$ L$_\odot$, and an SMBH mass of $8{\times}10^8$ M$_\odot$. It was followed-up with NOEMA resulting in the detection of bright [CII] emission and upper limits on several CO lines (B. P. Venemans et al., 2017). Novak et al. (2019) presented ALMA observations of the dust continuum and the ISM of the host galaxy J1342+0928. They well constrained the Rayleigh-Jeans tail of the dust SED, deriving a $M_{\rm dust} = 3.5{\times}10^7$ M$_\odot$ and a SFR$\sim$ 150 M$_\odot$ yr^{-1}, fixing the temperature at 47 K. They also detected many atomic fine structure line, such as [CII], [NII], [OIII], and limits on [CI], [OI] and multiple CO transitions (with a tentative stack detection).

SDSS J114816.64+525150.3 (HYPERION)

SDSS J114816.64+525150.3 (hereafter J1148+5251) at z = 6.42 was discovered by Fan et al. (2003) who reported an absolute magnitude of $M_{1450} = -27.82$. It is one of the most studied QSOs at high-z. It was observed by Subary Telescope (Iwamuro et al., 2004), *Spitzer* (Jiang et al., 2006; Hines et al., 2006) and *Herschel* (Leipski et al., 2013), and therefore this allowed a full modelling of the SED of this QSO (Valiante et al., 2011; R. Schneider et al., 2015; Carniani et al., 2019). In particular, R. Schneider et al. (2015) derived that the AGN contribution to the dust heating in this QSO can be between 30% and 70%. S. Gallerani et al. (2014) detected an exceptionally strong CO(17–16) line in this QSO with the Plateau de Bure interferometer (PdBI) and performed a detailed analysis of the CO SLED using previously detected lower CO transitions (Bertoldi et al., 2003a; Walter et al., 2003; Riechers et al., 2009).

J100758.264+211529.207 (HYPERION)

J100758.264+211529.207 (dubbed Pōniuā'ena, hereafter J1007+2115) at z = 7.5419 was discovered by J. Yang et al. (2020) and it is one of the three highest redshift QSO known, all located at the midpoint of the EoR, $z \sim 7.5$. By fitting the NIR spectrum, J. Yang et al. (2020) derived $M_{\rm BH} = (1.5 \pm 0.2) \times 10^9$ M$_\odot$ and an Eddington ratio of 1.06 ± 0.2, using the broad MgII emission line. This places the strongest constraint to the early SMBH growth requiring a BH seed of $\sim 10^5$ M$_\odot$ at z = 15.

SDSS J231038.88+185519.7

QSO SDSS J231038.88+185519.7 (hereafter J2310+1855), first discovered in SDSS (Jiang et al., 2006; R. Wang et al., 2013), is one of the most FIR-luminous QSOs and one of the brightest optical QSOs known at $z \sim 6$, with $L_{\rm bol} = 9.3 \times 10^{13}$ L$_\odot$. The redshift measured with the QSO rest-frame UV line emission is $z = 6.00 \pm 0.03$ (R. Wang et al., 2013). Feruglio et al. (2018) detected and analysed the CO(6-5) and [CII] emission lines and the sub-millimetre continuum of J2310+1855, deriving a size of the dense molecular gas of 2.9 ± 0.5 kpc and of 1.4 ± 0.2 kpc for the 91.5 GHz dust continuum and a molecular gas mass of $M(\rm H_2) = (3.2 \pm 0.2) \times 10^{10}M_\odot$. They estimated a dynamical mass of $M_{\rm dyn} = (4.1^{+9.5}_{-0.5}) \times 10^{10}M_\odot$, measuring a disk inclination of $i \sim 50$ deg. They also inferred the BH mass from the CIV emission line, measured in the X-shooter/VLT spectrum of the QSO, obtaining $M_{\rm BH} = (1.8 \pm 0.5) \times 10^9M_\odot$. Recently, Shao et al. (2019) presented a detailed analysis of the FIR and sub-mm SED and derived a dust temperature of $T \sim 40$ K, a dust mass of $M_{\rm dust} = 1.6 \times 10^9M_\odot$, a FIR luminosity $L_{\rm FIR}^{8-1000\mu m} = 1.6 \times 10^{13}$ L$_\odot$, and an SFR= 2400 − 2700 M$_\odot$yr^{-1}. V. D'Odorico et al. (2018) detected a very metal-poor, proximate damped Lyman α system (DLA) located at z=5.938646 ± 0.000007 in the X-shooter/VLT spectrum of J2310, which was associated with a CO emitting source at $z = 5.939$. This source, called Serenity-18, was detected through its CO(6-5) emission line at [RA, DEC] = 23:10:38.44, 18:55:21.95.

SDSS J205406.49-000514.8

SDSS J205406.49-000514.8 (hereafter J2054-0005) at $z = 6.39$ was selected from SDSS stripe 82 with $m_{1450} = 20.60$, i.e. about one magnitude fainter than the objects discovered from the SDSS main survey (Jiang et al., 2008). Leipski et al. (2014) reported observations in band z,y,J,H,K and with *Herschel*, however they were not able to fully study its SED due to lack of observations in the mm/sub-mm regime. R. Wang et al. (2013) reported a BH mass of $M_{\rm BH} = 8.6 \times 10^8$ M$_\odot$, later updated to $M_{\rm BH} = 1.48 \times 10^9$ M$_\odot$ using the MgII emission line (Neeleman et al., 2021). Neeleman et al. (2021) studied the rotation curve of J2054-0005 using an high-resolution ALMA observation of the [CII] emission of this object, and they determined a lower limit for the dynamical mass of $M_{\rm dyn} > 2.9 \times 10^{10}$ M$_\odot$.

ULAS J131911.29+095051.4

ULAS J131911.29+095051.4 (hereafter J1319+0950) at $z = 6.133$ was discovered in the UKIRT Infrared Deep Sky Survey (UKIDSS) with $m_{1450} = 19.65$, which lies in the typical magnitude range of the optically bright $z \sim 6$ quasars selected from the SDSS main survey (Mortlock et al., 2008). Ran Wang et al. (2011) detected the CO(6-5) emission line and its underlying continuum, deriving a gas mass of $M_{\rm gas} = 1.5 \times 10^{10}$ M$_\odot$. Later, R. Wang et al. (2013) analysed the [CII] line emission and underlying continuum, deriving a dynamical mass of $M_{\rm dyn} = 12.5 \times 10^{10}$ M$_\odot$ (also confirmed by Shao et al. 2017). Shao et al. (2017) estimated a BH mass $M_{\rm BH} = (2.7 \pm 0.6) \times 10^9$ M$_\odot$ from the MgII line, which contributes 2% of the dynamical mass of the system. Carniani et al. (2019) performed a detailed study of the cold dust SED of J1319+1950 deriving a dust mass of $\log(M_{\rm dust}/M_\odot) = 8.8 \pm 0.2$ and a dust temperature of $T_{\rm dust} = 66^{+15}_{-10}$ K. Herrera-Camus et al. (2020) tentatively detected the OH 119 μm doublet in absorption, which is blueshifted with a median velocity that suggests the presence of a molecular outflow, although characterized by a modest molecular mass loss rate of ~ 200 M$_\odot$ yr^{-1}.

SDSS J012958.51-003539.7

SDSS J012958.51-003539.7 (hereafter J0129-0035) at $z = 5.778$ is the faintest of the SDSS $z \sim 6$ quasars, with $m_{1450} = 22.16$ (Jiang et al., 2009). Ran Wang et al. (2011); R. Wang et al. (2013) studied the CO(6-5) and [CII] emission lines, deriving $M_{\rm gas} = 1.2 \times 10^{10}$ M$_\odot$ and $M_{\rm dyn} = 1.3 \times 10^{10}$ M$_\odot$. Neeleman et al. (2021) found that the galaxy showed no velocity gradient using high-resolution ALMA observation of [CII] emission and therefore derived a dynamical mass of 5.4×10^{10} M$_\odot$, assuming that the galaxy is dispersion dominated. They also measured a BH mass of 1.7×10^8 M$_\odot$ from MgII emission line.

PSO J183.1124+05.0926

PSO J183.1124+05.0926 (hereafter J183+05) at $z = 6.439$ was discovered by Bañados et al. (2018) using color-color selections from the Pan-STARRS1 database (Chambers et al., 2016) and follow-up photometric and spectroscopic observations. The [CII] luminosity in this source is the highest among 27 quasars at $z > 6$ surveyed in Decarli et al. (2018). J183+05 showed a clear velocity gradient however, given the resolution of the observation, only an upper limit to dynamical mass of has been derived $M_{\rm dyn} > 1.3 \times 10^{11}$ $\mathrm{M}_\odot$ from the study of its rotation curve (Neeleman et al., 2021). It has a BH mass of $M_{\rm BH} = 3.0 \times 10^9$ $\mathrm{M}_\odot$ derived from MgII emission line. Recently, Decarli et al. (2023) analysed the cold dust SED of this QSO in detail, deriving $T_{\rm dust} = 47 \pm 2$ K, $M_{\rm dust} = (8.7 \pm 1.1) \times 10^8$ $\mathrm{M}_\odot$ and SFR = 1330 $\mathrm{M}_\odot$ yr^{-1}. They also presented a multi-line study of this object, reporting detections of [CII], [OIII], [NII], CO(7-6), OH and two H_2O transitions.

CHAPTER 3

COLD GAS PROPERTIES

In this chapter, I present the results of the cold gas of the QSOs J2310+1855, J0100+2802, J1007+2115, J0224-4711, J1319+0950, J2054-0005 and J0129-0035. In Sect. 3.1, I will give a brief introduction to the study of the cold gas in high-z QSO's host galaxies, summarizing what already explained in Chap. 1.2.1. Observations and data reduction have been presented in Chap. 2 (see Sect. 2.2.1). In Sect. 3.2, I will focus on the analysis of the CO(6-5) and CO(7-6) line emission, and consequently on the derivation of the molecular gas mass from these tracers. In Sect. 3.3, I will firstly discuss the [CII] distribution and kinematics of the QSOs J2310+1855 and J0100+2802, and then I will present some dynamical studies of the rotation curve of the QSO J2310+1855. I will also show the analysis of cold outflows detected in both QSOs. The last part of Sect. 3.3 will be devoted to the study of the environment of J2310+1855. In Sect. 3.4, I will present the results on the detection the water vapour emission in QSO J2310+1855. Details on the properties of individual objects can be found in Chap. 2.

This chapter is based, with limited modifications, on the published papers Tripodi et al. (2022); Tripodi et al. (2023b); Feruglio et al. (2023); Tripodi et al. (2023c), and Tripodi in prep.

3.1 Introduction

In the past few decades, *Herschel*, NOEMA, the VLA, and particularly ALMA have been able to probe and give insights into the properties of the gas and dust inside the QSO's host galaxies, allowing us to derive the dynamical masses, star formation activity, and ISM properties.

The ISM of the QSO's host galaxies has compact sizes of a few kiloparsec (e.g. R. Wang et al. 2013; Shao et al. 2017; B. P. Venemans et al. 2020; Neeleman et al. 2021) and shows massive gas reservoirs (Feruglio et al., 2018). The [CII] $\lambda 158\mu$m is the dominant cooling line of the ISM and the brightest emission line, almost unaffected by attenuation. Therefore, it is the preferred tracer for studying the ISM and provides valuable information about cold, warm neutral and mildly ionised ISM (Cormier et al., 2015; Olsen et al., 2018). Its 158μm transition predominantly arises from PDRs (D. J. Hollenbach and Tielens, 1999) at the interface of the atomic and molecular media in the outskirts of molecular clouds in galaxy star-forming regions. Through kinematical studies of [CII], dynamical masses have been derived of $< 10^{11}$ $M_{\odot}$ (e.g. Shao et al. 2017; Pensabene et al. 2021; Izumi et al. 2021b; Neeleman et al. 2021), which place most of the $z \sim 6$ QSOs above the $M_{\rm BH} - M_{\rm dyn}$ relation by a factor of $\sim 3-10$. This in turn allows us to distinguish among the different growth paths of the SMBHs and their host galaxies (BH dominance, symbiotic growth, or BH adjustment, see M. Volonteri 2012 and Chap. 5).

The cold molecular phase is the least explored up to now at $z > 6$. A few tens of quasars at redshift up to $z \sim 6.8$ have been detected in CO rotational transitions, that are the most direct tracers of the cold molecular ISM, indicating massive molecular reservoirs of dense gas feeding both star formation and nuclear accretion (R. Wang et al., 2013; F. Wang et al., 2016; S. Gallerani et al., 2014; Carniani et al., 2019; B. P. Venemans et al., 2017; Decarli et al., 2022). Molecular gas mass estimates typically rely on intermediate ($J_{\rm up}$=5-7) transitions (B. P. Venemans et al., 2017; J. Yang et al., 2019; Decarli et al., 2022) which are found to be at the peak of the CO SLED (Li et al., 2020; Feruglio et al., 2023). The CO SLED modeling indicate that in addition to the far-UV radiation from young and massive stars, another gas heating mechanism (e.g., X-ray radiation and/or shocks) may be needed to explain the observed CO luminosities (Li et al., 2020; Pensabene et al., 2021; Decarli et al., 2022). Only in a few cases it was possible to spatially resolve the molecular reservoirs and map disks or dispersion-dominated hosts (Walter et al., 2004; Feruglio et al., 2018; Yue et al., 2021; Walter et al., 2022; Shao et al., 2022). At $z > 7$, the dense molecular gas reservoirs have been investigated in only two quasars, J1342+0928 at $z = 7.54$ and J1120+0641 at $z = 7.08$, and remained so far undetected (Novak et al., 2019).

In the past decade, the strong coupling between the ISM (and also the circum-galactic medium, CGM) and the SMBH energy output has been observed and was modelled theoretically. It occurs as mechanical and radiative QSO-driven feedback processes, and it affects the evolution of the whole galaxy. In particular, very powerful mechanisms that efficiently deposit energy and momentum into the surrounding gas are found to be QSO-driven outflows (Faucher-Giguère and Quataert, 2012; Zubovas and A. King, 2012). They have been extensively studied and detected from the local Universe back to the EoR in all gas phases, at all spacial scales, from sub-parsec to several kiloparsecs, even with high kinetic power (up to a few percent of the bolometric luminosity) and with mass outflow rates exceeding the star formation rate (Feruglio et al., 2010; Maiolino et al., 2012; Cicone et al., 2015; Aalto et al., 2015; Fiore et al., 2017; Bischetti et al., 2019a). Because of observational limitations, we unfortunately have very few detections of outflows in high-z QSOs (Maiolino et al., 2005; Bischetti et al., 2019b; Izumi et al., 2021b; Izumi et al., 2021a), but a precise determination of their masses, extension, and occurrence would give us valuable insights into the onset of the AGN feedback in the first QSOs.

Finally, the broad-band coverage of ALMA allows the serendipitous detection of additional emission lines arising from the galaxy ISM, such as H_2O, which can be used to provide additional constraints on the ISM properties. Water vapour emission lines have been detected from $z > 3$ galaxies and QSOs (e.g. Paul P. van der Werf et al. 2011; F. Combes et al. 2012; A. Omont et al. 2013; Riechers et al. 2013), but they are still rare and unresolved, if detected, at $z \gtrsim 6$ (e.g. J. Yang et al. 2019; Pensabene et al. 2021 and references therein). Although little information is still available at high-z, a correlation between L_{H_2O} and the total infrared luminosity has been found and studied, suggesting that the water vapour lines would be excited by an IR-pumping mechanism from the ISM UV radiation field (J. Yang et al., 2019; Pensabene et al., 2021).

In this chapter, we present high-resolution ALMA observations of the [CII], H_2O emission lines of QSO J2310+1855, high-resolution ALMA observations of the CO(6-5) emission line of QSOs J1319+0950, J2054-0005, J0129-0035, low-resolution ALMA observations of the [CII] of QSO J0100+2802 and of the CO(7-6) and [CI] of QSO J0224-4711, and NOEMA observations of the CO(7-6) and CO(6-5) of QSO J1007+2115.

3.2 Dense cold gas: CO

3.2.1 Results

Fig. 3.1 presents the CO(6-5) and (7-6) line profiles of J1007+2115, their velocity-integrated maps, and the underlying continuum emission in the LSB and USB. Both lines are consistent with an unresolved source in the uv plane with fluxes $S\,dv_{\mathrm{CO(6-5)}} = 0.44 \pm 0.06$ Jy km $\mathrm{s^{-1}}$and $S\,dv_{\mathrm{CO(7-6)}} = 0.40 \pm 0.07$ Jy km $\mathrm{s^{-1}}$(Tab. 3.1). Both lines are robustly detected with statistical significance of 7 and 6 σ, respectively. A fit with a Gaussian model gives a marginally resolved source and a lower signal-to-noise ratio in the flux, confirming that the source is unresolved in both transitions.

The average redshift derived from CO(6-5) and (7-6) lines is $z_{\mathrm{CO}} = 7.5149 \pm 0.0006$, consistent with that derived from the [CII] 158 μm line (J. Yang et al., 2020). The line widths, derived by fitting a single Gaussian to the spectra, are $\mathrm{FWHM_{CO(6-5)}} = 310 \pm 65$ km $\mathrm{s^{-1}}$and $\mathrm{FWHM_{CO(7-6)}} = 261 \pm 47$ km $\mathrm{s^{-1}}$, consistent within 1σ with the [CII] FWHM (J. Yang et al., 2020). The line fluxes derived from the Gaussian fit are 0.35 ± 0.08 Jy km $\mathrm{s^{-1}}$ for CO(6-5) and 0.36 ± 0.07 Jy km $\mathrm{s^{-1}}$ for CO(7-6), both consistent with the uv plane analysis (Tab. 3.1).

The line luminosities are $\mathrm{L'CO}(6-5) = (2.1 \pm 0.3) \times 10^{10}$ K km $\mathrm{s^{-1}pc^2}$and $\mathrm{L'CO}(7-6) = (1.4 \pm 0.2) \times 10^{10}$ K km $\mathrm{s^{-1}pc^2}$ (Carilli and Walter, 2013). The [CI](2-1) 370μm emission line is undetected and we derive a 3σ upper limit on the flux of 0.18 Jy km $\mathrm{s^{-1}}$, or L[CI]< 10^8 $\mathrm{L_\odot}$(Tab. 3.1), assuming an unresolved source with FWHM=350 km $\mathrm{s^{-1}}$(i.e. the average FWHM value

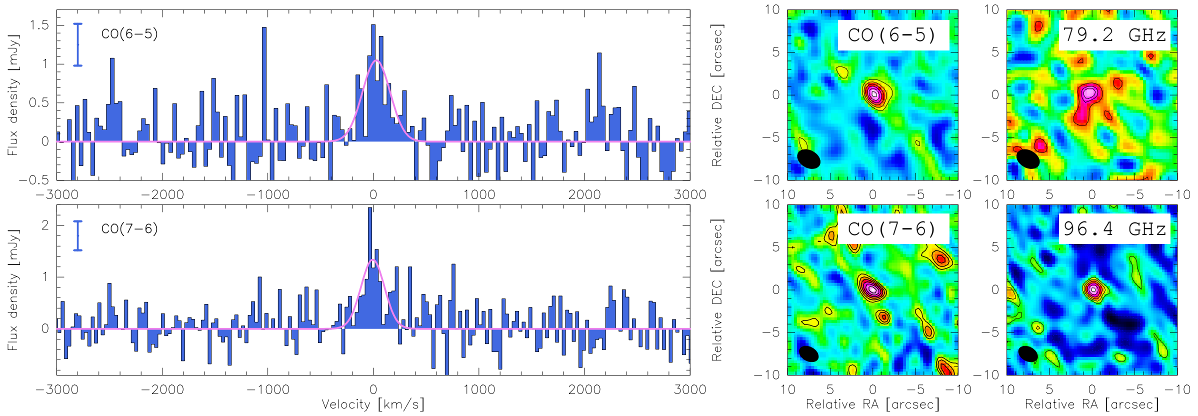

Figure 3.1: *Upper panels: (left to right) the CO(6-5) emission line spectrum, the corresponding velocity-integrated CO map and the 79.2 GHz continuum map of J1007+2115 (also dubbed Pōniuā'ena). Lower panels: the CO(7-6) emission line spectrum, the corresponding velocity-integrated map and the 96.4 GHz continuum map relative to the phase center set at [RA,DEC]=[10:07:58.260, 21:15:29.20]. The velocity zero point is set to the frequency 81.207 GHz for CO(6-5) and 94.734 GHz for CO(7-6). In each panel we report the error bar showing the* 1σ *errorbar in the 10 MHz spectral channel. Magenta lines show the fit with a single Gaussian component, FWHM is reported in Tab. 3.1. Contours are drawn starting at* 2σ *in steps of* 1σ *(*σ = 0.05 *Jy km* s^{-1} *for CO(6-5), 0.065 Jy km* s^{-1} *for CO(7-6), 15.5*μ*Jy for 79.2 GHz continuum, 12.2*μ*Jy for 96.4 GHz continuum.*

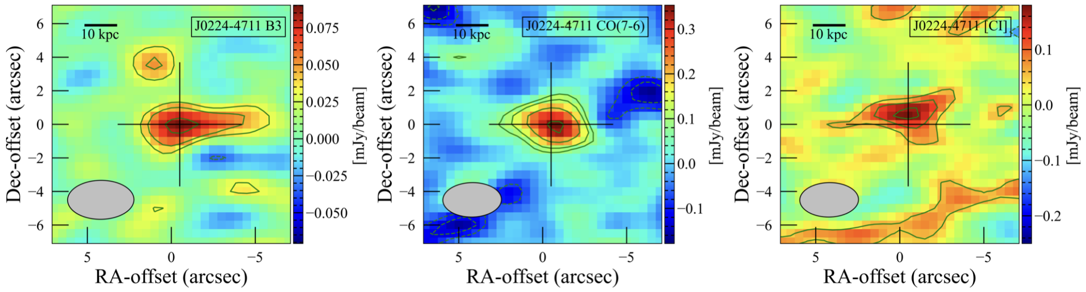

Figure 3.2: *Left panel: 95.33 GHz dust continuum map of QSO J0224-4711 (levels* $-3, -2, 2, 3,$ *and* 5σ, $\sigma = 0.016$ *mJy/beam). The clean beam (*3.95×2.32 arcsec^2*, PA=-89.43°) is indicated in the lower left corner of the diagram. The cross indicates the position of the continuum peak. Central panel: CO(7-6) emission line map of QSO J0224-4711 (levels* $-3, -2, 2, 3, 5,$ *and* 8σ, $\sigma = 0.042$ *mJy/beam). The clean beam (*3.49×2.05 arcsec^2*, PA=-89.06°) is indicated in the lower left corner of the diagram. The cross indicates the position of the B3 continuum peak. Right panel: [CI] emission line map of QSO J0224-4711 (levels* $-3, -2, 1, 2,$ *and* 3σ, $\sigma = 0.054$ *mJy/beam). The clean beam (*3.49×2.05 arcsec^2*, PA=-89.06°) is indicated in the lower left corner of the diagram. The cross indicates the position of the B3 continuum peak.*

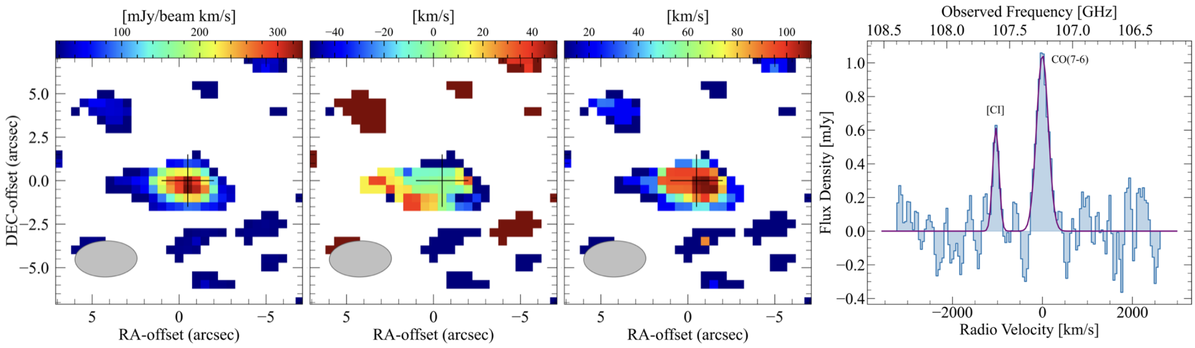

Figure 3.3: *Moment maps of the CO(7-6) emission line and spectrum of CO(7-6) and [CI] emission lines of J0224-4711. From left to right: integrated flux, mean velocity map, and velocity dispersion map, continuum-subtracted spectra of CO(7-6) and [CI]. The clean beam is plotted in the lower left corner of the moment maps. The cross indicates the peak position of the Band 3 continuum emission. The spectrum was extracted from the region included within* $\geq 2\sigma$ *in the CO(7-6) map.*

measured for the CO lines). A scan of the data cubes did not reveal any other line or continuum emitters.

The left, central and right panels of Fig. 3.2 present the maps of the Band 3 continuum, CO(7-6) and [CI] of J0224-4711 respectively, imaged using the MFS mode in the channels specified in Tab. 2.2. The CO(7-6) and [CI] emission are detected with a statistical significance of $\sim 8\sigma$ and $\sim 3\sigma$, respectively, and they are both not spatially resolved. Performing a 2D Gaussian fit, we obtained a peak flux of 0.364 ± 0.025 mJy/beam for CO(7-6) and of 0.192 ± 0.028 mJy/beam for [CI].

Fig. 3.3 shows the moment-0, -1, and -2 maps of the CO(7-6) emission, obtained by applying 2.5σ threshold to the continuum-subtracted cube in the line channels, and the spectrum extracted from the region with S/N> 2 in the CO(7-6) map. The moment-0 shows a velocity gradient oriented east to west with $\Delta v = 100$ km s^{-1}, and the moment-2 map shows a range of the velocity dispersion[1] between 20 and 120 km s^{-1}. The CO(7-6) line profile peaks at a frequency of 107.239 GHz, corresponding to $z = 6.5220 \pm 0.0002$, consistent with previous determinations (Reed et al., 2017). From the fit with a single Gaussian, the FWHM of the line is 307 ± 25 km s^{-1} and the integrated flux is 0.342 ± 0.052 Jy km s^{-1}, that corresponds to a luminosity of $L_{\rm CO(7-6)} = (1.6 \pm 0.2) \times 10^8$ L$_\odot$ and $L'_{\rm CO(7-6)} = (9.6 \pm 1.4) \times 10^9$K km s^{-1} pc^2 (following Eq.1 and Eq.3 of Solomon and Vanden Bout, 2005). The [CI] line is slightly blueshifted, peaking at 107.610 GHz that corresponds to $z = 6.5211 \pm 0.0004$. Performing a single Gaussian fit, we obtained that the FWHM of the line is 165 ± 29 km s^{-1} and the integrated flux is 0.108 ± 0.036 Jy km s^{-1}, that corresponds to a luminosity[2] of $L_{\rm [CI]} = (5.1 \pm 1.7) \times 10^7$ L$_\odot$ and $L'_{\rm [CI]} = (3.0 \pm 1.0) \times 10^9$K km s^{-1} pc^2. All line properties are reported in Tab. 3.1.

In order to analyse the CO(6-5) emission line of QSOs J1319+0950, J2054-0005 and

---

[1] The maximum value of the velocity dispersion towards the nucleus is usually affected by beam smearing (R. Davies et al., 2011).

[2] All luminosities are computed following Eq.1 and Eq.3 of Solomon and Vanden Bout (2005)

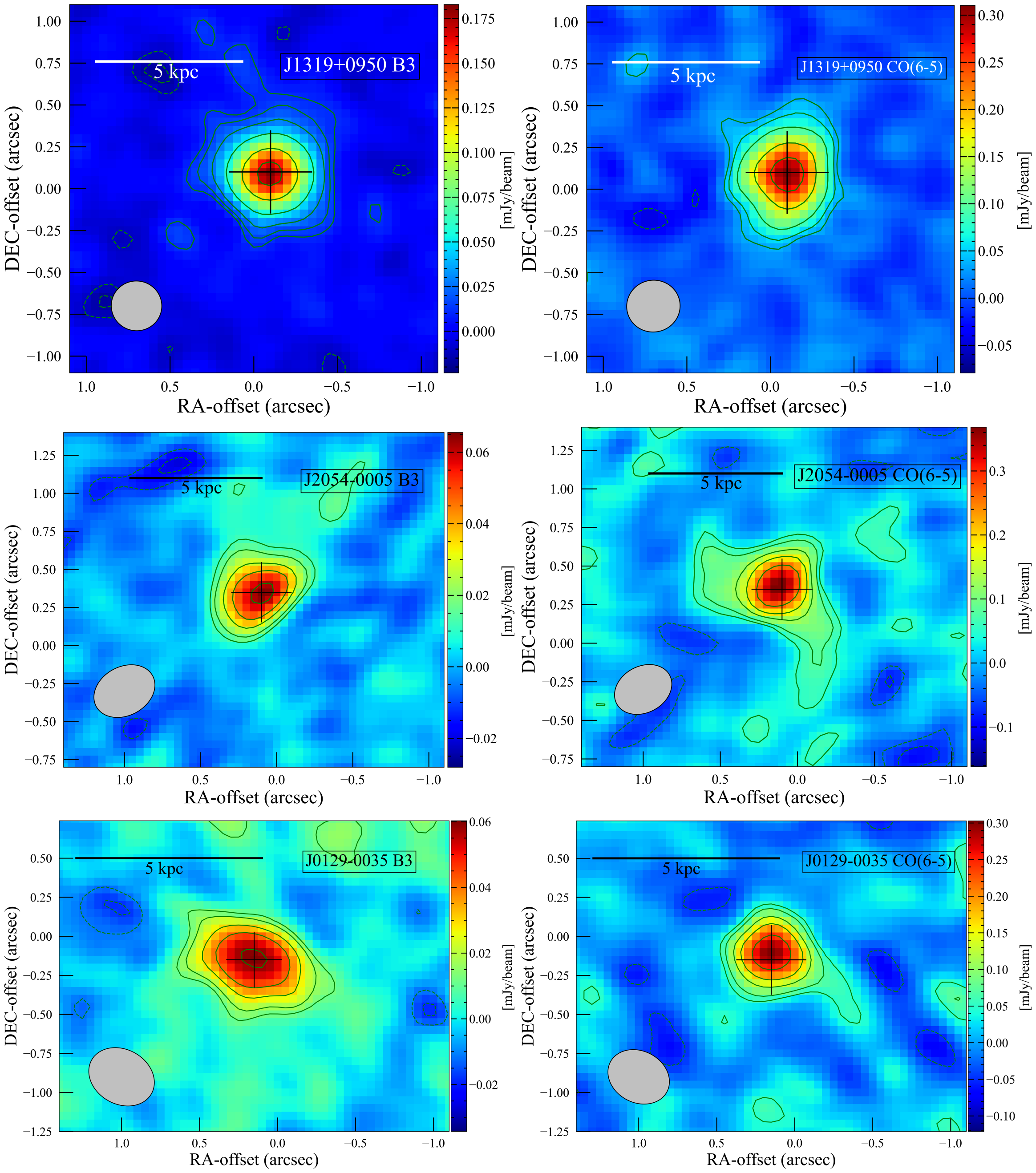

Figure 3.4: *Top left panel: 103 GHz dust continuum map of QSO J1319+0950 (levels* $-3, -2, 2, 3, 5, 10,$ *and* 20σ, $\sigma = 0.005$ *mJy/beam). The clean beam* (0.30×0.30 arcsec^2, *PA=-78.56°) is indicated in the lower left corner of the diagram. Top right panel: CO(6-5) map of QSO J1319+0950 (levels* $-3, -2, 2, 3, 5, 10,$ *and* 15σ, $\sigma = 0.017$ *mJy/beam). The clean beam* (0.32×0.31 arcsec^2, *PA=-78.56°) is indicated in the lower left corner of the diagram. Central left panel: 92 GHz dust continuum map of QSO J2054-0005 (levels* $-3, -2, 2, 3, 5, 7$*and* 10σ, $\sigma = 0.006$ *mJy/beam). The clean beam* (0.42×0.32 arcsec^2, *PA=-61.3°) is indicated in the lower left corner of the diagram. Central right panel: CO(6-5) map of QSO J2054-0005 (levels* $-3, -2, 2, 3, 5, 7$*and* 10σ, $\sigma = 0.025$ *mJy/beam). The clean beam* (0.39×0.30 arcsec^2, *PA=-61.4°) is indicated in the lower left corner of the diagram. The cross indicates the position of the continuum peak for each source. Bottom left panel: 96 GHz dust continuum map of QSO J0129-0035 (levels* $-3, -2, 2, 3, 5, 7,$ *and* 10σ, $\sigma = 0.006$ *mJy/beam). The clean beam* (0.44×0.35 arcsec^2, *PA=-60.72°) is indicated in the lower left corner of the diagram. Bottom right panel: CO(6-5) map of QSO J0129-0035 (levels* $-3, -2, 2, 3, 5, 7,$ *and* 10σ, $\sigma = 0.024$ *mJy/beam). The clean beam* (0.41×0.33 arcsec^2, *PA=-62.31°) is indicated in the lower left corner of the diagram.*

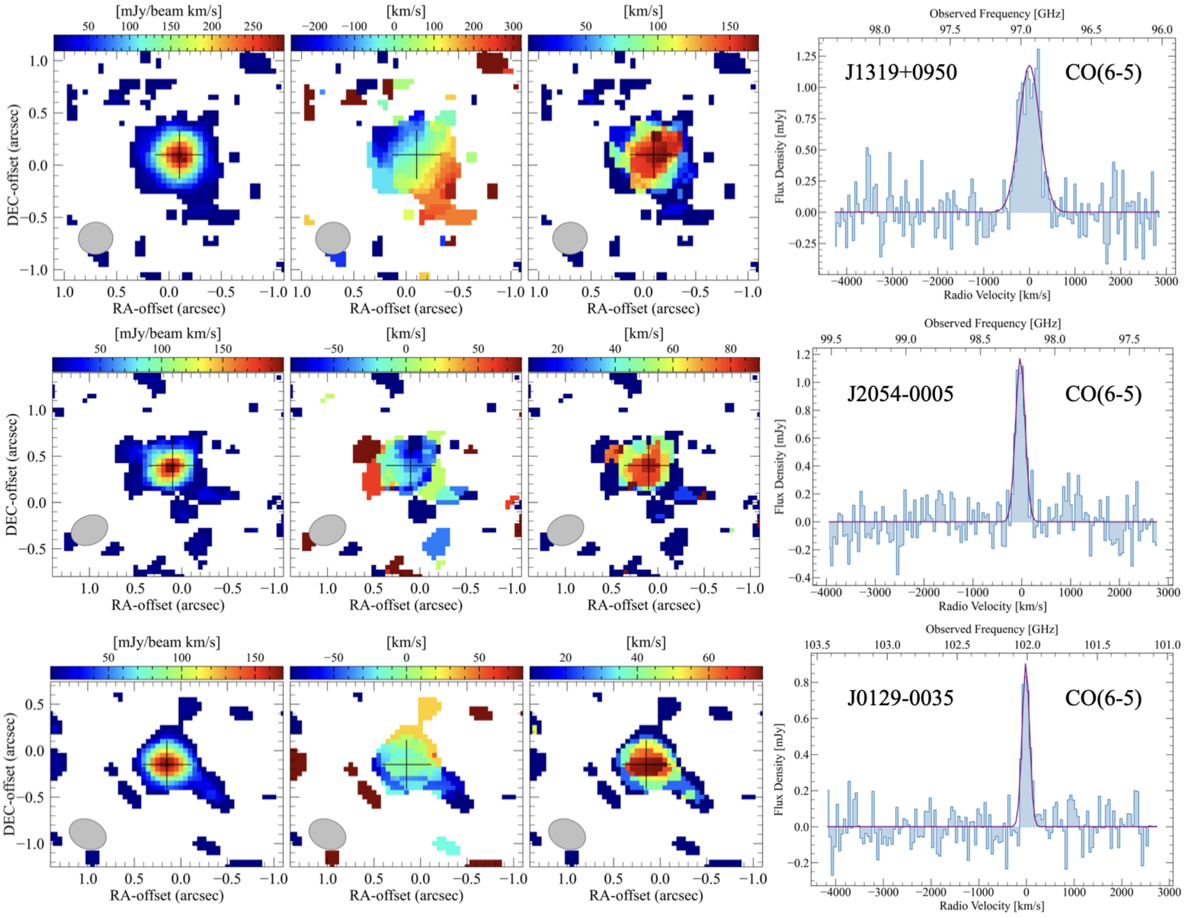

Figure 3.5: *Moment maps of the CO(6-5) emission lines and spectra of J1319+0950 (top row), J2054-0005 (central row), and J0129-0035 (bottom row). From left to right: integrated flux, mean velocity map, and velocity dispersion map, continuum-subtracted spectrum of CO(6-5). The clean beam is plotted in the lower left corner of the moment maps. The cross indicates the peak position of CO(6-5). The spectra were extracted from the region included within* $\geq 2\sigma$ *in the CO(6-5) map of each source.*

J0129-0035, we re-binned to 50 km s^{-1} the continuum subtracted data cubes.

The top row of Fig. 3.4 presents the map of the CO(6-5) emission line of J1319+0950 and its underlying continuum, imaged using the MFS mode in the channels specified in Tab. 2.2. The CO(6-5) is detected with a statistical significance of $\sim 15\sigma$ and, performing a 2D Gaussian fit, we obtained a peak flux of 0.303 ± 0.014 mJy/beam, and integrated flux of 0.570 ± 0.038 mJy. The emission is spatially resolved with a size of $(0.350 \pm 0.032) \times (0.233 \pm 0.030)$ arcsec^2.

The top row of Fig. 3.5 shows the moment-0, -1, and -2 maps of the CO(6-5) emission of J1319+0950, obtained by applying 3σ threshold to the continuum-subtracted cube in the line channels, and the spectrum extracted from the region with S/N> 2 in the CO(6-5) map. The moment-0 shows a velocity gradient oriented north-east to south-west with $\Delta v = 400$ km s^{-1}, and the moment-2 map shows a range of the velocity dispersion between 20 and 160 km s^{-1}. The CO(6-5) line profile peaks at a frequency of 96.939 GHz, corresponding to $z = 6.1331 \pm 0.0004$. Performing a single Gaussian fit to the line spectral profile, we obtained a FWHM of the line of 529 ± 41 km s^{-1} and an integrated flux of 0.662 ± 0.094 Jy km s^{-1}, that corresponds to a luminosity of $L_{CO(6-5)} = (2.4 \pm 0.3) \times 10^8$ $L_\odot$ and $L'_{CO(6-5)} = (2.3 \pm 0.3) \times 10^{10}$K km s^{-1} pc^2.

The central row of Fig. 3.4 presents the map of the CO(6-5) emission line of J2054-0005 and its underlying continuum, imaged using the MFS mode in the channels specified in Tab. 2.2. The CO(6-5) is detected with a statistical significance of $\sim 10\sigma$. Performing a 2D Gaussian fit, we obtained a peak flux of 0.349 ± 0.036 mJy/beam, and integrated flux of 0.496 ± 0.080 mJy, and the emission is spatially resolved with a size of (0.303 ± 0.088) × (0.082 ± 0.158) $arcsec^2$.

The central row of Fig. 3.5 shows the moment-0, -1, and -2 maps of the CO(6-5) emission of J2054-0005, obtained by applying 3σ threshold to the continuum-subtracted cube in the line channels, and the spectrum extracted from the region with S/N> 2 in the CO(6-5) map. The moment-0 shows a velocity gradient oriented south-east to north-west with Δv = 120 km s^{-1}, and the moment-2 map shows a range of the velocity dispersion between 20 and 80 km s^{-1}. The CO(6-5) line profile peaks at a frequency of 98.233 GHz, corresponding to $z = 6.0391 \pm 0.0002$. Performing a single Gaussian fit to the line spectral profile, we obtained a FWHM of the line of 229 ± 20 km s^{-1} and an integrated flux of 0.288 ± 0.047 Jy km s^{-1}, that corresponds to a luminosity of $L_{CO(6-5)} = (1.0 \pm 0.2) \times 10^8$ $L_\odot$ and $L'_{CO(6-5)} = (9.8 \pm 1.6) \times 10^9$K km s^{-1} pc^2.

The bottom row of Fig. 3.4 presents the map of the CO(6-5) emission line of J0129-0035 and its underlying continuum, imaged using the MFS mode in the channels specified in Tab. 2.2. The CO(6-5) is detected with a statistical significance of $\sim 15\sigma$ and, performing a 2D Gaussian fit, we obtained a peak flux of 0.313 ± 0.022 mJy/beam. The emission is not spatially resolved.

The bottom row of Fig. 3.5 shows the moment-0, -1, and -2 maps of the CO(6-5) emission of J0129-0035, obtained by applying 3σ threshold to the continuum-subtracted cube in the line channels, and the spectrum extracted from the region with S/N> 2 in the CO(6-5) map. The moment-0 shows a velocity gradient oriented south-east to north-west with Δv = 50 km s^{-1}, and the moment-2 map shows a range of the velocity dispersion between 20 and 80 km s^{-1}. The CO(6-5) line profile peaks at a frequency of 102.01 GHz, corresponding to $z = 5.7785 \pm 0.0002$. Performing a single Gaussian fit to the line spectral profile, we obtained a FWHM of the line of 183 ± 16 km s^{-1} and an integrated flux of 0.177 ± 0.029 Jy km s^{-1}, that corresponds to a luminosity of $L_{CO(6-5)} = (5.9 \pm 0.9) \times 10^7$ $L_\odot$ and $L'_{CO(6-5)} = (5.6 \pm 0.9) \times 10^9$K km s^{-1} pc^2.

3.2.2 Molecular gas mass

In this section, we aim at inferring the molecular gas mass of QSOs J1007+2115, J0224-4711, J1319+0950, J2054-0005 and J0129-0035 from molecular tracers such us CO(7-6) and CO(6-5) emission lines. Indeed molecular gas mass estimates in high-z QSO's host galaxies rely on CO observations, and especially on intermediate (J_{up}=5-7) transitions (B. P. Venemans et al., 2017; J. Yang et al., 2019; Decarli et al., 2022) which are found to be at the peak of the

Table 3.1: Line properties of QSOs J1007+2115, J0224-4711, J1319+0950, J2054-0005 and J0129-0035

	J1007+2115		J0224-4711	J1319+0950	J2054-0005	J0129-0035
CO transition	CO(6-5)	CO(7-6)	CO(7-6)	CO(6-5)	CO(6-5)	CO(6-5)
z_{CO}	$7.5149 \pm 0.0006^{(a)}$	$7.5149 \pm 0.0006^{(a)}$	6.5220 ± 0.0002	6.1331 ± 0.0004	6.0391 ± 0.002	5.7785 ± 0.0002
$\mathrm{FWHM_{CO}}$ [km s^{-1}]	310 ± 65	261 ± 47	307 ± 25	529 ± 41	229 ± 20	183 ± 16
$\mathrm{F_{CO}}$ [Jy km s^{-1}]	0.44 ± 0.06	0.40 ± 0.07	0.34 ± 0.05	0.66 ± 0.09	0.29 ± 0.05	0.18 ± 0.03
$\mathrm{L'_{CO}}$ [K km s^{-1} pc^{2}]	$(2.1 \pm 0.3) \times 10^{10}$	$(1.4 \pm 0.2) \times 10^{10}$	$(9.6 \pm 1.4) \times 10^{9}$	$(2.3 \pm 0.3) \times 10^{10}$	$(9.8 \pm 1.6) \times 10^{9}$	$(5.6 \pm 0.9) \times 10^{9}$
$\mathrm{L_{CO}}$ [$\mathrm{L_\odot}$]	$(2.2 \pm 0.3) \times 10^{8}$	$(2.3 \pm 0.4) \times 10^{8}$	$(1.6 \pm 0.2) \times 10^{8}$	$(2.4 \pm 0.3) \times 10^{8}$	$(1.0 \pm 0.2) \times 10^{8}$	$(5.9 \pm 0.9) \times 10^{7}$
$\mathrm{M^{(b)}_{H2,CO}}$ [$\mathrm{M_\odot}$]	$(1.3 \pm 0.2) \times 10^{10}$		$(1.0 \pm 0.1) \times 10^{10}$	$(1.5 \pm 0.2) \times 10^{10}$	$(6.4 \pm 1.0) \times 10^{9}$	$(3.7 \pm 0.6) \times 10^{9}$
$z_{\mathrm{[CI]}}$	–		6.5211 ± 0.0004	–	–	–
$\mathrm{FWHM_{[CI]}}$ [km s^{-1}]	–		165 ± 29	–	–	–
$\mathrm{F_{[CI]}}$ [Jy km s^{-1}]	< 0.18		0.11 ± 0.04	–	–	–
L′[CI] [K km s^{-1} pc^{2}]	$< 6 \times 10^{9}$		$(3.0 \pm 1.0) \times 10^{9}$	–	–	–
L[CI] [$\mathrm{L_\odot}$]	$< 1.0 \times 10^{8}$		$(5.1 \pm 1.7) \times 10^{8}$	–	–	–

Notes. $^{(a)}$: average of CO(6-5) and CO(7-6) redshifts. $^{(b)}$: assuming a conversion factor $\alpha_{\mathrm{CO}} = 0.8\ \mathrm{M_\odot (K\,km\,s^{-1}\,pc^2)^{-1}}$ and assuming a brightness temperature ratio $r_{76} = \mathrm{CO}(7-6)/\mathrm{CO}(1-0) = 0.76$ for J0224-4711, $r_{65} = \mathrm{CO}(6-5)/\mathrm{CO}(1-0) = 1.23$ for J1007+2115, J1319+0950, J2054-0005, and J0129-0035.

CO SLED (Li et al., 2020; Feruglio et al., 2023). In principle, low-J transitions should be preferred, as they are less sensitive to uncertainties on the CO excitation. However, these are quite challenging to detect because of their intrinsic faintness.

Hence molecular gas mass is derived as:

$$M_{\mathrm{H2,CO}} = \alpha_{\mathrm{CO}} r^{-1}_{\mathrm{J-(J-1)}} L_{\mathrm{CO(J-(J-1))}} \tag{3.1}$$

where $\alpha_{\mathrm{CO}} = 0.8$ $\mathrm{M_\odot}$ $(\mathrm{K\,km\,s^{-1}\,pc^2})^{-1}$ is the CO-to-$\mathrm{H_2}$ conversion factor typical for ULIRG and QSOs (Carilli and Walter, 2013), and $r_{\mathrm{J-(J-1)}}$ is the CO(J-(J-1))/CO(1-0) luminosity ratio. Fig. 3.6 shows the CO SLEDs normalized to the $\mathrm{J_{up}}$=6 transition of J036+03 (Decarli et al., 2022) and J2054-4711, limited to the (6-5) and (7-6) transitions (for CO(7-6) of J2054-0005 see Decarli et al., 2022), compared with other $z > 6$ QSOs, and QSO APM0879+5255 at $z = 3.9$ and QSO Cloverleaf at z=2.56 (Li et al., 2020; Feruglio et al., 2023), for which the CO SLED is well constrained down to $\mathrm{J_{up}}$=1. We note that the CO SLED for QSO at $z > 6$ presents a flattening at the CO(6-5) and (7-6) transitions on average, and that all CO SLEDs have similar slopes from CO(6-5) to CO(2-1) transitions.

APM0879+5255 and Cloverleaf are the only objects for which the CO(1-0) transition is detected and the ratio between the transition CO(2-1) and (1-0) is consistent between the two sources. The upper-limit on the CO(1-0) of J1148+5251 also points towards a similar CO(2-1)-to-CO(1-0) ratio. Therefore, in order to estimate the molecular gas mass for J1007+2115, J1319+0950, J2054-0005 and J0129-0035 from CO(6-5), we assume r_{65} =CO(6-5)/CO(1-0)=1.23 ± 0.66, considering the average between $r_{65} = 1.35 \pm 0.54$ of APM0879+5255 and $r_{65} = 0.75 \pm 0.18$ of Cloverleaf. We then obtained $M_{\mathrm{H2}} = (1.3 \pm 0.2) \times 10^{10}$ $\mathrm{M_\odot}$ for J1007+2115, $M_{\mathrm{H2}} = (1.5 \pm 0.2) \times 10^{10}$ for J1319+0950, $M_{\mathrm{H2}} = (6.4 \pm 1.0) \times 10^{9}$ $\mathrm{M_\odot}$ for J2054-0005, and $M_{\mathrm{H2}} = (3.7 \pm 0.6) \times 10^{9}$ for J0129-0035. Regarding J0224-4711, we assume that CO(7-6)~CO(6-5), given the averaged CO SLED of high-z QSO (see Fig. 3.6), and $r_{76} = 0.76 \pm 0.41$, considering the average between APM0879+5255 and Cloverleaf. This gives $M_{\mathrm{H2}} = (1.0 \pm 0.1) \times 10^{10}$ $\mathrm{M_\odot}$ for J0224-4711.

For the purposes of this Thesis, we also investigated the properties of QSO J036+03, and thus we computed its molecular gas mass from CO(6-5) consistently to the rest of the sample. Decarli et al. (2023) reported the detection of the CO(6-5) emission line of J036+03, finding $L'_{\mathrm{CO(6-5)}} = (1.27 \pm 0.11) \times 10^{10}$ $\mathrm{K\,km\,s^{-1}\,pc^2}$. This yield $M_{\mathrm{H2}} = (7.5 \pm 0.64) \times 10^{9}$ $\mathrm{M_\odot}$ following our assumptions.

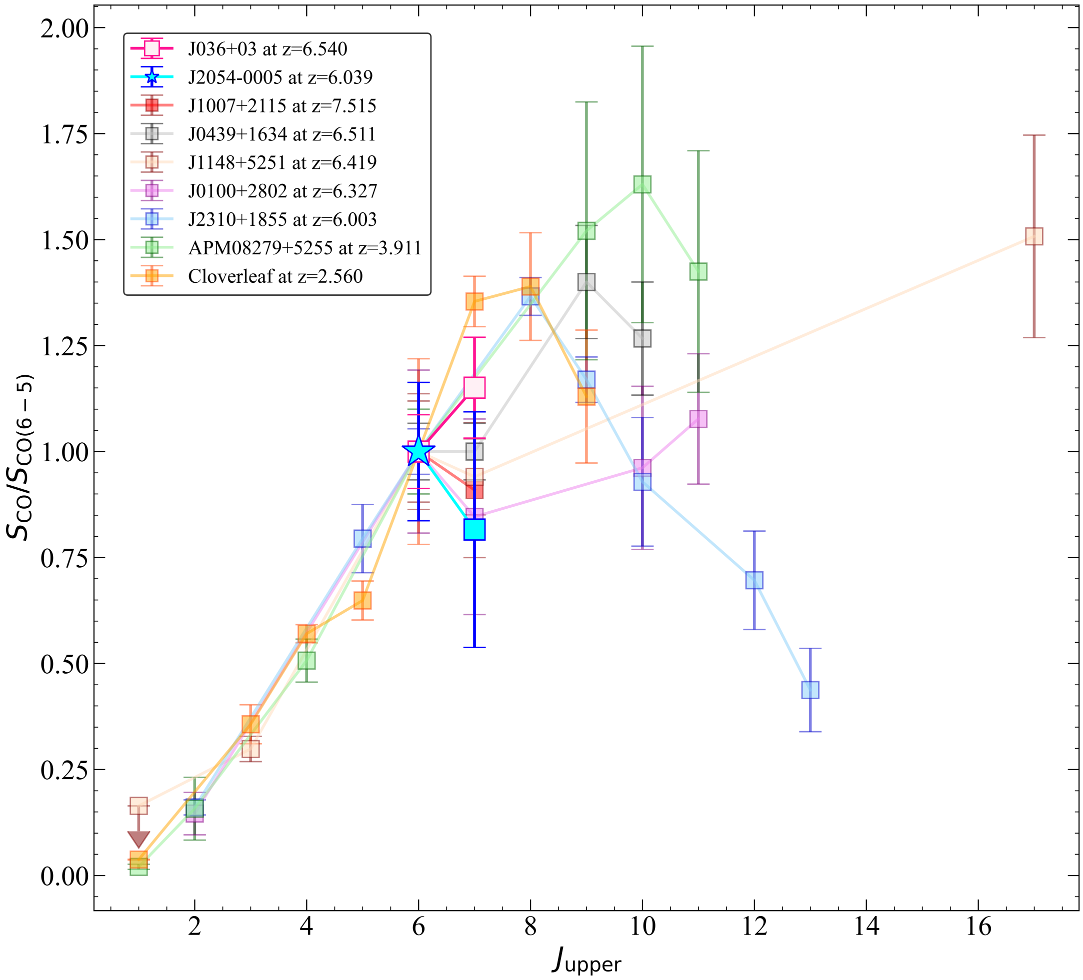

Figure 3.6: *CO SLED of J036+03 and J2054-0005 compared with those of other QSOs at $z > 6$ and at lower redshift. The CO SLEDs for J036+03 and J2054-0005 are shown as pink squares and cyan markers, respectively. For J2054-0005 the star refers to the CO(6-5) line studied in this work, while the square to the CO(7-6) in Decarli et al. (2022). Results of J036+03 are taken from Decarli et al. (2022). All other sources are displayed as shadowed squares: J1007+2115 at z=7.5419 in red (Feruglio et al., 2023); J0439+1634 at $z = 6.511$ in grey (J. Yang et al., 2019); J1148+5251 at $z = 6.419$ in brown (Riechers et al., 2009; S. Gallerani et al., 2014); J0100+2802 at $z = 6.327$ in purple (F. Wang et al., 2019); J2310+1855 at $z = 6.003$ in blue (Li et al., 2020); APM08279+5255 at $z = 3.911$ in green (P. Papadopoulos et al., 2001; Weiß et al., 2007); Cloverleaf at $z = 2.560$ in orange (Bradford et al., 2009; Uzgil et al., 2016).*

Our analysis revealed that gas masses in our sample of QSOs, estimated with the smallest statistical uncertainties, are on average $\sim 10^{10}$ M$_\odot$. However, it is worth noticing that our assumptions on the CO(6-5)-CO(1-0) (or CO(7-6)-CO(1-0)) line ratios introduce significant systematic uncertainties to our estimates, of the order of $\gtrsim 50\%$. Our results are -on average- in good agreement with the gas masses found in Neeleman et al. (2021) derived from converting the [CII] underlying continuum flux into a dust mass and then assuming a constant GDR. On the contrary, the gas mass estimated from converting the [CII] luminosity directly into a molecular mass using the conversion of Zanella et al. (2018) are mostly one order of magnitude larger than ours. Specifically, molecular gas masses for QSOs J1319+0950, J2054-

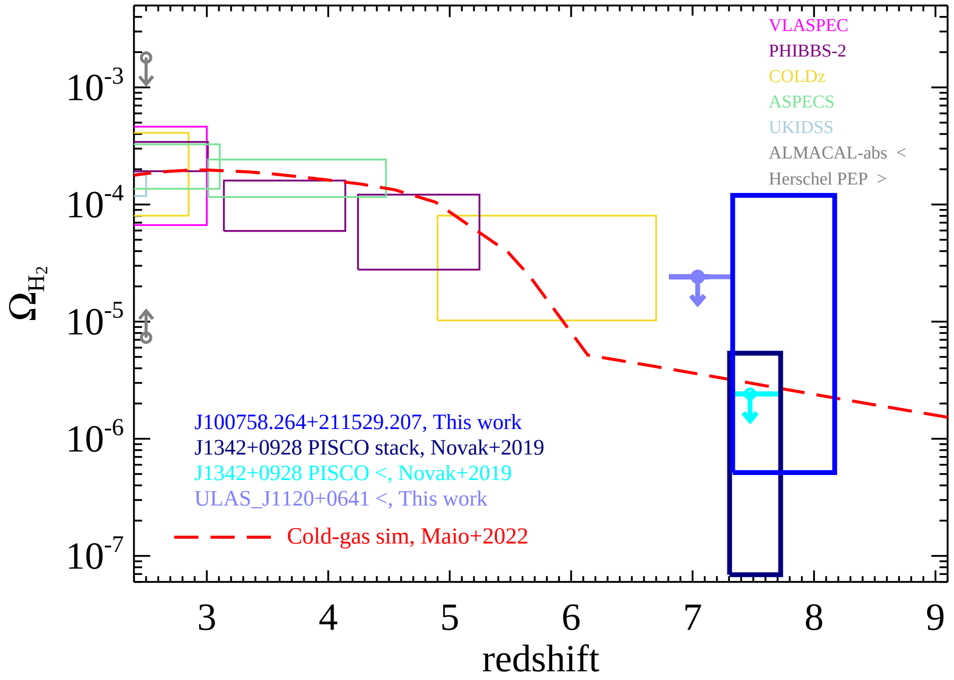

Figure 3.7: *Comoving cosmic mass density of cold molecular gas as a function of redshift. Vertical sizes indicate the uncertainties in each bin. Data are from Riechers et al. (2020b); Riechers et al. (2020a) (VLASPEC, COLDz), Decarli et al. (2020) (ASPECS), Lenkić et al. (2020) (PHIBSS-2), Garratt et al. (2021) (UKIDSS-UDS), and Hamanowicz et al. (2023) (ALMACAL-CO), and upper/lower limits from ALMACAL-abs (Klitsch et al., 2019) and Herschel PEP (Berta et al., 2013). Theoretical expectation from cold-gas simulations (dashed line) are by Maio, Péroux, and Ciardi (2022). As a work of caution, we recall that our determination of* Ω_{H_2} *may suffer of high uncertainties, as it is derived from an individual field around a QSO, i.e., a small and highly biased region in the sky.*

0005 and J0129-0035 were derived in Neeleman et al. (2021) finding larger values than ours using both the GDR and the Zanella's conversion factor. In the former case, the GDR assumed in Neeleman et al. (2021) (GDR=100) may not be valid for every QSO (see the results and discussion on GDR in our sample in Sect. 4.4). In the latter, the Zanella's conversion factor, which is calibrated for $z \sim 2$ main-sequence galaxies, may not be applicable for high-z QSO's hosts. This was also reported in Tripodi et al. (2022) for the case of QSO J2310+1855 at $z \sim 6$.

Molecular gas masses and line properties are summarized in Tab. 3.1. The uncertainties reported on the gas mass are statistical only. Systematics uncertainties are induced by the choice of α_{CO} (factor of 0.2-0.3 dex) and by the scaling from high-J CO transition to J=1 using the CO excitation ladder (factor of 20-30%).

Finally, we derive an estimate of the cosmic mass density of molecular mass, Ω_{H_2}, for J1007+2115 at z~ 7.5. Thanks to the wide band covered by our observation, we probe the redshift range between 7.33 and 8.17, or the range 600-700 Myr of cosmic time, the field of view is taken as the primary beam of the observation, about 50 arcsec. We use the

M(H_2) estimated in Feruglio et al. (2023) (i.e. $M(\mathrm{H_2}) = (2.2 \pm 0.2) \times 10^{10}\ \mathrm{M_\odot}$, considering $r_{61} = 0.75$) in the corresponding cosmic volume, V, to derive the H_2 mass density parameter $\Omega_{\mathrm{H_2}} = \mathrm{M(H_2)/V}/\rho_{\mathrm{crit,0}}$, where $\rho_{\mathrm{crit,0}} \simeq 277.4\,h^2\,\mathrm{M_\odot/kpc^3}$ is the present-day cosmological critical density and $h = H_0/(100\ \mathrm{km\ s^{-1}Mpc^{-1}})$.

Fig. 3.7 shows the $\Omega_{\mathrm{H_2}}$ redshift evolution derived from this observation and those of two other quasars at $z > 7$ for which CO upper limits are measured, i.e. J1342+0928 for which we also report the tentative stack detection by Novak et al., 2019, and ULAS J1120+0641 (ALMA archive). Literature values at lower z are from VLASPEC, COLDz (Riechers et al., 2020b; Riechers et al., 2020a), ASPECS (Decarli et al., 2020), PHIBSS-2 (Lenkić et al., 2020), UKIDSS-UDS (Garratt et al., 2021), and ALMACAL-CO (Hamanowicz et al., 2023) , and upper (lower) limits from ALMACAL-abs (Klitsch et al., 2019) and Herschel PEP (Berta et al., 2013). The value inferred by our analysis of J1007+2115 is $\Omega_{\mathrm{H_2}} \simeq 1.31 \times 10^{-5}$.

Upper and lower limits are evaluated by considering a statistical error on H_2 mass determination of $0.16 \times 10^{10}\ \mathrm{M_\odot}$, a systematic calibration error of 10%, and CO SLED lower and upper errors of 0.65 and $5.94{\times}10^{10}\ \mathrm{M_\odot}$. For J1342+0928 (Novak et al., 2019) the resulting upper limit between $z \simeq 7.30$ and 7.72 suggests $\Omega_{\mathrm{H_2}} < 2.42 \times 10^{-6}$, while the stacking analysis gives $\Omega_{\mathrm{H_2}} \simeq 1.13 \times 10^{-6}$. In this latter case, a statistical error on H_2 mass of $2.2 \times 10^8\ \mathrm{M_\odot}$ and an upper limit of a factor of 2 for the stacking error have been considered. The ALMA archival observation of ULAS J1120+0641 allows us to estimate an $\Omega_{\mathrm{H_2}}$ upper limit of 2.42×10^{-5} at $z \simeq 6.80 - 7.13$.

As a comparison, we also show the trend expected by the latest, accurate, non-equilibrium molecular-chemistry cosmological simulations of cold gas at early times by Maio, Péroux, and Ciardi (2022). The predicted $\Omega_{\mathrm{H_2}}$ behaviour at $z > 6$ is mainly driven by H_2 formation via the H^- channel, since in the simulation the dust growth is inefficient at such primordial epochs. At later times the effects of UV radiation (that enhances production of free charges at temperatures around or below 10^4 K) and dust grain catalysis in progressively enriched media boost $\Omega_{\mathrm{H_2}}$ expectations. Overall, the values we find are in line with the general trend suggested by literature estimates at $z < 7$ and agree fairly well with the latest theoretical expectations.

Although $\Omega_{\mathrm{H_2}}$ determinations by quasar data might be highly biased, as individual objects do not necessarily represent a fair sample of the Universe, our results suggest that it is possible to leverage on this by combining different objects at similar cosmological epochs. We note that this work represents the first attempt to set constraints on H_2 abundances by combining state-of-the-art interferometric observations of the cold dense molecular gas in the first 700 Myr with state-of-the art cold-gas modelling.

Previous works (e.g., Abel et al., 1997; Maio et al., 2007) have indeed either neglected a fully complete modeling of primordial molecules or could not rely on constraints from observational data for early regimes probed here.

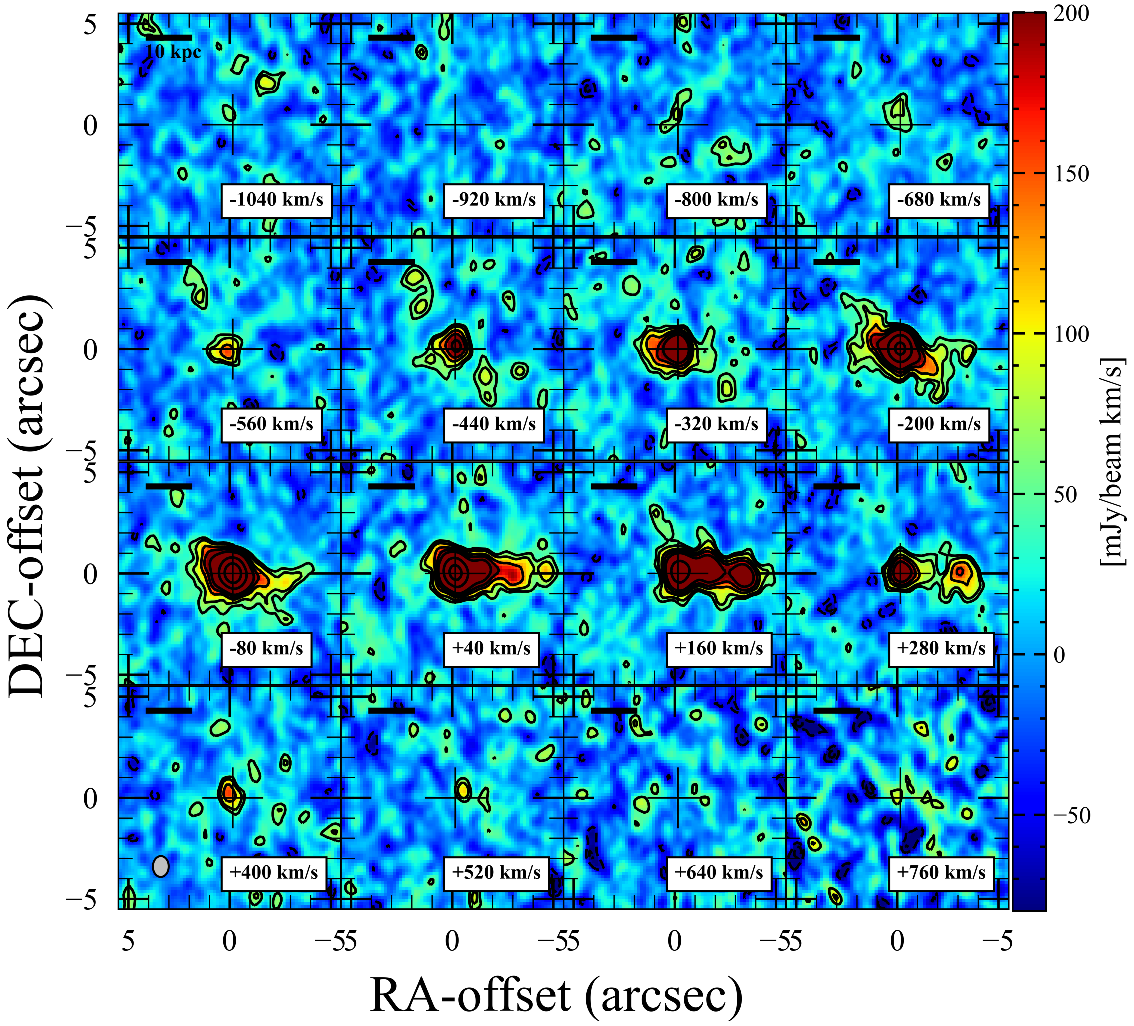

Figure 3.8: *Channel maps of the [CII] emission line for J0100+2802. The cross indicates the peak position of the continuum and velocities are relative to the redshift of the [CII] as determined in F. Wang et al. (2019). Contours are at* $-3, -2, 2, 3, 5, 7, 10, 25$ *and* 50σ. *The clean beam is shown in the inset in the lower left corner.*

3.3 Less dense and more extended cold gas: [CII]

In this section, I present the results of the analysis of the [CII] emission in QSOs J0100+2802 and J2310+1855. Even though this part is mainly focused on investigating the properties of the [CII] emission, it is sometimes useful to show and discuss some results on the continuum emission of these QSOs. Indeed this enriches the picture of the host-galaxy properties, especially for the case of J0100+2802.

3.3.1 [CII] distribution and kinematics

J0100+2802

We used the continuum-subtracted data cube to study the [CII] line emission of J0100+2802 with natural weighting. Details of the complex kinematics of this system can be seen in the channel maps of Fig. 3.8, obtained collapsing bins of 120 km s^{-1} from the continuum-subtracted cube. A prominent, elongated feature is clearly seen at velocities between +40 and +280 km s^{-1}. Although it could be interpreted as a jet or an outflow, the fact that it is also detected in continuum, as discussed further below, indicates that it is likely tracing a star forming companion, extending on scales of ~4 arcsec, i.e. ~20 kpc, that is interacting with the QSO's host-galaxy. As inferred by the channel maps, the companion is highly structured, with clumps at different velocities. There is also a nearly symmetric and smaller extension on the opposite side and negative velocities (-320 km s^{-1}), which is likely tracing a tidal tail of the same interacting system.

The top left panel of Fig. 3.9 shows the [CII] map, imaged with MFS mode in the velocity range from ~ -1000 to $+600$ km s^{-1}, that presents the elongated and complex structure already seen in the channel maps, tracing the interacting companion. Performing a 2D Gaussian fit in a region enclosing the QSO's host emission (S/N> 3, RA:[-2,1.5] arcsec, DEC:[-1.3, 1.5] arcsec), we found a peak flux of 1.52 ± 0.06 mJy/beam and a flux density of 2.78 ± 0.17 mJy. Even though the fully resolved, and tidally stretched structure of the companion is clearly revealed in the channel maps, especially at $v = +40$ km s^{-1} and $v = +280$ km s^{-1}, in the [CII] flux map and in the PV diagram, we performed a PSF subtraction to better quantitatively assess the flux of the companion, especially for the continuum emission. We first computed the flux density from the [CII] map within a region with S/N> 2 (see 2σ contours in Fig. 3.9), obtaining 3.8 ± 0.05 mJy. Then, we subtracted from the [CII] map the PSF normalized to the QSO's host peak flux. The flux density of the companion is computed from the PSF-subtracted [CII] map (top right panel of Fig. 3.9) in a region with S/N> 2 and RA-offset< -1.3 arcsec, to exclude the ring-like feature in the center that can be still associated with the QSO's host, and it is 1.00 ± 0.04 mJy. Considering this averaged flux within the [CII] line width, we derive $L_{\text{[CII],comp}} = (1.68 \pm 0.06) \times 10^9\ L_\odot$ (using Eq. 1 in Solomon and Vanden Bout 2005). Consequently, the estimated flux density associated to the QSO emission is 2.8 ± 0.07 mJy, that is consistent with the flux estimated from the 2D fit and corresponds to a luminosity of $L_{\text{[CII],host}} = (4.70 \pm 0.12) \times 10^9\ L_\odot$[3]. This is ~ 1.25 times higher than the luminosity derived in B. P. Venemans et al. (2020), and this discrepancy is likely due to the higher sensitivity and lower resolution of our observation that enabled us to observe the more diffuse and fainter [CII] emission, and the high-velocity emission. The [CII] emission of the QSO is not resolved, while if considering the whole system, the FWHM size is $(0.89 \pm 0.09) \times (0.70 \pm 0.12)$ arcsec^2, corresponding to $\sim (5.03 \times 3.96)$ kpc^2 at the rest frame. The PSF-subtracted [CII] map presents multiple peaks towards the West and they arise from the clumps at different velocities that are clearly seen in the channel maps. We may interpret these as the complex morphology of tidally stretched galaxy in the merging process. This makes the position of the companion difficult to determine precisely and, in principle, these features can also arise from the presence of multiple companions or gas clumps. However, the resolution of our observation prevents us to

---

[3] $L_{\text{[CII],comp}}$ and $L_{\text{[CII],host}}$ are computed considering that the [CII] line width is ~1600 km s^{-1}.

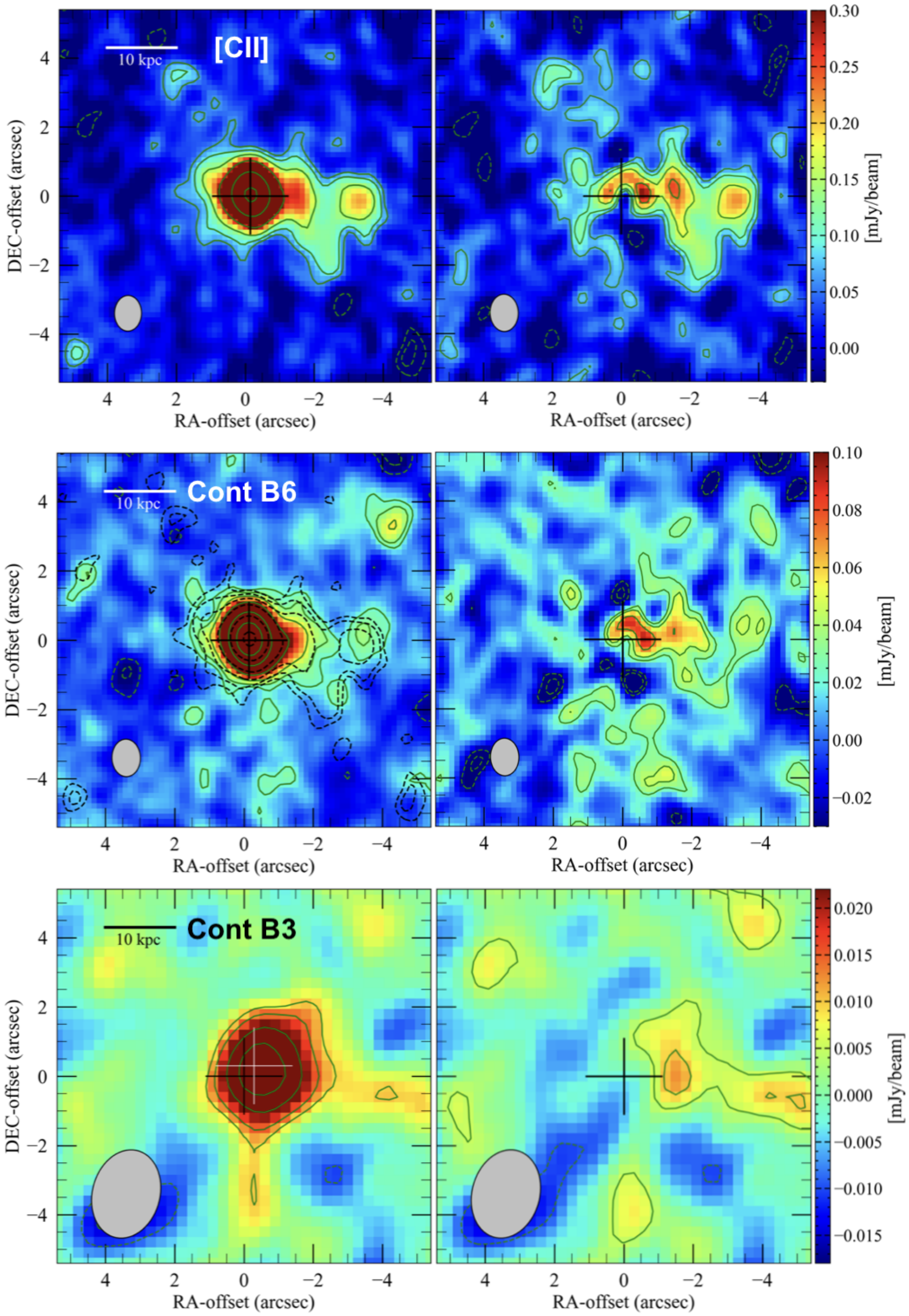

Figure 3.9: *[CII] and continuum maps of J0100+2802. In each panel, the clean beam is plotted in the lower left corner and the cross indicates the peak position of the QSO continuum in B6. Top panels: [CII] map with green contours at* $-3, -2, 2, 3, 5, 10, 25$ and 50σ*, with* $\sigma = 0.03$ *mJy/beam (left). Psf-subtracted [CII] map with green contours at* $-3, -2, 2, 3, 5\sigma$*, with* $\sigma = 0.03$ *mJy/beam (right). Central panels: continuum map in B6 with green contours at* $-3, -2, 2, 3, 5, 10, 25$ and 50σ*, with* $\sigma = 0.01$ *mJy/beam (left). [CII] contours are overplotted as black dashed line at* $-3, -2, 2, 3, 5, 10, 25$ and 50σ*, with* $\sigma = 0.03$ *mJy/beam. Psf-subtracted continuum map with green contours at* $-3, -2, 2, 3, 5\sigma$*, with* $\sigma = 0.01$ *mJy/beam (right). Bottom panels: continuum map in B3 map with green contours at* $-3, -2, 2, 3, 5,$ and 7σ*, with* $\sigma = 0.005$ *mJy/beam (left). Psf-subtracted continuum map with green contours at* $-3, -2, 2, 3\sigma$*, with* $\sigma = 0.005$ *mJy/beam (right). The white cross marks the peak of the continuum in B3.*

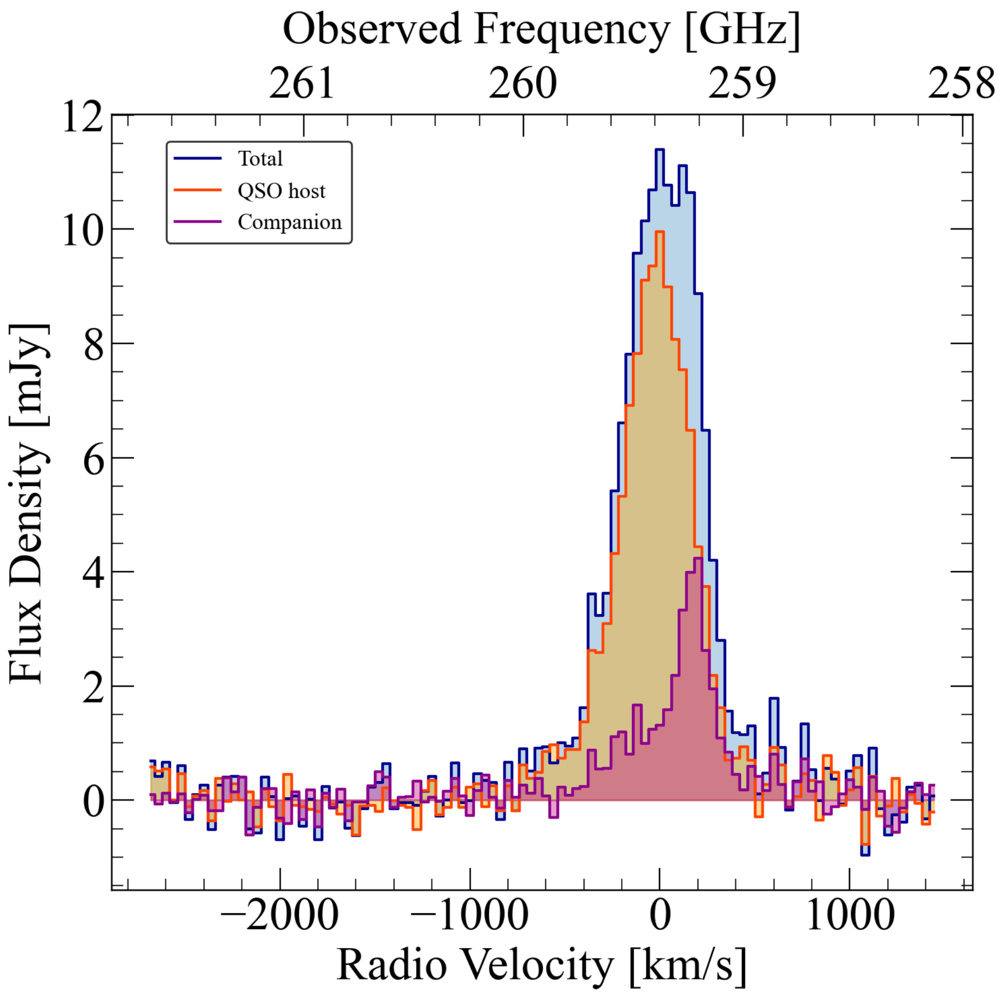

Figure 3.10: *Spectra extracted from three different spatial regions: from a region with a S/N> 2 in blue; from a region with a S/N> 2 and RA-offset< −1.3 arcsec in purple; from a region with a S/N> 2 and RA-offset> −1.3 arcsec in orange. We set the 0-velocity reference of the spectrum as done for the spectrum in Fig. 3.20.*

distinguish between these different scenarios. To be conservative we associate all the elongated feature at S/N> 2 to a single interactive companion. Spectra extracted from three different spatial regions are presented in Fig. 3.10: the spectrum in blue is extracted from a region with S/N> 2 including both the QSO and companion contribution; the one in purple is extracted from a region with S/N> 2 and RA-offset< −1.3 arcsec to better isolate the contribution of the companion to the [CII] emission; the one in orange is extracted from a region with S/N> 2 and RA-offset> −1.3 arcsec that mostly encloses the QSO's host contribution. The [CII] emission arising from the companion peaks at 259.220 GHz (i.e., corresponding to $z = 6.3317$), slightly redshifted with respect to the QSO's host emission that peaks at 259.378 GHz.

The top panels of Fig. 3.11 show the moment-0, -1, and -2 maps of the [CII] emission obtained applying a 3σ threshold to the continuum-subtracted cube. The moment-1 map shows a gradient towards the direction of the companion. The moment-2 map shows a range of the velocity dispersion between 10 and 180 km s^{-1}, where the maximum value towards the

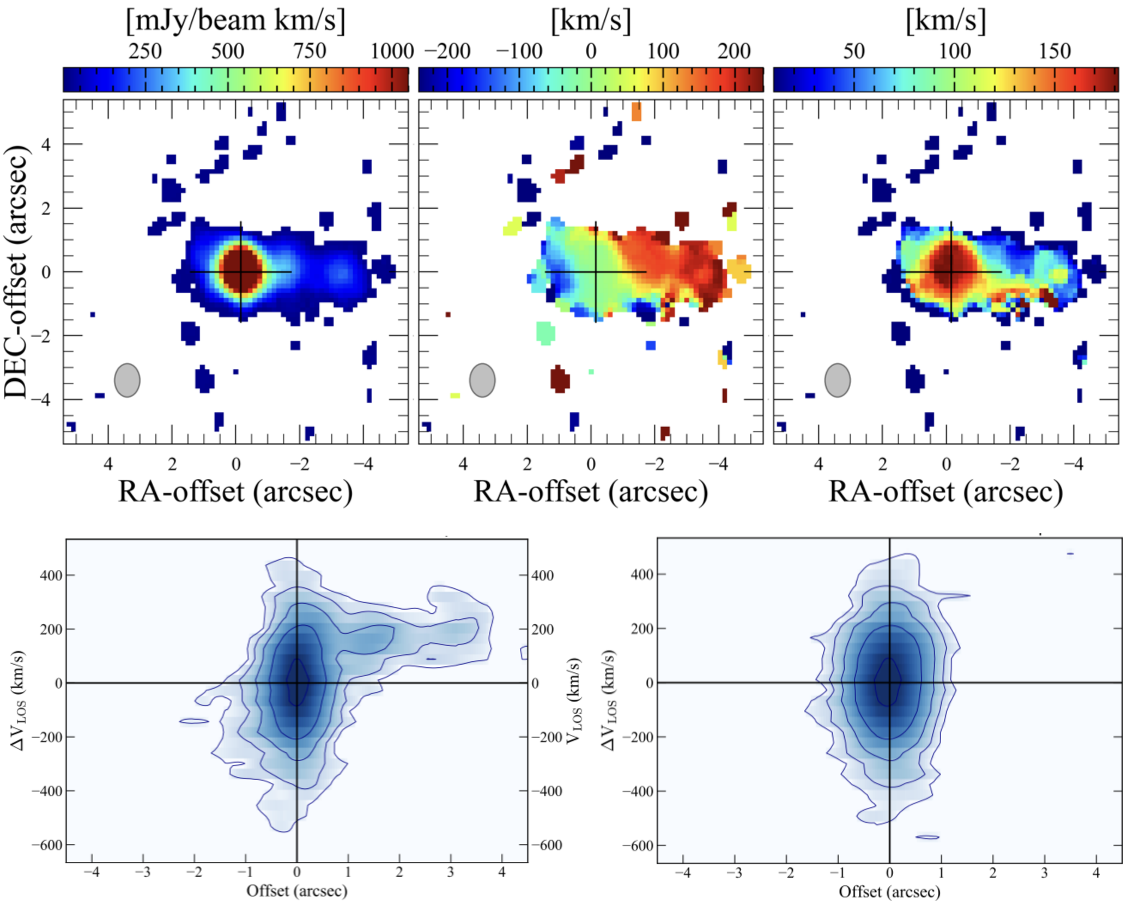

Figure 3.11: *Moment maps and PV diagram of the [CII] emission line. Top panel: integrated flux, mean velocity map, velocity dispersion map, and continuum-subtracted spectrum of [CII]. The clean beam is plotted in the lower left corner of the moment maps. The cross indicates the peak position of the integrated flux. Bottom panel: PV diagrams of the [CII] emission line along the line of nodes (PA=275°) and orthogonal to it (PA=185°).*

nucleus is affected by beam smearing (R. Davies et al., 2011). Left and right bottom panels of Fig. 3.11 present the position-velocity (PV) diagrams of the disk along the major and minor kinematic axes, respectively. The position angle, PA, of the major axis is 275°. The PV diagram shows an asymmetric structure that partially mimic the S-shape commonly seen in rotating disks. The structure seen both in the PV diagram and in the momenta suggests two possible interpretations: (1) the arm at positive velocities in the PV may arise from the gas that is moving from the companion to the QSO's host galaxy (called 'merging bridge'); (2) we might be witnessing the initial phases of the settling of a rotating gas structure during the merging process between the two sources.

Indeed similar kinematics has been found in a simulated merging system, called Adenia, in Rizzo et al. (2022). It is formed by two merging galaxies and presents a similar structure in the [CII] flux distribution, in the velocity map and in the dispersion map (see Fig. 4 of Rizzo et al. 2022). However, the PV diagram of the Adenia galaxy is much more disturbed than the PV of J0100+2802. This may suggest the presence of some rotation entangled with the merging process, supporting a scenario in which we are witnessing the first phases of the settling of a rotating disk. However, the resolution of our observation did not allow us to distinguish between merging and rotation processes. Neeleman et al. (2021) analysed a higher resolution ($\sim$ 0.2 arcsec) and lower sensitivity observation of the [CII] of J0100+2802 and they did not find any sign of merger or any velocity gradient in the velocity map which, on the contrary, seemed quite disturbed. This, once again, highlights the role of sensitivity in allowing a detailed analysis of the characteristics of the host galaxies.

The central left panel of Fig. 3.9 shows the 253 GHz dust continuum map obtained through natural weighting. The continuum shows an elongated structure westwards, coincident with the [CII] elongation (black contours). Analogously to the [CII] analysis we performed a 2D Gaussian fit in the region enclosing the QSO emission, and we derived a peak flux of 0.81 ± 0.02 mJy/beam and a flux density of 1.16 ± 0.05 mJy, that is consistent with the flux 1.26 ± 0.08 mJy found by F. Wang et al. (2019). We computed the flux density in a region $> 2\sigma$ from the map, obtaining 1.44 ± 0.05 mJy, and we subtracted from the continuum map the PSF normalized to the QSO peak flux. The emission in the PSF-subtracted continuum extends for $\sim$4 arcsec from the centre westwards (see central right panel of Fig. 3.9), i.e. similar extension and clumpiness as the [CII] emission. This supports the scenario in which the extended [CII] emission is associated with an interacting system and not an outflowing/jetted component. The flux density obtained in the PSF-subtracted continuum map inside a region with S/N> 2 and RA-offset< -1.3 arcsec is 0.25 ± 0.01 mJy. Therefore, the QSO continuum emission is 1.19 ± 0.06 mJy, that is consistent with the one computed from the 2D fit. The QSO emission is unresolved in the present data at our resolution, and considering the whole interacting system, the FWHM size of $(0.68 \pm 0.09) \times (0.54 \pm 0.12)$ arcsec^2, corresponding to $\sim (3.84 \times 3.05)$ kpc^2 at the rest frame.

We performed a similar analysis for the continuum emission at 99.5 GHz (bottom left panel of Fig. 3.9), in order to determine whether the companion emission was detected. By doing a 2D Gaussian fit, the source has a peak flux 0.04 ± 0.004 mJy/beam and a flux density of 0.05 ± 0.007 mJy. The morphology of the emission is asymmetric and slightly elongated westwards, and coincident with the interacting companion. The elongated feature is less evident than in the B6 continuum, since the resolution in B3 is $\sim$ 2 times lower. We subtracted the PSF normalized to the QSO peak flux, and indeed we found emission at 3σ in the same region of the companion emission in B6. In this case, the emission seems to extend up to -5 arcsec RA-offset from the center, however this can be an artefact caused by the low resolution. Therefore, we conservatively extracted the continuum flux for the companion from the 2σ contours enclosed in the region with RA-offset> -4 arcsec, obtaining 0.011 ± 0.003 mJy.

The presence of a companion is consistent with the picture of QSOs living in overdense environments. In particular, a suite of simulations by F. Di Mascia et al. (2021) showed that bright QSOs are part of complex, dust-rich merging systems, containing multiple sources (accreting black holes and/or star-forming galaxies). Costa, Rosdahl, and Kimm (2019) also found a large number of satellite galaxies that will eventually fall on the central QSO-host at

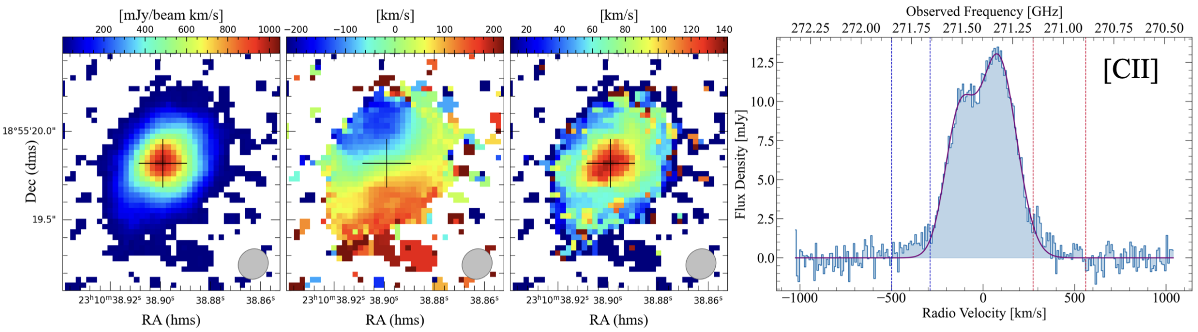

Figure 3.12: *Moment maps and line profile of the [CII] emission line. From left to right: integrated flux, mean velocity map, and velocity dispersion map, continuum-subtracted spectrum of [CII]. The clean beam is plotted in the lower right or left corner of the moment maps. The cross indicates the peak position of the integrated flux for each line. The spectrum has been extracted from the region included within* $\geq 2\sigma$ *in the velocity integrated map. The vertical blue and red lines highlight the spectral regions in which the flux is higher than in the Gaussian fit (solid purple line).*

high-z in cosmological, radiation-hydrodynamic simulations. J0100+2802 is indeed found to have a exceptionally small proximity zone, given its extreme brightness, (Eilers et al., 2017; F. B. Davies et al., 2020) and no detected Lyα nebula (Farina et al., 2019). These are consistent with a scenario of a young black hole accretion episode and a recent merger, and also with the presence of a weak outflow, since the majority of the outflow emission would be intercepted by an over-abundance of neutral/dusty gas in the host galaxy (Costa et al., 2022). Moreover, J0100+2802 is found to reside in a strong overdensity composed of 24 galaxies (Kashino et al., 2022), detected in JWST-NIRCam slitless spectroscopy. However, thanks to the powerful capabilities of ALMA we were able to reveal this nearest interacting companion, which was undetected even by JWST-NIRCam imaging (Eilers et al., 2022), probably because of both the overwhelming light from the QSO at optical/UV wavelengths and heavy dust obscuration, also supported by the substantial mass of dust detected at the position of the companion ($M_{\rm dust} \sim (0.3-2.6)\times10^7$ M$_{\rm dust}$).

J2310+1855

In order to study the [CII] distribution and kinematics of QSOs J2310+1855, we adopted the Briggs cleaned data cube that enhances the angular resolution.

Fig. 3.12 shows the moment-0, -1, and -2 maps of the [CII] emission and the spectrum of J2310+1855, obtained by applying a 3σ threshold to the Briggs clean cube. The [CII] distribution is spatially resolved with a size of $(0.449\times0.325)\pm(0.028\times0.021)$ arcsec^2 estimated from a 2D Gaussian fit on the velocity-integrated map (see Table 3.2), and it shows a velocity gradient oriented north-east to south-west with Δv = 400 km s^{-1}. The moment-2 map shows a range of the velocity dispersion between 20 and 140 km s^{-1}, where the maximum value towards the nucleus is affected by beam smearing (R. Davies et al., 2011).

Fig. 3.12 also shows the continuum-subtracted [CII] line profile, which peaks at a fre-

Table 3.2: [CII] emission line properties of J2310+1855

		J2310+1855
F_{obs}	[GHz]	271.382
$z_{[CII]}$		6.0031 ± 0.0001
FWHM	[km s^{-1}]	422 ± 15
$S\,dv$	[Jy km s^{-1}]	5.2 ± 0.01
$L_{[CII]}$	[$10^9\ L_\odot$]	5.1 ± 0.1
size	[arcsec^2]	0.449 × 0.325
size	[kpc^2]	2.6 × 1.9

Notes. Line fluxes are derived by integrating over the line profiles extracted from the region included within $> 2\sigma$ in the velocity integrated map. Sizes are estimated with a 2D Gaussian fit in CASA.

quency of 271.382 GHz, corresponding to $z = 6.0031 \pm 0.0001$, consistent with previous determinations (e.g. R. Wang et al. 2013; Shao et al. 2019, see Table 3.2). The FWHM of the line is 422 ± 15 km s^{-1}, derived from the fit with a single Gaussian. Because the [CII] line shows two peaks, the value of the integrated flux would be ~ 10% overestimated using a single Gaussian. Therefore, we fitted the line profile with two Gaussian functions and derived an integrated flux of [5.2 ± 0.01] Jy km s^{-1}. This is 40% lower than the flux reported by Feruglio et al. (2018), obtained using a dataset with a clean beam of about 0.9 arcsec. This suggests that these higher-resolution observations filter out part of the flux. The [CII] profile shows excess emission with respect to the best fit at the red and blue sides of the line, which would require additional Gaussian components.

We measured a total line luminosity of $L_{[CII]} = 5.1 \pm 0.1 \times 10^9$ L$_\odot$ and derived an $L_{[CII]}/L_{TIR} = 8 \times 10^{-5}$ (for the computation of L_{TIR} see Sect. 4.3.1). This value is at the lower end of the distribution found for QSOs at this redshift (Walter et al., 2022; Decarli et al., 2018; Shao et al., 2019). This [CII] deficit is also predicted for high-z galaxies by semi-analytical models of galaxy evolution (e.g. Lagache, Cousin, and Chatzikos 2018), where the [CII] deficit arises from the high intensity of the interstellar radiation field. Our estimate of $L_{[CII]}/L_{TIR}$ agrees well with their results at $z \sim 6$ when we extrapolate their predictions at higher L_{TIR}. Carniani et al. (2018) studied the $L_{[CII]}$ − SFR relation for high-z galaxies and reported that the local relation for star-forming galaxies (see De Looze et al. 2014) is still valid at high z, but with a twice higher dispersion than observed locally. Our results agree very well ($< 1\sigma$) with the correlation of Carniani et al. (2018), with the relation for local star-forming galaxy of Herrera-Camus et al. (2018), and with the results for high-z galaxies of Lagache, Cousin, and Chatzikos (2018).

The neutral gas mass in the disk, based on [CII] emission, can be derived with the relation from Hailey-Dunsheath et al. (2010) (see also Bischetti et al. 2019a),

$$\frac{M_{HI}}{M_\odot} = 0.77\left(\frac{0.7L_{[CII]}}{L_\odot}\right)\left(\frac{1.4\times10^{-4}}{X_{C^+}}\right)\times\frac{1+2e^{-91\mathrm{K}/T}+n_{crit}/n}{2e^{-91\mathrm{K}/T}}, \tag{3.2}$$

where X_{C^+} is the [CII] fraction per hydrogen atom, T is the gas temperature, n is the gas

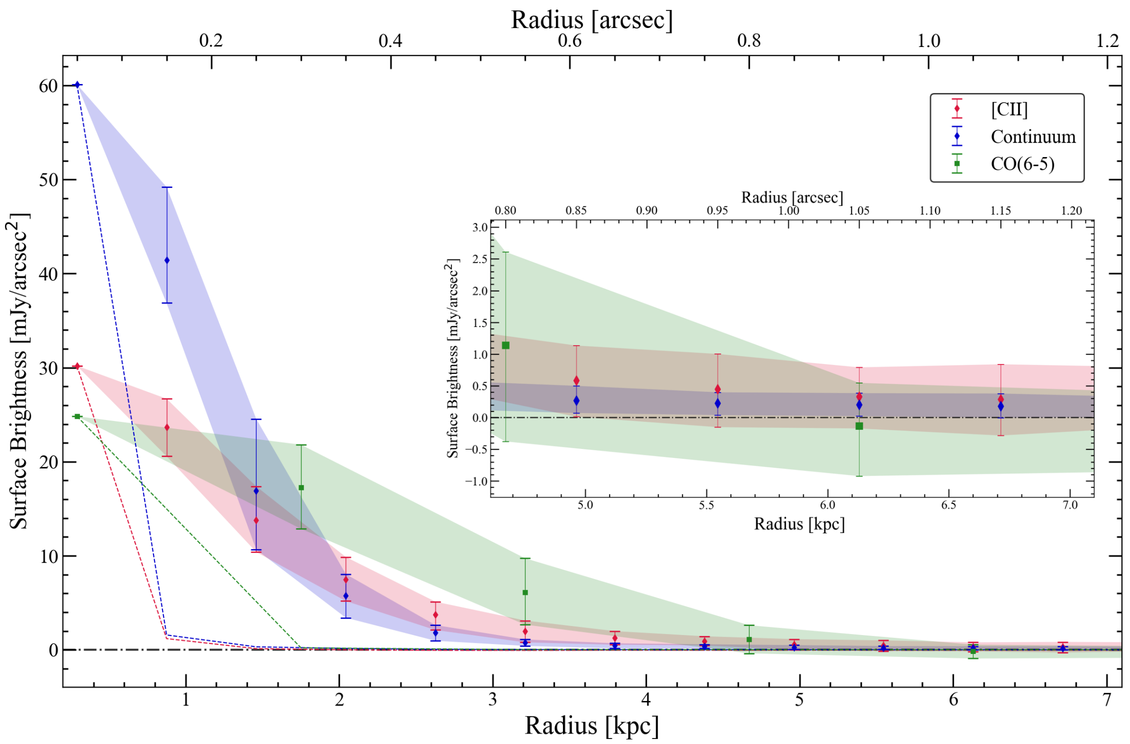

Figure 3.13: *Natural weighting surface brightness for [CII] (red), CO(6-5) (green), and continuum (blue) of J2310+1855, normalised to the respective r.m.s. level, as a function of the radius from the peak position of the source. The lower and upper error bars are the 16th and 84th percentiles, respectively. The shadowed regions connect the uncertainties given by the percentiles. The coloured dashed lines show the synthetic beams for each observation. The dashed black lines mark the 0 level of surface brightness. The inset shows a zoomed view at large radii. The CO(6-5) data are taken from Feruglio et al. (2018) and have a clean beam of* 0.6×0.4 *arcsec*^{2}.

density, and $n_{\rm crit} \sim 3 \times 10^3$ cm^{-3} is the [CII]$\lambda158\mu$m critical density for collisions with neutral hydrogen that frequently occur in PDRs (M. G. Wolfire, Livia Vallini, and Chevance, 2022; D. J. Hollenbach and Tielens, 1999). We estimated the lower limit for the molecular mass in the regime $n \gg n_{\rm crit}$ (Maiolino et al., 2005; Aalto et al., 2012; Aalto et al., 2015), and we considered a $X_{C^+} \sim 10^{-4}$ and a gas temperature of 200 K, both typical of PDRs (Maiolino et al., 2005; Hailey-Dunsheath et al., 2010; Cicone et al., 2015; Bischetti et al., 2019b). We found $M_{\rm HI} = 6.6 \times 10^9$ M$_\odot$, significantly lower than the molecular mass obtained through molecular tracers (Feruglio et al., 2018; Shao et al., 2019).

In Fig. 3.13, we show the observed surface brightness profiles of the [CII] compared with that of its underlying dust continuum emission, and of molecular gas traced by CO(6-5) (the latter taken from Feruglio et al. 2018). To compute the profiles, we used natural weighted maps and defined concentric annular regions centred at the QSO continuum position peak (RA, DEC = 23:10:38.90, 18:55:19.8). The first point for the surface brightness was taken at the peak pixel, and the next annuli are 0.1 arcsec thick for the [CII] and dust continuum, and 0.25 arcsec thick for the CO(6-5). To compute the surface brightness at each annulus, we averaged the flux within each annulus and divided it by the area of each annulus. The error bars associated with the surface brightness at each annulus (plotted in Fig. 3.13) mark the 16th and 84th percentiles inside each annulus, which corresponds to $\sim$ 68% of the surface brightness distribution centred on the mean value (i.e. $\pm 1\sigma$ for a Gaussian distribution). To determine the rms level, we associated a Poisson error with each region that we obtained as follows. We computed the rms per beam over a 10×20 arcsec^2 background, target-free area, and divided it by the square root of the number of beams in each annulus. To compare the [CII], CO, and continuum profiles, which have different rms levels, we subtracted the rms from each respective profile, so that the three distributions approached zero at high radii. All profiles are more extended than their respective synthetic beam, shown as dashed lines in Fig. 3.13. The [CII] and dust emission show consistent profiles for radii $r \gtrsim 1.5$ kpc. In the inner region of the source, we found that the continuum is more peaked at the centre than [CII] (and CO). The half-light radii are 1.3 kpc for the dust, 1.9 kpc for [CII], showing that the [CII] emission is more extended than the continuum emission (e.g. Li et al. 2022), and 2.2 kpc for the CO emission[4]. These results are also consistent with values that are commonly measured in QSOs at this redshift (Decarli et al., 2018; Carniani et al., 2019; B. P. Venemans et al., 2020). A similar behaviour of reduced [CII] emissivity close to the QSO was observed in the $z \sim 7$ QSO J2348-3054 (Walter et al., 2022) and in the $z = 6.6$ QSO J0305-3150 (Li et al., 2022). This is likely due to the contribution of the QSO to the dust heating, which reduces the $L_{[CII]}/L_{FIR}$ ratio in the nuclear region. We estimated the total gas surface density, including the contribution of HI from [CII] and H$_2$ from CO within the half-light radius $r_{[CII],HI} \sim 1.08$ kpc. We find $\Sigma_{gas(HI+H_2)} = 13809$ M$_\odot$ pc^{-2}. However, the gas traced by [CII] reaches a (azimuthally averaged) maximum size[5] of $r_{[CII]} \sim 5$ kpc, and the dust emission reaches an even larger radius of $r_{dust} = 6.7$ kpc, probably owing to the better sensitivity reached in the aggregated bandwidth. The molecular gas traced by CO(6-5) shows a smoother profile and reaches a size similar to the [CII], $r_{CO} \sim 4.7$ kpc. A similar behaviour with a steeper dust continuum distribution is seen in other high z QSOs (e.g., Walter et al., 2022) and has been attributed to the contribution of the QSO to the dust heating.

Although [CII] probes mildly ionised gas, it has recently been proposed as a possible molecular gas tracer. Zanella et al. (2018) derived a $L_{[CII]}$-to-H$_2$ conversion factor of $\alpha_{[CII]} \sim 22$ M$_\odot$/L$_\odot$ for star-forming galaxies at $z \sim 2$. Applying this conversion to J2310+1855 would imply a molecular mass of $M_{H_2} \sim 1.1 \times 10^{11}$ M$_\odot$. In addition to being a factor of 4 larger than the molecular mass derived from CO (Feruglio et al., 2018), this is also about three times higher than the dynamical mass derived from [CII]. This suggests that the empirical correlation between [CII] luminosity and molecular mass (e.g. Zanella et al. 2018) does not apply to high-z hyper-luminous QSOs. The total gas surface density $\Sigma_{(HI+H_2)}(= 13809$ M$_\odot$ pc^{-2}) within the [CII] half-light radius, together with the AGN-corrected SFR surface density $\Sigma_{SFR} =$

---

[4] The half-light radii reported here are different from those in Tripodi et al. (2022). In the published paper values are wrong due to an error in the transcription.

[5] The maximum size coincides with the radius at which the brightness profile reaches the zero level, within the error bars. It is shown more clearly in the zoomed panel of Fig. 3.13.

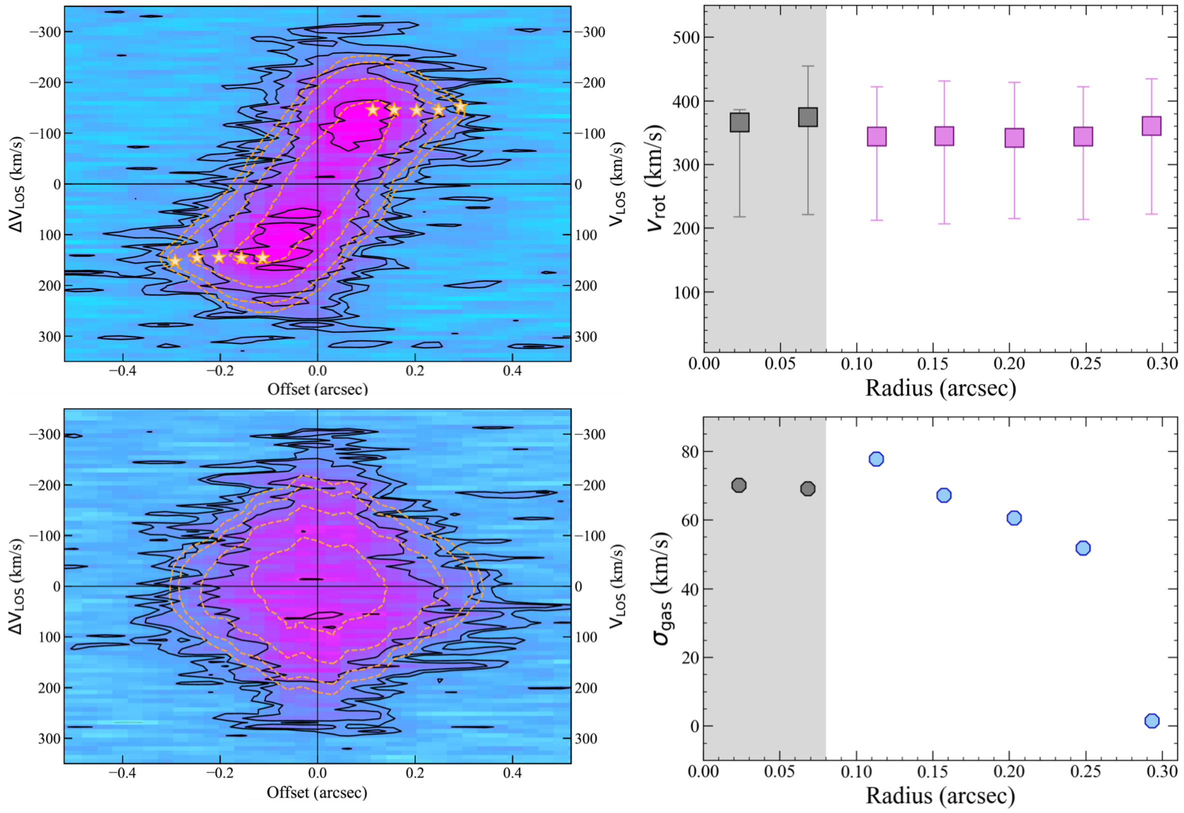

Figure 3.14: *Results of the* ^{3D}*Barolo dynamical modelling of the [CII] emission line. Top and bottom left: PV diagrams of the [CII] emission line along the line of nodes (PA=*200 *deg) and orthogonal to it (PA=*290 *deg), performed with* ^{3D}*Barolo. Contours are at* $2, 3, 6,$ *and* 12σ*, with* σ = 0.22 *mJy, for the data (solid black lines) and the best-fit model (dashed orange lines). Sampling is performed with five radii, spaced by* 0.045 *arcsec. Yellow stars show the disk model. Top and bottom right: Rotational velocity,* $v_{\rm rot}$*, and gas velocity dispersion,* $\sigma_{\rm gas}$*, as a function of radius for the best-fit disk model. To compute the top and bottom error bars for the rotational velocity, we performed the modelling by varying the disk inclination* i = 20 *and* 45 *deg, respectively. The grey shaded area marks the central beam (*$r_{\rm beam} \sim 0.08$ *arcsec), and grey points are those computed including the central beam.*

(521 M$_\odot$yr^{-1}kpc^{-2}, for SFR of J2310+1855 see Sect. 4.3.1), shows that the host galaxy lies above the region of the local Kennicutt-Schmidt (KS) relation that is usually occupied by starbursting galaxies (e.g. Bigiel et al. 2008). Recent zoom-in high-resolution simulations (Pallottini et al., 2022) and semi-analytical models (L. Vallini et al., 2021) found burstiness parameters, k_s, in the range $\sim 3 - 100$ for $z \gtrsim 6$ galaxies. For J2310+1855, we find $k_s \sim 5$, implying a starbursting host galaxy.

3.3.2 Dynamical modelling of the [CII] emission of J2310+1855

We modelled the [CII] line-of-sight (LOS) velocity distribution of J2310+1855 with an inclined-disk model, using the 3D-based analysis of rotating objects from line observations (^{3D}Barolo), a software package for the fitting of 3D tilted-ring models to emission line observations from high-resolution to very low resolution data cubes (Di Teodoro and Fraternali, 2015). ^{3D}Barolo builds a number of models in the form of artificial 3D observations and compares them with the input cube, finding the set of geometrical and kinematical parameters that better describes the data, correcting for beam-smearing effects. Fixed parameters of the fit are the centre of the disk, set to the continuum peak, and the position angle PA= 200 deg. The rotational velocity $v_{\rm rot}$ and velocity dispersion $\sigma_{\rm gas}$ are free parameters with initial-guess values of 50 km s^{-1} and 70 km s^{-1}, respectively. Since even in the case of high-resolution data the inclination, i, is the strongest source of uncertainty in determining the rotation curve and the dynamical mass, we performed a first run with i set as a free parameter, retrieving a value of $i \sim 25$ deg for the best-fitting disk model. In the second run, we fixed the inclination to $i = 25$ deg, with all the other parameters as before. The sampling was initially performed with seven radii, spaced by 0.045 arcsec, starting from a galactocentric radius of 0.023 arcsec. This produced a rotation curve with an average $v_{\rm rot} \simeq 354$ km s^{-1} and a flat profile, while we would expect a decreasing trend towards the galactic centre. The excess velocity in the central part of the rotation curve could be due to a residual beam-smearing effect or to an additional kinematic component in the centre. In order to avoid the systematics induced by the inclusion of innermost region and to obtain a reliable modelling of the disk, we excluded the central beam (radius ∼ 0.08 arcsec) from the fit, and performed a sampling with 5 radii, spaced by 0.045 arcsec, starting from 0.113 arcsec. The top and bottom left panels of Fig. 3.14 show the position-velocity (PV) diagrams of the disk along the major and minor kinematic axes with contours of the disk model as dashed orange lines and the modelled LOS velocities as orange stars. Exploring the $v_{\rm rot} - i$ parameter space with the task `SPACEVAR` of $^{\rm 3D}$Barolo, we found that models with i in the range $[20, 45]$ deg give similar results in modelling the PV diagram and the velocity dispersion profile. The $v_{\rm rot}$ is most affected by the variation of i because $v_{\rm rot} = v_{\rm LOS}/\sin(i)$, and in this case, models with $i < 20$ lead to unreasonably high values for the velocity rotation ($v_{\rm rot} \gtrsim 500-1000$ km s^{-1}). In the top and bottom right panels of Fig. 3.14, the velocity rotation and velocity dispersion curves are presented, where the error bars arise from the lower and upper limit inclination ($i = 20, 45$ deg). The intrinsic (i.e. beam-smearing corrected) rotational velocity $v_{\rm rot}$ shows a rather flat rotation curve, and the velocity dispersion $\sigma_{\rm gas}$ is boosted at $r \sim 0.1$ arcsec, reaching ∼ 80 km s^{-1}, while it decreases to 50 km s^{-1} at larger radii. We found $v_{\rm rot} \simeq 347$ km s^{-1} and $\sigma_{\rm gas} \simeq 60$ km s^{-1} on average within $r < 1.5$ kpc (values corrected for beam smearing). We derive $v_{\rm rot}/\sigma_{\rm gas} \sim 6$, indicating a disk that is rotationally supported.

The total dynamical mass enclosed within a radius r=1.7 kpc (∼ 0.3 arcsec) is $M_{\rm dyn} = 5.2^{+2.3}_{-3.2} \times 10^{10}\ M_{\odot}$, consistent with that derived from CO(6-5) in approximately the same region (Feruglio et al., 2018) and from previous [CII] lower-resolution observations (R. Wang et al., 2013). The uncertainties on $M_{\rm dyn}$ were obtained by propagating the error for $v_{\rm rot}$ at R=1.7 kpc. Since the gas mass measured from CO is $M_{\rm H_2} = 4.2 \times 10^{10}$ M$_{\odot}$ (see Chap. 3.3.1), dynamical models with $i > 30$ deg, which imply $M_{\rm dyn} \lesssim 4 \times 10^{10}\ M_{\odot}$, can be ruled out. This restricts the range of possible values for the inclination to [20,30] deg, supporting the choice of $i = 25$ deg in the dynamical modelling of the disk. We were able us to derive a rough estimate of

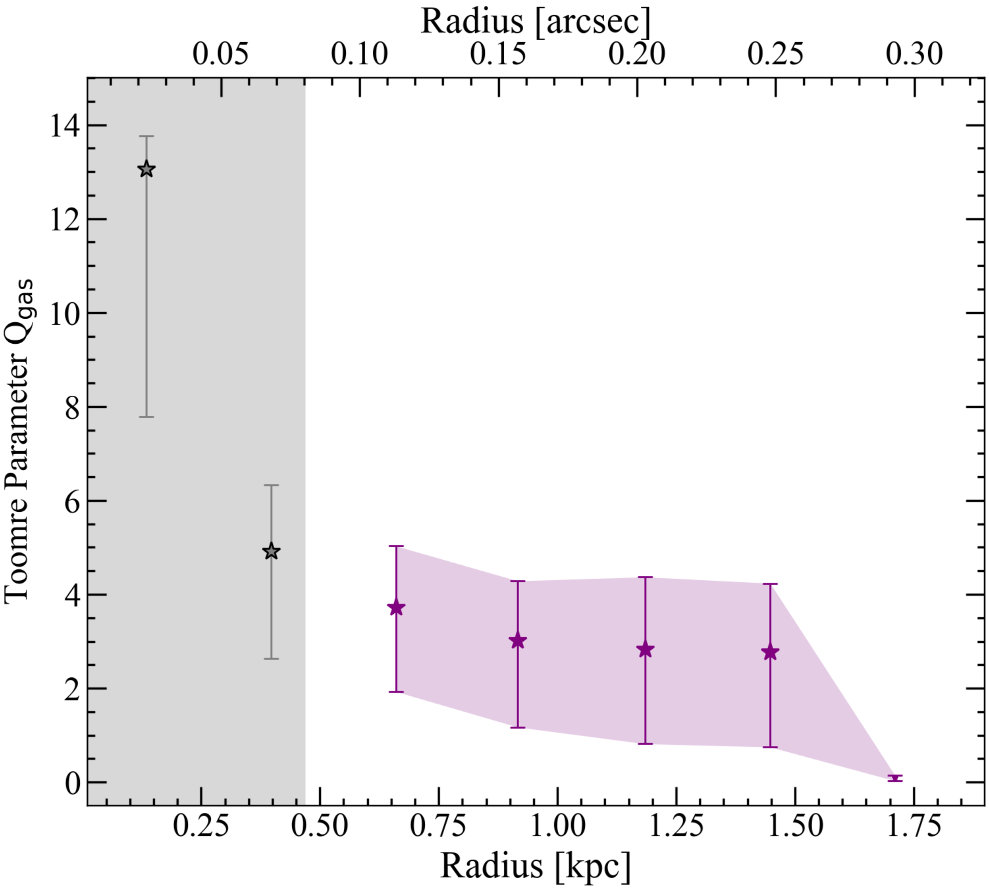

Figure 3.15: *Gas Toomre parameter $Q_{\rm gas}$ as a function of the radius from the centre position of the [CII] emission, computed for the annuli used in the $^{\rm 3D}$Barolo [CII] modelling (see Chap. 3.3.1 and Fig. 3.14). The grey shaded area marks the region of the central beam ($r_{\rm beam}$ ~ 0.08 arcsec), and grey points are computed using the $v_{\rm rot}$ and σ_v of the $^{\rm 3D}$Barolo model including the central beam.*

the stellar mass of the QSO's host galaxy, $M_* = M_{\rm dyn} - M_{\rm H_2} - M_{\rm BH} \sim 3 \times 10^9$ M$_\odot$, using $M_{\rm BH} = 5 \times 10^9$ M$_\odot$ derived from the MgII emission line profile (uncertainty of ~ 0.1 dex, see Mazzucchelli in prep)[6]. This stellar mass, together with the AGN-corrected SFR, place the QSO's host galaxy well above the main sequence for star-forming galaxies at $z \sim 6$ (see e.g. Mancuso et al. 2016; Pearson et al. 2018), indicating a strongly star-bursting host galaxy.

The Toomre parameter, spatially averaged across the entire emission within $r < 1.5$ kpc, is $Q_{\rm gas} = \sqrt{2}\sigma_v v_{\rm rot}/\pi G r \Sigma_{\rm gas} \approx 3$ for a flat rotation curve, where $\Sigma_{\rm gas}$ is the gas surface density derived from [CII] within the radius r. Considering also the Toomre parameter for the stellar component, the global Q would be lower than this value (Aumer et al., 2010). In Fig. 3.15 we show the radial profile of $Q_{\rm gas}$, where we computed the molecular gas surface mass density, taken in the same annuli as defined for the dynamical modelling (see Fig. 3.14), and we propagated the uncertainties of $v_{\rm rot}$ and $\Sigma_{\rm gas}$. The $v_{\rm rot}$ and σ_v are those derived by the model

---

[6] At the time of this analysis, published in Tripodi et al. (2022), we obtained the BH mass of J2310+1855 via private communication. Now $M_{\rm BH,J2310}$ has been published in Mazzucchelli et al. (2023) with a slightly lower value, $M_{\rm BH} = 4.7 \times 10^9$ M$_\odot$. This does not affect our conclusions.

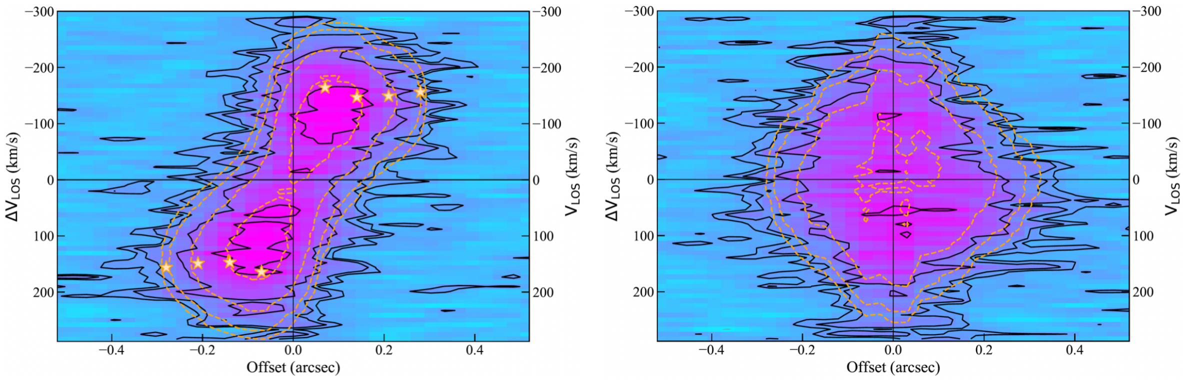

Figure 3.16: *PV diagrams of the [CII] emission line along the kinematic major axis (left panel) and kinematic minor axis (right panel), performed with* $^{\rm 3D}$*Barolo. Contours are at* $2, 3, 6,$ *and* 12σ*, with* $\sigma = 0.22$ *mJy/beam, for the data (solid black lines) and the best-fit model (dashed orange lines). Yellow stars show the projected rotation curve modelled by* $^{\rm 3D}$*Barolo.*

of $^{\rm 3D}$Barolo at different radii (see top and bottom right panels of Fig. 3.14). The grey shaded area, as before, marks the region of the central beam, and the grey points are computed using the $v_{\rm rot}$ and σ_v of the $^{\rm 3D}$Barolo model including the central beam. $Q_{\rm gas}$ is in the range 3-13 at $r < 0.4$ kpc, reflecting the flat rotation curve and high value of $v_{\rm rot}$ at the centre. For $r > 0.8$ kpc, $Q_{\rm gas} \approx 1 - 5$ is close to the critical value commonly adopted for the gas component (R. Genzel et al., 2014; Leroy et al., 2008), indicating that the disk is unstable against gravitational collapse, can fragment, and may eventually lead to star formation. $Q_{\rm gas} \sim 1$ was reported for QSO J234833.34–305410.0 at $z \sim 7$ (Walter et al., 2022).

3.3.3 Dynamical signature of a stellar bulge in J2310+1855

In the previous section, we interpreted the high [CII] velocities seen near the galactic centre of J2310+1855 as due to a [CII] outflow. An alternative possible explanation for the high-velocity [CII] emission is fast rotation due to the presence of a central mass concentration. In this section, we investigate whether a bulge can indeed be the most likely cause for the velocity enhancement in the innermost region of J2310+1855 by modelling the rotation curve with different mass models.

We derived a new rotation curve of J2310+1855 using the software $^{\rm 3D}$Barolo (Di Teodoro and Fraternali, 2015), improving the preliminary kinematic modelling of Tripodi et al. (2022) (reported in Chap. 3.3.2). For (x_0, y_0), $V_{\rm sys}$, and i, we adopted the same estimates as in Tripodi et al. (2022). We fixed z_0 to 300 pc, but this parameter has a negligible effect on our results because our spatial resolution is ~900 pc and the disc is nearly face-on ($i \simeq 25°$). Since the kinematic major axis is perpendicular to the minor axis, we fixed the radial velocity to zero. With respect to Tripodi et al. (2022), we changed the PA to 195° because the data-model residual maps in their Figure 8 suggest that their value of 200° was slightly overestimated (see Warner, Wright, and Baldwin, 1973). We also changed the radial sampling to avoid aggressive over-sampling; we used four rings spaced by 0.07 arcsec, which corresponds to 0.409 kpc.

In order to minimise the impact of the outflowing material on our results, we cropped the [CII] cube considering the velocity range [-290, +270]km s^{-1}. This excludes the blue and red wings seen in the spatially integrated [CII] spectrum (see Fig. 3.12 in Chap. 3.3.1). We then ran ^{3D}Barolo with $v_{\rm rot}$ and σ_v as free parameters. ^{3D}Barolo provides asymmetric uncertainties (δ_+, δ_-), corresponding to a variation of 5% in the residual from the global minimum. We treated them as 1σ uncertainties and took the mean value of (δ_+, δ_-) to compute symmetric uncertainties that were used in subsequent rotation-curve fits.

Fig. 3.16 shows PV diagrams along the major and minor axes of the disc. In Tripodi et al. (2022), the comparison between disc model and observations showed a mismatch at line-of-sight velocities $V_{\rm LOS}$ of ±300km s^{-1}along both the major and minor axes. This mismatch was interpreted as due to the gas outflow. The overall symmetry of the PV diagrams, however, may suggest that the high-velocity emission is associated with fast rotation. With the new rotation curve, the central mismatch at $\gtrsim$ 300km s^{-1}has now decreased along both axes, indicating that the new model fits the data better.

The rotation curve shown in Fig. 3.16 is approximately flat, with a slight increase towards the centre. The average deprojected rotation velocity is ~365 km s^{-1}, similar to what was found in Tripodi et al. (2022). The velocity dispersion profile (not shown) increases towards the centre and reaches $\sigma_{\rm gas} \simeq 80$ km s^{-1}, with an average value of ~70 km s^{-1}. This gives $V_{\rm rot}/\sigma_{\rm gas} \simeq 5$, so that the disc is rotation supported and the observed rotation velocities are a good tracer of the circular velocity of a test particle in the equilibrium gravitational potential. The circular velocity approximately goes as $(V^2_{\rm rot} + \sigma^2_{\rm gas})^{0.5}$, therefore corrections for pressure support are a few km s^{-1}at most and are therefore negligible.

We used the observed rotation curve to constrain the mass distribution within the galaxy. We considered three to four mass contributions: a gaseous disc, a stellar disc, an SMBH, and possibly, a stellar bulge. The model circular velocity at radius R is then given by

$$V^2_{\rm mod} = \Upsilon_{\rm gas} V^2_{\rm gas} + \Upsilon_{*\rm disc} V^2_{*\rm disc} + \Upsilon_{\rm bulge} V^2_{\rm bulge} + V^2_{\rm BH}, \tag{3.3}$$

where $\Upsilon_j = \dfrac{M_j}{10^{10}\,{\rm M}_\odot}$ are dimensionless parameters of the order of one (with j = gas, $*$disc, bulge). Essentially, for numerical convenience, we normalised the gravitational contributions to a mass of 10^{10} M$_\odot$ and scaled them using Υ_j.

The gravitational contribution of the gas disc was computed using the task `Rotmod` in the GIPSY software (Vogelaar and Terlouw, 2001). It numerically solves the equation from Casertano (1983) for a truncated disc of finite thickness. For the radial column density distribution, we used the observed [CII] surface brightness profile as input, which is close to exponential (see Fig. 3.13). For the vertical density distribution, we assumed an exponential profile with a scale height z_0 = 160 pc. This is motivated by the scaling relation between scale length and scale height that is observed in edge-on disc galaxies at $z = 0$ (e.g. Bershady et al., 2010), but the precise value of $z_{0,\rm gas}$ has a minor effect on our results. In the limiting case of a razor-thin

Table 3.3: MCMC priors

Parameter	Prior Type	Center	Standard Deviation
i [°]	G	25	5
$\log(\Upsilon_{\rm gas})$	LN	0.64	0.11
$\log(\Upsilon_{*\rm disc})$	LN	0.0	1.0
$\log(\Upsilon_{\rm bulge})$	LN	0.0	1.0
$\log(\Upsilon_{\rm BH})$	LN	0.0	1.0
$M_{\rm BH}$ [M$_\odot$]	Fixed	5×10^9	...

Notes. G = Gaussian. LN = Lognormal. A prior for $\log(\Upsilon_j)$ of 0.0 ± 1.0 corresponds to $(1 \pm 10) \times 10^{10}M_\odot$.

exponential disc (i.e. $z_{0,\rm gas} = 0$), our results would vary within 15%, which is well within our current uncertainties on the fitted quantities. We did not use the CO(6-5) surface brightness emission (Tripodi et al., 2022) because it was derived from data with lower resolution (~ 0.5 arcsec; Feruglio et al. 2018), therefore the observed CO surface brightness profile is more sparsely sampled than the [CII] profile. For J2310, precise determinations for $M_{\rm gas}$ were obtained using the CO(6-5) emission line together with the CO spectral line energy distribution (Feruglio et al., 2018; Li et al., 2020; Tripodi et al., 2022); we used the value of 4.4×10^{10}M$_\odot$as a tight prior on $M_{\rm gas}$. This estimate was derived by fitting the spectral line energy distribution of high-J CO lines and assuming a CO-to-H$_2$ conversion factor $\alpha_{\rm CO} = 0.8$ M$_\odot$(K km s^{-1} pc^{-2})$^{-1}$, which is currently thought to be most appropriate for QSO-host galaxies (Carilli and Walter, 2013). Systematic uncertainties on $\alpha_{\rm CO}$ in starburst AGN-host galaxies can be large even at $z \simeq 0$ (Bolatto, M. Wolfire, and Leroy, 2013), but there is mounting evidence that their $\alpha_{\rm CO}$ are systematically smaller than those of Milky-Way-like galaxies (Accurso et al., 2017; Pearson et al., 2018; Lelli et al., 2022). We associate a 25% uncertainty with $M_{\rm gas}$. This tight prior is necessary to break a degeneracy between $\Upsilon_{\rm gas}$ and $\Upsilon_{*\rm disc}$ that arises because gas disc and stellar disc provide velocity contributions with a similar shape. The actual gas mass may be more uncertain than assumed here, but this assumption mostly impacts the relative masses of the stellar and gas discs but leaves our conclusions on the central mass concentration unaltered.

The gravitational contribution of the star-forming stellar disc was computed in a similar way as for the gas disc. For the radial column density profile, we used the surface brightness profile from the ALMA sub-millimeter continuum map, which traces hot dust heated by young stars. The sub-millimeter emission can be used as a proxy for the distribution of the stellar disc because dust absorbs UV radiation from young stars and re-emits it at far-infrared wavelengths (Lelli et al., 2021). The continuum surface brightness profile shown in Fig. 3.13 (Tripodi et al., 2022) is well described by an exponential profile with scale length $R_{*\rm disc} = 0.71$ kpc, which further supports the use of dust emission as a proxy for the star-forming disc. For the distribution of the vertical surface density, we assumed an exponential profile with $z_0 \simeq 160$ pc as for the gas disc, but this assumption has a very minor effect on our results.

The stellar bulge was modelled as a spherical projected Sérsic profile, so that its gravitational contribution is given by (Lima Neto, Gerbal, and Márquez, 1999; Terzić and Graham, 2005)

$$V_{\rm bulge}(R) = \sqrt{\frac{{\rm G}M_{\rm bulge}}{R}\frac{\gamma(n(3-p), b(R/R_e)^{1/n})}{\Gamma(n(3-p))}}, \tag{3.4}$$

where $M_{\rm bulge}$ is the stellar bulge mass, R_e is the effective radius, n is the Sérsic index, $b = 2n - 1/3 + 0.009876/n$ for $0.5 < n < 10$, γ and Γ are the incomplete and complete gamma function, respectively, and $p = 1.0 - 0.6097/n + 0.05563/n^2$ for $0.6 < n < 10$ and $10^{-2} \leq R/R_e \leq 10^3$. We fixed $n = 4$ (a De Vaucouleurs profile) and set $R_e = 0.07$ arcsec ~409 pc, that is, ~ beam size/2. Lower values of R_e would not significantly change the contribution of the bulge in the centre, making it similar to a point source. In principle, R_e could be determined from high-resolution rest-frame optical and/or near-infrared images after subtracting the QSO contribution, but data like this are currently not available. Alternatively, R_e may be set as a free parameter in our model, but we do not have enough data points in the rotation curve to fit more than four parameters.

The SMBH gives the velocity contribution of a point source,

$$V_{\rm BH}(R) = \sqrt{\frac{{\rm G}M_{\rm BH}}{R}}, \tag{3.5}$$

where $M_{\rm BH}$ is the BH mass. In our models, $M_{\rm BH}$ could be either a free or a fixed parameter. In the latter case, it was fixed to $M_{\rm BH} = 5.0 \times 10^9$ $\rm M_\odot$, derived from the MgII emission line profile (Mazzucchelli in prep., Tripodi et al. 2022).

In our modelling, we did not consider the contribution of a dark matter (DM) component for several reasons: (1) in general, the DM contribution in massive galaxies becomes important in the outer regions, beyond the stellar disc, because it has a rising trend with the radius. This component would therefore not affect our main results about the central mass component. (2) In our specific case, the rotation curve was measured out to a radius of just 1.7 kpc, within which the gravitational potential is likely dominated by baryons (in analogy to star-forming galaxies at slightly lower redshifts; e.g. Reinhard Genzel, 2017; R. Genzel et al., 2020; Rizzo et al., 2020; Rizzo et al., 2021; Lelli et al., 2021). (3) Our four data points do not enable us to fit for additional free parameters, which would be required if we were to add a DM component. Therefore, we opted for the simplest physically motivated mass model with the smallest number of free parameters.

Summarizing, the gaseous and stellar disc were both modelled as thick discs with a radial density profile given by the observed [CII] and dust surface brightness profiles, respectively (following Lelli et al. 2021). For the vertical density profile, we assumed an exponential function with a fixed scale height. The stellar bulge was modelled as a spherical projected De Vaucouleurs profile with a fixed effective radius of 0.07 arcsec (~409 pc). This is the maximum effective radius allowed by the data, so that our bulge model maximises the difference between an extended mass distribution and a point source. The SMBH was modelled as a point mass.

The masses of the stellar and gas discs are degenerate because their velocity contributions

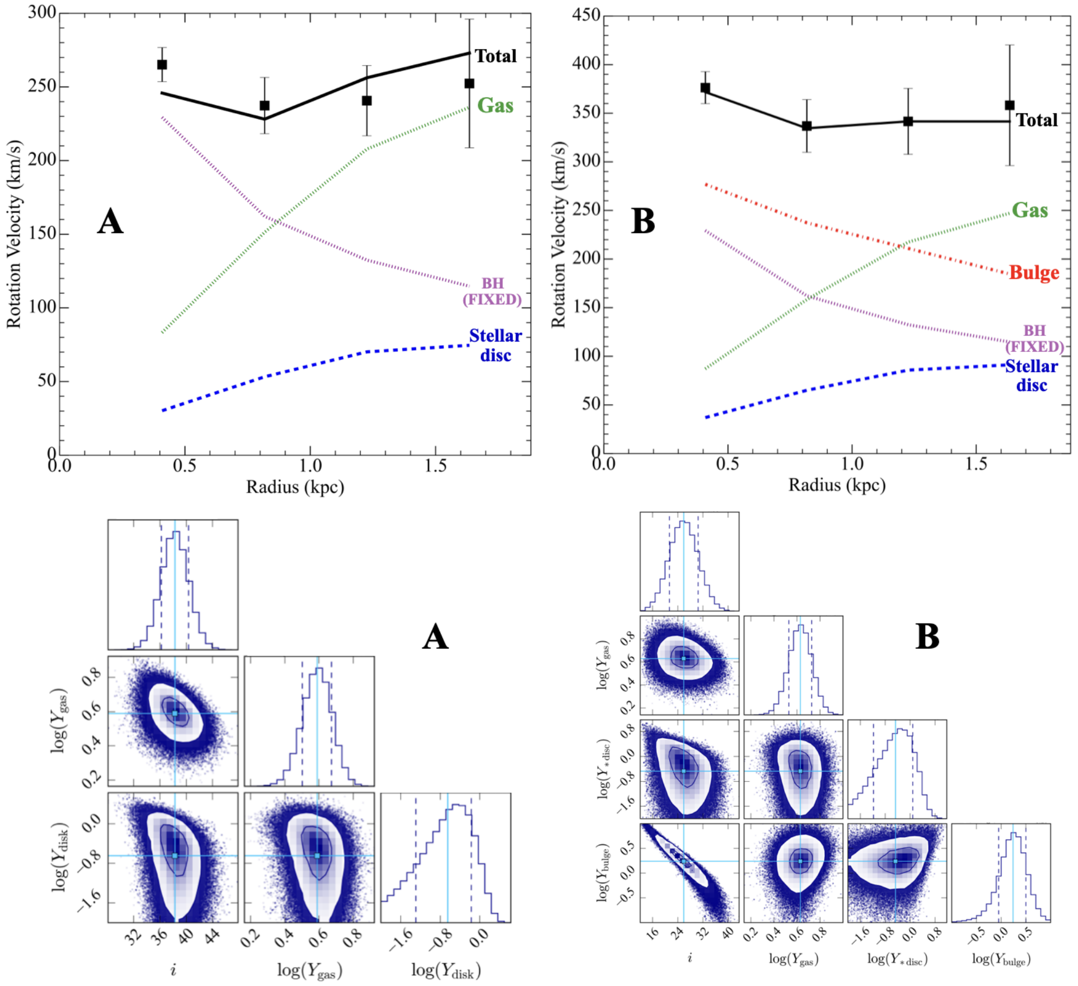

Figure 3.17: *Results for mass models. Top panels: Two different mass models are fitted to the observed rotation curve (black squares): no bulge and fixed BH mass (A), bulge and fixed BH mass (B). The best-fitting model (solid black line) is the sum of the contributions from the stellar disc (dashed blue line), the cold gas disc (dotted green line), the BH (dotted purple line), and the stellar bulge (when present; dot-dashed red line). The different values of the rotation velocities in models A and B are due to different best-fitting values for the inclination:* $i = 38 \pm 2^\circ$ *for model A and* $i = 26 \pm 4^\circ$ *for model B. Bottom panels: Posterior distributions of the fitting parameters for models A and B.*

have a similar shape, which rises with radius. To break this degeneracy, we imposed a tight prior on $\Upsilon_{\rm gas}$ by adopting a gas mass of 4.4×10^{10} $M_\odot$(Feruglio et al., 2018; Li et al., 2020; Tripodi et al., 2022). Similarly, the masses of bulge and SMBH are degenerate because their velocity contributions declines with radius. This occurs because the spatial resolution of the rotation curve cannot discern a central point source from a more extended central mass concentration. To break this degeneracy, we fixed the SMBH mass to 5×10^9 $M_\odot$(Mazzucchelli et al. in prep.; Bischetti et al. 2022). This estimate comes from X-SHOOTER spectroscopy of the MgII and CIV lines, which has a high signal-to-noise ratio and assumes the $z \simeq 0$ scaling relations provided by Vestergaard and Osmer (2009b), Vestergaard and Peterson (2006), and Coatman et al. (2017).

Depending on the chosen model, we therefore had three or four free parameters: the incli-

Table 3.4: MCMC results for mass model B.

Parameter	Best-fitting values
i [°]	26 ± 4
$M_{\rm gas}[10^{10}\ {\rm M}_\odot]$	4.26 ± 0.97
$M_{*\rm disc}[10^{10}\ {\rm M}_\odot]$	$0.34^{+0.43}_{-0.55}$
$M_{\rm bulge}[10^{10}\ {\rm M}_\odot]$	$1.74^{+1.04}_{-1.17}$
$M_{\rm BH}[10^{10}\ {\rm M}_\odot]$	0.5 (Fixed)

nation i of the [CII] disc that changes the observed rotation velocities as $V_{\rm obs}\sin(i)$, and two or three parameters among $\Upsilon_{\rm gas}$, $\Upsilon_{*\rm disc}$, and $\Upsilon_{\rm bulge}$. The best-fitting parameters were determined using a Markov chain Monte Carlo (MCMC) method in a Bayesian context. We adopted a Gaussian prior on i and lognormal priors on the Υ_j parameters. The choices for the central and standard deviation values for all the fitting parameters are listed in Tab. 3.3.

To assess whether the bulge is a truly essential component, we started with a conservative model that considered only stellar disc, gas disc, and SMBH with a fixed mass. Fig. 3.17 (model A, left panel) shows that this model misses the first point of the rotation, and the inclination is pushed up to 38° (more than 2.5σ from the prior value) to decrease the rotation velocities as much as possible. When we instead consider a model in which the BH mass is entirely free, we obtain a good result, but the required BH mass is higher than the expected value derived from the MgII line by a factor of 2 (i.e. $M_{\rm BH} = 1.1 \pm 0.4 \times 10^{10}\ {\rm M}_\odot$). This high mass is still within the systematic uncertainties of ~0.3 dex associated with BH masses from MgII measurements (Vestergaard and Peterson, 2006). An increase in the BH mass of a factor of 2 would therefore be able to remove the need for an additional central stellar concentration. However, this scenario seems unlikely according to galaxy formation models (see following discussion and Fig. 3.18).

Finally, we considered a mass model that included both an SMBH with a fixed mass and a bulge component. Fig. 3.17 (model B, right panel) shows that this model reproduces the observed rotation curve well and preserves the prior value of $i \simeq 25°$. The best-fitting values are reported in Tab. 3.4. We find a bulge mass of $\sim 1.7 \times 10^{10}{\rm M}_\odot$that implies $M_{\rm bulge} \simeq 0.27 \times M_{\rm baryon}$, where $M_{\rm baryon} = M_{\rm gas} + M_{*\rm disc} + M_{\rm bulge}$. The best-fit mass also implies an effective surface mass density $\Sigma_{\rm eff} \simeq 3 \times 10^4\ {\rm M}_\odot\ {\rm pc}^{-2}$, which is consistent with that of the most compact spheroids at $z \simeq 0$. It seems unlikely that such a compact mass component can be in the form of [CII]-dark or CO-dark gas because it should lead to a strong central enhancement of star formation that is not visible in the sub-millimeter continuum map. At larger radii, however, the gas contribution becomes strong, and the galaxy has $M_{\rm gas} \simeq 0.67 \times M_{\rm baryon}$; this result is largely driven by the tight prior on the gas mass.

Recently, Shao et al. (2022) presented a similar analysis of the rotation curve of J2310, using a razor-thin gas disc and a single spherical stellar component. They obtained a stellar mass of $5.8 \times 10^9\ {\rm M}_\odot$ when they fixed the BH mass to the value of 1.8×10^9 that was derived

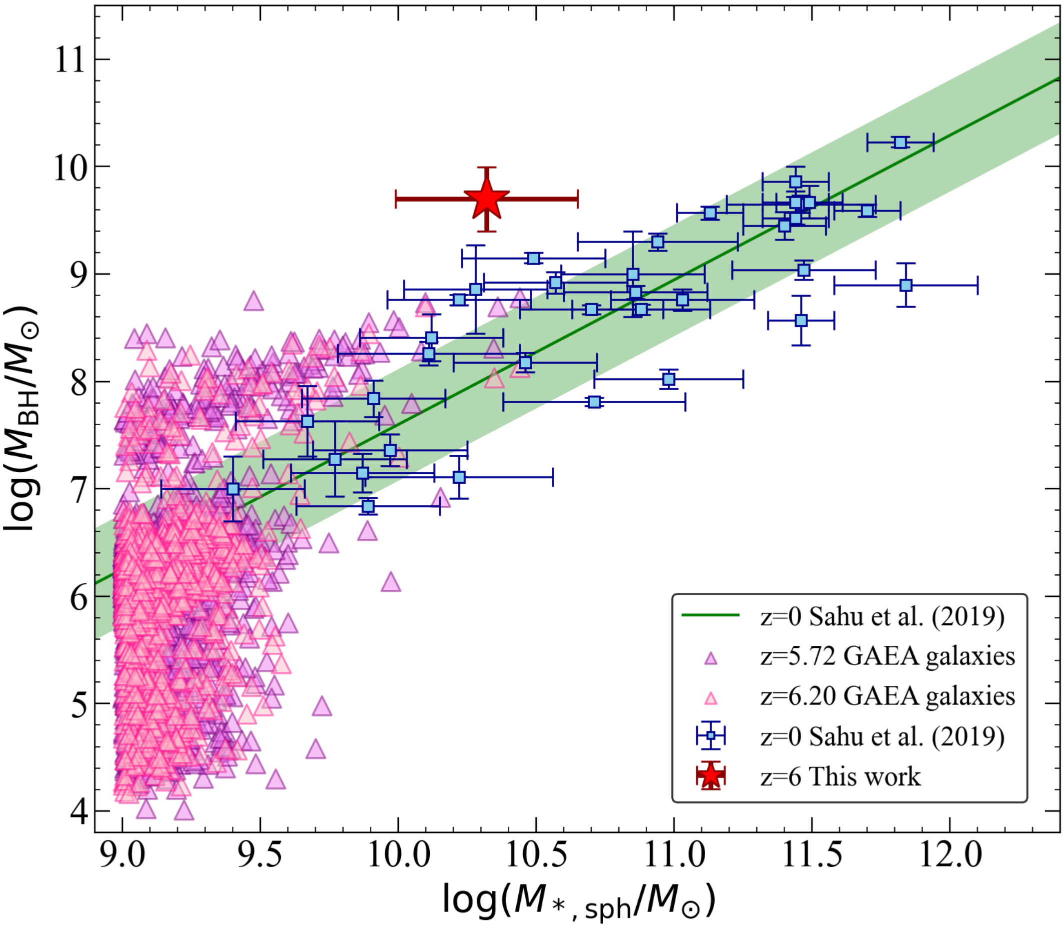

Figure 3.18: *Black hole mass vs. spheroid stellar mass. Comparison between the z = 0 sample of early-type galaxies from Sahu, Graham, and Davis (2019) (blue squares) and our results for the z = 6 QSO J2310+1855 (red star). The green line is the best-fit relation for the z = 0 sample. Its scatter (green shadowed region) is taken from Sahu, Graham, and Davis (2019). The purple and pink triangles are the z = 5.72 and z = 6.20 galaxies, respectively, that were modelled by the GAEA-F06 run (Fontanot et al., 2020).*

from the analysis of the CIV emission line (Feruglio et al., 2018). Our mass models are different from theirs because we distinguish between a star-forming stellar disc and a spherical bulge, which is crucial to locate J2310+1855 on the BH-bulge scaling relation. In addition, in our models, the gas and stellar discs have a realistic finite thickness. Importantly, Shao et al. (2022) concluded that they measured the dynamical mass of a black hole for the first time at $z \simeq 6$, whereas we find that the BH mass and bulge mass are degenerate. To break this degeneracy, the BH mass must be fixed using independent information, given the low spatial resolution of the ALMA data (~900 pc). For comparison, dynamical BH mass measurements in AGN-host galaxies at $z \simeq 0$ require spatial resolutions better than 100 pc (e.g. F. Combes et al., 2019; Lelli et al., 2022). The observed rotation curve of J2310+1855 clearly indicates a central mass concentration, but the ALMA data themselves cannot determine whether this is entirely due to a BH, a stellar bulge, or a combination of both. In our view, the latter scenario is the most likely.

Two crucial questions that arise from this result are first, how a bulge of $\sim 10^{10}\mathrm{M}_{\odot}$was able to form in less than 1Gyr, and second, what the implications of our results are for the overall picture of SMBH-galaxy co-evolution. The main proposed scenarios for bulge formation involve major mergers, which produce spheroids with a large Sérsic index (Hernquist and Barnes, 1991), and disc instabilities such as the formation of thick, buckling bars, which produce profiles with a smaller Sérsic index (the so-called pseudo-bulges; see e.g. F. Combes and R. H. Sanders 1981). The latter imply long timescales and therefore occur mainly at late cosmic times. At high redshift, disc instabilities manifest as turbulent discs hosting giant clumps that can coalesce to form bulges (Bournaud, B. G. Elmegreen, and D. M. Elmegreen, 2007; B. G. Elmegreen, Bournaud, and D. M. Elmegreen, 2008). In addition, when a luminous active galactic nucleus (AGN) is present, its energy output in the form of radiation pressure on dust or shocks can contribute to the formation of a spheroidal component by triggering both galactic outflows and SF (Ishibashi and Fabian, 2014; Maiolino et al., 2017).

For J2310+1855, disc instabilities can probably be ruled out because these secular processes occur on long timescales (~3-5 Gyr), while the age of the Universe at $z \simeq 6$ is only ~900 Myr in the adopted cosmology. All the other mechanisms appear viable, however. The host galaxy of J2310+1855 does not show any evidence of ongoing mergers based on the high-resolution ALMA data that are available to date, but the orbital time at the last measured point of the rotation curve is only 26 Myr, which means that the [CII] disc may relax in just ~100 Myr (about four revolutions) after a violent event. This implies that the last potential merger between (proto-)galaxies with masses of a few times 10^9 $\mathrm{M}_{\odot}$ must have occurred at $z > 6.5$. Feedback from AGN in the form of large-scale outflows driven by the radiation pressure on dust or by shock propagation may trigger the formation of new stars at outer radii, leading to the development of extended stellar envelopes (Ishibashi and Fabian, 2014). Observational evidence supporting this scenario was provided by Maiolino et al. (2017), who found that SF can occur within galactic outflows where the newly formed stars follow ballistic trajectories that can fall back in the potential and thus form a spheroidal component. In this scenario, the accreting BH triggers SF and contributes to the formation of the stellar bulge. This scenario may form extended and diffuse bulges, while in J2310+1855, we find evidence for a compact mass concentration with a high effective surface density.

Regarding the BH-galaxy co-evolution, for J2310+1855, Tripodi et al. (2022) found that the SMBH growth efficiency is ~50% lower than that of its host galaxy. This suggests that AGN feedback effectively slows down the accretion onto the SMBH, while the host galaxy is still growing fast. The onset of significant BH feedback hampering BH growth marks the transition from a phase of BH dominance to a phase of symbiotic growth of the BH and the galaxy (M. Volonteri, 2012). In Fig. 3.18, we locate J2310+1855 on the local $M_{\mathrm{BH}} - M_{\mathrm{bulge}}$ relation (green region) and the local observational data (blue squares) from Sahu, Graham, and Davis (2019). J2310+1855 deviates from the $z \simeq 0$ relation because it has $M_{\mathrm{BH}} \simeq 0.3 M_{\mathrm{bulge}}$, while in local galaxies, $M_{\mathrm{BH}} \simeq (0.01 - 0.1) \times M_{\mathrm{bulge}}$. When we assume that the BH of

J2310+1855 evolves into one of the most massive BH at $z = 0$ ($M_{\rm BH} \simeq 2 \times 10^{10}$ M$_\odot$), it can grow in mass by only a factor of 4 during ~13 Gyr, while the bulge should grow by a factor of ~40 to reach a mass around $10^{11.8}$M$_\odot$at $z \simeq 0$. This suggests an asynchronous growth between SMBH and bulges. Moreover, the available molecular gas in J3210+1855 is estimated to be $\sim 4 \times 10^{10}$ M$_\odot$. To reach a stellar mass of $\sim 10^{11.8}$ M$_\odot$ at $z \simeq 0$, the galaxy needs to accrete a comparable amount of mass (in gas or directly in stars) over ~13 Gyr, giving an average mass accretion rate of ~ 40 M$_\odot$ yr^{-1}. For example, if the galaxy continues to form stars with SFR $\simeq 10^3$ M$_\odot$ yr^{-1}, a stellar mass of $(5-10) \times 10^{11}$ M$_\odot$ can be formed in only 0.5-1.0 Gyr (by $z \simeq 3.5-4.0$), but would then require a mass-accretion rate comparable to the SFR. In any case, our result seems to highlight the absence of any symbiotic growth between the SMBH and the host galaxy at high redshift; it appears that the SMBH firstly experiences a phase of rapid and intense growth (reaching up to 5×10^9M$_\odot$in less than 1 Gyr), followed by the growth of the galaxy.

Finally, we compared our result with theoretical predictions of the GAlaxy Evolution and Assembly (GAEA) model (in detail the GAEA-F06 run, Fontanot et al. 2020), to shed light on the mechanism leading to the formation of this bulge. This semi-analytic model includes two different channels of bulge formation (i.e. galaxy mergers and disc instabilities; see e.g. De Lucia et al. 2011): both physical processes also help bringing cold gas onto the central SMBH, thus feeding accretion and AGN events. In Fig. 3.18 we also show the distribution of model galaxies[7] in the $M_{\rm BH} - M_{\rm bulge}$ plane (purple and pink triangles) compared with a local $z \sim 0$ sample (Sahu, Graham, and Davis, 2019). From the comparison, we can conclude that (a) GAEA-F06 predicts a relevant population of $M_{\rm bulge} > 10^9$M$_\odot$bulges in high-z galaxies despite the relatively young cosmic epoch, and (b) the scatter around the $z \sim 6$ $M_{\rm BH} - M_{\rm bulge}$ relation is much larger than in the local Universe. This is likely due to the different contribution of the two bulge-forming channels (mergers and disc instabilities) to the corresponding SMBH accretion (see Fontanot et al., 2020): in this interpretation, at fixed $M_{\rm bulge}$, higher (lower) $M_{\rm BH}$ corresponds to sources that experienced more mergers (disc instabilities). We plan to further test this hypothesis in forthcoming work. We verified that GAEA predicts that all objects lying above the $M_{\rm BH} - M_{\rm bulge}$ relation at $z \sim 6$ converge towards the $z \sim 0$ relation at later times. Nonetheless, none of the model galaxies reaches $z \sim 6$ $M_{\rm BH}$ as high as the one estimated for J2310+1855, which thus represents the main difference between data and model predictions.

3.3.4 [CII] outflows and energetics

J2310+1855

In Fig. 3.19, the velocity-integrated contour maps of the blue and red wings, obtained by collapsing the spectral channels within the regions marked with blue and red lines in the [CII]

---

[7] The GAEA-F06 realisation has been defined on merger trees extracted from the Millennium Simulation. We considered model galaxies in the two snapshots closer to the estimated J2310+1855 redshift, $z = 6.20$ and $z = 5.72$.

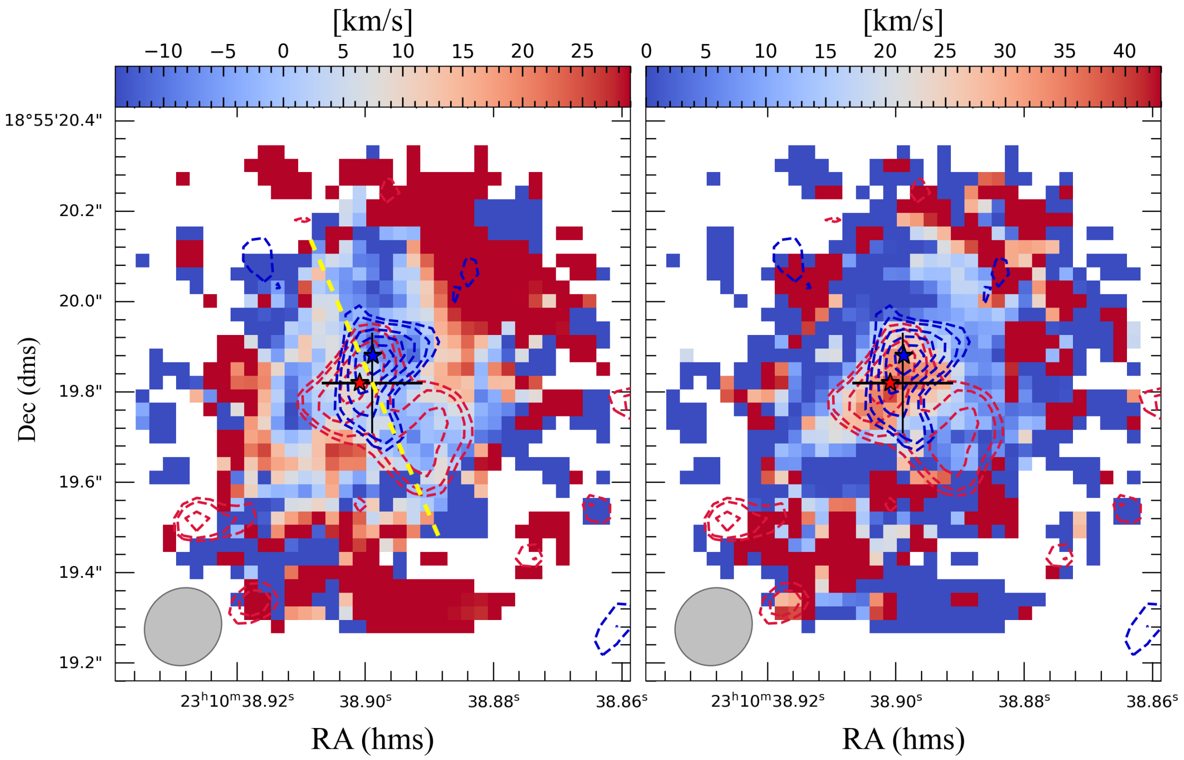

Figure 3.19: $^{3\mathrm{D}}$*Barolo residuals of mean velocity map (left panel) and velocity dispersion map (right panel) of the [CII] emission line of J2310+1855. The contours of red and blue wings are overplotted. Levels are* $2.5, 3, 4, 5,$ *and* 6σ, *with* $\sigma = 39$ μ*Jy for the red wing and* $\sigma = 43$ μ*Jy for the blue wing. The red and blue wings have been selected from the [CII] spectrum as shown in Fig. 3.12. The dashed yellow line is the kinematic major axis of the [CII] line, at PA* = 200 *deg. The clean beam is indicated in the lower left corner. The excesses at the border of the source should not be considered because they are due to the poor subtraction of the noise.*

spectrum of J2310+1855 (Fig. 3.12), are shown overplotted on the $^{3\mathrm{D}}$Barolo residuals of the [CII] velocity and velocity dispersion maps. The contour maps contain a contribution from the disk because the disk model is not subtracted from the data cube and from the corresponding maps, from which we extracted the contours. To evaluate the disk contribution to the wings, we used the [CII] spectrum and the double-Gaussian fit in Fig. 3.12. After subtracting the double-Gaussian components from the [CII] spectrum, we found that the integrated fluxes for the red and blue wings are $F_{\mathrm{red}} = 118$ mJy km s^{-1} and $F_{\mathrm{blue}} = 144$ mJy km s^{-1} , respectively, evaluated by integrating the flux in the spectral regions marked by the vertical blue and red lines in the [CII] spectrum of Fig. 3.12. Comparing these integrated fluxes with the total integrated flux in the same velocity range, we obtained that $F_{\mathrm{red}}/F_{\mathrm{tot}} \sim 65\%$ and $F_{\mathrm{blue}}/F_{\mathrm{tot}} \sim 80\%$. This implies that for the blue wing, the contribution of the disk is modest in the contours of Fig. 3.19; for the red wing, the disk has a greater impact, but the contribution of the wing is still dominant. The dashed yellow line is the kinematic major axis, and the stars mark the peak positions of the emission of the blue and red wings. These high-velocity emission regions are seen up to 3σ in the PV diagrams taken along the major and minor axes, within the offset $r \sim 0.1$ arcsec, and with an LOS velocity about ±300 km s^{-1} on the blue and red sides of the line. Along the minor kinematic axis, the disk dynamical model (orange contours) is not able to reproduce this excess emission, indicating that the latter is not produced by the beam-smearing effect, but is rather due to a different kinematic component.

These high-velocity blue- and redshifted emissions located in the nuclear region do not follow the rotation curve of the main disk and may be due either to an unresolved circumnuclear disk tilted with respect to the main one, or to an outflow. The high excess in LOS velocity between these components and the best-fit disk ($v_{\rm LOS,disk} \sim 100$ km s^{-1}) suggests that these blue- and redshifted emissions are due to an outflow and not to a tilted, unresolved nuclear disk. We derived the flux density $S_\nu \Delta v$ of these two components by subtracting the double-Gaussian fit from the total [CII] spectrum, and integrating in the respective velocity ranges (see Fig. 3.12). We computed the luminosity of the wings straightforwardly by applying Eq.1 from Solomon and Vanden Bout (2005) and their outflow mass using Eq. 3.2. We obtained an outflow mass of $M_{\rm out} = 1.9 \times 10^8$ M$_\odot$ and $M_{\rm out} = 1.6 \times 10^8$ M$_\odot$ for the blue and red wings, respectively. Altogether we have $M_{\rm out} = 3.5 \times 10^8$ M$_\odot$ that is about 5% of the neutral gas mass in the disk, consistent with expectations of recent zoom-in hydrodynamical simulations presented by Valentini, Simona Gallerani, and Ferrara (2021). Assuming the scenario of time-averaged expelled shells or clumps (Rupke, Veilleux, and D. B. Sanders, 2005), we computed the mass outflow rate for the blue and red wings,

$$\dot{M}_{\rm out} = \frac{v_{\rm out} \times M_{\rm out}}{R_{\rm out}}, \tag{3.6}$$

where $v_{\rm out}$ is the projected outflow velocity defined as the velocity at which the integrated flux of each wing is 98% of their total integrated flux with respect to the systemic velocity. We estimated $v_{\rm out,blue} = -490$ km s^{-1} and $v_{\rm out,red} = 535$ km s^{-1} from the line profile in Fig. 3.12. We defined as outflow radius, $R_{\rm out}$, the projected separation between the peaks of the red and blue wings and the [CII] peak position, that is, $R_{\rm out,blue} = 0.6$ kpc and $R_{\rm out,red} = 0.3$ kpc. We then obtain an upper limit $\dot{M}_{\rm out} \lesssim 450$ M$_\odot$ yr^{-1} by adding the red and blue components, and adopting as outflow radius the maximum $R_{\rm out}(= 0.6$ kpc). However, depending on the LOS inclination, the intrinsic $R_{\rm out}$ may be larger than our estimate. Because these data do not allow resolving the kinematics of the outflow, an estimate of the lower limit for the mass outflow rate can be derived assuming an outflow size equal to the clean beam, $R_{\rm out} \sim 1$ kpc. This implies that a lower-limit outflow rate would be $\dot{M}_{\rm out} \gtrsim 180$ M$_\odot$ yr^{-1}.

We computed the kinetic power associated with the outflow as $\dot{E}_{\rm out} = \frac{1}{2}\dot{M}_{\rm out} \times v_{\rm out}^2 = (1.5 - 3.7) \times 10^{43}$erg s^{-1}, and the wind momentum load

$$\frac{\dot{P}_{\rm out}}{\dot{P}_{\rm AGN}} = \frac{\dot{M}_{\rm out} \times v_{\rm out}}{L_{\rm bol}/c}, \tag{3.7}$$

where $\dot{P}_{\rm AGN}$ is the AGN radiation momentum rate[8]. We adopted a bolometric luminosity of

---

[8] The values of mass outflow rate, kinetic power and momentum load are one order of magnitude lower than the ones reported in Tripodi et al. (2022). Those in Tripodi et al. (2022) are wrong due to a typo in the code, but

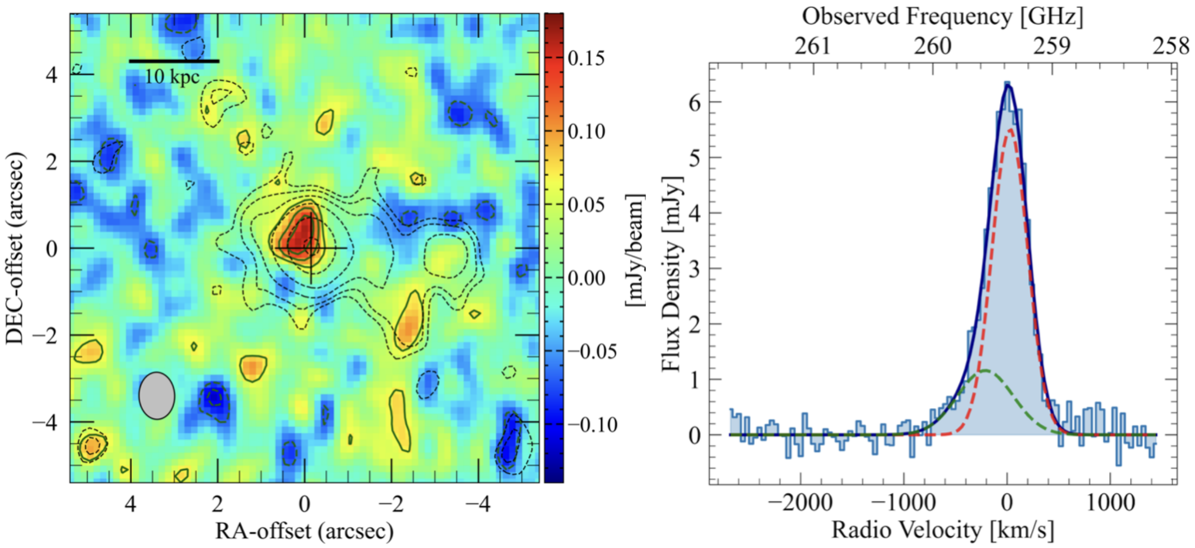

Figure 3.20: *Outflow map and optimized [CII] spectrum. Left panel: [CII] outflow map made with v=[-500,-1000] km* s^{-1} *with green contours at* $-3, -2, 2, 3, 4\sigma$*, with* $\sigma = 0.034$ *mJy/beam, and black dashed contours from the full [CII] map as in the top left panel of Fig. 3.9. Right panel: the [CII] spectrum have been extracted from a central region of 1.2 arcsec radius and is binned at 40 km* s^{-1}*. The blue solid line is the total fit, composed by two Gaussian components (narrow, as red dashed line; broad, as green dashed line). The broad component is associated to an outflowing emission.*

$L_{\rm bol} = 3.13{\times}10^{47}$erg s^{-1}, derived from the rest-frame continuum at 3000 Å(Bischetti, Feruglio, V. D'Odorico, et al., 2022) and the bolometric correction from Runnoe, Brotherton, and Shang (2012). This yields $\dot{E}_{\rm out}/L_{\rm bol} \sim 0.00005 - 0.0001$ and $0.6 \lesssim \dot{P}_{\rm out}/\dot{P}_{\rm AGN} \lesssim 1.4$.

J0100+2802

The [CII] spectrum of J0100+2802 extracted from a circular region of $\sim$ 2 arcsec radius showed emission towards high velocities (up to $\sim$ 1000 km s^{-1}) on the blue side of the [CII] line (see also Fig. 3.10). To ensure the highest S/N for this high-velocity emission, we optimized the aperture considering a central region of $\sim$ 1.2 arcsec radius, from which we extracted the [CII] spectrum shown in the right panel of Fig. 3.20. Firstly, we modelled the line with one single Gaussian, obtaining FWHM= 467 ± 10 km s^{-1}, and peak frequency of 259.378 GHz, corresponding to $z = 6.327$ that is in agreement with that found by F. Wang et al. (2019). We set the 0-velocity reference of the spectrum based on our peak frequency. As first order approach to estimate the flux and velocity of the high-velocity emission, we subtracted the Gaussian fit to the spectrum and we found residual emission in [-800,-300] km s^{-1}. We integrated the spectrum in that range, finding an integrated flux of 0.155 Jy km s^{-1}. This corresponds to a luminosity of 1.64×10^8 $L_\odot$. We computed the projected velocity, v_{98}, defined as the velocity at which the integrated flux of the high-velocity emission is 98% of their total integrated flux with respect to the systemic velocity, finding v_{98}=720 km s^{-1}.

Secondly, we fitted the [CII] line with two Gaussian components, in order to model the nar-

---

this does not affect our results or conclusions.

Table 3.5: Properties of [CII] line and outflow energetics of J0100+2802

Quantity	Units	Value
$(S\,\mathrm{d}v)_\mathrm{N}$	[Jy km s^{-1}]	2.39 ± 0.11
$\mathrm{FWHM_N}$	[km s^{-1}]	407 ± 10
$\mathrm{peak_N}$	[km s^{-1}]	27 ± 5
$(S\,\mathrm{d}v)_\mathrm{B}$	[Jy km s^{-1}]	0.78 ± 0.21
$\mathrm{FWHM_B}$	[km s^{-1}]	635 ± 20
$\mathrm{peak_B}$	[km s^{-1}]	-211 ± 57
$(S\,\mathrm{d}v)_\mathrm{tot}$	[Jy km s^{-1}]	3.17 ± 0.16
$L_\mathrm{[CII]}$	[$\mathrm{L}_\odot$]	3.36×10^9
v_out	[km s^{-1}]	560
$\dot{M}_\mathrm{out}$	[$\mathrm{M}_\odot$ yr^{-1}]	118-269
$\dot{E}_\mathrm{out}$	[10^{43} erg s^{-1}]	$(1.2 - 2.7)$
$\dot{P}_\mathrm{out}/\dot{P}_\mathrm{AGN}$		0.01-0.02

Notes. Subscript 'N' refers to the narrow component, 'B' to the broad component, 'tot' to the total [CII] emission line shown in Fig. 3.20. $L_\mathrm{[CII]}$ is computed from the total integrated flux. The results for the outflow energetics are reported under the purple line.

row and broader emission simultaneously, running the Markov chain Monte Carlo (MCMC) algorithm implemented in the `EMCEE` package (Foreman-Mackey et al., 2013) with 6 free parameters: mean peak frequency, peak value and FWHM for both the narrow and the broad component. We adopted uniform priors for all the parameters, ensuring that the mean peak frequencies of the narrow and the broad component do not overlap. We were able to disentangle the two components finding $\mathrm{FWHM_N} = 407 \pm 10$ km s^{-1}, $\mathrm{peak_N} = 27 \pm 5$ km s^{-1}, integrated flux $(S\,\mathrm{d}v)_\mathrm{N} = 2.39 \pm 0.11$ Jy km s^{-1} for the narrow component (shown as red dashed line), and $\mathrm{FWHM_B} = 635 \pm 20$ km s^{-1}, $\mathrm{peak_B} = -211 \pm 57$ km s^{-1} and integrated flux $(S\,\mathrm{d}v)_\mathrm{B} = 0.78 \pm 0.21$ Jy km s^{-1} for the broad one (shown as green dashed line). The total integrated flux of the line is indeed $(S\,\mathrm{d}v)_\mathrm{tot} = 3.17 \pm 0.16$ Jy km s^{-1}, corresponding to a luminosity of $L_\mathrm{[CII]} = 3.36 \times 10^9$ $\mathrm{L}_\odot$. The left panel of Fig. 3.20 shows the map of the high velocity component of [CII], obtained from collapsing the velocity channels $[-500, -1000]$ km s^{-1} from the continuum-subtracted cube[9] and overplotting the total [CII] emission map (black dashed line). Performing a 2D Gaussian fit we obtained a peak flux of 0.16 ± 0.02 mJy/beam, a flux density of 0.30 ± 0.07 mJy and a FWHM size of $(0.95 \pm 0.37) \times (0.71 \pm 0.46)$ arcsec^2 (that corresponds to $\sim 5.4 \times 4.0$ kpc^2), and offset by 0.3 arcsec ($\sim$ 1.7 kpc) towards the North-East, i.e. in a direction almost perpendicular to the plane of the interacting system.

We interpret such a broad [CII] wing as indication for a cold outflow, since velocities as high as 1000 km/s are unlikely associated with tidally stripped gas, especially given that, even more interestingly, it is elongated in the North-East direction similarly to the radio jet found by Sbarrato et al. (2021), suggesting that the outflow is likely jet-driven. Both the outflow

---

[9] We selected the velocity range $[-500, -1000]$ km s^{-1} in order not to be contaminated by the narrow component (that tends to zero at ~ -500 km s^{-1}), and since the broad component goes to zero at ~ -1000 km s^{-1}.

and the jet are aligned almost perpendicularly to the western extension (merger). Alternative interpretations of the broad wing could be inflowing gas or a fainter companion. However, the alignment with the radio jet, together with the high dispersion found for the broad component ($\mathrm{FWHM_B} = 635$ km s^{-1}) suggest that these interpretations are unlikely, and favour the outflow scenario. Indeed, the high dispersion would imply a very massive companion, that however remains undetected in JWST observations (Kashino et al., 2022; Eilers et al., 2022). The presence of only a blue component of the wing, may appear problematic in the context of simple bi-polar outflow models. However, asymmetric outflows have already been observed (Fluetsch et al., 2019; Bischetti et al., 2019b). Moreover, seeing the blueshifted [CII] component only can also be due to an high [CII] optical depth, which is often found in such gas rich and compact galaxies (P. P. Papadopoulos et al., 2010; Neri et al., 2014; Gullberg et al., 2015), and this would prevent us to see the redshifted component.

We computed the [CII] luminosity $L_{\mathrm{out}} = 8.27 \times 10^8$ L$_\odot$ of the outflowing gas, and an upper and lower limit for the outflow radius: $R_{\mathrm{min}} = 2.4$ kpc, $R_{\mathrm{max}} = 5.5$ kpc[10] . Assuming a $L_{\mathrm{[CII]}}$ to gas mass conversion as in PDR regions, the corresponding neutral gas mass in PDR can be derived using Eq. 3.2 (Hailey-Dunsheath et al., 2010; Bischetti et al., 2019a). This yields $M_{\mathrm{out}} = 1.1 \times 10^9$ M$_\odot$. Assuming the scenario of time-averaged expelled shells or clumps (Rupke, Veilleux, and D. B. Sanders, 2005), we computed the mass outflow rate as in Eq. 3.6 where $v_{\mathrm{out}} = |\Delta v_{\mathrm{broad}}| + \mathrm{FWHM_B}/2 = 560$ km s^{-1} and is $\Delta v_{\mathrm{broad}}$ is the velocity shift between the centroids of the narrow and the broad component. Considering the upper and lower limit for the outflow radius we have $118 < \dot{M}_{\mathrm{out}} < 269$ M$_\odot$ yr^{-1}. The average mass outflow rate is comparable to the SFR found for both the QSO's host galaxy and the companion. This may support a scenario in which the outflow is mostly driven by SF. Moreover, in simulations QSOs companions that are directly impacted by the outflow are found to have their SFR increased by a factor of 2-3, and tend to be more massive (Zana et al., 2022). Considering the SFR of the QSO's host, the mass outflow rate and the molecular gas mass of 5.4×10^9 M$_\odot$ found by F. Wang et al. (2019), we infer a depletion time of 10-13 Myr, which seems to imply a rapid quenching of the QSO's host galaxy. However, given that the outflow velocity is ~560 km/s, the evacuated gas may not escape the halo and eventually fall back on the host galaxy, triggering another phase of galaxy growth. Indeed the host galaxy of J0100+2802 is expected to experience a massive growth, since this QSO is already strongly off the local relation in the $M_{\mathrm{BH}} - M_{\mathrm{dyn}}$ plane (see Fig. 3 of Tripodi et al. 2023a), given the high BH mass. We also derived the kinetic power associated with the outflow as $\dot{E}_{\mathrm{out}} = \frac{1}{2}\dot{M}_{\mathrm{out}} \times v_{\mathrm{out}}^2 = (1.2 - 2.7) \times 10^{43}$erg s^{-1}, and the wind momentum load as in Eq. 3.7 where $\dot{P}_{\mathrm{AGN}}$ is the AGN radiation momentum rate, and where we adopted the bolometric luminosity of $L_{\mathrm{bol}} = 4.29 \times 10^{14}L_\odot$ estimated by Wu et al. (2015) from the luminosity at 3000 Å.

The results for the spectrum fitting and the outflow energetics are reported in Tab. 3.5.

---

[10] The upper and lower outflow radii are derived considering the uncertainties on the estimates of the FWHM size and the displacement between the peak of QSO emission and of the outflow emission, that is 0.3 arcsec~ 1.7 kpc.

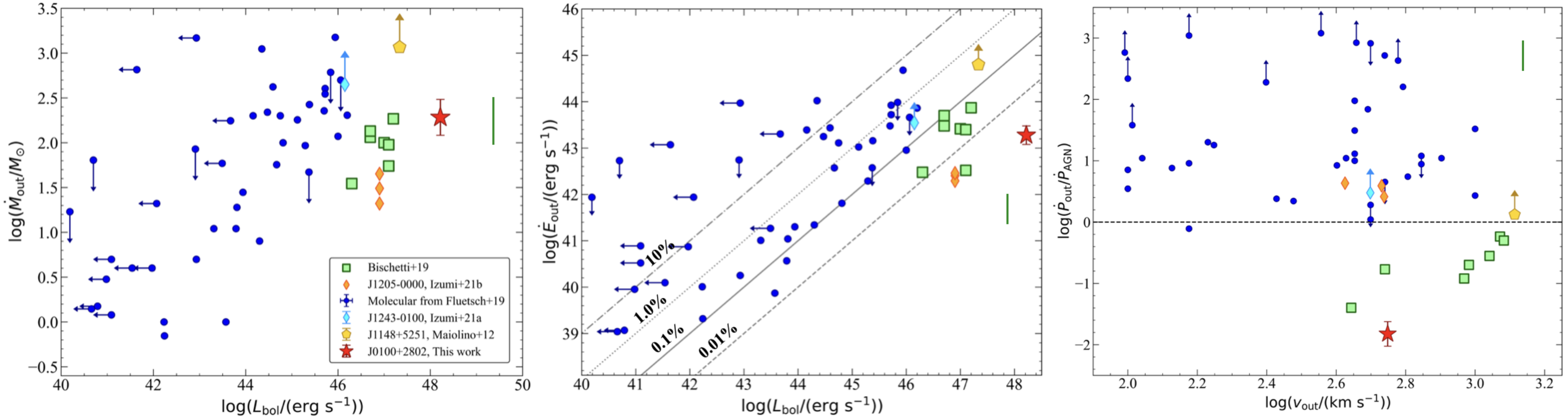

Figure 3.21: *Energetics for the outflow in J0100+2802 (red star) compared with different stacked spectra (hollow green squares, see legend; Bischetti et al. 2019b), [CII] outflows in QSO J1148+5251 at z=6.42 (gold pentagon, Maiolino et al., 2012), and in two QSOs at z=6.7 and z=7.07 belonging to the Subaru High-z Exploration of Low-luminosity Quasars (SHELLQs) sample (diamonds, Izumi et al., 2021b; Izumi et al., 2021a), molecular outflows in a sample of low-z AGNs (blue dots, Fluetsch et al., 2019). Left panel: mass outflow rate as a function of the bolometric luminosity. The typical* ~ 0.3dex *uncertainty on the outflow rate found in the sample of Bischetti et al. (2019b) is shown by the vertical green line The errorbars associated to the red stars marks the lower and upper limits found for J0100+2802, reported in Tab. 3.5. Central panel: Kinetic power as a function of the bolometric luminosity. The dot-dashed, dotted, solid and dashed lines indicate kinetic powers that are 10%, 1%, 0.1%, 0.01% of the bolometric luminosity. Right panel: momentum load factor as a function of the outflow velocity. The horizontal line corresponds to* $\dot{P}_{out} = \dot{P}_{AGN}$.

We also estimated these quantities using the luminosity and v_{98} from the first order approach and the upper and lower limits for the radius, $R_{\rm min} = 2.4$ kpc, $R_{\rm max} = 5.5$ kpc, obtaining $30 < \dot{M}_{\rm out} < 68\ {\rm M}_{\odot}\ {\rm yr}^{-1}$, $4.9 < \dot{E}_{\rm out} < 11.3 \times 10^{42}{\rm erg\ s}^{-1}$, and $0.002 < \dot{P}_{\rm AGN} < 0.006$. We consider these as lower limits for the outflow energetics. Since the double Gaussian analysis is the approach commonly used in literature to determine the outflow energetics at high-z (Maiolino et al., 2012; Stanley et al., 2019; Bischetti et al., 2019b), in the next paragraph, we will compare the results derived by that approach (i.e., double Gaussian fit, see Tab. 3.5) with the results found in the literature for [CII] outflows in high-z QSOs and molecular outflows in low-z AGNs.

In Fig. 3.21, we compare our results (red stars) with those of [CII] outflows in QSOs at $4.5 < z < 7.1$ from spectra stacking (Bischetti et al., 2019b), of [CII] outflows in QSO SDSS J1148+5251 (Maiolino et al., 2012; Cicone et al., 2015), in QSO HSC J1205-0000[11] and in QSO HSC J1243+0100 at z=7.07 belonging to the Subaru High-z Exploration of Low-luminosity Quasars (SHELLQs) sample (Izumi et al., 2021b; Izumi et al., 2021a). We found that the properties of our [CII] outflow are at the extreme end of the population for the mass outflow rate and the kinetic power. This is expected given the high luminosity of this QSO. The low momentum load factor suggests that the outflow is either energy-driven but with poor coupling with the host galaxy ISM, or is driven by direct radiation pressure onto the dusty clouds (e.g., Ishibashi, Fabian, and Maiolino, 2018; Bischetti et al., 2019b; Bischetti et al., 2019a). Either cases support the fact that the outflow cannot be effective in removing gas from the entire galaxy (Gabor and Bournaud, 2014; Costa, Sijacki, and Haehnelt, 2015; Costa et al., 2018; Bourne, Zubovas, and Nayakshin, 2015; Roos et al., 2015; Valentini, Simona Gallerani, and Ferrara, 2021).

3.3.5 Environment of J2310+1855

Since the observation in B6 of J2310+1855 was primarily designed to detect [CII] emission towards Serenity-18 (V. D'Odorico et al., 2018), we studied the field at the position of the line emitter. Serenity-18 is a candidate CO(6-5) emitter at a redshift $z = 5.9386$, associated with a proximate DLA system located at $z = 5.938646 \pm 0.000007$ on the QSO sightline. The frequency setup of this observation covers the [CII] emission line, expected at 273.9 GHz, and the sub-mm continuum of Serenity-18 (Fig. 3.22). At the position of Serenity-18 (RA, DEC=[23:10:38.44, 18:55:21.95]), we derived a 3σ upper limit on the 265 GHz dust continuum of $S_{\rm 265.4GHz} < 0.026$ mJy. Assuming a dust temperature of 40 K, an emissivity $\beta = 1.5$ (Sommovigo et al., 2021), and a source size equal to the clean beam size, this translates into an upper limit on the dust mass of $M_{\rm dust} < 6 \times 10^6\ {\rm M}_{\odot}$. For the [CII] emission line, we derived a 3σ upper limit of $S dv_{\rm [CII]} < 28.2$ mJy km s^{-1}, assuming a line width of 200 km s^{-1} (equal to the FWHM reported in V. D'Odorico et al. 2018). This implied an upper limit on the lumi-

---

[11] Note that Izumi et al. (2021a) also propose a merger as a possible interpretation for the broad component in J1205-0000.

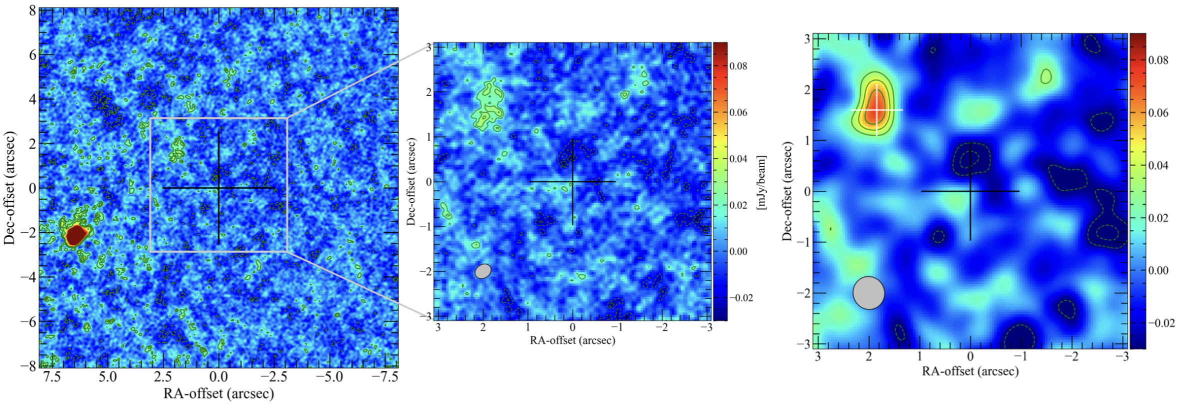

Figure 3.22: *Dust continuum maps of the QSO field with different resolutions. Left panel: dust continuum map of the QSO field centred on the phase-tracking centre of the observation. Levels are* $-3, -2, 2, 3,$ *and* 4σ, $\sigma = 8.8$ *μJy/beam. The cross indicates the phase centre. In this map the QSO is located at offset [6,-2] arcsec. Central panel: Zoomed view towards the phase centre. The clean beam is plotted in the lower left corner. Right panel: 260 GHz dust continuum uv-tapered map of Serenity-18 (levels* $-4, -3, -2, 2, 4,$ *and* 5σ, $\sigma = 15$ *μJy/beam). The imaging has been performed with* `uvtaper`*=[0.5 arcsec]. The clean beam is indicated in the lower left corner. The black cross indicates the position of the phase-tracking centre, which coincides with the expected position of the CO-emitter Serenity-18 (V. D'Odorico et al., 2018). The white cross indicates the continuum emitter detected in the beam (see text).*

nosity of the [CII] line of $L_{\rm [CII]} < 2.7 \times 10^7$ L$_\odot$. Adopting the SFR – $L_{\rm [CII]}$ correlation from Carniani et al. (2018), this yielded an upper-limit star formation rate of SFR < 2.5 M$_\odot$yr^{-1}. By applying the SFR – $L_{\rm [CII]}$ correlation found by Herrera-Camus et al. (2018) for star-forming main-sequence galaxies with normal star formation efficiency, we found a consistent upper limit of SFR < 3 M$_\odot$yr^{-1}. This upper limit on the SFR, together with the luminosity ratio of CO(6-5) and [CII], $R_{\rm CO-[CII]} > 15$, makes it unlikely that DLA J2310+1855 has a [CII]-emitting counterpart, suggesting that the line emitter Serenity-18 is most likely a foreground source at lower redshift, as discussed in V. D'Odorico et al. (2018).

We scanned the data cubes in each of the four spectral windows with the aim of searching for any additional line emitters within the ALMA beam. To do this, we used a detection threshold of S/N> 3 per spectral channel, and we required S/N> 3 at the peak position of each detected structure over at least 20 adjacent channels (i.e. $\Delta v \gtrsim 150$ km s^{-1}). We did not detect any sources other than those described above.

Another scan of the data cube did not reveal any line emitter at any position down to a luminosity $L_{\rm [CII]} = 2.7 \times 10^7$ L$_\odot$, assuming a typical line width of 200 km s^{-1}.

One continuum emitter was detected at the 4σ significance level at position (RA, DEC) = (23:10:38.57, +18:55:23.55) (Fig. 3.22) after we had downgraded the resolution of our observation applying `uvtaper`=[0.5 arcsec] within `tclean`. We obtained a clean beam of 0.65×0.62 arcsec^2 for the continuum map. The distribution of this structure is spatially resolved with a size of $(0.918 \times 0.125) \pm (0.194 \times 0.111)$ arcsec^2 and a flux of 0.137 ± 0.015 mJy, estimated from a 2D Gaussian fit. Another scan of the data cube yielded no additional

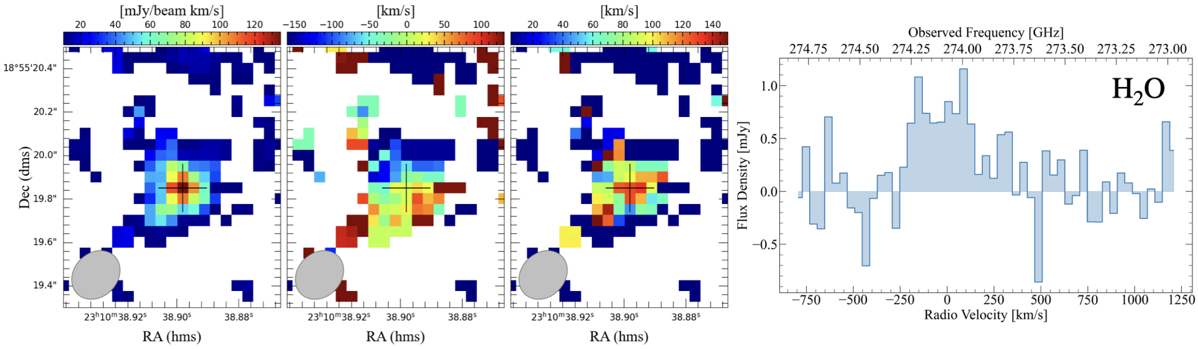

Figure 3.23: *Moment maps of the line detected at 274.084 GHz, identified as the H_2O v=0 3(2,2)-3(1,3) of J2310+1855. From left to right: integrated flux, mean velocity map, and velocity dispersion map, continuum-subtracted spectrum of H_2O . The clean beam is plotted in the lower right or left corner of the moment maps. The cross indicates the peak position of the integrated flux for each line. The spectrum has been extracted from the region included within* $\geq 2\sigma$ *in the velocity integrated map and it has been re-binned to 40 km* s^{-1}.

continuum or line emitters in the field above the detection threshold of S/N> 1 per channel.

This led us to conclude that the QSO J2310+1855 does not show any evidence of companions, interaction, or merger at least on scales of ~ 50 kpc. Other observations suggested that 20-50% of QSOs show mergers or close companions, independent of their luminosity (Decarli et al., 2018; B. P. Venemans et al., 2020; Neeleman et al., 2021). In a recent cosmological simulation of a $z \sim 6$ QSO, Zana et al. (2022) computed the number of companions associated with a QSO. Based on their results, we would expect to detect three companions with $L_{\rm [CII]} \sim 10^8$ $L_\odot$ within 250 kpc from the QSO, and seven companions with $L_{\rm [CII]} = 2.7 \times 10^7$ $L_\odot$ in approximately the same region.

3.4 Water vapour resolved emission

Analysing the Band 6 ALMA observation of J2310+1855, we detected an emission line at a sky frequency of 274.074 GHz towards the QSO position with a statistical significance of 10σ and an integrated flux of $S_\nu dv = 0.36 \pm 0.01$ mJy km s^{-1}. The emission appears to be spatially resolved with size of 1.94 × 1.12 kpc^2. We identified it as the H_2O v=0 $3_{(2,2)} - 3_{(1,3)}$ transition at rest frequency 1919.359 GHz, and derived a $z_{\rm H_2O} = 6.0031 \pm 0.0006$, consistent with the [CII] redshift of the QSO. Water vapour emission traces the molecular warm dense phase of the interstellar medium (L. Liu et al., 2017), and is detected in only a few QSOs at z>6 (Pensabene et al., 2021; Lehnert et al., 2020; J. Yang et al., 2019).

Fig. 3.23 shows the moment maps of this emission line, obtained through natural weighting to maximise sensitivity, and the line profile. A velocity gradient is detected along a PA that appears to be consistent with that detected in the [CII] line. This is the first time that the emission is spatially resolved and consistent with a rotating water vapour disk. We estimated a first-order dynamical mass using H_2O. Adopting the same inclination as for the [CII] disk, i

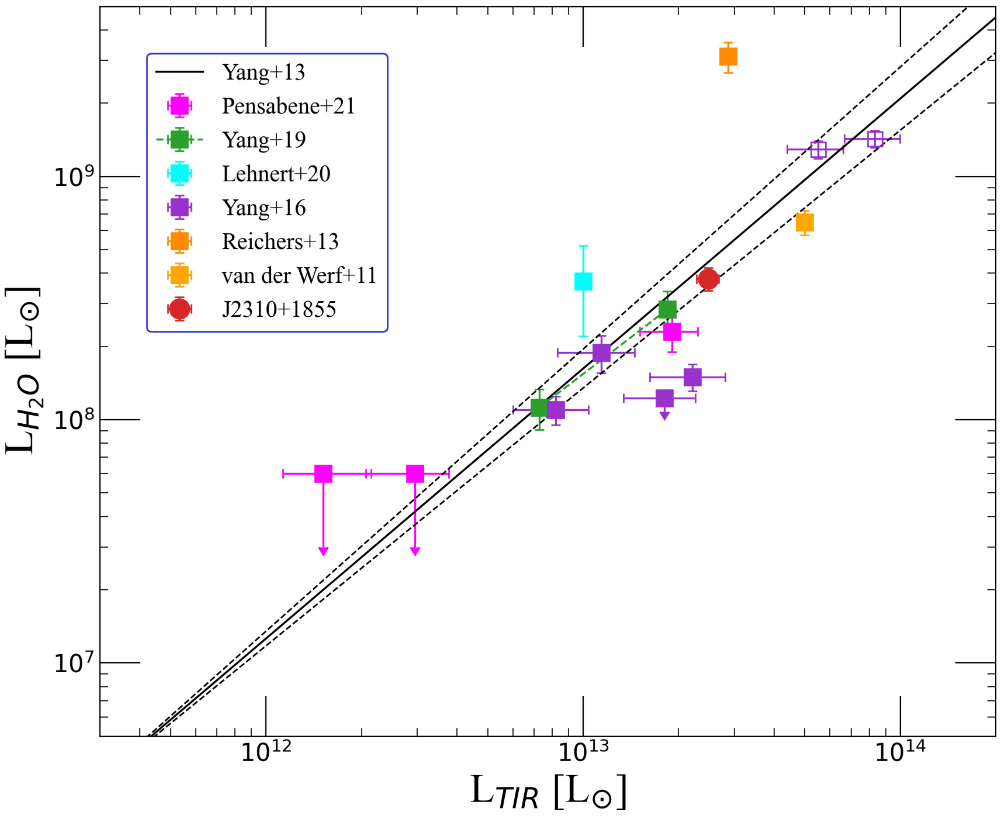

Figure 3.24: *$L_{\mathrm{H_2O}} - L_{\mathrm{TIR}}$ relation for QSO J2310+1855 and a compilation of high-redshift QSOs and SMGs with H_2O detection. The solid black line traces the best power-law fit from C. Yang et al., 2013. The dashed lines are the 1σ confidence limit.*

= 25 deg, we derived $M_{\mathrm{dyn,H_2O}} = 1.16 \times 10^5 (0.75 \times \mathrm{FWHM_{H_2O}})^2 \times D/\sin^2(i) = 6.4 \times 10^{10}$ M$_\odot$, with $\mathrm{FWHM_{H_2O}}$ = 340 km s^{-1} and D = 1.5 kpc (averaged source size in kiloparsecs).

An alternative scenario for the identification of this line would be the [CII] line from the DLA J2310+1855 located at z=5.938646 (V. D'Odorico et al., 2018). If the DLA had a line-emitting counterpart on the QSO sightline, its [CII] emission would happen at 273.906 GHz, which is also consistent with the observed line frequency. However, because the velocity gradient, the FWHM of the line, and the dynamical mass are consistent with those derived from [CII] for the QSO's host galaxy, we discard this scenario and conclude that this line is due to H_2O from the ISM of the QSO's host galaxy and not to [CII] from the proximate DLA.

In Fig. 3.24 we compare the H_2O $3_{22} - 3_{13}$ line luminosity with the total IR luminosity of J2310+1855 obtained through the fit of the dust SED (MBB component only, see Chap. 4.3), together with a compilation of $z \sim 2.5 - 3.5$ Hy/ULIRGs from C. Yang et al. (2016), APM 08279+5255 at $z \simeq 3.9$ (Paul P. van der Werf et al., 2011), the $z \simeq 6.34$ SMG HFLS 3 (Riechers et al., 2013), the QSO's host galaxy J0439+1634 at $z \simeq 6.5$ (J. Yang et al., 2019), QSO BR1202-0725 at $z = 4.695$ (Lehnert et al., 2020), and two QSO's host galaxies at $z > 6$ PJ231-20 and PJ308-21 (Pensabene et al., 2021), which all have a H_2O $3_{21} - 3_{12}$ detection, except for the one of Lehnert et al. (2020), which has H_2O $2_{20} - 2_{11}$. We also show the best power-law fit found by C. Yang et al. (2013) with 1σ confidence limits, $L_{\mathrm{H_2O}} \propto L_{\mathrm{TIR}}^{1.1\pm0.5}$. Our result for J2310+1855 agrees well with the increasing trend of the data and the linear relation of C. Yang et al. (2013). We note that when the contribution of the hot dust heated by the QSO is implied, it would imply $L_{\rm TIR} = 8.4 \times 10^{13}\ {\rm L}_{\odot}$, and would move J2310+1855 well below the correlation. These data suggest that the H_2O line is mainly excited by IR-pumping mechanism of the dust-reprocessed UV radiation field in the ISM of the host galaxy (C. Yang et al., 2013; C. Yang et al., 2016; Pensabene et al., 2021).

3.5 Brief summary

In this chapter, we investigated the properties of the cold gas in a sample of QSOs at $z \gtrsim 6$, analysing the [CII], H_2O, CO(6-5) and/or CO(7-6) line emissions. Here I briefly summarize our main findings.

- From the analysis of the CO(6-5) emission line of QSOs J1007+2115, J1319+0950, J2054-0005, J0129-0035 and of the CO(7-6) of J0224-4711, we aimed at estimating the molecular gas mass of these QSOs with the smallest statistical uncertainties. To achieve this, we leveraged the observed CO SLED in QSOs at comparable redshifts that either had detected low-J transitions or upper limits. Since the CO(6-5)-to-(1-0) integrated flux ratio is approximately constant in $z \gtrsim 6$ QSOs and that the CO SLED is quite flat between CO(6-5) and CO(7-6), we assumed a common scaling for all the sources. We used the conversion factor commonly adopted for high-z QSOs, $\alpha_{\rm CO} = 0.8\ {\rm M}_\odot({\rm K\ km\ s^{-1}\ pc^{-2}})^{-1}$. It follows that our assumptions introduce significant systematic uncertainties into the determination of the molecular gas mass, as the conversion factor is not known a priori. We found on average $M_{\rm H_2,CO} \sim 10^{10}\ {\rm M}_\odot$ in agreement with the gas masses commonly found for high-z QSOs. Notably, the detection of CO(6-5) and CO(7-6) reported here for J1007+2115 is the highest-redshift measurement of the cold and dense molecular gas to date.
- New ALMA observations of the [CII] emission line and of the continuum emission in Band 6 and Band 3 of the QSO J0100+2802 revealed a new interesting picture for the most luminous QSO at $z > 6$. We found an interactive companion and high-velocity cold outflow that were undetected by previous higher resolution observations and by JWST-NIRCam imaging. The [CII] emission and its underlying continuum are elongated in the East-West direction with multiple peaks, and the [CII] channel maps show even more clearly a clumpy morphology and a tidal tale. These, together with the enhanced [CII] velocity dispersion along the direction of the elongation, support the scenario in which the companion is merging with the QSO-host. We derived a range for the SFR of the companion given also the upper-limit in Band 9, yielding SFR$\sim$ [35 – 344] $\rm M_\odot yr^{-1}$. From the analysis of the outflow in the [CII] spectrum, we obtained a mass outflow rate of $\dot{M}_{\rm out} = (118 - 269)\ {\rm M}_\odot\ {\rm yr}^{-1}$ considering that the outflow emission is resolved with a size of $\sim 5.4 \times 4.0\ {\rm kpc}^2$. Computing the outflow energetics, we concluded that the outflow cannot be very effecting in removing the gas from the galaxy. These results stress the importance of deep low-resolution ALMA observations for the study of QSOs at the EoR.
- We presented results derived from an extensive ALMA observation featuring high-resolution (900 pc) imaging of the sub-mm continuum, [CII], and H2O emission lines in conjunction with multiple archival ALMA datasets for probing the infrared continuum

emissions of the $z \sim 6$ QSO J2310+1855. This high-resolution dataset facilitated a comprehensive analysis of dust properties and the kinematics and dynamics of cold gas. In our investigation, SDSS J2310+18655 exhibited indications of a [CII] outflow, located in the central kpc, with an outflow mass of $M\mathrm{out} = 3.5 \times 10^8$ M$_\odot$. The energetics of this outflow align with the scaling relations for ionized winds and agrees with expectations for momentum-conserving winds, comparing with the scaling relations derived by Fiore et al. (2017). Comparing the surface brightness profiles of the continuum, [CII] and CO(6-5), we found that the dust ($r \sim 6.7$ kpc) is more extended than [CII] ($r \sim 5$ kpc) and CO ($r \sim 4.7$ kpc), whereas it is more peaked at the centre. A similar behaviour with a steeper dust continuum distribution is seen in other high-z QSOs and has been attributed to the contribution of the QSO to the dust heating. For the first time, we were able to map a spatially resolved H_2O v=0 $3_{(2,2)} - 3_{(1,3)}$ emission line at $\nu_{\rm obs} = 274.074$ GHz at a statistical significance of 10σ. Its emission is consistent with a water vapour disk whose kinematics agrees with the [CII] disk.Furthermore, this observation allowed for an exploration of J2310+1855's environment, including a search for line emitters. No line emitter was detected down to a 3σ upper limit of $L_{\rm [CII]} < 2.7 \times 10^7$ L$_\odot$, or SFR < 2.5 M$_\odot$yr^{-1}. We also note that the proximate DLA J2310+1855 did not show any line-emitting counterpart down to this limit, and therefore, the line emitter reported in V. D'Odorico et al. (2018), called Serenity-18, is most likely a lower-z interloper. In the continuum data, we found a low-significance (4σ) continuum emitter located 4 arcsec offset from the QSO position, whose physical association with the QSO remains to be confirmed. This led us to conclude that J2310+1855 does not show any evidence of companions, interaction, or merger at least on scales of ~ 50 kpc. This is a interesting scenario, since observations suggested that 20-50% of QSOs show mergers or close companions, independent of their luminosity.

- We performed a detailed and refined kinematical and dynamical study of the [CII] emission of J2310+1855. Our dynamical analysis suggests the presence of a central compact mass component in J2310+1855, which is composed by a SMBH and a stellar bulge having similar masses of the order of $\sim 1.7 \times 10^{10}$ M$_\odot$. We discussed different mechanisms of bulge formation (disc instabilities, major mergers, SF in AGN driven outflows, direct dissipative collapse), also comparing with galaxy simulations. For J2310+1855, disc instabilities can be likely ruled out because such secular processes occur on long timescales (~3-5 Gyr) while the age of the Universe at $z \simeq 6$ is only ~900 Myr in the adopted cosmology. All the other mechanisms, instead, appear viable. To end up on the local $M_{\rm SMBH} - M_{\rm bulge}$ relation, the bulge mass should increase by a factor of ~40 from $z = 6$ to 0, while the SMBH mass should grow at most by a factor of 4, pointing to asynchronous galaxy-BH co-evolution. A robust interpretation of our results is strongly dependent on the accuracy of the determination of the physical quantities at play. This is why higher resolution observations are required to validate our scenario.

CHAPTER 4

ACCURATE STUDY OF COLD DUST PROPERTIES AND STAR FORMATION RATE

In this chapter, I present results for the dust properties and SFR for 11 out to 12 QSOs in our sample[1]. In Sect. 4.1, I will briefly introduce the study of dust in high-z QSOs, and I will report the properties and results of the continuum observations used in this work. In Sect. 4.2, I will illustrate the model adopted to fit the SEDs, and in Sect. 4.3 I will report the analysis of the cold dust SEDs of QSOs J2310+1855, J0100+2802, J036+03, J0224-4711, J231-20, and J2054-0005, that enabled us to estimate the dust properties and SFR of their host galaxies precisely. In Sect. 4.3.3, I will show the analyses of the cold dust SEDs of J1007+2115 and of the companion of J0100+2802 based on the few ALMA and/or NOEMA observations available, that allowed us to derive rough estimates for the dust mass and SFR of these sources. Finally, in Sect. 4.4, I will illustrate our final sample, consisting of 10 QSOs at $z \gtrsim 6$, for which we derived precise estimates for the dust parameters and SFR, and I will provide context for our findings by drawing comparisons with observations in sources at lower redshifts.

This chapter is based, with limited modifications, on the published papers Tripodi et al. (2022); Tripodi et al. (2023a); Feruglio et al. (2023); Tripodi et al. (2023c), and Tripodi in prep.

4.1 Continuum emission of QSOs in the mm/sub-mm regime

In the past decade, observations using, for instance, the instruments on *Herschel*, NOEMA, and ALMA have detected the dust continuum in the host galaxies of many $z \sim 6$ QSOs, with far-IR (FIR) luminosities of 10^{11-13} $L_\odot$ and dust masses of about 10^{7-9} $M_\odot$ (Decarli et al.,

---

[1] The analysis of the SED of J0129-0035 is currently work in progress. In any case, the derived dust properties and SFR will be uncertain, since there are not any high-frequency (band 8,9 or 10) observations available for this source.

2018; Carniani et al., 2019; Shao et al., 2019). The rest-frame FIR continuum emission in these sources originates from dust heated by the ultraviolet (UV) radiation from young and massive stars in the host galaxies and the QSO radiation field. It is often hard to determine the temperature and mass of the dust precisely since they are both highly degenerate and the FIR SED is sparsely probed, often relying on single-frequency continuum detection. However, if multi-frequency ALMA observations are available in the FIR, it is possible to constrain the dust temperature and mass with statistical uncertainties $< 10\%$ (see e.g. Carniani et al. 2019), implying a high accuracy in the determination of the SFR. An accurate estimate of the dust mass would also allow us to derive the molecular gas mass of the host galaxy through the GDR. Although it is possible to directly probe the molecular reservoirs of the QSO's host galaxies using the rotational transitions of the CO (e.g. L. Vallini et al. 2018; Madden et al. 2020), very few high-z QSOs are observed in CO because this emission line is typically faint at high z. The GDR indeed has often been assumed in order to compute the gas mass, implying an high degree of uncertainty in its estimate. Studies of $z \sim 2.4 - 4.7$ hyper-luminous QSOs show that the GDR spans a broad range of values, [100-300], with an average GDR $\sim$ 180 (Bischetti et al., 2021), consistent with the results found for sub-millimetre galaxies out to $z \sim 3 - 5$ with GDR$\sim 150 - 250$ (e.g. Saintonge et al. 2013; Miettinen et al. 2017). In low-z galaxies, a GDR$\sim$ 100 is typically observed (Draine et al., 2007; Leroy et al., 2011), implying that the GDR increases with redshift. However, if we are able to derive a reliable estimate of the gas mass from CO, this could be used, together with the accurate estimate for the dust mass, to determine the GDR instead of assuming it, and to use it for other high-z QSOs.

4.1.1 Results

Figure 4.1 shows the 260 GHz dust continuum map of J2310+1855 obtained through natural weighting. The continuum shows resolved emission with an approximate size of 1.5 arcsec across, corresponding to 8.7 kpc at the rest frame. This is the underlying continuum of the [CII] emission presented in Chap. 3.3.1, and whose surface brightness profile is reported in Chap. 3.3.1. Using a 2D Gaussian fit, we derived a flux density of 6.43 ± 0.16 mJy, 30% lower than the value reported by Shao et al. (2019) from lower-resolution data, and a FWHM size of 0.22×0.19 arcsec^2, corresponding to 1.3×1.1 kpc^2 at the QSO redshift. We note, however, that the Gaussian 2D fitting procedure fails to fit the surface brightness distribution and shows strong residual flux. Integrating the flux in the map over the region with $> 2\sigma$, we derived a flux density of 7.12 ± 0.2 mJy. This flux density is still lower than that reported previously by Shao et al. (2019), meaning that the high-resolution data miss about 25% of the flux. Measurement of the flux density at lower resolution, with a 2D Gaussian fit, indeed led to a value of 8.81 ± 0.13 mJy, which is in agreement with the measurement reported by Shao et al. (2019). To be conservative, we therefore used the flux density from lower resolution observation to study the dust continuum SED (see Sect. 4.3.1). Table 4.2 reports the continuum data from a reanalysis of ALMA archival data and Herschel data from Shao et al. (2019).

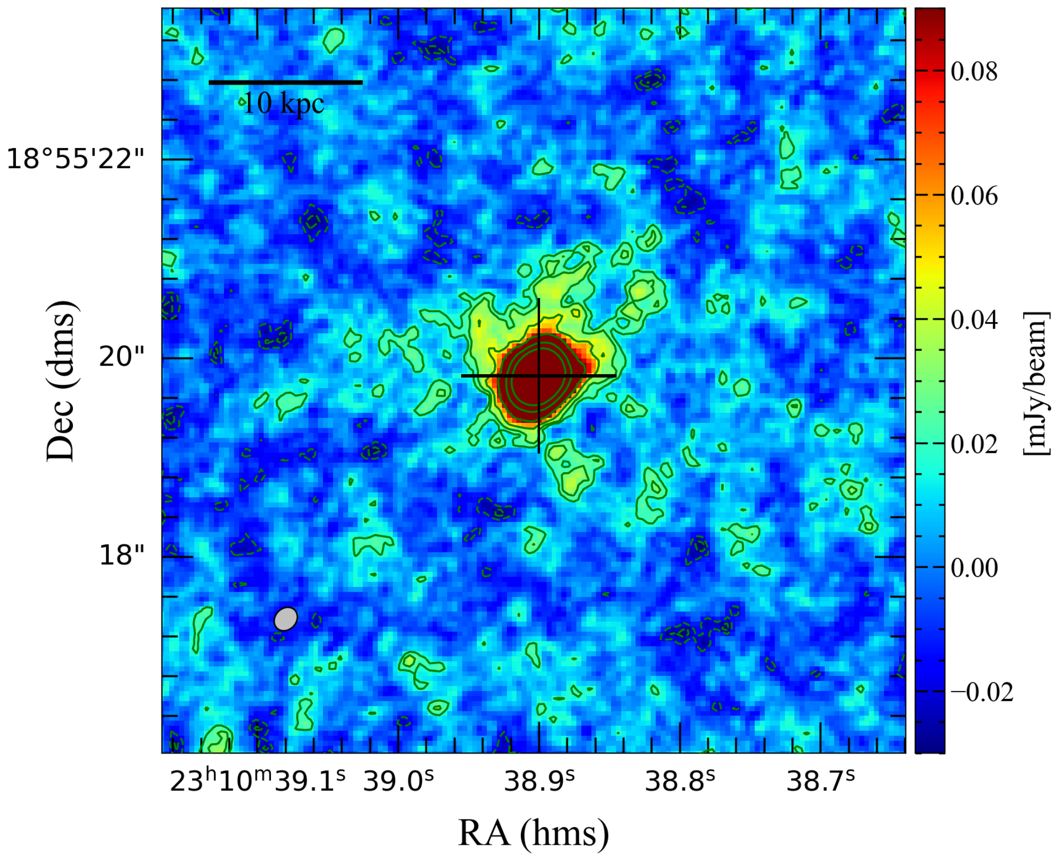

Figure 4.1: *260 GHz dust continuum map of QSO J2310+1855 (levels* $-4, -3, -2, 2, 3, 5, 10, 25,$ *and* 50σ*,* $\sigma = 9.15$ *μJy/beam). The clean beam* (0.26×0.21 arcsec^2*) is indicated in the lower left corner of the diagram. The cross indicates the position of the continuum peak.*

Figure 4.2 presents the 670.9 GHz continuum emission map of J0100+2802. The peak flux density is 6.99 ± 0.71 mJy/beam. The source is not spatially resolved. We checked that the other FIR and radio flux measurements were extracted from a region similar to our resolution. F. Wang et al. (2019) used tapered maps at 1.5 arcsec in order not to miss the fainter extended emission. Y. Liu et al. (2022) also tapered their 6 and 10 GHz maps, that had a resolution of ∼ 1.5 arcsec, to match the resolution of the 1.5 GHz map (∼ 4 arcsec), and they do not find significant differences in flux density between the tapered and the full-resolution maps.

Left and right panels of Fig. 4.3 show the continuum emission at 404.9 GHz and 670.9 GHz of J036+03, respectively. Both emission are not spatially resolved, therefore we considered the peak flux as total flux of the source, that is 6.63 ± 0.39 mJy/beam at 404.9 GHz and 5.60 ± 0.69 mJy/beam at 670.9 GHz. The emission at 670.9 GHz presents a secondary peak at RA,DEC=[-1.5,-1.5], that is likely an artefact due to the low resolution of the B9 observation. This interpretation is supported by the absence of line and continuum emission at the same spatial position in all lower frequency observations, and by the presence of another less bright peak located symmetrically with respect to the QSO position (RA,DEC=[1.0,-1.5]).

We analysed the other three ALMA observations available in B6 and B7, and we derived

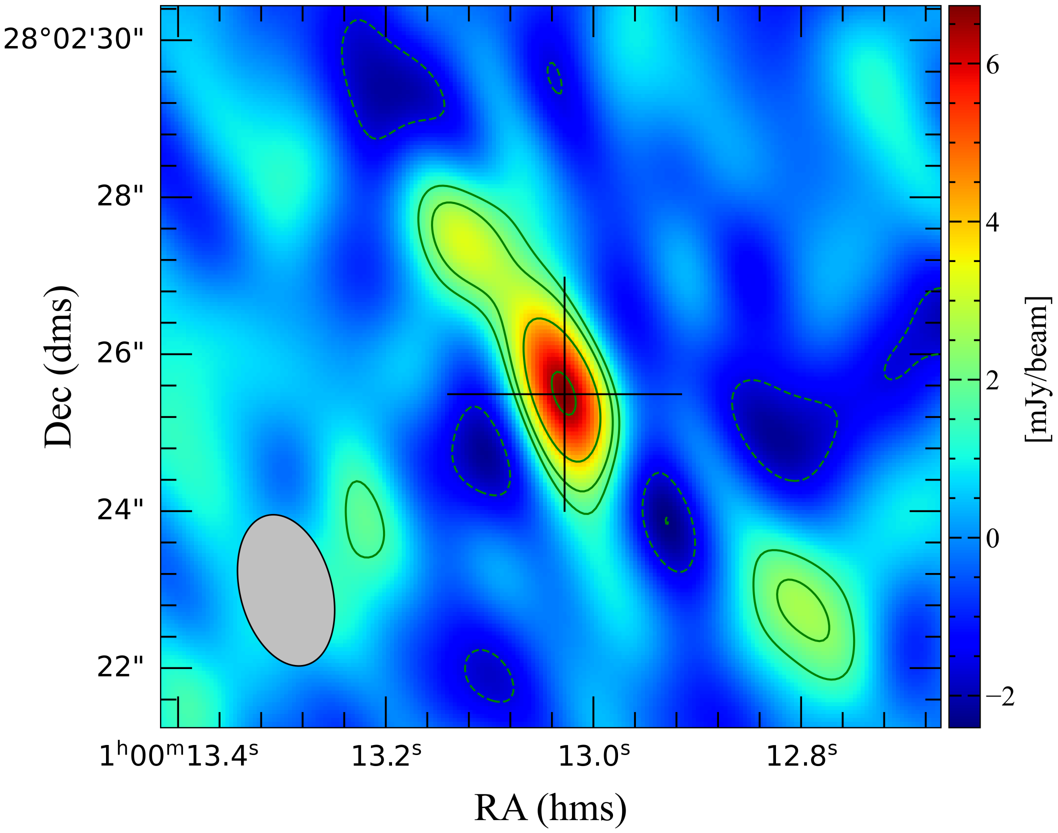

Figure 4.2: *670.9 GHz dust continuum map of QSO J0100+2802 (levels* $-3, -2, 2, 3, 5,$ *and* 8σ*,* $\sigma = 0.8$ *mJy/beam). The clean beam (*1.97×1.17 arcsec^2*) is indicated in the lower left corner of the diagram. The cross indicates the position of the continuum peak.*

continuum flux densities and sizes at 243.11 GHz, 260.53 GHz and 338.71 GHz, performing a 2D Gaussian fit with CASA for each observation. All continuum emissions at these frequencies are spatially resolved and the values for flux densities, peak fluxes and sizes are reported in Tab. 4.1.

In order not to miss the fainter and more extended flux, we tapered the higher resolution observations at 243.1 GHz and 260.5 GHz, performing the imaging with `uvtaper`=[0.9 arcsec], reaching a resolution of $\sim 0.7 \times 0.7$ arcsec^2 and of $\sim 0.88 \times 0.83$ arcsec^2 respectively. The sources in the tapered maps were fitted with the CASA 2D Gaussian fit, and the new continuum fluxes are reported in bold within brackets in Tab. 4.1. In one case, the higher resolution observation missed $\sim 20\%$ of the flux. Similar flux losses were also seen by F. Wang et al. (2019) when analysing high resolution observations of QSO J0100+2802. We checked that there was no further flux gain if tapering at even lower resolution.

Left and right panels of Fig. 4.4 show the continuum emission at 405.2 GHz and 670.9 GHz of J0224-4711, respectively. Both emission are not spatially resolved, therefore we consider the peak flux as total flux of the source, which are 8.73 ± 0.38 mJy/beam at 405.2 GHz and 19.9 ± 0.96 mJy/beam at 670.9 GHz.

We analysed the other three ALMA observations available in B3 and B6, and we derived

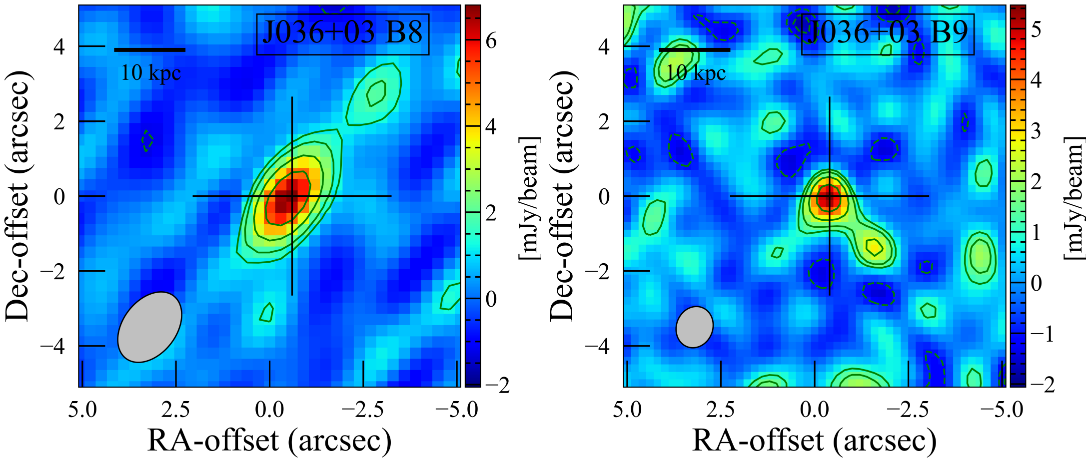

Figure 4.3: *Left panel: 404.9 GHz dust continuum map of QSO J036+03 (levels* $-3, -2, 2, 3, 5,$ *and* 8σ, $\sigma = 0.6$ *mJy/beam). The clean beam* (2.10×1.43 arcsec^2, *PA=37.40°) is indicated in the lower left corner of the diagram. The cross indicates the position of the continuum peak. Right panel: 670.9 GHz dust continuum map of QSO J036+03 (levels* $-3, -2, 2, 3, 5,$ *and* 8σ, $\sigma = 0.5$ *mJy/beam). The clean beam* (1.12×0.97 arcsec^2, *PA=21.11°) is indicated in the lower left corner of the diagram. The cross indicates the position of the continuum peak.*

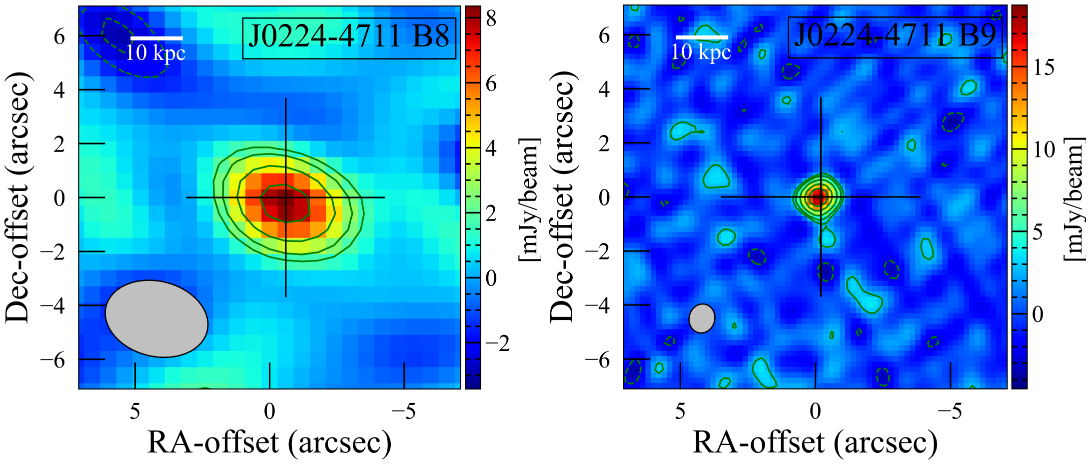

Figure 4.4: *Left panel: 405.2 GHz dust continuum map of QSO J0224-4711 (levels* $-3, -2, 2, 3, 5,$ *and* 8σ, $\sigma = 0.88$ *mJy/beam). The clean beam* (3.87×2.79 arcsec^2, *PA=-76.45°) is indicated in the lower left corner of the diagram. The cross indicates the position of the continuum peak. Right panel: 670.9 GHz dust continuum map of QSO J0224-4711 (levels* $-3, -2, 2, 3, 5, 8,$ *and* 11σ, $\sigma = 1.3$ *mJy/beam). The clean beam* (1.08×0.95 arcsec^2, *PA=14.05°) is indicated in the lower left corner of the diagram. The cross indicates the position of the continuum peak.*

Table 4.1: Continuum emission at different frequencies for J0100+2802, J036+03, J0224-4711, J231-20 and J2054-0005

QSO	Obs freq (GHz)	Beam cont [arcsec^2]	r.m.s. cont [mJy/beam]	Flux density [mJy]	Peak flux [mJy]	Size [arcsec^2]	Size [kpc^2]	Refs
J0100+2802	670.9	1.97 × 1.17	0.8	6.99 ± 0.71	6.99 ± 0.71	–	–	TP
J036+03	106.97	6.1 × 3.5	0.038	0.13 ± 0.02	–	–	–	[1]
	243.11	0.12 × 0.08	0.007	2.05 ± 0.1 (**2.43 ± 0.06**)	0.54 ± 0.02 (**2.22 ± 0.03**)	0.17 × 0.14	0.94 × 0.78	TP
	260.53	0.18 × 0.17	0.01	2.84 ± 0.13 (**2.95 ± 0.03**)	1.28 ± 0.04 (**2.71 ± 0.01**)	0.22 × 0.18	1.22 × 1.00	TP, [2]
	338.71	0.77 × 0.54	0.03	5.54 ± 0.05	4.69 ± 0.03	0.31 × 0.22	1.72 × 1.22	TP
	404.99	2.10 × 1.43	0.60	6.63 ± 0.39	6.63 ± 0.39	–	–	TP
	670.92	1.12 × 0.97	0.50	5.60 ± 0.69	5.60 ± 0.69	–	–	TP
J0224-4711	95.33	3.95 × 2.32	0.016	0.094 ± 0.010	0.094 ± 0.010	–	–	TP
	245.67	0.56 × 0.56	0.024	2.03 ± 0.05	1.49 ± 0.02	0.35 × 0.33	1.95 × 1.84	TP
	260.51	0.13 × 0.11	0.013	3.01 ± 0.25	0.80 ± 0.05	0.20 × 0.18	1.11 × 1.00	TP
	405.19	3.87 × 2.79	0.88	8.73 ± 0.38	8.73 ± 0.38	–	–	TP
	670.96	1.08 × 0.95	1.3	19.9 ± 0.96	19.9 ± 0.96	–	–	TP
J231-20	406.848	4.35 × 2.90	0.50	8.43 ± 0.39 6.74 ± 0.31$^{(a)}$	8.43 ± 0.39	–	–	TP
J2054-0005	92.26	0.42 × 0.32	0.006	0.082 ± 0.009	0.066 ± 0.004	0.27 × 0.07	1.57 × 0.41	TP
	262.6	0.33 × 0.29	0.019	2.82 ± 0.06 (**2.93 ± 0.07**)	2.17 ± 0.03 (**2.74 ± 0.04**)	0.19 × 0.15	1.10 × 0.87	TP
	263.93	1.23 × 1.12	0.010	3.08 ± 0.03	2.90 ± 0.02	0.33 × 0.23	1.92 × 1.34	TP
	488.31	0.43 × 0.37	0.064	11.32 ± 0.25 (**11.71 ± 0.11**)	9.05 ± 0.12 (**10.77 ± 0.06**)	0.24 × 0.15	1.39 × 0.87	TP
	674.97	0.65 × 0.57	0.50	9.87 ± 0.94	8.25 ± 0.48	0.29 × 0.24	1.68 × 1.39	TP

Notes. Columns: (1) Target QSO; (2) observed frequency of the continuum emission; (3) clean beam of the continuum map; (4) r.m.s of the continuum map; (5) flux density of the continuum emission at the nominal resolution of the observation and at a tapered resolution when necessary (in bold and brackets); (6) peak flux of the continuum emission at the nominal resolution of the observation and at a tapered resolution when necessary (in bold and brackets); (7) size in arcsec^2 of the resolved continuum emission; (8) size in kpc^2 of the resolved continuum emission; (9) References: This paper (TP); [1] Decarli et al. (2022); [2] B. P. Venemans et al. (2020). $^{(a)}$: flux corrected for the contribution of the companion to the QSO emission.

continuum flux densities and sizes at 95.33 GHz, 245.67 GHz, and 260.51 GHz, performing a 2D Gaussian fit with CASA for each observation. The two B6 continuum emissions are spatially resolved and the values for flux densities, peak fluxes and sizes are reported in Tab. 4.1. The emission in B3 is not resolved (see left panel of Fig. 3.2), therefore we considered the peak flux as total flux of the source, which is 0.103 ± 0.009 mJy/beam, analogously to B8 and B9.

In order not to miss the fainter and more extended flux, we tapered the higher resolution observations at 245.67 GHz and 260.51 GHz, performing the imaging with `uvtaper`=[0.7 arcsec], reaching a resolution of $\sim 0.7 \times 0.7$ arcsec^2. The sources in the tapered maps were fitted with the CASA 2D Gaussian fit, and we found no gain in flux even when tapering both observations at even lower resolution.

Regarding J231-20, it was found to have a close companion detected in multiple emission lines and in the continuum emission from ~ 100 GHz up to ~ 250 GHz at a distance of ~ 2 arcsec from the QSO (Pensabene et al., 2021; Decarli et al., 2017; Neeleman et al., 2019). Pensabene et al. (2021) were able to disentangle the continuum emission of the QSO from that of the companion using ~ 1 arcsec resolution ALMA observations. Unfortunately, the low resolution of the new Band 8 observation (beam of 4.3×2.9 arcsec^2) did not allow us to distinguish the two emissions. Performing a 2D fit with CASA on the continuum map, we found a peak flux of 8.43 ± 0.39 mJy/beam and the source was unresolved. The B8 flux is indeed contaminated by the continuum emission of the companion, thus this can bias the SED fitting and the determination of the dust properties. We correct for the companion contribution using the results found by Pensabene et al. (2021). Looking at their SED modelling, the flux of the companion at ~ 400 GHz is $\gtrsim$0.6 dex lower than that of the QSO. Conservatively considering the highest temperature model for the companion, i.e. that the flux of the companion is 0.6 dex lower than that of the QSO, we can correct our flux in Band 8 obtaining 6.74±0.31, which is a lower limit to the flux of the QSO.

4.2 Cold dust spectral energy distribution modeling

Following Carniani et al., 2019, we modelled the SED of the cold dust emission with a modified black-body (MBB) function given by

$$S^{\rm obs}_{\nu_{\rm obs}} = S^{\rm obs}_{\nu/(1+z)} = \frac{\Omega}{(1+z)^3}[B_\nu(T_{\rm dust}(z)) - B_\nu(T_{\rm CMB}(z))](1-e^{-\tau_\nu}), \tag{4.1}$$

where $\Omega = (1+z)^4 A_{\rm gal} D_{\rm L}^{-2}$ is the solid angle with $A_{\rm gal}$, and $D_{\rm L}$ is the surface area and luminosity distance of the galaxy, respectively. The dust optical depth is

$$\tau_\nu = \frac{M_{\rm dust}}{A_{\rm galaxy}} k_0 \left(\frac{\nu}{\nu_0}\right)^\beta, \tag{4.2}$$

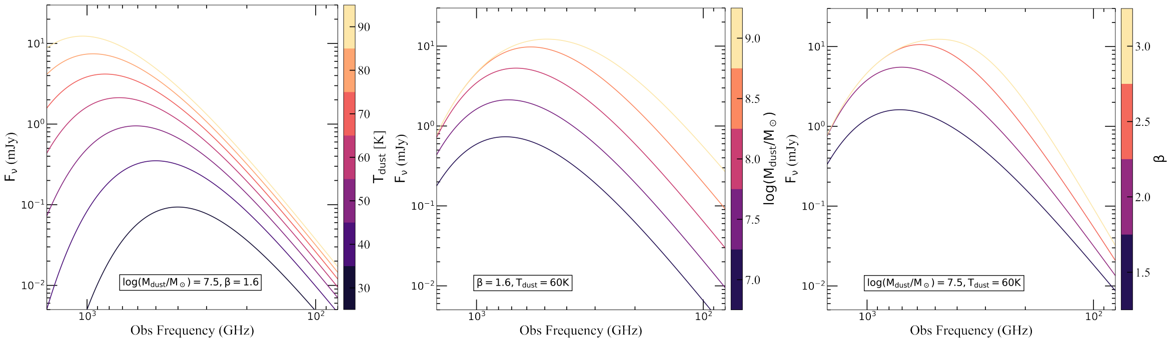

Figure 4.5: *Mock SEDs. Left panel: SEDs at different values of dust temperatures with fixed* $\log(M_{\rm dust}/M_\odot) = 7.5$ *and* $\beta = 1.6$. *Central: SEDs at different values of dust mass with fixed* $T_{\rm dust} = 60$ *K and* $\beta = 1.6$. *Right panel: SEDs at different values of dust emissivity index with fixed* $\log(M_{\rm dust}/M_\odot) = 7.5$ *and* $T_{\rm dust} = 60$ *K.*

with β the emissivity index and k_0 the mass absorption coefficient at ν_0. The values of the latter two terms depend on the adopted opacity model and are usually assumed from either observations (e.g., Alton et al., 2004; Beelen et al., 2006) or dust models (e.g., Bianchi and Raffaella Schneider, 2007). Hereafter we adopt $k_0 = 0.45$ cm^2 g^{-1} and $\nu_0 = 250$ GHz (Beelen et al., 2006). However, since the detailed dust composition is, in principle, unknown, the choice of a particular opacity model carries with it a systematic uncertainty that can lower dust masses by ~three times or increase them by ~ 1.5×. The solid angle is estimated using the continuum emission mean size of the source. The effect of the CMB on the dust temperature is given by

$$T_{\rm dust}(z) = ((T_{\rm dust})^{4+\beta} + T_0^{4+\beta}[(1+z)^{4+\beta} - 1])^{\frac{1}{4+\beta}}, \tag{4.3}$$

with $T_0 = 2.73$ K.

We also considered the contribution of the CMB emission given by $B_\nu(T_{\rm CMB}(z) = T_0(1+z))$ (da Cunha et al., 2013). It is worth to stress that the galaxy is likely characterized by a distribution of dust temperatures, that may reach hundreds of K close to the AGN (see e.g., Walter et al. 2022) and may decreases toward the outskirts, hence the temperature derived from the SED fitting should be interpreted as an 'effective' dust temperature[2].

Fig. 4.5 presents some examples of SEDs with different dust properties (i.e., $T_{\rm dust}, M_{\rm dust}, \beta$) of a mock galaxy at $z \sim 6.5$ with a radius of ~ 0.7 kpc, which is typical for a QSO's host galaxy at this redshift (see e.g. Tab. 4.1). In the left, central and right panels, we show how the variation of the dust temperature, dust mass and dust emissivity index, respectively, changes the shape of the MBB function expressed in Eq. 4.1. Specifically, a variation of temperature affects the position of the peak and the normalization of the curve: higher temperatures imply higher normalization and peak moved towards higher frequencies. A variation of dust mass is directly proportional to the normalization of the curve.

Finally, an increase of the emissivity index implies an increase of the slope of the curve

---

[2] We adopt the term 'effective temperature' since we are not able to map the spatial distribution of the dust temperatures across the galaxy, similarly to the definition of the effective temperature of a star.

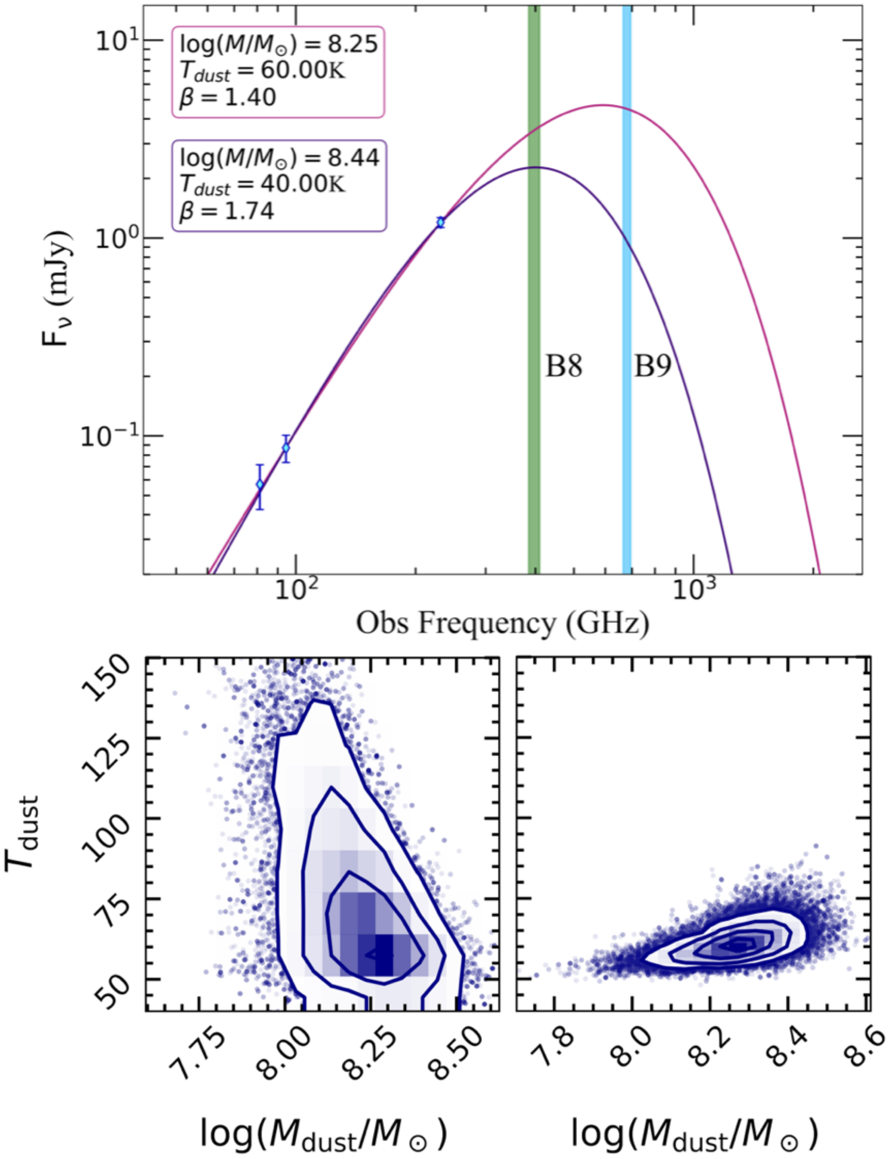

Figure 4.6: *Top panel: SEDs at different temperatures based on the observations of J1007+2115. Purple line is the best fit SED at* $T_{\rm dust} = 40$ *K, and violet line is the best fit SED at* $T_{\rm dust} = 60$ *K. Green and cyan vertical lines marks the mean frequency of an ALMA B8 and B9 observation, respectively. Bottom panels: confidence ellipses for* $T_{\rm dust}$ *and* $\log(M_{\rm dust}/M_\odot)$ *in case of having only a B8 observation (left) or both B8 and B9 observations (right).*

in the Rayleigh-Jeans regime. Both a positive variation of the dust mass and of the emissivity index move the position of the peak towards lower frequencies, and this trend is more evident for high dust mass and high emissivity index. The position of the peak depends also from the redshift of the source: higher is the redshift, lower is the frequency at which the MBB function peaks. From these few examples, it is clear that these tree parameters are tightly correlated and therefore, in order to estimate them with high precision, observations that probe both the Rayleigh-Jeans regime and the peak region of the SEDs are required (e.g., at least one for the peak region and three for the Rayleigh-Jeans regime).

Using the data typically available so far in the sub-mm range, the dust properties remains poorly constrained or unconstrained for most quasars resulting into SFR uncertain by at least a factor of ~ 5 (e.g., F. Wang et al., 2019). The SFR is indeed related to the cold dust SED analysis since it is proportional to the TIR luminosity. The TIR luminosity is derived from the integration of the MBB from 8 to 1000 μm rest-frame. Consequently, the SFR is estimated as follows

$$\text{SFR}[\text{M}_\odot\ \text{yr}^{-1}] = 1.73 \times 10^{-10}\ L_{\text{TIR}}[\text{L}_\odot],\ \text{assuming Salpeter IMF} \tag{4.4a}$$

$$\text{SFR}[\text{M}_\odot\ \text{yr}^{-1}] = 10^{-10}\ L_{\text{TIR}}[\text{L}_\odot],\ \text{assuming Chabrier IMF} \tag{4.4b}$$

$$\text{SFR}[\text{M}_\odot\ \text{yr}^{-1}] = 1.496 \times 10^{-10}\ L_{\text{TIR}}[\text{L}_\odot],\ \text{assuming Kroupa IMF} \tag{4.4c}$$

Hereafter, we will consider the results with the Kroupa initial mass function (IMF, Kroupa and Weidner, 2003), since it seem more indicated for QSO's host galaxies as suggested by Kennicutt and Evans (2012). We still keep in mind that assuming a Salpeter or Chabrier IMF (Salpeter, 1955; Chabrier, 2003) would imply an SFR higher by factor of 1.16 or lower by factor of 0.67.

When only 1 or 2 data points at < 300 GHz are available, T_{dust} remains unconstrained, and M_{dust} and SFR are uncertain by more than one order of magnitude. Similarly, assuming a fixed β leads to an estimate of M_{dust} with up to an order of magnitude uncertainty, and large systematic errors on important derived quantities, such as the gas-to-dust ratio and the molecular mass - thus biasing our understanding of the growth of these massive galaxies. Exceptions are the very few quasars detected by Herschel, which observed the peak of the cold dust SED emission, despite having coarse angular resolution. B9 observations, in synergy with measurements at lower frequencies, is the only method to measure reliably T_{dust} and SFR. Top panel of Fig. 4.6 shows the case in point of a $z \sim 6.5$ quasar for which data are available in only B3 and B6. The lack of high frequency data does not provide a constraint on T_{dust}, since the peak of the SED is not probed. B8 and B9 together are able to probe the SED peak for both low and high T_{dust} (blue and red curves) in QSOs at $5 < z < 8$, leading to a precise estimate of T_{dust} (lower right panel of Fig. 4.6). B8 alone leaves T_{dust} unconstrained if $T_{\text{dust}} \geq 50$K (lower left panel of Fig. 4.6).

4.3 Results on observed cold dust SEDs

In this section, I firstly present the study of the cold dust SED of QSO J2310+1855, for which we included a treatment of the dusty torus emission. I will then discuss the contribution of the AGN to the dust heating, and will give the general prescription adopted for the analysis of the cold dust SED of QSOs J0100+2802, J036+03, J0224-4711, J231-20 and J2054-0005. We derived estimates of the dust properties and SFR with the smallest statistical uncertainties for all QSOs, mainly thanks to ALMA observations in B8 and B9 targeting the continuum emission of these objects.

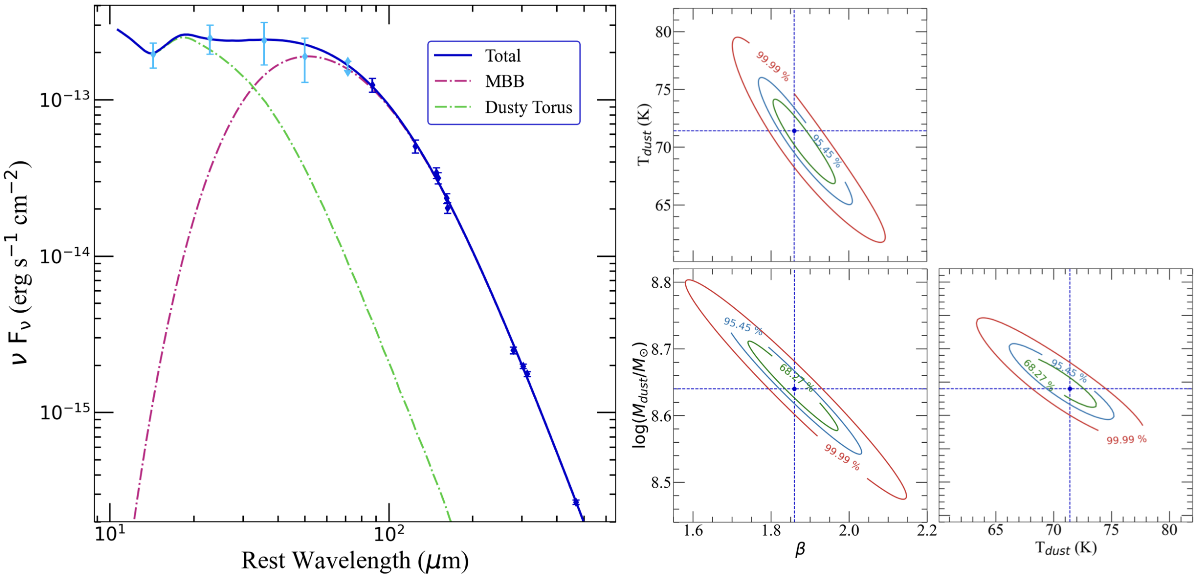

Figure 4.7: *Results of the SED fitting of J2310+1855. Left panel: SED of J2310+1855 using ALMA and Herschel data reported in Table 4.2, fitted with an MBB function (for the dust emission) and the* $a = 0.0002, \tau = 3, \mathrm{p} = 0, \mathrm{q} = 1.5, \mathrm{oa} = 80, \mathrm{R} = 30$, *and* $\mathrm{i} = 20°$ *dusty torus model from the SED library SKIRTOR (Stalevski et al., 2016). Dark blue diamonds are computed based on ALMA observations and light blue diamonds based on Herschel observations, as listed in Table 4.2. Right panel: Confidence ellipses for the MBB free parameters* $T_{\mathrm{dust}}, M_{\mathrm{dust}},$ *and* β *computed at* 68.27%, 95.45%, *and* 99.99% *confidence levels. The dotted blue lines indicate the best-fit parameters.*

4.3.1 Dusty torus emission and AGN contribution to the dust heating

In Fig. 4.7, we show the mm to FIR SED of J2310+1855 starting from a rest frame wavelength of 10 μm derived from the measurements in Table 4.2. In this wavelength range, two main components contribute to the QSO emission: the large-scale dust in the ISM, and the dusty torus. The flux excess with respect to the MBB that is probed by Herschel photometric points requires a warmer dust component, which we modelled with a dusty torus component. We used SKIRTOR, a library of SED templates to model the AGN dusty torus, calculated with SKIRT, a custom radiative transfer code based on Monte Carlo techniques (Stalevski et al., 2016). This library is made of 19200 templates with different values of the optical depth τ at 9.7 μm, of the power-law exponent that sets the radial gradient of dust density (p), of the index for dust density gradient with polar angle (q), eight different half-opening angles (OAs) between the equatorial plane and the edge of the torus, ten inclinations i, from face-on (0 deg, for typical unobscured type I AGN) to edge-on (90 deg, obscured type II AGN) view, and three values for the ratio R of the outer to inner radius of the torus.

Thus, we used Eq. 4.1 of the MBB and the torus templates to fit the flux continuum densities measured with ALMA and Herschel. We set the T_{dust}, $\log(M_{\mathrm{dust}}/M_\odot)$, β, and a (the normalisation of the torus template) as free parameters and explored the parameter space using a non-linear least-squares fit. We forced T_{dust}, $\log(M_{\mathrm{dust}}/M_\odot)$, β as before, and $10^{-5} \lesssim a \lesssim 1$.

Fig. 4.7 shows the results of the SED modelling with a combination of a dusty torus and an MBB, and the χ^2 confidence contours for $T_{\rm dust}$, $\log(M_{\rm dust}/M_\odot)$, β. Tab. 4.3 reports the best-fitting results. The best-fitting parameters for the MBB are $\beta = 1.86 \pm 0.12$, $T_{\rm dust} = 71 \pm 4$ K, and $M_{\rm dust} = (4.4 \pm 0.7) \times 10^8$ $M_\odot$. These values are consistent with those obtained from the fit with the MBB alone, implying that the warmer dusty torus component has little impact on the cool dust component from the host galaxy. Our best-fit $T_{\rm dust}$ is a factor of ~ 2 higher than that derived by Shao et al. (2019) ($T = 39$ K), and $M_{\rm dust}$ is a factor of ~ 4 smaller than their estimate. This also implies a higher gas to dust mass ratio compared to their estimates. We find GDR $= 101 \pm 20$ based on our $M_{\rm dust}$ estimate and the molecular mass $M(\mathrm{H_2}) = (4.4 \pm 0.2) \times 10^{10}$ $M_\odot$, measured from CO(2-1) and CO(6-5) by Li et al. (2020) and Feruglio et al. (2018), using the commonly adopted conversion factor for QSO's host galaxies $\alpha_{\rm CO} = 0.8$ $M_\odot$ (K km s^{-1} pc^2)$^{-1}$ (Downes and Solomon, 1998; Carilli and Walter, 2013).

We note that the photometric data at $\lambda_{\rm rest} < 15\mu$m can be equivalently well fitted by a broad range of SKIRTOR templates (that differ by $\Delta\chi^2 = 0.01$ at most), depending on the combination of the torus parameters. In particular the torus inclination, i, is a great source of degeneracy: when the other torus parameters are fixed to the best-fitting values, the variation in i yields a set of equivalent templates, with $\Delta\chi^2 = 0.01$. The inclination of the torus can be properly determined by observations in the wavelength regime $\lambda_{\rm rest} < 10\mu$m, which is not covered by our dataset. Although the contribution of the dusty torus, clearly seen in the flux excess at $\lambda_{\rm rest} < 15\mu$m, should be considered in the fitting procedure to properly characterize the physics of the QSO and its host galaxy, we were not able to uniquely determine the structural and physical properties of the dusty torus with this dataset. Nonetheless, we were able to use the best-fitting function MBB+template to compute the TIR luminosity from 8 to 1000 μm rest-frame[3], retrieving a value of $L_{\rm TIR,MBB+Torus} = 6.44^{+0.62}_{-0.52} \times 10^{13}$ $L_\odot$ (see Table 4.3)[4]. We also estimated the TIR luminosity for the best-fit MBB model by integrating from 8 to 1000 μm rest-frame, and we obtained $L_{\rm TIR,MBB} = 2.48^{+0.62}_{-0.52} \times 10^{13}$ $L_\odot$, that is just $\sim 40\%$ of the total $L_{\rm TIR,MBB+Torus}$. This underlines the major role played by the dusty torus emission on the total emission observed in the 8 to 100 μm wavelength regime, while it only has a minor effect on the emission from the cold dust, modelled by the MBB. Assuming that this latter emission derives from the dust reprocessed radiation produced by newly born stars only, we obtain a SFR $= 3710^{+928}_{-778}$ $M_\odot \mathrm{yr}^{-1}$, considering $L_{\rm TIR,MBB}$ and Kroupa IMF (see Sect. 4.2).

One should also consider that the presence of an AGN at the center of the host galaxy likely plays a role in heating the surrounding dust. As we anticipated in Sect. 4.2, the galaxy is characterized by a distribution of dust temperatures, that rise towards the center. Both observations and simulations have shown that in the innermost region of the host galaxy ($\sim$ few hundreds pc) $T_{\rm dust}$ can be as high as hundreds of K, and this is mainly due by the presence of the AGN as heating source (Walter et al., 2022; F. Di Mascia et al., 2021; Fabio Di Mascia

---

[3] As is customary for observations, hereafter we neglect that the SED might be anisotropic and derive the luminosity integrating over the whole solid angle (i.e. we multiply the integral under the SED by $4\pi D_{\rm L}^2$).

[4] Due to a typo, the value of $L_{\rm TIR,MBB+Torus}$ reported in Tripodi et al. (2022) is wrong. Therefore, the ratio between the [CII] and the TIR luminosity becomes $L_{\rm [CII]}/L_{\rm TIR} = 8 \times 10^{-5}$. This does not affect any of the results of the paper.

Table 4.2: Continuum observations of J2310+1855

Frequency (GHz)	Synth. beam [arcsec^2]	r.m.s. [mJy/beam]	Flux density [mJy]	Size [arcsec^2]	Telescope	References
91.500	0.71×0.43	0.0053	0.29 ± 0.01	0.261×0.171	ALMA	TP, [1]
136.627	0.74×0.71	0.015	1.29 ± 0.03	0.345×0.212	ALMA	TP, [2], [3], [4]
140.995	0.79×0.65	0.015	1.40 ± 0.02	0.263×0.212	ALMA	TP, [2], [3], [4]
153.070	0.21×0.17	0.0091	1.63 ± 0.06	0.214×0.189	ALMA	This paper
263.315	0.14×0.11	0.016	7.73 ± 0.31	0.190×0.180	ALMA	This paper
265.369	1.62×1.3	0.056	8.81 ± 0.13	0.456×0.422	ALMA	This paper
284.988	0.51×0.39	0.073	11.05 ± 0.16	0.233×0.220	ALMA	TP, [3]
289.180	0.58×0.47	0.025	11.77 ± 0.12	0.330×0.246	ALMA	TP, [2], [3], [4]
344.185	0.53×0.43	0.051	14.63 ± 0.34	0.289×0.229	ALMA	TP, [2], [3], [4]
490.787	0.7×0.6	0.10	25.31 ± 0.19	0.318×0.229	ALMA	This paper, [5]
599.584	...	...	< 29.4	...	*Herschel*/SPIRE	[2]
856.549	...	...	22.0 ± 6.9	...	*Herschel*/SPIRE	[2]
1199.169	...	...	19.9 ± 6.0	...	*Herschel*/SPIRE	[2]
1873.703	...	...	13.2 ± 2.8	...	*Herschel*/PACS	[2]
2997.924	...	...	6.5 ± 1.2	...	*Herschel*/PACS	[2]

Notes. All ALMA observations listed in this table are archival, and we have analysed them, even if the data-set was already been studied (see Ref. column). References: This paper (TP); [1] Feruglio et al. (2018); [2] Shao et al. (2019); [3] Carniani et al. (2019); [4] Li et al. (2020); [5] Hashimoto et al. (2019).

Table 4.3: Results of the SED fitting with MBB and dusty torus models for J2310+1855

Dust emission		
$\log(M_{\rm dust}/M_\odot)$		8.64 ± 0.07
$M_{\rm dust}$	$[10^8\ M_\odot]$	4.4 ± 0.7
$T_{\rm dust}$	[K]	71 ± 4
β		1.86 ± 0.12
$L_{\rm TIR,MBB}$	$[10^{13}\ {\rm L}_\odot]$	$2.48^{+0.62}_{-0.52}$
$L_{\rm TIR,MBB+Torus}$	$[10^{13}\ {\rm L}_\odot]$	$6.44^{+0.62}_{-0.52}$
SFR	$[{\rm M}_\odot]$	1855^{+464}_{-389}
GDR[a]		101 ± 20

Notes. SED fits are performed using two components, MBB and dusty torus. The table reports the individual contribution of the MBB component and the global contribution of MBB+torus for TIR (8-1000 μm).
[a] Gas-to-dust mass ratio derived from $M_{\rm dust}$ (this work) and molecular mass $M({\rm H}_2) = (4.4 \pm 0.2) \times 10^{10}$ $M_\odot$ derived from CO(2-1) and (6-5) (Li et al., 2020; Feruglio et al., 2018).

et al., 2023). The resolution of our observations do not allow us to perform a spatially resolved study of the dust emission, and therefore to isolate the warmer central dust component. That is why we modelled the dust emission with a single temperature BB, hence mixing the dust emission heated by the stellar distribution with the dust heated by the central AGN. This implies that the SFR derived above from the best-fit MBB is contaminated by the contribution of the AGN in heating the dust in the center. To overcome this problem, there are two different possibilities, that can also be used simultaneously. First, one can use $\sim 100-300$ pc-resolution observations to disentangle the warmer dust component that mainly resides in the center from the colder and more extended one. Then it is possible to fit the warm and cold dust component separately, either using two MBBs or with a MBB for the cold dust emission and a radiative transfer modelling for the warm dust AGN heated. This approach has been adopted at high-z only by Tsukui et al. (2023) for a QSO's host galaxy at $z = 4.4$. They found a warm dust component with $T_{\rm dust,warm} = 87$ K (see Fig. 4.8), and an AGN contribution to the dust heating of $\sim 60\%$.

The availability of very high-resolution data is still quite rare at high-z, and indeed this approach has not been applied to any QSO at $z > 4.4$ yet. Alternatively to the spatially resolved study of the SED, one can take advantage of radiative transfer models to determine the AGN contribution to the dust heating. R. Schneider et al. (2015) used a radiative transfer code to follow the transfer of radiation from the central source and from stellar sources through the dusty environment of the host galaxy of QSO SDSS J1148+5251 at $z = 6.4$. For the stellar sources in the host galaxy, they adopted the SED computed with the PÉGASE population synthesis model using as input the star formation histories, age, and metallicities of the stellar populations predicted by GAMETE/QSOdust. Left panel of Fig. 4.9 shows the observed SED of J1148+5251 (black points) fitted by the SED of accretion disk and dusty torus using a SKIRTOR template (as analogously done for J2310+1855). To account for the emission of the dust in the host at longer wavelength, they considered two heating sources, (1) the stellar

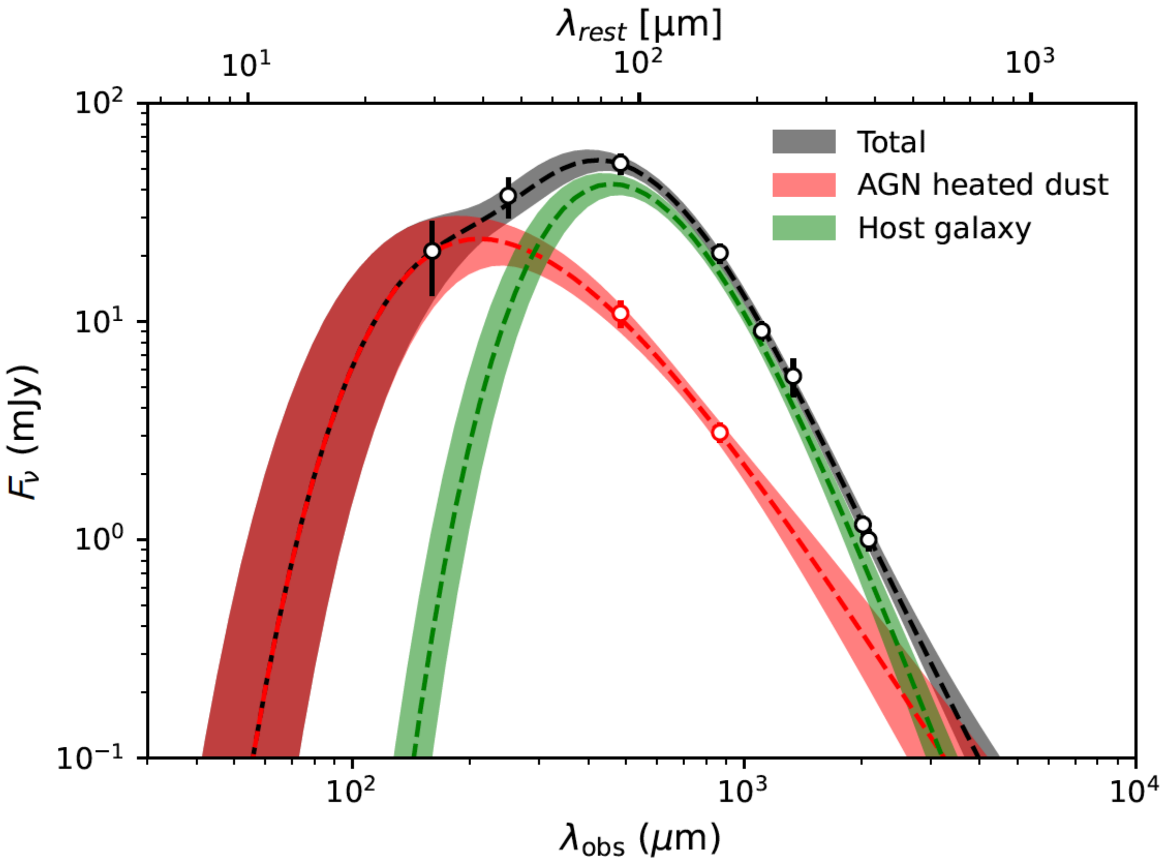

Figure 4.8: *The far infrared spectral energy distribution of BRI1335-0417 at* $z = 4.4$ *(black points) with the best-fit model (grey) composed of two greybody spectra: a warm dust component heated by the AGN (red) and a cold dust component associated with the host galaxy (green). In addition to the total photometric points, we used point source fluxes,* $f_{\lambda_\mathrm{rest}=161\ \mu\mathrm{m}}$ *and* $f_{\lambda_\mathrm{rest}=90\ \mu\mathrm{m}}$ *(red points), measured by the image decomposition to constrain the flux contributed by the AGN-heated warm dust component. Taken from Tsukui et al. (2023).*

component and (2) the central AGN. Right panel of Fig. 4.9 shows the effect of the two components on the resulting SED: the solid line is the best-fitting model considering both sources, while the dashed line is obtained with the AGN as heating source only. This latter can account for the $\sim 70\%$ of the dust emission, supporting the idea of AGN having a strong impact on heating the surrounding dust. The exact amount of the contribution of AGN to the dust heating depends on the prescription adopted to model the central source and the torus. R. Schneider et al. (2015) tested alternative, but still reasonable, models (different from the one presented in Fig. 4.9), and found that the AGN contribution can vary from 30% to 70%. Duras et al. (2017) also investigated the effect of the AGN to the FIR emission in the WISE-SDSS Selected Hyper-luminous (WISSH) quasars at $1.8 < z < 4.6$, using the same approach as in R. Schneider et al. (2015). In particular, considering the least and most luminous QSOs in their sample, they found that the AGN contribution to the FIR fluxes is 43% and 60% respectively, pointing towards a mild trend with luminosity. Therefore, they assumes an average contribution of $\sim 50\%$ to the total FIR luminosity, which also accounts for the uncertainties in the radiative

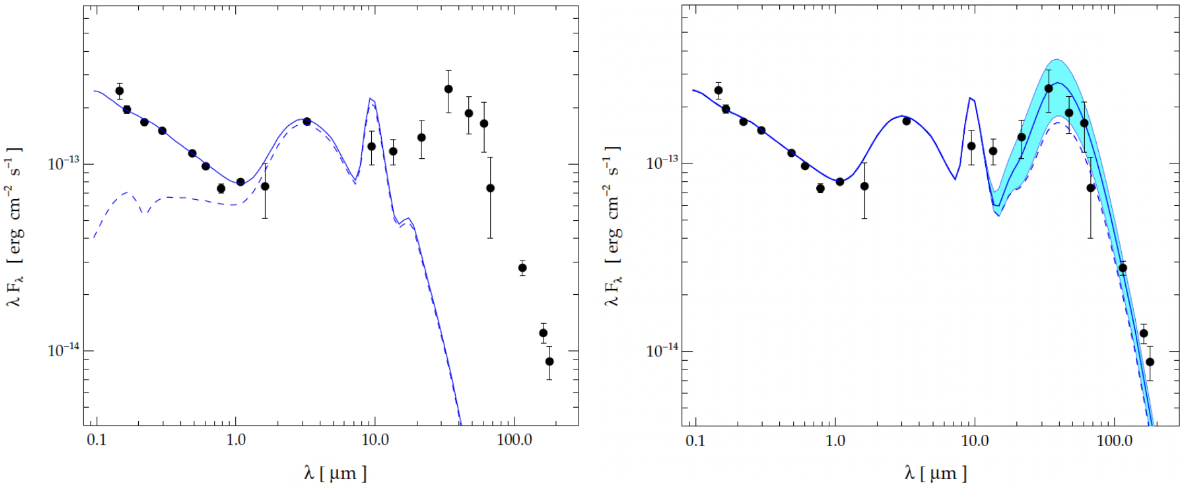

Figure 4.9: *Left panel: Rest-frame SED of J1148+5251 (black points) compared to the SED of the central source from SKIRTOR template t0.1_p1_q6_oa50_1pC11_8 (solid line for the face-on view, dashed line for the edge-on view). Right panel: SED of J1148+5251 obtained by the radiative transfer calculation including the central source and the stellar component (solid blue line), with the shaded region illustrating the variations of the stellar SED induced by the 1σ scatter of the SFR. The dashed line shows the results obtained using only the central source. Adapted from* R. Schneider et al. (2015)*.*

transfer model and is in line with the average result found in R. Schneider et al. (2015).

Considering that the bolometric luminosity, black hole mass, redshift and properties of the host galaxy of J1148+5251 are remarkably alike those of J2310+1855, we are confident that the impact of the AGN on the dust heating would be similar in both sources. Therefore, we consider an AGN contribution of ~ 50% to the dust heating for J2310+1885, implying $L_{\rm TIR,MBB} = 1.24 \times 10^{13}$ L$_\odot$, and therefore a SFR = 1855^{+464}_{-389} M$_\odot$yr^{-1}. The precise estimate of the AGN impact on the FIR emission would require either a spatially resolved study of the SED or radiative transfer modelling. The former is not feasible due to the lack of high resolution data, and the latter is beyond the scope of this project but will be the goal of future investigations.

4.3.2 Basic cold dust SEDs

Fig. 4.10 shows the observed SED (cyan markers) from the mm regime to the radio band of J0100+2802. We perform an SED fitting using the continuum emission measured at ~ 671 GHz (cyan star), together with the emissions presented in F. Wang et al. (2019) from 32 GHz to 353 GHz, and in Y. Liu et al. (2022) at 1.5, 6 and 10 GHz. Although we are interested in the cold dust properties of the QSO's host galaxy, such as $T_{\rm dust}$, $M_{\rm dust}$ and β, we consider also the contribution of the lower frequency emission to the dust SED, since in general it may not be negligible. Y. Liu et al. (2022) noticed a time variability among their and previous measurements of the radio continuum in the range [6-10] GHz. For the sake of simplicity, we consider the most recent measurements of the radio continuum emission (i.e., those from Y.

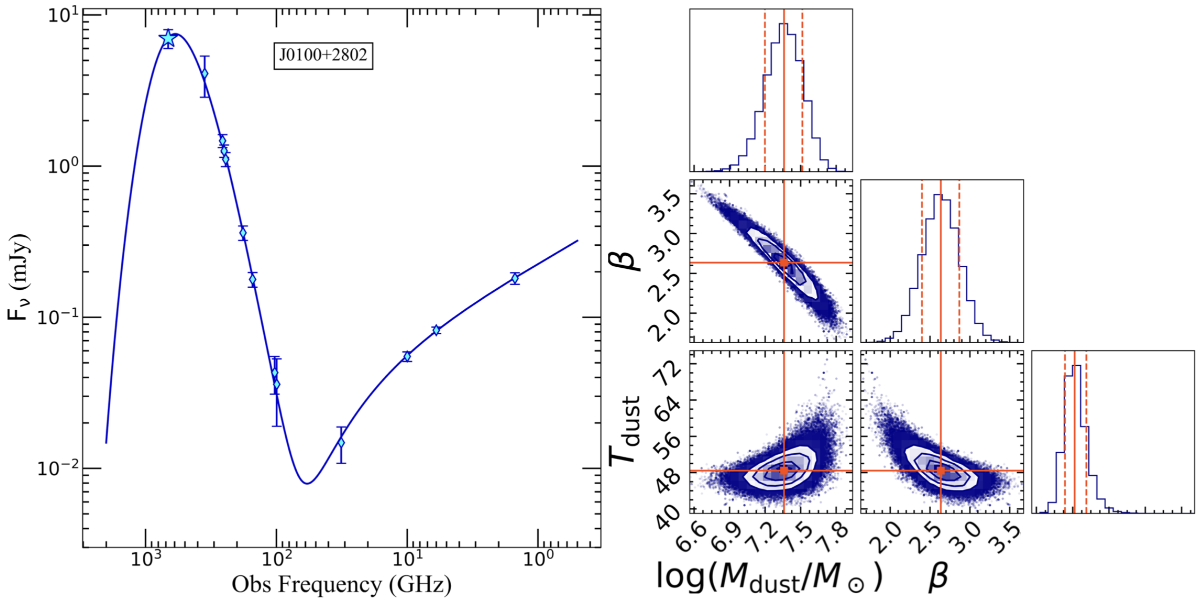

Figure 4.10: *Left panel: SED of J0100+2802 using our new ALMA 670.91 GHz data (cyan star), the continuum fluxes from 32 GHz to 353 GHz (F. Wang et al., 2019), and at 1.5, 6 and 10 GHz (Li et al., 2022) (cyan diamonds). The best-fitting curve is shown as a blue solid line. Right panel: Corner plot showing the posterior probability distributions of* $T_{\rm dust}$, $M_{\rm dust}$, β. *Orange solid lines indicate the best-fitting value for each parameter, while the dashed lines mark the 16th and 84th percentiles for each parameter.*

Liu et al. 2022). However, we verified that our results do not change by considering all the measurements available in the radio band.

We model the dust continuum with a MBB function (see Eq. 4.1), and the low frequency radio emission using a power law with an exponential cut-off (PLCO) as follows

$$F_{\nu_{\rm rest}} = n \times (\nu_{\rm rest}/\nu_0)^{-\alpha} \times \exp(-\nu_{\rm rest}/\nu_{\rm cutoff}) \tag{4.5}$$

where n is the normalization, α is the radio power-law spectral index, ν_0 and $\nu_{\rm cutoff}$ are the reference frequency and the cutoff frequency, respectively. We set $\nu_0 = 59$ GHz to ease the fitting procedure and in order to minimize the covariance between n and α. This choice does not affect our results. The model has six fitting parameters: dust temperature ($T_{\rm dust}$), dust mass ($M_{\rm dust}$), dust emissivity index (β) entering in the MBB function, and the normalization (n), the radio power-law spectral index (α), and the cut-off frequency ($\nu_{\rm cutoff}$) for the PLCO.

We explore the six dimensional parameter space using a Markov chain Monte Carlo (MCMC) algorithm implemented in the `EMCEE` package (Foreman-Mackey et al., 2013). We assume uniform priors for the fitting parameters: $10\ {\rm K} < T_{\rm dust} < 300$ K, $10^5\ {\rm M}_\odot < M_{\rm dust} < 10^9\ {\rm M}_\odot$, $1.0 < \beta < 3.0$, $0.001\ {\rm mJy} < n < 0.5$ mJy, $0.01 < \alpha < 1.0$, $75.0\ {\rm GHz} < \nu_{\rm cutoff} < 500$ GHz. The best-fit model has $T_{\rm dust} = 48.4 \pm 2.3$ K, $M_{\rm dust} = (2.29 \pm 0.83) \times 10^7\ {\rm M}_\odot$, $\beta = 2.63 \pm 0.23$, $n = 0.08 \pm 0.01$ mJy, $\alpha = 0.48 \pm 0.09$ and $\nu_{\rm cutoff} = 235 \pm 100$ GHz. Fig. 4.10 shows the observed SED fitted by our best-fit model (left panel) and the posterior distributions for the dust parameters (right panel). Posterior distributions of all parameters is shown in Fig. 4.11.

Table 4.4: Results of the SED fitting

		J0100+2802	J036+03	J0224-4711	J231-20	J2054-0005	J183+05	J1342+0928	J1319+0950	J1148+5251
HYP		Y	Y	Y	Y	N	N	Y	N	Y
z		6.327	6.540	6.522	6.587	6.390	6.439	7.540	6.133	6.419
$M_{\rm dust}$	[10^7 $M_\odot$]	2.3 ± 0.8	6.1 ± 2.5	9.3 ± 2.7	53 ± 5	10.6 ± 2.4	45 ± 9	2.6 ± 1.4	63 ± 29	32 ± 8
$T_{\rm dust}$	[K]	48 ± 2	59 ± 2	85^{+12}_{-8}	51 ± 3	64 ± 2	54 ± 5	55 ± 20	66^{+15}_{-12}	75 ± 8
β		2.6 ± 0.2	2.4 ± 0.2	1.7 ± 0.2	1.6 ± 0.1	2.1 ± 0.1	1.7 ± 0.2	1.8 ± 0.4	1.5 ± 0.3	1.5 ± 0.2
$L_{\rm TIR}$	[10^{12} L$_\odot$]	5.3 ± 0.6	6.2 ± 1.0	33.2^{+22}_{-10}	6.6 ± 1.6	9.8 ± 1.0	11.9 ± 4.0	$2.4^{+3.7}_{-2.3}$	16^{+13}_{-6}	21 ± 7
SFR	[M$_\odot$ yr^{-1}]	396 ± 48	466 ± 75	2485^{+1682}_{-768}	496 ± 118	730 ± 75	894 ± 299	180^{+280}_{-170}	1197^{+972}_{-449}	1570 ± 524
Refs-D		This work	This work	This work	This work	This work	TW,[1]	TW,[2]	[3]	[3]
$M_{\rm gas}$	[10^{10} M$_\odot$]	0.5 ± 0.2	0.7 ± 0.1	1.0 ± 0.1	1.4 ± 0.1	0.6 ± 0.1	4.5	< 0.35	1.5 ± 0.2	2.6
GDR		236	123	110	26	60	100	< 130	24	81
Refs-G		[1]	This work	This work	TW,[4]	This work	[1]	[2]	This work	[5]

Notes. Results for the QSOs on the left side of the vertical line are entirely obtained from this work, i.e., all observations were analysed by the author. On the right side of the vertical line, results for J183+05 and J1342+0928 are obtained fitting their observed SEDs presented in Decarli et al. (2023) and Novak et al. (2019), respectively; results for J1319+0950 and J1148+5251 are taken from Carniani et al. (2019). SFRs are computed from $L_{\rm TIR}$ assuming Kroupa IMF, and are corrected by a factor of 50% in order to take into account the contribution of the AGN to the dust heating. First raw is whether the QSO belongs or not to the HYPERION sample. The gas mass for J231-20 is computed from the CO(7-6) luminosity in [4] using the r_{76} derived in Sect. 3.2.2 for J1007+2115, and is in agreement with that derived from [CI] in [2]. Refs-D: references for dust properties and SFR. Refs-G: references for the gas mass. Refs: This work (TW); [1] Decarli et al. (2023); [2] Novak et al. (2019); [3] (Carniani et al., 2019); [4] Pensabene et al. (2021); [5] Stefan et al. (2015).

We find a gas-to-dust ratio GDR = 236 ± 155 based on our $M_{\rm dust}$ estimate and the molecular gas mass obtained by F. Wang et al. (2019) (see Tab. 4.4). This is in agreement with GDRs found in ultraluminous QSOs at $z \sim 2-4$ (Bischetti et al., 2021), and in local galaxies at solar metallicities (De Vis et al., 2019). This latter comparison would imply that J0100+2802's host galaxy has already been highly enriched with metals. From the best fit SED we derived $L_{\rm TIR} = 5.30 \pm 0.64 \times 10^{12}$ L$_\odot$, implying an SFR of 793 ± 96 M$_\odot$ yr^{-1}. However, several observations and radiative transfer simulations suggested that the radiative output of luminous QSOs substantially contributes to dust heating on kpc scale (R. Schneider et al., 2015; F. Di Mascia et al., 2021; Walter et al., 2022). As already mentioned in the previous section, Duras et al. (2017) and R. Schneider et al. (2015) showed that on average $\sim$ 50% of the total IR luminosity in QSOs with $L_{\rm bol} > 10^{47}$ erg s^{-1} is due to dust heated by the AGN radiation. Recently, Fabio Di Mascia et al. (2023) found a correction factor of 1/30 for the SFR of the brightest object in their sample. However, the $L_{\rm bol}$ of J0100+2802 is above the range explored in their simulations and, moreover, J0100+2802 has peculiar properties in terms of UV magnitude and dust temperatures with respect to the simulated QSOs in Fabio Di Mascia et al. (2023). Therefore, we consider the average correction on $L_{\rm TIR}$ proposed by Duras et al. (2017); R. Schneider et al. (2015) as the most appropriate choice, and we obtain SFR = 396 ± 48 M$_\odot$yr^{-1}.

We found that our observation in B9 favours $T_{\rm dust}$ lower than the effective dust temperatures found in simulations in bright ($L_{\rm bol} > 10^{13}$ L$_\odot$) quasar-hosts ($\sim$ 90 K, e.g. Fabio Di Mascia et al. 2023). This discrepancy can be due to different dust spatial distributions between the simulated objects and J0100+2802, or to limits in the dust modelling and radiative transfer post-processing (e.g. the absence of a dusty torus in F. Di Mascia et al. 2021). With the current unresolved observation we are not able neither to constrain different temperature components, nor to determine the temperature distribution across the galaxy. The value found for the emissivity index is higher than $\beta = 1.6$ found for the average SED of high-z QSOs (Beelen et al., 2006). However, as noted by Beelen et al. (2006), large variations of β are found when considering individual QSO SED. Only excluding the B9 data, we would obtain a good fit with $\beta < 2$, having then a factor of two higher temperature (see also F. Wang et al., 2019). This shows that the results can be misguided by relying only on the lowest frequency data points, while B9 is essential to reliably estimate dust parameters up to the highest redshifts. Indeed, Novak et al. (2019), using observations up to B8 at ~404 GHz, could not constrain $T_{\rm dust}$ in the $z = 7.54$ quasar ULAS J1342+0928. This result provides the first measurement of the B9 continuum of a luminous QSO's host galaxy. Similarly, Bakx et al. (2021) used B9 observations to constrain $T_{\rm dust}$ for a galaxy at $z = 7.13$.

The strong anti-correlation between $T_{\rm dust}$ and β can arise from the MCMC fitting procedure itself, mainly if there is a massive amounts of cold dust (i.e., $T \lesssim 10$ K, Galliano, Galametz, and Anthony P. Jones 2018). However, in our case, the accurate sampling of the SED from low to high frequency significantly relaxed the strength of $T_{\rm dust} - \beta$ anti-correlation (Fig. 4.10). Therefore, we are confident that the estimates of β and $T_{\rm dust}$ are not strongly biased due to the

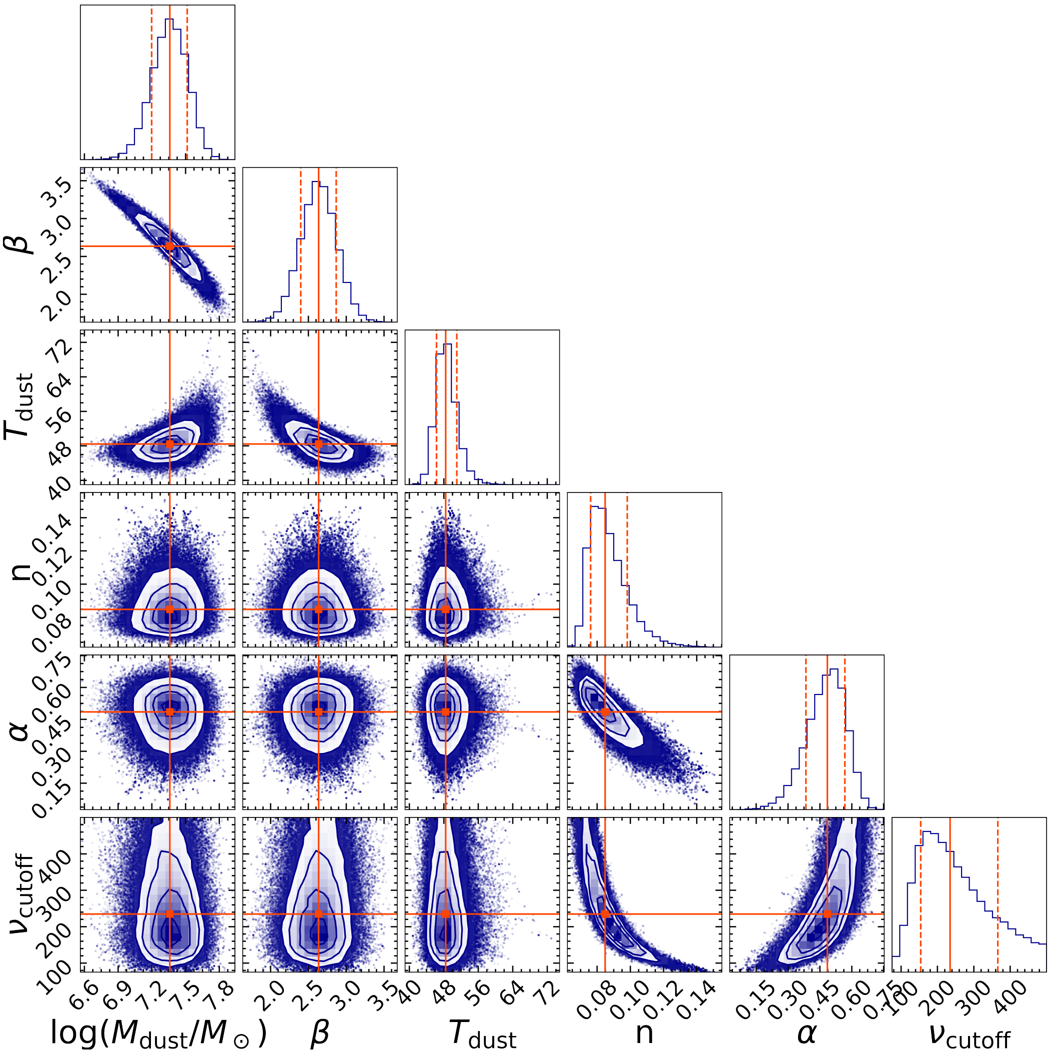

Figure 4.11: *Corner plot showing the six dimensional posterior probability distributions of* $T_{\rm dust}, M_{\rm dust}, \beta, n, \alpha,$ *and* $\nu_{\rm cutoff}$ *of J0100+2802. Orange solid lines on the posterior probability distributions indicate the best-fitting value for each parameter, while the dashed lines mark the 16% and 84% percentiles for each parameter.*

effect of this anti-correlation.

In order to ensure a self-consistent analysis of the cold dust SEDs of J036+03, J0224-4711, J231-20 and J2054-0005, we performed SED fitting of the flux densities reported in Tab. 4.1 considering the tapered fluxes for the higher resolution observations if needed. The observations of J231-20 in Pensabene et al. (2021) did not need additional tapering given that their resolution was well matched and low enough to account for the fainter and more extended emission. Moreover, for J231-20, we considered the flux corrected for the contribution of the companion to the QSO emission as explained in Sect. 4.1.1. We modelled the dust continuum with a MBB function (see Eq. 4.1), with three free parameters $T_{\rm dust}$, $M_{\rm dust}$, and β. We explored the three dimensional parameter space using a MCMC algorithm implemented in the `EMCEE` package (Foreman-Mackey et al., 2013), assuming uniform priors for the fitting parameters: $10\ {\rm K} < T_{\rm dust} < 300\ {\rm K}$, $10^5\ {\rm M}_\odot < M_{\rm dust} < 10^9\ {\rm M}_\odot$, $1.0 < \beta < 3.0$. The best-fitting $T_{\rm dust}$,

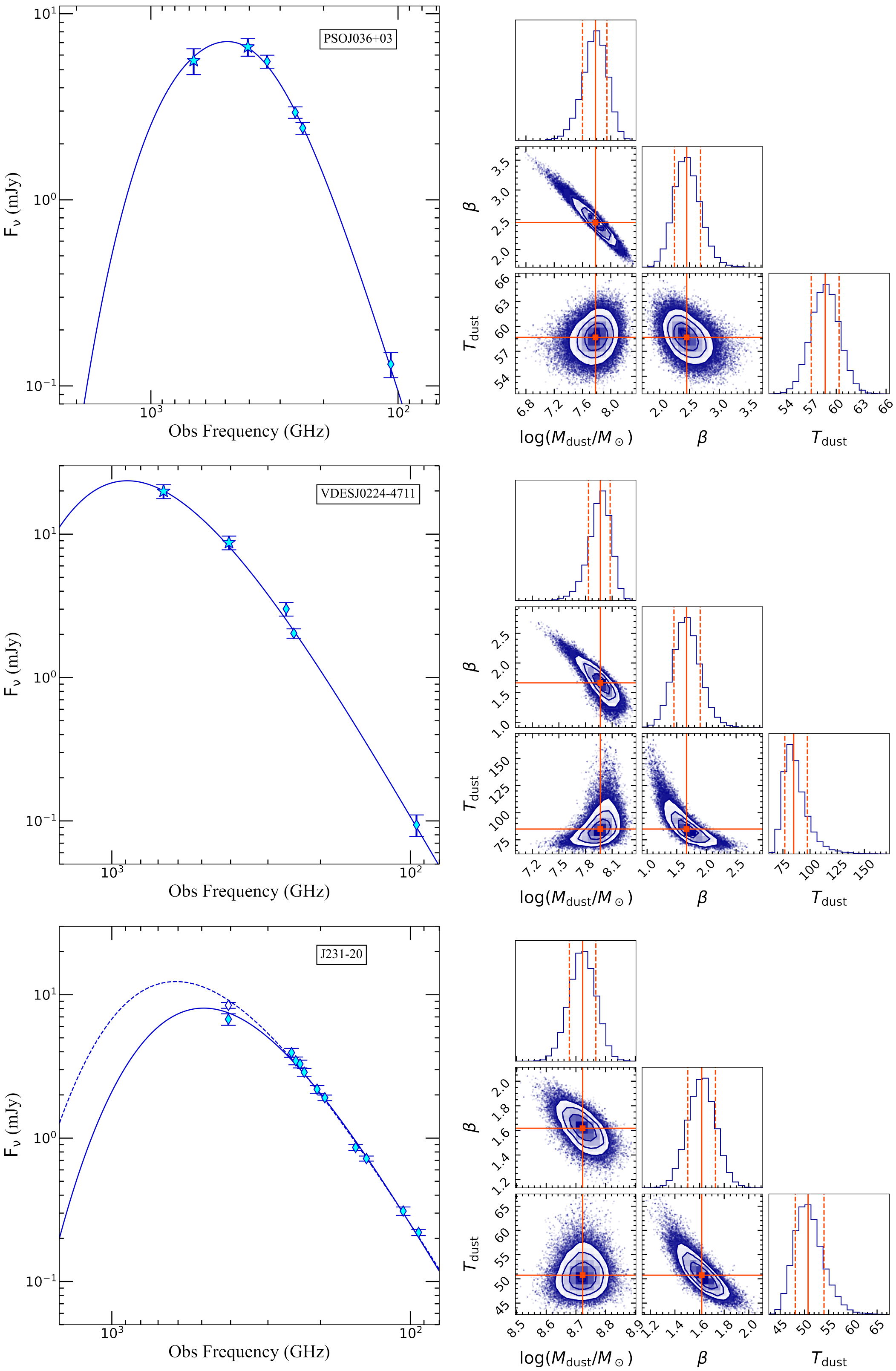

Figure 4.12: *Left panels: observed SEDs of QSOs J036+03, J0224-4711 and J231-20 (top, central, bottom row). Our new ALMA B8 and B9 data are shown as cyan star, while other archival observations as cyan diamonds. The best-fitting curve is shown as a blue solid line. Right panels: Corner plot showing the posterior probability distributions of* $T_{\rm dust}, M_{\rm dust}, \beta$. *Orange solid lines indicate the best-fitting value for each parameter, while the dashed lines mark the 16th and 84th percentiles for each parameter. For the dashed line and empty diamond in J231-20 see text.*

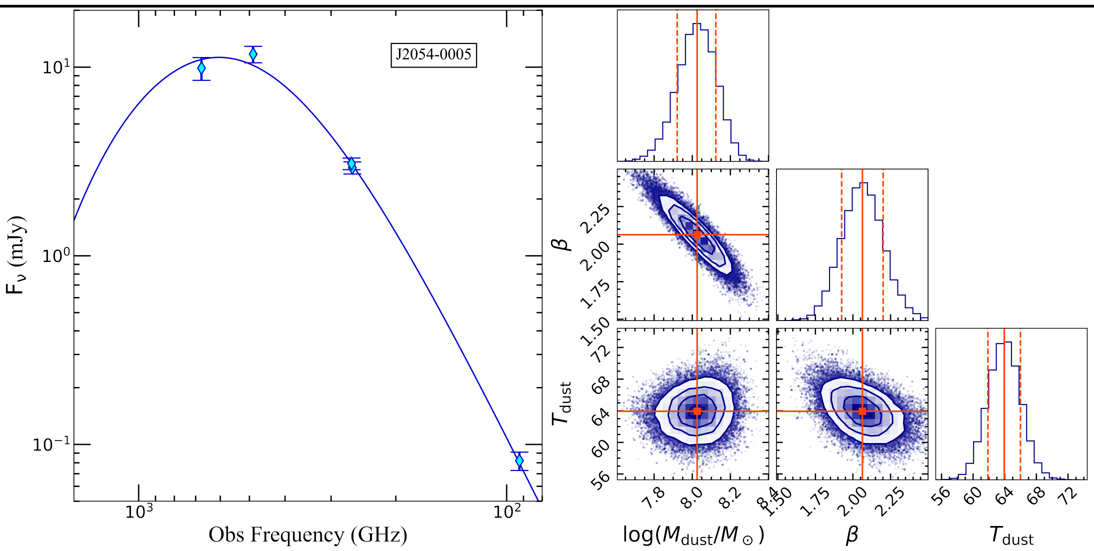

Figure 4.13: Same as Fig. 4.12 for QSO J2054-0005.

$M_{\rm dust}$, and β, obtained from a MCMC with 40 chains, 6000 trials and a burn-in phase of $\sim$ 100 for each QSO are reported in Tab. 4.4. The errors on the best-fitting parameters are computed considering the 16th and 84th percentiles of the posterior distribution of each parameter. Overall we found $T_{\rm dust} = 50 - 80$ K, $M_{\rm dust} \sim 10^8$ $M_\odot$ and $\beta = 1.6 - 2.5$. Fig. 4.12 show the observed SEDs with the best fitting function and the posterior distributions of $T_{\rm dust}$, $M_{\rm dust}$, and β for J036+03, J0224-4711, and J231-20, and Fig. 4.13 for J2054-0005. Consequently, we obtained $L_{\rm TIR} = 6.2 \pm 1.0 \times 10^{12}$ $L_\odot$ for J036+03, $L_{\rm TIR} = 3.3^{+2.2}_{-1.0} \times 10^{13}$ $L_\odot$ for J0224-4711, $L_{\rm TIR} = 6.6 \pm 1.6 \times 10^{12}$ $L_\odot$ for J231-20, and $L_{\rm TIR} = 9.8 \pm 1.0 \times 10^{12}$ $L_\odot$ for J2054-0005, implying an SFR of 933 ± 150 $M_\odot$ yr^{-1} for J036+03, an SFR of 4970^{+3364}_{-1537} $M_\odot$ yr^{-1} for J0224-4711, an SFR of 992 ± 236 $M_\odot$ yr^{-1} for J231-20, and an SFR of 1460 ± 150 $M_\odot$ yr^{-1} for J2054-0005.

As a word of caution, we recall that we adopted a lower limit for the flux in B8 of J231-20 and thus, in principle, $T_{\rm dust}$ and SFR can be under-estimated. Indeed, by performing another fit considering the B8 flux not corrected for the contribution of the companion (which is an upper limit to the flux of the QSO), we derived $T_{\rm dust} = 61$ K and SFR= 1913 $M_\odot$ yr^{-1}, a factor of 2 higher than that obtained considering the lower limit in B8, while the dust mass and emissivity index are in good agreement with the previous values. The best-fitting curve is displayed as a dashed line in the bottom left panel of Fig. 4.12, along with the uncorrected B8 flux as an empty diamond. Hereafter, we conservatively use the results of the SED fitting with the B8 flux corrected for the companion emission, considering that the SFR can vary of a factor of 2 at most.

We adopt a contribution of the AGN emission to the dust heating of 50% considering that all our sources are hyperluminous QSOs at $z \gtrsim 6$, likely sharing similar properties with the QSOs in Duras et al. (2017) and with J1148+5251 in R. Schneider et al. (2015), which also belongs to the HYPERION sample. This assumption decreases $L_{\rm TIR}$ of a factor of 2 and therefore yields SFR= 466 ± 75 $M_\odot$ yr^{-1} for J036+03, an SFR= 2485^{+1682}_{-768} $M_\odot$ yr^{-1} for J0224-4711, an SFR= 496 ± 118 for J231-20, and an SFR= 730 ± 75 for J2054-0005.

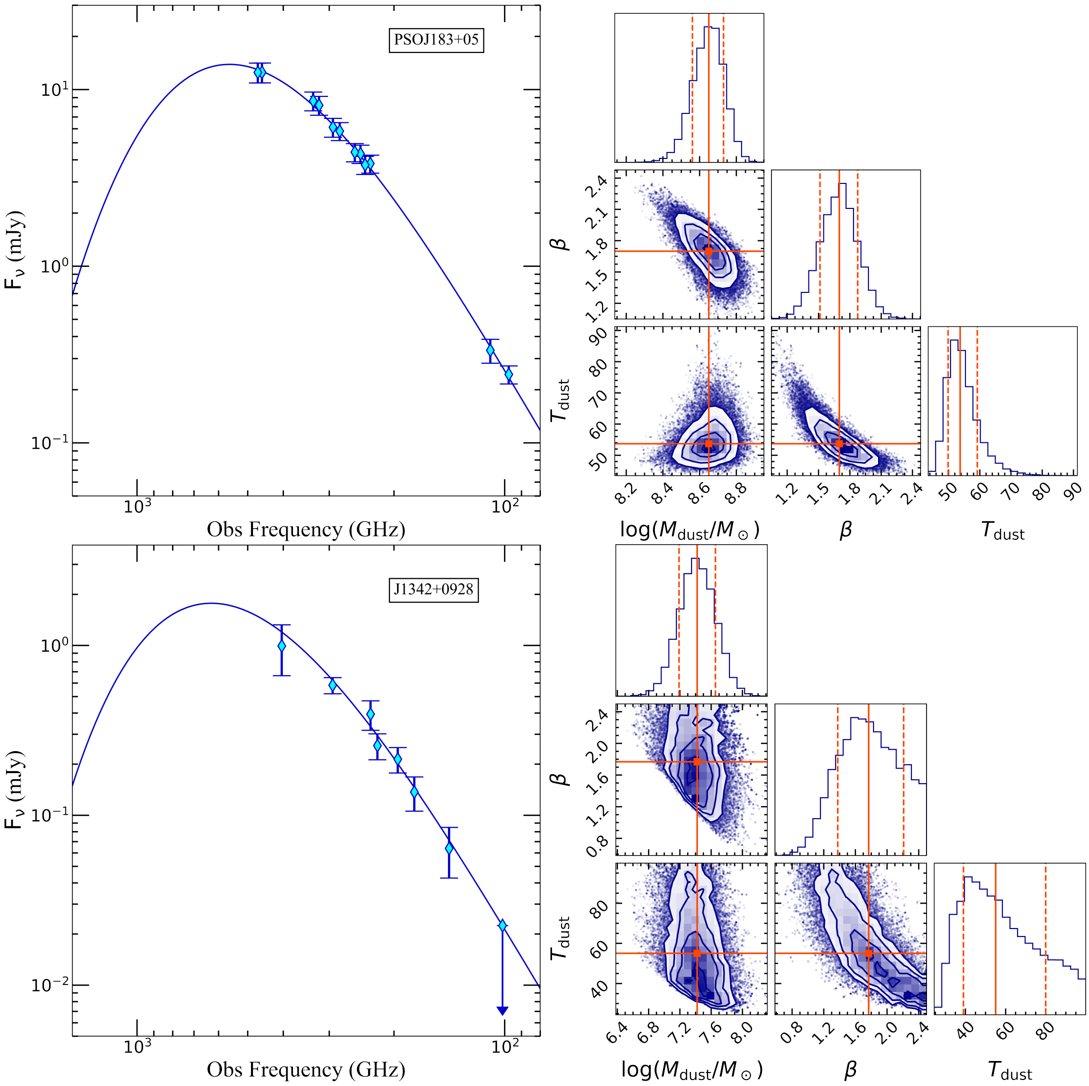

Figure 4.14: *Left panels: observed SEDs of QSOs J183+05, J1342+0928 (top and bottom row) as cyan diamonds. The best-fitting curve is shown as a blue solid line. Right panels: Corner plot showing the posterior probability distributions of* $T_{\rm dust}, M_{\rm dust}, \beta$*. Orange solid lines indicate the best-fitting value for each parameter, while the dashed lines mark the 16th and 84th percentiles for each parameter.*

Since we aim at performing a statistically sound investigation of the dust properties in a sample of $z > 6$ QSOs, we explored the archives and the literature searching for other suitable candidates for our analysis of cold dust SED, i.e, with ALMA and/or NOEMA observations of the continuum emission that probed both the Rayleigh-Jeans regime and the peak region of the SED. Up to now and to our knowledge, there are only other 4 QSOs at $z > 6$ that have multiple-frequency observations sampling the Rayleigh-Jeans part and, even barely, the peak of the cold dust SED: QSOs J1319+0950, J1148+5251, J1342+0928 and J183+05. Their SEDs have already been analysed in Carniani et al. (2019) (J1319+0950 and J1148+5251), in Novak et al. (2019); Witstok et al. (2023) (J1342+0928), and in Decarli et al. (2023) (J183+05). Since we adopt the same methodology as in Carniani et al. (2019), we just report the results on dust properties and SFRs of J1319+0950 and J1148+5251 in Table 4.4. For consistency, we modelled the observed SEDs of the other two QSOs using the procedure described in the previous paragraph, since the methodology and/or the opacity models adopted in Novak et al. (2019); Witstok et al. (2023); Decarli et al. (2023) were different from ours. The best-fitting SEDs are shown in Fig. 4.14 and the results can be found in Tab. 4.4. Within the uncertainties, our results are overall in good agreement with those in Novak et al. (2019); Witstok et al. (2023); Decarli et al. (2023). The discrepancies in the best-fitting values arise from the different regime assumed (optically thin in Novak et al. 2019, thick in Witstok et al. 2023; Decarli et al. 2023) and in the different opacity models. It is worth noticing how the uncertainties on $T_{\rm dust}$ (SFR), increase to $\sim 30\%$ ($> 80\%$) when the peak of the cold dust SED is not probed: this is the case of J1319+0950, J1342+0928 that have not any ALMA observations in Bands 8 and 9, and of J0224-4711, for which even Band 9 is not able to reach the peak of the SED given that this QSO has an extremely bright dust emission. The strongest effect is seen in J1342+0928, for which $T_{\rm dust}$ is determined with an uncertainty of $\sim 40\%$ leaving the SFR basically unconstrained. This highlights the importance of high-frequency observations (Bands 8,9,10) in providing us precise and reliable estimates of the dust properties and SFR.

In Sect. 4.3.1, we showed that the dusty torus does not affect the determination of the cold dust parameters significantly. However, one may wonder if this stands also for the other QSOs for which the dust peak has been constrained. In this regards, we run few tests considering the dusty torus templates presented in Sect. 4.3.1. Unfortunately, high-frequency ALMA observations (B8-B9) are not able to put constraints on the dusty torus emission and therefore, we preliminary considered the best-fitting dusty torus template of J2310+1855. We fitted the dusty torus template and the MBB simultaneously to the other QSO's SEDs, and we retrieved dust properties in perfect agreement within the uncertainties with those found in the MBB-only fitting procedure presented above. Given that the OA of the torus is the parameter that mainly affects the normalization of the torus template near the region of the cold dust emission (see e.g. Fig. 4 in Duras et al., 2017), we varied the OA of the best-fitting torus template of J2310+1855 from 20° to 80° to increase the normalization. Also in this case the derived cold dust parameters are in agreement with those of the MBB-only case.

4.3.3 Cold dust SEDs of J1007+2115 and J0100+2802-C

J1007+2115

Observations were taken with the NOEMA interferometer under project W21ED in March 2022. The continuum visibility tables at two representative frequencies in LSB and USB were derived using the task `uv_filter` within `MAPPING` to filter out a spectral region 400 MHz wide around the emission lines, and `uv_continuum`. The noise reaches 15.5 μJy/beam in LSB and 13.7 μJy/beam in USB over a bandwidth of 7.4 GHz in each sideband (excluding the 400 MHz spectral window containing the emission lines). The continuum uv-tables were analyzed in the uv plane. We find flux densities of 57 ± 14 μJy at 81.2 GHz and 87 ± 14

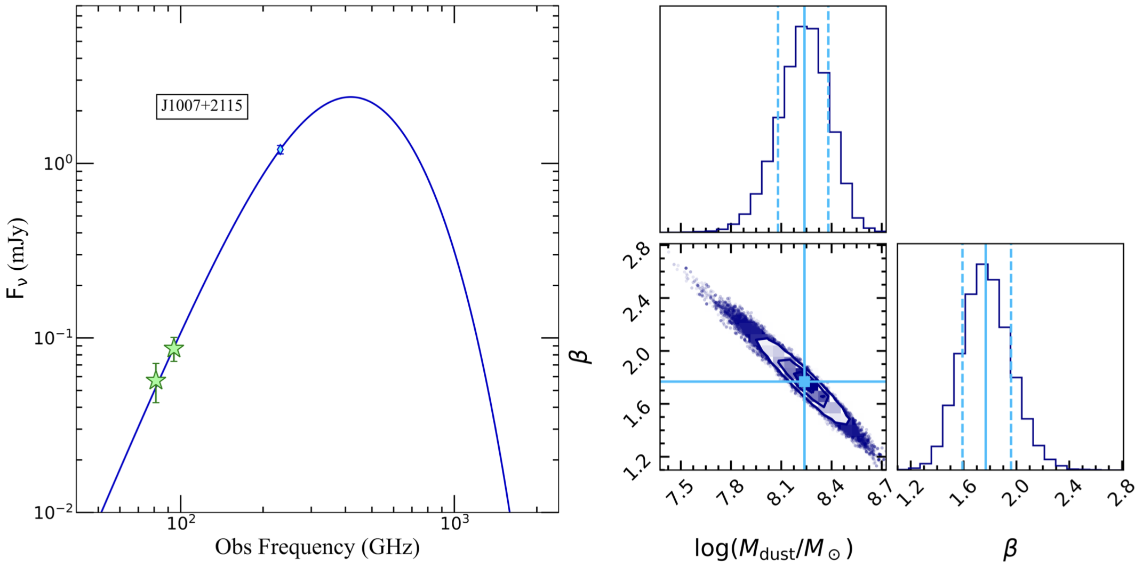

Figure 4.15: *Results of the SED fitting of Pōniuāʻena. Left panel: SED using our new NOEMA data at 3mm (i.e.,* ∼ 80 *and* ∼ 90 *GHz; green stars), and the ALMA data at* ∼ 230 *GHz taken from* J. Yang et al. (2020) *(cyan diamond). The best-fitting curve with dust temperature fixed at* 50 *K is shown as a blue solid line. Right panel: Corner plot showing the two dimensional posterior probability distributions of $M_{\rm dust}, \beta$. Cyan solid lines indicate the best-fitting parameter, while the dashed lines mark the 16% and 84% percentiles for each parameter.*

μJy at 94 GHz, with both measurements consistent with point sources. Deconvolution using natural weighting leads to a synthesized beam of 3.1×2.2 arcsec^2 (PA=30 deg) in LSB and 2.5×1.8 arcsec^2 (PA=30 deg) in USB. Cleaning of the image cube was done using the `Hogbom` algorithm without applying any mask.

The SED of the cold dust component of J1007+2115, based on these observations and ALMA Band 6 observations from J. Yang et al. (2020), is shown in Fig. 4.15 and it has been modelled with the MBB function described in Sect. 4.2. Since the source is unresolved, the adopted area of the galaxy is the dust size commonly found in high-z QSOs (Tripodi et al., 2022; Walter et al., 2022; Shao et al., 2022), that is 0.2×0.2 arcsec, corresponding to $\sim 1.0 \times 1.0$ kpc^2 at the rest-frame of our source. Dust temperature cannot be constrained with the low-frequency data in hand, hence we fix it to $T_{\rm dust} = 50$ K. This may be considered the median value in $z = 6-7$ quasars, for which a range in $T_{\rm dust}$ of 30 to 70 K is found (Leipski et al., 2014; R. Schneider et al., 2015; Carniani et al., 2019; F. Wang et al., 2019; Tripodi et al., 2023a; Tripodi et al., 2022). We explored the two dimensional parameter space using a MCMC algorithm implemented in the `EMCEE` package (Foreman-Mackey et al., 2013), assuming uniform priors for $M_{\rm dust}$ and β. We derive a cold dust mass of $M_{\rm dust} = (1.7 \pm 0.6) \times 10^8$ M$_\odot$ and a dust emissivity index of $\beta = 1.77 \pm 0.18$. The dust mass is in agreement with the median dust mass found in quasars at z=6-6.6 (B. P. Venemans et al., 2018). Varying the temperature up to $T_{\rm dust} = 70$ K, the dust mass and emissivity index both decreases to $M_{\rm dust} = 1.4 \times 10^8$ M$_\odot$ and $\beta = 1.41$, respectively.

The gas-to-dust ratio is about GDR $\sim 80-100$, in line with quasars at lower redshift

Table 4.5: Properties of QSO's host and companion

		QSO	Companion
$S_{\text{cont, 253GHz}}$	[mJy]	1.19 ± 0.06	0.25 ± 0.01
$S_{\text{cont, 99GHz}}$	[mJy]	0.043 ± 0.005	0.007 ± 0.002
$L_{\text{[CII]}}^{(*)}$	[10^9 $L_\odot$]	4.70	1.68
M_{HI}	[10^9 $M_\odot$]	6.43	2.30
T_{dust}	[K]	48±2	30-50
M_{dust}	[$10^7 M_\odot$]	2.3±0.8	0.3-2.6
β		2.6±0.2	2.0-3.1
SFR	[$M_\odot$ yr^{-1}]	396±48$^{(**)}$	52-515

Notes. The dust properties and SFR for the QSO's host galaxy are taken from Tripodi et al. (2023a). $^{(*)}$: $L_{\text{[CII]}}$ are computed inside a region > 2σ from the [CII] maps shown in the top panels of Fig. 3.9, as explained in Sect. 3.3. $^{(**)}$ The SFR for the QSO's host galaxy is corrected by a factor of 50% to account for the possible contribution of the AGN to the dust heating (Tripodi et al., 2023a).

(Tripodi et al., 2022; Bischetti et al., 2021), and consistent even with the Milky Way (135, A. P. Jones et al., 2017) and local values (Dunne et al., 2021). We computed the SFR taking into account the contribution of the luminous QSO to the dust heating with a factor of 50% (Duras et al., 2017), and we obtained SFR$\sim$ 150 $M_\odot$ yr^{-1}, in agreement with the broad range suggested by J. Yang et al. (2020). By using the [CII] line detection and a single continuum measurement at 231 GHz, and assuming $T_{\text{dust}} = 47$ K and $\beta = 1.6$, they found a SFR in the range 80 to 700 $M_\odot$ yr^{-1}. However this value has a large systematic uncertainty since T_{dust} is not determined. Observations in ALMA Band 9 are needed to possibly resolve the host galaxy and tightly constrain both T_{dust} and SFR (Tripodi et al., 2023a).

J0100+2802-C

We analysed the continuum emission at 252.8 GHz (Band 6) and 99.5 GHz (Band 3) of J0100+2802, belonging to the dataset 2021.1.00211.S (PI: R. Maiolino) from the ALMA 12m array. We imaged the continuum in Band 6 and Band 3 using the multi-frequency synthesis (MFS) mode in all line-free[5] channels, selected by inspecting the visibilities in all 4 spectral windows. The r.m.s noise reached for the continuum in Band 6 is 0.01 mJy/beam, and we obtained a clean beam of (1.03 × 0.78) arcsec^2; in Band 3, the r.m.s noise is 5 μJy/beam, and we obtained a clean beam of (2.59 × 1.95) arcsec^2.

The middle-left panel of Fig. 3.9 shows the 253 GHz dust continuum map. The continuum shows an elongated structure westwards, coincident with the [CII] elongation (black contours, see Sect. 3.3). Analogously to the [CII] analysis, we performed a 2D Gaussian fit in the region enclosing the QSO emission, and we derived a peak flux of 0.81 ± 0.02 mJy/beam and a flux density of 1.16 ± 0.05 mJy, that is consistent with the flux 1.26 ± 0.08 mJy found by F. Wang et al. (2019). We computed the flux density from the continuum map in a region with

---

[5] [CII] is detected in channels 90-240 for spw2 and 0-40 for spw3. CO(6-5) is detected in channels 95-145 for spw3.

S/N> 2, obtaining 1.44 ± 0.05 mJy, and we subtracted the PSF normalized to the QSO peak flux from the continuum map. The emission in the PSF-subtracted continuum extends for ~4 arcsec from the centre westwards (see central right panel of Fig. 3.9), i.e. similar extension and clumpiness as the [CII] emission. This supports the scenario in which the extended [CII] emission is associated with an interacting system and not an outflowing/jetted component. The flux density obtained in the PSF-subtracted continuum map inside a region with S/N> 2 and RA-offset< -1.3 arcsec is 0.25 ± 0.01 mJy. Therefore, the QSO continuum flux is 1.19 ± 0.06 mJy, consistent with the one computed from the 2D fit, and is unresolved at our resolution. The whole emission from the interacting system is spatially resolved with a FWHM size of $(0.68 \pm 0.09)\times(0.54 \pm 0.12)$ arcsec^2, corresponding to $\sim (3.84 \times 3.05)$ kpc^2 at the rest frame.

We performed a similar analysis for the continuum emission at 99.5 GHz (bottom left panel of Fig. 3.9), in order to determine whether the companion emission was detected. By doing a 2D Gaussian fit, the source has a peak flux 0.04 ± 0.004 mJy/beam and a flux density of 0.05 ± 0.007 mJy. The morphology of the emission is asymmetric and slightly elongated westwards, and coincident with the interacting companion. The elongated feature is less evident than in the Band 6 continuum, since the resolution in Band 3 is ~ 2 times lower. We subtracted the PSF normalized to the QSO peak flux, and indeed we found emission at 3σ in the same region of the companion emission in Band 6. In this case, the emission seems to extend up to -5 arcsec RA-offset from the center, however this can be an artefact caused by the low resolution. Therefore, we conservatively extracted the continuum flux for the companion from the 2σ contours enclosed in the region with RA-offset> -4 arcsec, obtaining 0.007 ± 0.002 mJy.

The dust SED of the QSO has been previously studied with high accuracy by Tripodi et al. (2023a) (see also Sect. 4.3.2). Both in the low and high frequency previous observations there were no signatures of a companion, probably due to a combination of low sensitivity and high resolution which were filtering out the extended emission (F. Wang et al., 2019; Tripodi et al., 2023a). Using our new ALMA observations in Band 3 and Band 6, we were able to detect an interacting companion and disentangle its emission from the one of the QSO. Fig. 4.16 shows the SED of the dust emission associated to the companion derived from the measurements in Band 3 and Band 6. We modelled it with a MBB function as described in Sect. 4.2. The solid angle is estimated using the size of the region where we extracted the flux of the companion, that is ~ 4.0 arcsec^2.

We considered one free parameter, $M_{\rm dust}$, and we fix $T_{\rm dust} = 50$ K, since $T_{\rm dust}$ cannot be constrained due to the lack of higher frequency data and we assume a temperature similar to that found for the QSO ($T_{\rm dust,QSO} = 48 \pm 2$ K, see Tripodi et al., 2023a). We explored the one dimensional parameter space using a MCMC algorithm implemented in the `EMCEE` package (Foreman-Mackey et al., 2013), assuming a uniform prior for the fitting parameter: $10^4\ {\rm M}_\odot < M_{\rm dust} < 10^{12}\ {\rm M}_\odot$. Considering β to be in the range [1.0,3.0], we ran a MCMC with 20 chains and 1000 trials for each value of β in that range with a step of 0.1. We found that only models with $2.0 \le \beta \le 2.7$ are able to fit simultaneously the two points in Band 6

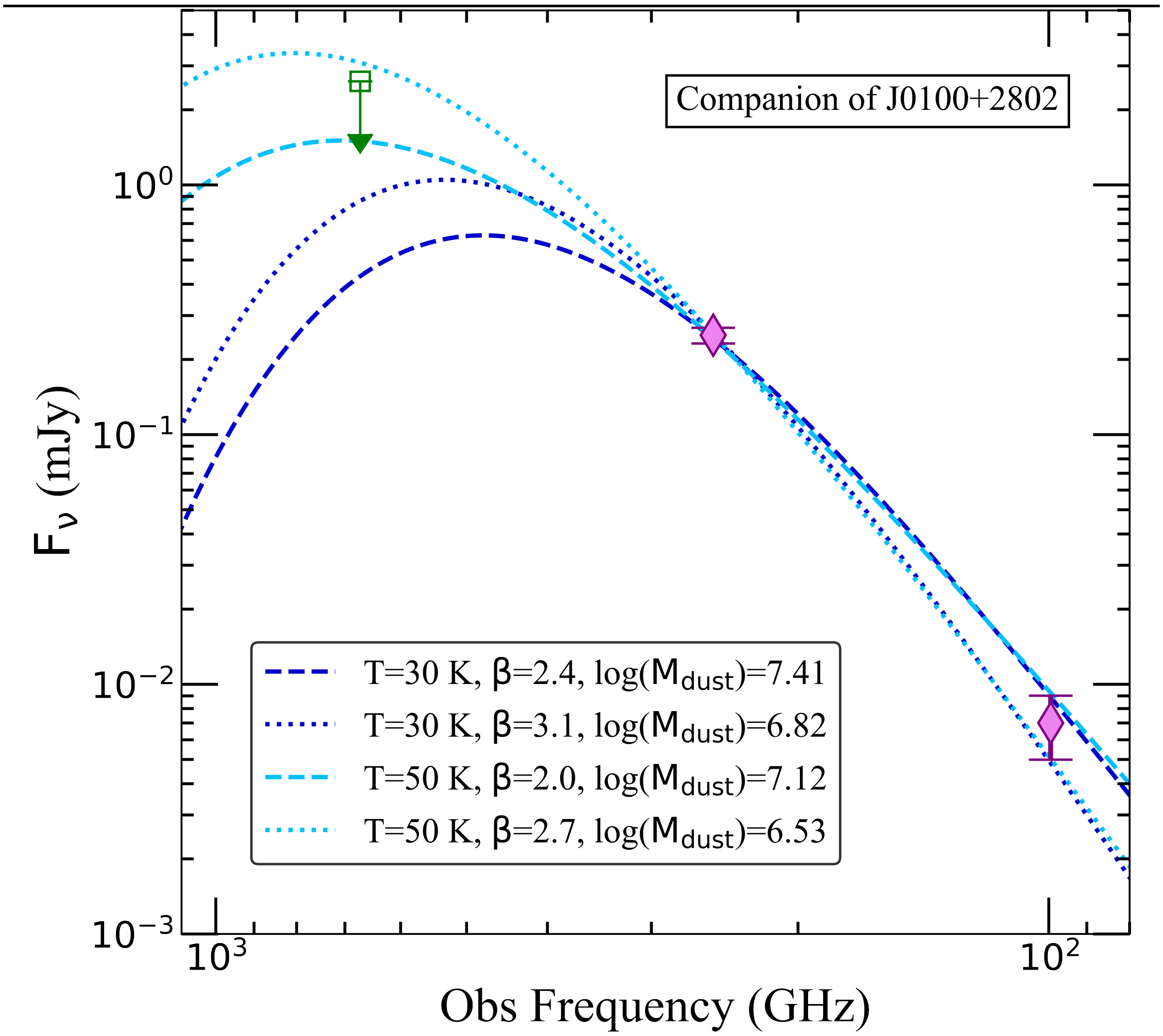

Figure 4.16: *SED of the interacting companion of J0100+2802, using our ALMA data at 252.8 GHz and 99.5 GHz. The best fitting curve at fixed* $T_{\rm dust}$ = 50 *K and* β = 2.0 (β = 2.7) *is shown as a cyan dashed (dotted) line; the curves at fixed* $T_{\rm dust}$ = 30 *K and* β = 2.4 (β = 3.1) *is shown as a blue dashed (dotted) line. The green hollow square is the upper limit derived in Band 9. The estimated value of the dust mass for each model is reported in the legend.*

and Band 3, yielding 0.34×10^7 M$_\odot$ < $M_{\rm dust}$ < 1.3×10^7 M$_\odot$, with burn-in phases of ∼ 20 for each model. The best fitting model with $T_{\rm dust}$ = 50 K, β = 2.0 and $M_{\rm dust}$ = 1.3×10^7 M$_\odot$ is shown as a cyan dashed line in Fig. 4.16, and the one with $T_{\rm dust}$ = 50 K, β = 2.7 and $M_{\rm dust}$ = 3.4×10^6 M$_\odot$ as a cyan dotted line. The recent ALMA 7m observation in Band 9 did not detected any companion emission, probably due to the low resolution and sensitivity of the observation (Tripodi et al., 2023a). However, we were able to derive a 3σ upper limit from the continuum map presented in Tripodi et al. (2023a), that is 2.6 mJy. This upper limit is shown as a green hollow square and favours temperatures ≤ 50 K (and β > 2.0 for $T_{\rm dust}$ = 50 K). We have considered a lower $T_{\rm dust}$ of 30 K, and we performed similar MCMC fitting, yielding $2.4 \leq \beta \leq 3.1$ and 0.7×10^7 M$_\odot$ < $M_{\rm dust}$ < 2.6×10^7 M$_\odot$, with burn-in phases of ∼ 20 for each model. The dashed and dotted blue lines are the best fitting curves at $T_{\rm dust}$ = 30 K, β = 2.4, $M_{\rm dust}$ = 2.6×10^7 M$_\odot$, and $T_{\rm dust}$ = 30 K, β = 3.1, $M_{\rm dust}$ = 6.7×10^6 M$_\odot$, respectively.

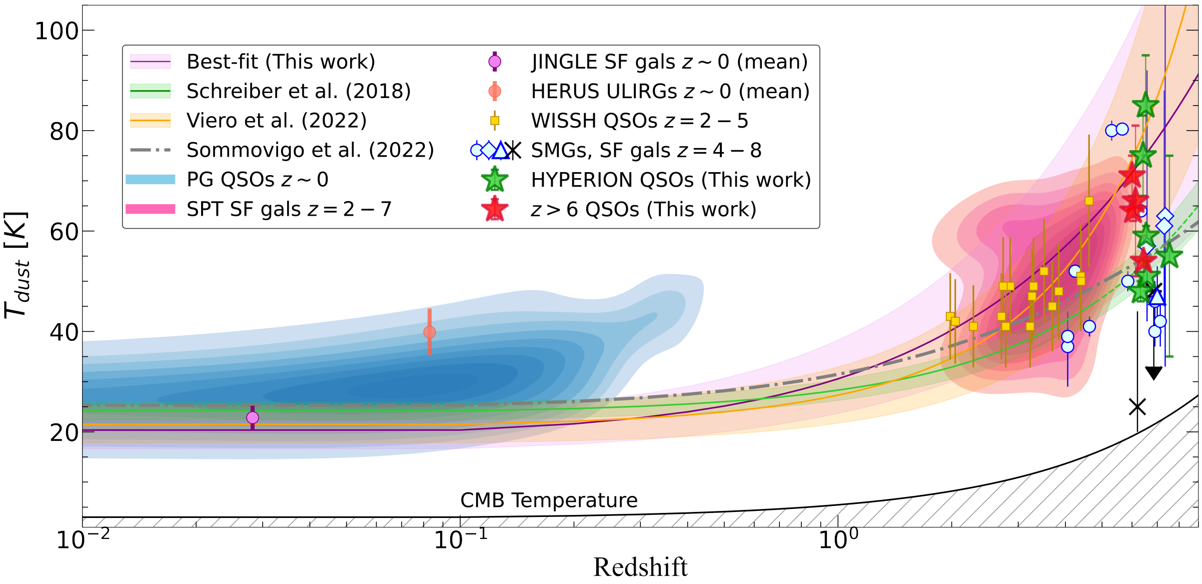

Figure 4.17: *Dust temperature as a function of redshift. Our sample is shown as stars (red for HYPERION QSOs, green otherwise). Top panel: we compare our results with samples of local QSOs (PG, blue colormap with contours, Petric et al., 2015), local star-forming galaxies (JINGLE, mean value as pink dot, Lamperti et al., 2019), local ULIRGs (HERUS, mean value as orange dot, Clements et al., 2018),* $2 < z < 7$ *star-forming galaxies (SPT, pink colormap with contours Reuter et al., 2020),* $2 < z < 5$ *QSOs (WISSH, yellow squares, Duras et al., 2017),* $4 < z < 7.5$ *SMGs and star-forming galaxies (light blue dots, Witstok et al., 2023), three* $z > 6.7$ *REBELS galaxies (light blue diamonds, Algera et al., 2023), average-REBELS galaxy (light blue triangle, Sommovigo et al., 2022), and two galaxies with very low dust temperatures at* $z > 6$ *(black crosses, Witstok et al., 2022; Harikane et al., 2020). The observed trends inferred by Viero et al. (2022) and Schreiber et al. (2018) are shown as an orange and green lines and shaded regions, respectively. Our best-fitting curve is shown as a purple line with shaded region. The theoretical relation found in Sommovigo et al. (2022) is shown as a dashed gray line. The black solid line marks the CMB temperature level.*

We also estimated the TIR luminosity for the four best fitting models by integrating from 8 to 1000 μm rest-frame, obtaining $L_{\rm TIR}$ in the range $[0.3 - 3.4] \times 10^{12}$ $L_{\odot}$. This implies an SFR in the range [52 − 515] $M_{\odot}$ yr^{-1}. Tab. 4.5 lists the gas and dust properties of the QSO's host and the companion.

4.4 Properties of our sample

In this section, I will contextualize our findings concerning the dust within our high-z QSO sample, conducting a comparative analysis with the characteristics observed in lower-z sources.

Our final sample comprises 10 QSOs at $6 \lesssim z < 7.5$, out of which six belong to the HYPERION sample. In the previous sections, we analysed the cold dust spectral energy distribution in a homogeneous way for all quasars, and the results are summarised in Tabs. 4.3 and 4.4. In the following, I will briefly describe the compilation of galaxy and AGN hosts samples used for comparison.

For the local Universe we considered the JCMT dust and gas In Nearby Galaxies Legacy Exploration (JINGLE) survey, the *Herschel* (U)LIRG Survey (HERUS), and a sample of QSOs selected from the Palomar-Green (PG) survey (as also done in Witstok et al., 2023). The JINGLE sample is composed of 192 nearby ($0.01 < z < 0.05$) galaxies, for which Lamperti et al. (2019) studied their cold dust SED using photometric data in the 22-850 μm range from *Herschel*, applying a hierarchical Bayesian fitting approach. We use the dust properties derived from their two MBBs models, which also take into account the warm dust component, in the optically thin regime. These results are in good agreement with those from a single MBB model. The HERUS sample comprises 43 nearby (ultra)-luminous infrared galaxies or (U)LIRGs observed with the *Infrared Astronomical Satellite* (IRAS) and *Herschel* (D. B. Sanders et al., 2003; Clements et al., 2018). Clements et al. (2018) derived the dust properties for this sample assuming a MBB function in the optically thin regime. Witstok et al. (2023) recalculated the dust properties of the JINGLE and HERUS datasets, employing a method analogous to ours (see Sect. 4.2 and Witstok et al. 2022), except for the variation in the chosen opacity model. Their results are in agreement with those presented in Lamperti et al. (2019); Clements et al. (2018) within the uncertainties. Therefore, for the sake of simplicity, we will use the results from the original papers. The dust properties of the PG sample, consisting of 85 nearby QSOs, are obtained by Petric et al. (2015) modelling the photometry taken by *Herschel* by means of an MBB function with β fixed to 2.0 and the dust model of Draine et al. (2007)[6].

At higher redshift we selected a sample of 81 $2 < z < 7$ strongly gravitationally lensed, dusty star-forming galaxies identified by SPT. Reuter et al. (2020) analysed the cold dust SEDs of the objects in this sample employing a MBB function in the optically thick regime with β fixed to 2. We also included the dust properties inferred for 16 QSOs belonging to the WISE-SDSS selected hyper-luminous (WISSH) sample at $2 < z < 5$ (Duras et al., 2017). Their SEDs were analysed accounting for the cold dust, dusty torus and warm dust emission components. In particular, the cold dust emission was modelled by a MBB function in the optically thin regime with $\beta = 1.6$. Finally, at $4 < z < 7.5$ we considered a sample composed of 3 submillimetre galaxies (SMGs) and 8 star-forming (SF) galaxies from Witstok et al. (2023). As stated before, they adopt a model for SED fitting analogous to ours. For the QSO's host galaxy samples, we note that the PG QSOs have lower bolometric luminosity $L_{\rm bol}$ compared to our $z \gtrsim 6$ sample ($L_{\rm bol,PG} =\sim 10^{44-47}$ erg s^{-1}), whereas the WISSH quasars are the most luminous with $L_{\rm bol,WISSH} >\sim 10^{47.5}$ erg s^{-1} (see e.g., Vietri et al., 2018).

In the last few years, the trend of $T_{\rm dust}$ as a function of time has been the object of multiple studies (e.g., Faisst et al., 2017; Schreiber et al., 2018; Sommovigo et al., 2020; Bakx et al., 2021; Viero et al., 2022). However, the behaviour of the $T_{\rm dust} - z$ relation - increasing or plateauing at $z > 4$ - has remained unclear. Fig. 4.17 presents the redshift distribution of dust temperatures in our sample compared to the comparison samples described above.

---

[6] They also derived the dust properties using the dust model of Compiègne et al. (2011) with $\beta = 1.91$ finding that the dust masses are systematically larger by about 20%-40%when adopting the Draine & Li's model.

Additionally, we display the average $T_{\rm dust}$ derived for REBELS[7] galaxies by Sommovigo et al. (2022) as a light blue triangle, and $T_{\rm dust}$ found for three REBELS galaxies at $z > 6.7$ by Algera et al. (2023) as light blue diamonds. As a word of caution, the dust temperatures for REBELS galaxies derived in Sommovigo et al. (2022) carry large uncertainties since they are based on a single photometric point in Band 6. Hence, in this context, we exclusively present the mean value. Algera et al. (2023) analysed Bands 8 and 6 observations of REBELS-12[8], REBELS-25 and REBELS-38 considering both optically thin and thick cases. Here we present the results for the optically thick case, fixing $\beta = 1.5$. Since relying only on two photometric points per galaxy, the inferred $T_{\rm dust}$ are still uncertain ($\Delta T_{\rm dust} = 30 - 60\%$); the results obtained in the thin and thick regime agree within the large uncertainties. To make the plot clearer, we show the mean values of the temperature distribution for the JINGLE and HERUS samples with their corresponding standard deviation[9]. Interestingly, there is no significant difference in $T_{\rm dust}$ between QSOs and normal SF galaxies at fixed redshift, also considering that our sample is biased towards high-luminosity and therefore possibly higher dust temperatures. We observe an increasing trend of $T_{\rm dust}$ with redshift that is naturally expected from a theoretical perspective as a result of decreasing gas depletion times, as seen in Sommovigo et al. (2022). They theoretically derived that $T_{\rm dust} \propto t_{\rm dep}^{-1/6} \propto (1+z)^{5/2(4+\beta)}$, where β is the dust emissivity index. This $T_{\rm dust} - z$ relation is shown in Fig. 4.17 (dash-dotted gray line) for $\beta = 2.03$ and assuming optical depth and metallicity (in solar unit) both equal unity, as presented in Sommovigo et al. (2022), implying $T_{\rm dust} \propto (1+z)^{0.42}$. This theoretical relation is able to reproduce the trend observed in many SF galaxies (e.g., considering REBELS and ALPINE galaxies), and in Schreiber et al. (2018) from the stacking of star-forming galaxies at $0.5 < z < 4$ in the deep CANDELS fields. The stacked SEDs have been fitted with a library of template SEDs generated with $\beta = 1.5$. Schreiber et al. (2018) found a linear trend with redshift, and we show also an extrapolated curve at $z > 4$ as dashed green line.

On the other hand, the population of SPT SF galaxies, QSOs and SF with $T_{\rm dust} > 60$ K shows a steeper increase of $T_{\rm dust}$ with z, which is well captured by the observed relation inferred by Viero et al. (2022). They employed stacked maps in the FIR/sub-mm of 111227 galaxies at $0 < z < 10$ from the COSMOS2020/FARMER catalogue to derive dust temperatures at different redshift. Their observed relation for $T_{\rm dust}(z)$, which is a second-order polynomial in z, is in good agreement with the observed trend of the WISSH QSOs, with the sources at $z > 5$ that shows the most extreme temperatures ($\sim 70 - 80$ K), and with the lower limit of Bakx et al. (2020) and estimate of Behrens et al. (2018) based on data from Laporte et al. (2017) (see Viero et al., 2022). However, it fails to describe the bulk of the PG QSOs and HERUS ULIRGs, and the sources at $z > 5$ with temperatures below 60 K (Faisst et al. 2020; Béthermin et al. 2020; Hashimoto et al. 2019; Sommovigo et al. 2022, see Viero et al. 2022). As a word of

---

[7] 'Reionization Era Bright Emission Line Survey' (REBELS; PI: Bouwens) is an ALMA large program targeting 40 of the brightest known galaxies at $z > 6.5$ (Bouwens et al., 2022).

[8] The Band 8 continuum of REBELS-12 was undetected, therefore they derived an upper-limit.

[9] For both samples, the mean value of the distribution corresponds to the median.

caution, these latter low temperature estimates are very uncertain, given that they are derived from ALMA observations that did not actually bracket the peak of the SED and therefore not adequate to model hotter dust components.

In order to find a general relation that can be applied to SF galaxies, SMGs and QSOs' host galaxies at high-z, we fitted the observed data (excluding the stacked results) adopting the parametrization of $T_{\rm dust}(z)$ theoretically found in Sommovigo et al. (2022), therefore using a power law of the form:

$$T_{\rm dust}(z) = A \times (1 + z)^{B} \tag{4.6}$$

where A and B are free fitting parameters. The latter is linked with β, since $\beta = -4 + 5/2B$ (considering the derivation of Sommovigo et al. 2022). We found $A = 19 \pm 2$ K and $B = 0.7 \pm 0.1$, implying a value of β that is non physical. This underlines that $T_{\rm dust}$ does not depends uniquely on redshift, especially when considering different galaxy populations. Indeed, Sommovigo et al. (2022) pointed out that at fixed redshift the scatter in $T_{\rm dust}$ derive from variations either in optical depth or in metallicity. This is a likely scenario for different galaxy populations. Our best-fitting function, shown as a purple line and shaded region in the top panel of Fig. 4.17, slightly less steep than Viero's at $z > 1$, but still agrees with it pretty well in both the low- and high-z regimes. The majority of the sources are within the uncertainties, including those from Schreiber et al. (2018). Therefore, our parametrization captures both the flattening and the increasing trends at $z > 4$, i.e., describes the populations with both higher and lower $T_{\rm dust}$. Three sources belonging to the sample of Witstok et al. (2023), SPT0311-58W, SPT0311-58E and A1689-zD1, are in agreement only within 2σ from our relation, along with other three sources well known for their low dust temperatures (J0217-0208, COS-3018555981, and REBELS-25, see Witstok et al., 2023; Witstok et al., 2022). As a word of caution, the dust temperature estimated for J0217-0208, COS-3018555981 suffers of large uncertainties, given the poor data available for both sources (one or two detections and an upper limit) and the assumption of $\beta = 1.5$. In particular, for COS-3018555981, we show the upper limit on $T_{\rm dust}$ derived in Witstok et al. (2022). Even if excluding these two sources from our fit of $T_{\rm dust} - z$ relation, our results would not change.

Now, our focus is directed towards the investigation of β, which is physically related to the microscopic properties of dust. Fig. 4.18 shows the redshift distribution of β for our sample and the comparison samples. As also found in Witstok et al. (2023), β is approximately constant as a function of z with a value of $\sim 1.6 \pm 0.2$ (see also Beelen et al., 2006), indicating that the effective dust properties do not change drastically. Also in this case there is no difference - on average - between the QSOs belonging to the HYPERION sample and the others. As a word of caution, we note that high-z sample are biased towards high luminosity and this can introduce a bias towards lower values of β (see also Witstok et al., 2023). There are only three exceptions that show β higher than 2, all in the high-z regime: J0100+2802, J036+03 from our sample, and GN10 from Witstok et al. (2023). It is not straightforward to assess the

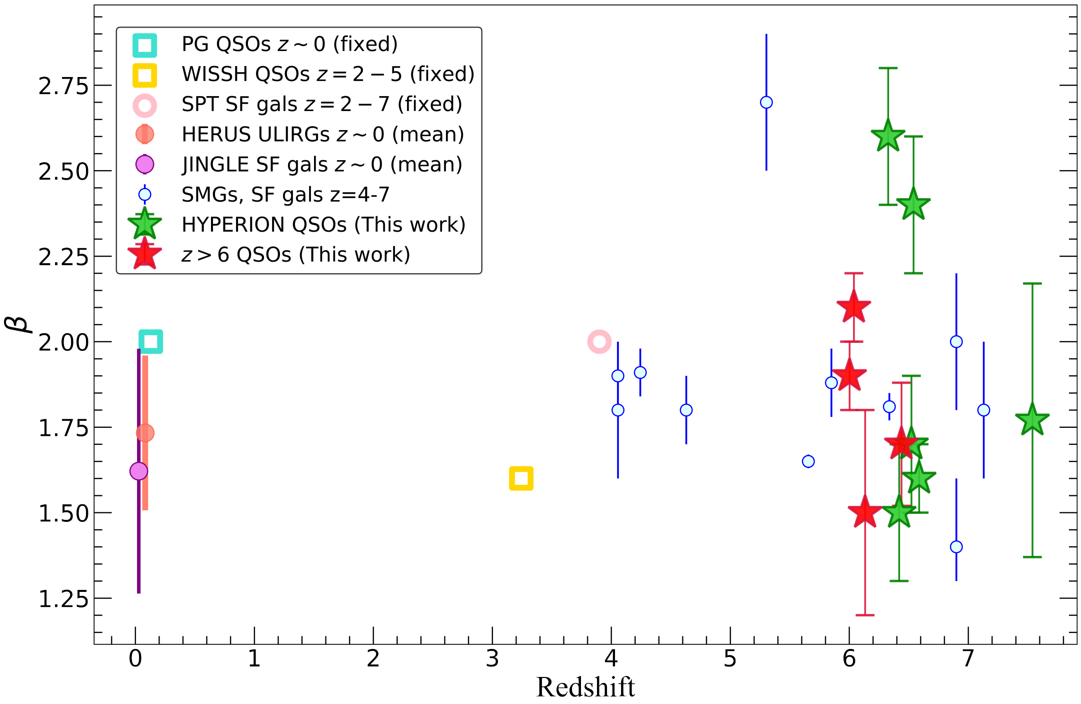

Figure 4.18: *Dust emissivity index, β, as a function of redshift. Symbols and colors are the same as Fig. 4.17. For the PG, WISSH and SPT samples, the symbols are empty to indicate that the value of β in these cases are fixed and not derived from SED analyses.*

physical reasons of these high β value. In principle, β depends on the physical properties and chemical composition of the grains, and possibly on environment and temperature. There are cases in which β can be larger than 2 (see e.g., Valiante et al., 2011; Galliano, Galametz, and Anthony P. Jones, 2018). Spatially resolved studies in low-z galaxies showed a spread of β within a single galaxy, probably due to the temperature mixing or the different properties of the grain populations, or a combination thereof. A physical explanation for the high value of β would require studies of the properties of the dust grains and/or of a detailed analysis of the temperature mixing and is beyond the scope of this work.

In Fig. 4.19, we compare the SFR vs dust mass of our sample with results from the PG and WISSH sample of QSOs. Within our sample, 5 QSOs are the first at $z > 6$ for which the SFR has been derived with the smallest statistical uncertainty thanks to high frequency observations. As already mentioned in Sect. 4.3, the uncertainty of $\sim 40\%$ on $T_{\rm dust}$ of J1342+0928 strongly affect the determination of the SFR, that has a large uncertainty. Therefore, this QSO is marked with a green circle in the plot. A correlation between the dust content and the star formation activity is evident in all the three samples, which are at different redshifts, with some scatter. This correlation is thought to be a consequence of the Schmidt-Kennicutt relation, linking the SFR to the gas content (see e.g., Santini et al., 2014). As shown later below, the dust mass is related to the gas mass by means of the GDR. Overall, the SFR is higher in the highest-z samples (by $\sim$ 2 order of magnitudes on average), supporting the well-known concept that high-z QSOs are hosted in highly star-forming galaxies. The dust masses are higher at high-z as well, by $\lesssim$ 2 order of magnitudes on average. Observations of galaxies at low- and high-z

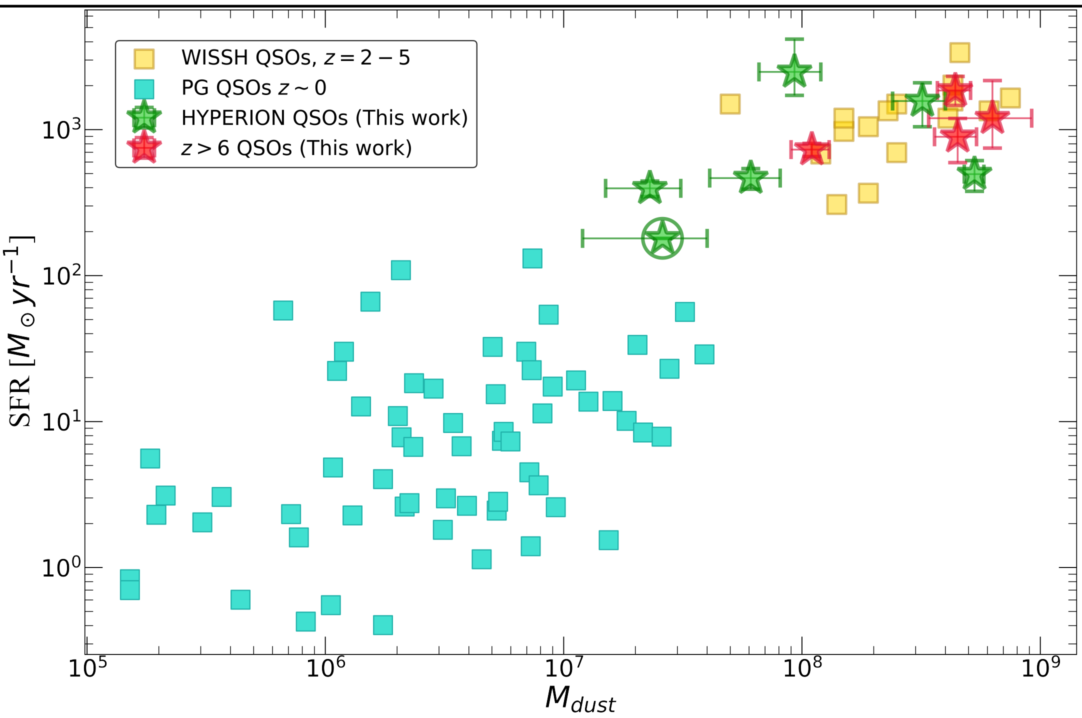

Figure 4.19: *Star formation rate as a function of dust mass. Symbols and colors are the same as Fig. 4.17. SFRs for the WISSH and our sample are corrected for a factor of 50% to take the AGN contribution to the dust heating into account.*

(Dunne et al., 2011; Driver et al., 2018; Pozzi et al., 2020; Beeston et al., 2018) found that the amount of dust in galaxies has decreased by a factor of $\sim 2-3$ during the last $\sim$ 8 Gyr, and it has been recently reproduced by Parente et al. (2023) using the semi-analytic model (SAM) L-GALAXIES2020. Considering an average value, we also observe a mild increase of dust mass from our HYPERION sample ($M_{\rm dust,HYP}^{\rm mean} = 1.8 \times 10^8$ M$_\odot$) to the WISSH sample at lower-z ($M_{\rm dust,WISSH}^{\rm mean} = 3 \times 10^8$ M$_\odot$), and followed by a drop of 2 orders of magnitude at $z \sim 0$. Interestingly, here we observe a difference within our sample: HYPERION QSOs have -on average- smaller dust mass than the others, of ~ 1 order of magnitude. However, this is a preliminary result, since 2/3 of the sample still has to be analysed, and we are going to design future ALMA and NOEMA observation to complete the overview of the sample. Even though we focused on QSOs, it is important to remind that the relation between SFR and dust mass has also been studied in normal galaxies (Santini et al., 2014; da Cunha et al., 2010; Hjorth, Gall, and Michałowski, 2014). Santini et al. (2014) used *Herschel* observations to estimate the dust mass of a large sample of galaxies extracted from the GOOD-S, GOOD-N and COSMOS fields, and performed a stacked analysis on a grid of redshifts, stellar masses and SFR. Similarly to us, they found correlations between SFR and dust mass at different redshifts, from the local Universe out to $z = 2.5$. Their analysis revealed no clear evolution of the dust mass with redshift at a given SFR and stellar mass, indicating that galaxies with similar properties (in terms of SFR and stellar mass) do not show significant difference in terms of dust content across the cosmic epochs, out to $z = 2.5$. Regarding the samples of QSOs considered in our work, it is challenging to assess whether or not there is an evolution

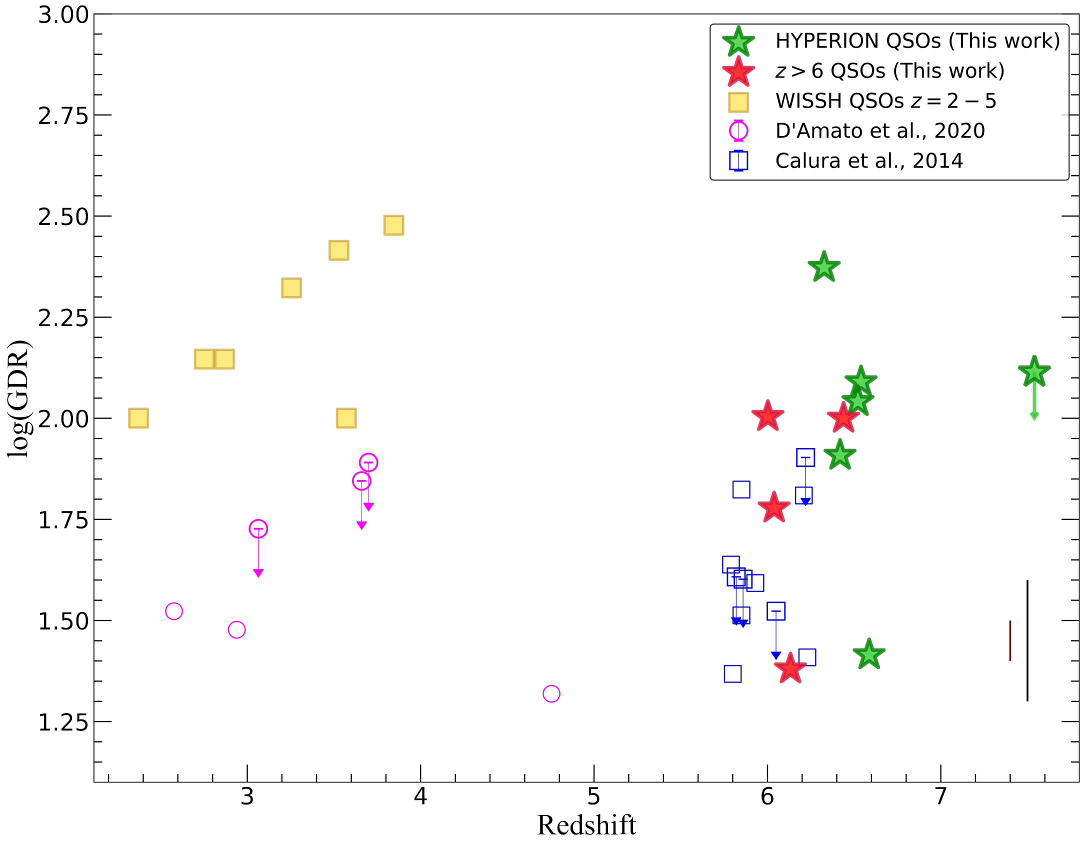

Figure 4.20: *Redshift distribution of gas-to-dust ratio (GDR). Symbols and colors for the WISSH and our sample are the same as Fig. 4.17. We compare our results with the WISSH sample (Bischetti et al., 2021), a sample of* $2 < z < 5$ *star-forming galaxies hosting a heavily obscured AGN in the Chandra Deep Field-South (magenta dots, D'Amato et al., 2020), and a sample of* $z > 5.5$ *QSOs (blue squares Calura et al., 2014). The vertical black line (0.3 dex) and the vertical brown line (0.1 dex) are the systematic uncertainties induced by the choice of* $\alpha_{\rm CO}$ *and* r_{65} *or* r_{76} *in computing the gas mass.*

of $M_{\rm dust}$ with z at fixed SFR as the statistics is still poor at high-z, especially for the low $M_{\rm dust}$ regime. Moreover, we are not able to explore the relation involving the stellar mass in our sample, since M_* estimates are not available yet for our high-z sample. Certainly future JWST campaigns devoted to the investigation of the stellar content in QSOs and galaxies at $z \gtrsim 6$ will allow us to perform these studies in detail (as done in e.g., Harikane et al., 2023; Santini et al., 2023).

Finally, in Fig. 4.20, we present the redshift distribution of the GDR in our sample compared with the WISSH sample (Bischetti et al., 2021), a sample of $2 < z < 5$ star-forming galaxies hosting a heavily obscured AGN in the Chandra Deep Field-South (magenta dots, D'Amato et al., 2020), and a sample of $z > 5.5$ QSOs (blue squares Calura et al., 2014). D'Amato et al. (2020) derives the dust mass by modelling the SEDs with a MBB in the optically thin regime assuming $\beta = 2.0$, and Calura et al. (2014) also adopt a MBB in the optically thin regime but assuming both $T_{\rm dust} = 47$ K and $\beta = 1.6$ since both these works mostly rely on single data point at 250 GHz. Therefore, these latter estimates for $M_{\rm dust}$ are highly uncertain and, for instance, $M_{\rm dust}$ (GDR) would be ~ 2.4 times lower (higher) if a lower temperature,

$T_{\rm dust}$ = 33 K, was assumed. Systematic uncertainties are also significant when deriving the gas mass from CO transitions higher than J=1-0, since this require assuming a scaling between the luminosity of the considered CO transition and of CO(1-0) (see Sect. 3.2). This correction depends on the CO excitation ladder, which may vary from source to source depending on the ISM conditions. Given the large systematics in the gas mass determination (0.2-0.3 dex for $\alpha_{\rm CO}$, and 20-30% for r_{65} or r_{76}), we do not include error bars in the GDR plot. Though, we do stress that the dust masses in our sample are derived with the smallest statistical uncertainties. This has never been achieved before in a sample of QSOs at $z \gtrsim 6$. In low-z galaxies, a GDR$\sim$ 100 is typically observed (e.g., Draine et al., 2007; Leroy et al., 2011), while studies of massive star forming galaxies and SMGs out to $z \sim 3-5$ found a GDR possibly increasing with z, with typical GDR$\sim$ 120 – 250 at $z \sim 2-4$ (e.g., Saintonge et al., 2013; Miettinen et al., 2017). Overall, the WISSH sample and our sample of QSOs show -on average- GDRs above 100 (value that is also commonly assumed when deriving the dust mass). In particular, our HYPERION QSOs show -on average- the highest GDRs (GDRs> 100) among the sources at $z > 6$. Two QSOs, J1319+0950 and J231-20, exhibit particularly low (< 50) GDRs, comparable with other QSOs from Calura et al. (2014). The two regimes of GDRs in our sample, i.e., GDR> 100 and GDR< 50, can be attributed mostly to the different values of dust masses, given that the gas masses are approximately around $\sim 10^{10}$ for all the sources (see Sect. 3.2). Indeed, both J1319+0950 and J231-20 have the largest dust masses in our sample, $M_{\rm dust} \sim 5-6 \times 10^{8}$ M$_{\odot}$.

CHAPTER 5

EVOLUTIONARY PATHS OF HIGH-Z QSOS AND THEIR HOST GALAXIES

In Chap. 1, I showed that BH masses of luminous QSOs at $z \gtrsim 6$ can be extremely high for their cosmic epoch, of the order of $\gtrsim 10^9$ $M_\odot$. The temporal window within which they could have accrued their mass spans approximately 650-750 Myr (considering a possible seeding era at $z = 15 - 22$). These masses are not lower than those of hyper-luminous QSOs at lower redshift, meaning that BH growth had to be a fast process, and that the process had to stop with a similar high efficiency after the rapid build-up.

The correlations between massive BHs and bulges are tight, suggesting that the same process that assembled galaxy bulges may be responsible for most of the growth of massive BHs. Which, between the galaxy and the BH, is the regulator of the process, and how this correlation has been established are highly debated open questions in astrophysics (M. Volonteri, 2010; M. Volonteri, 2012; Johnson and Haardt, 2016). One can envisage three possible growth paths for the BH-galaxy system (see Fig. 5.1). Following the red arrow, massive BHs may have grown in symbiosis with their hosts; following the green arrow, the black hole may have dominated the process growing first, with the galaxy catching up at later times; or following the blue arrow the galaxy grew first, and the black hole adjusted to its host. However, current observations show that high-z QSOs may lie above the local $M_{\rm BH}$ - $M_{\rm dyn}$ correlation[1], thus they likely follow the BH-dominance growth or BH-dominance evolutionary path (i.e. the green line, see Fig. 5.1, M. Volonteri, 2012). Once started, it is unknown what slowed down the BH growth, and when this process occurred, leading towards the symbiotic growth with the host galaxy observed in the local Universe. Candidate processes are inefficient gas accretion and/or feedback through BH winds. At the same time, the host galaxies of high-z QSOs are likely growing rapidly. Therefore, the onset of significant BH feedback hampering BH growth would

---

[1] As mentioned in Sect. 1.1.3, SMBH masses may be overestimated of a factor of 10 or more if considering the effect of possible winds on the BL clouds. This may drastically change the picture of formation and evolution of BH, relaxing the problem involving the existence of SMBHs at $z \sim 6$.

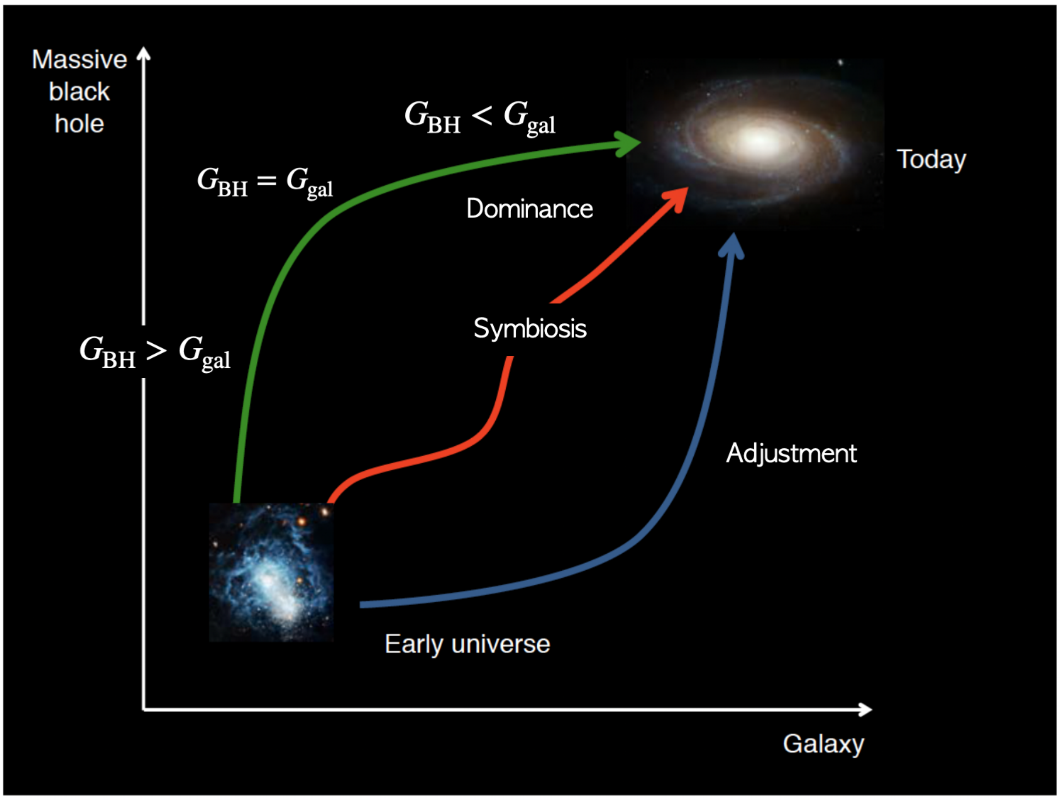

Figure 5.1: *Possible routes to massive BH and galaxy co-evolution, starting from black holes forming in distant galaxies in the early universe. Adapted from M. Volonteri (2012).*

mark the transition from a phase of BH dominance to a phase of symbiotic growth of the BH and the galaxy. Cosmological hydrodynamic simulations of early BH and galaxy evolution support this scenario by identifying z~6-7 as the transition epoch during which QSO feedback increases in strength and starts to significantly slow down BH growth. In this context, the QSO host galaxies provide a unique opportunity to characterize both the physical properties of the ISM in such extreme conditions (e.g. Bertoldi et al. 2003a; Bertoldi et al. 2003b; Decarli et al. 2018; B. P. Venemans et al. 2020; Neeleman et al. 2021; Pensabene et al. 2021), and to study the formation and build-up of massive galaxies in the early Universe in detail.

In this chapter, I will investigate the evolutionary paths of the 10 QSOs in our sample, exploiting the results about the properties of their host galaxies derived in Chaps. 3 and 4.

5.1 Observational evidences

Focusing on the green line of Fig. 5.1 that seems to be the most likely scenario of formation of local massive galaxies, we can distinguish two big regimes: the first characterized by an intense and predominant growth of the BH; the second one marked by an intense and predominant growth of the host galaxy[2]. Additionally, one can imagine a transition phase when the growth

---

[2] As a note of caution, we must emphasizes that during the BH (galaxy) dominated regime, the galaxy (BH) is still growing, but slower and/or less efficiently than the BH (galaxy).

of the two components are almost in perfect balance (a symbiotic growth). Already at $6 < z < 8$, SMBHs have reached masses akin to those observed in the most massive local galaxies (see e.g. Fig. 1.20). This implies that SMBH growth has to slow-down and therefore, at these redshifts, we likely be able to witness QSOs in their transition phase towards the galaxy regime or in the galaxy regime. That is high-z QSOs are moving towards the local relation in the $M_{\rm BH} - M_{\rm dyn}$ plane.

In the following, we quantitatively characterize the three different regimes outlined above (BH dominated, galaxy dominated, symbiotic). For this purpose, we can define the growth efficiency of the galaxy as $G_{\rm gal} = {\rm SFR}/M_{\rm gal}$, where $M_{\rm gal} = M_{\rm dyn} - M_{\rm BH}$ is the mass of the galaxy, and the SFR is corrected for the QSO contribution. This term is a lower limit to the specific SFR of the galaxy defined as ${\rm SFR}/M_*$ that, in principle, might be a better probe of the galaxy growth. We do not use the specific SFR since the stellar mass is not yet available for most high redshift QSOs[3]. We derive the BH growth efficiency as $G_{\rm BH} = (1-\epsilon)\dot{M}_{\rm BH}/M_{\rm BH}$, where ϵ is the radiative efficiency, $\dot{M}_{\rm BH}$ is the BH accretion rate that depends on the bolometric luminosity of the source. We assume $\epsilon = 0.1$ (e.g., Marconi et al., 2004) and we use the BH mass derived from the MgII emission line. Comparing these two terms we distinguish among (1) $G_{\rm BH} > G_{\rm gal}$ or black hole dominance regime; (2) $G_{\rm BH} = G_{\rm gal}$ or symbiotic growth; (3) $G_{\rm BH} < G_{\rm gal}$ or galaxy dominance regime. The proportionality factor between $G_{\rm BH}$ and $G_{\rm gal}$ that allows to discriminate among these different regimes can be straightforwardly translated into an angle, i.e., an angle $> 45°$ corresponds to the BH dominance regime, an angle $\sim 45°$ to the symbiotic growth, and an angle $< 45°$ to the galaxy regime. We note that, given the definitions of $G_{\rm BH}$ and $G_{\rm gal}$, the former conveys instantaneous information by being directly proportional to the BH accretion rate at the moment of observation. In contrast, the latter provides insight into a longer time-scale, approximately 100 Myr, as it is linked to the dust-reprocessed SFR (Kennicutt and Evans, 2012; Orr et al., 2018)[4]. The properties derived for our sample of QSOs are summarized in Tab. 5.1.

Before discussing our results, it is important to illustrate briefly the possible caveats. As reported in Tab. 5.1, both $M_{\rm BH}$ and $M_{\rm dyn}$ carries large systematic uncertainties[5] (0.1-0.3 dex). Additionally, even though the $L_{\rm TIR}$ (and therefore SFR) has been derived with high statistical accuracy and corrected for a reasonable AGN contribution (50%, see Sect. 4.3.1), this contribution may vary from $\sim 30\%$ to 70% in principle. These uncertainties (a factor of ~ 2 for $M_{\rm BH}$, $M_{\rm dyn}$ and a factor of ~ 1.5 for SFR) have an impact on the inferred evolutionary scenario, since $G_{\rm BH}$ may vary of a factor of 2 and $G_{\rm gal}$ of a factor of 3, at most. It is also important to bear in mind that the slope of the arrow in our results corresponds to the specific case of $M_{\rm dyn} \gtrsim M_{\rm gas}$,

---

[3] For a more detailed discussion about stellar masses in high-z QSOs and the role played by JWST see Sect. 1.3

[4] Recently, Flores Velázquez et al. (2021) pointed out that the time-scale probed by the FUV SFR may be lower than 100 Myr, down to 10 Myr, depending on whether the SFH is bursty or time-steady.

[5] The errors reported on $M_{\rm dyn}$ take into account the systematics due to the circular velocity and the radius of the galaxy used to derive $M_{\rm dyn}$ (see also discussion in Neeleman et al. 2021). Note that, for the majority of the QSOs in our sample, $M_{\rm dyn}$ has been derived in Neeleman et al. (2021) in a consistent way.

Table 5.1: Properties of QSOs in our sample

QSO	z	$\log(L_{\rm bol}/{\rm erg\ s^{-1}})$	$\log(M_{\rm BH}/M_\odot)$	$\log(M_{\rm dyn}/M_\odot)$	SFR $[{\rm M_\odot\ yr^{-1}}]$	$G_{\rm BH}$ $[10^{-8}\ {\rm yr^{-1}}]$	$G_{\rm GAL}$ $[10^{-8}\ {\rm yr^{-1}}]$	angles [deg]	Refs
J0100+2802	6.327	48.24 ± 0.04	10.04 ± 0.27	10.51 ± 0.1	396	2.5	1.8	54	[1],[2]
J036+03	6.540	47.33 ± 0.05	9.49 ± 0.12	10.46 ± 0.1	466	1.1	1.8	31	[1],[2]
J0224-4711	6.522	47.53 ± 0.01	9.36 ± 0.08	10.58 ± 0.3	2485	2.3	6.9	19	[1],[3]
J231-20	6.587	47.31 ± 0.01	9.50 ± 0.09	10.15 ± 0.2	496	1.0	4.5	13	[1],[2]
J1342+0928	7.540	47.19 ± 0.01	8.90 ± 0.14	10.56 ± 0.3	180	3.1	0.5	81	[1],[2]
J1148+5251	6.419	47.57 ± 0.01	9.74 ± 0.03	10.18 ± 0.3	1570	1.1	16	4	[1],[4]
J2310+1855	6.003	$47.49^{+0.10}_{-0.13}$	$9.67^{+0.06}_{-0.08}$	10.72 ± 0.1	1855	1	4	15	[5],[6]
J2054-0005	6.390	47.03	9.17 ± 0.3	> 10.46	730	1.1	2.7	23	[2]
J1319+0950	6.133	$47.30^{+0.07}_{-0.08}$	$9.53^{+0.05}_{-0.11}$	11.09 ± 0.1	1197	0.9	1.0	43	[5],[2]
J183+05	6.439	$47.20^{+0.16}_{-0.25}$	$9.41^{+0.21}_{-0.41}$	> 11.11	894	1.0	0.7	54	[5],[2]

Notes. Columns: QSO name; redshift; BH mass; dynamical mass; SFR computed in Chap. 4; slope of the relation $G_{\rm BH} - G_{\rm gal}$, exemplified by the slope of the arrows in Fig. 5.2; references for BH and dynamical masses. QSOs above the double black line belong to the HYPERION sample. SFRs are corrected by a factor of 50% to account for the possible contribution of the AGN to the dust heating (see Sect. 4.3.1). The dynamical mass for J0224-4711 has been preliminary estimated using the [CII] FWHM from an archival ALMA observations in Band 6. This work is still in progress (Tripodi in prep.). We recall that a radiative efficiency $\epsilon = 0.1$ has been assumed to compute the BH accretion rate in $G_{\rm BH}$. References: [1] Zappacosta et al. (2023); [2] Neeleman et al. (2021); [3] Tripodi in prep.; [4] Riechers et al. (2009); [5] Mazzucchelli et al. (2023); [6] Tripodi et al. (2022).

which is plausible at high z, and of a BH radiation efficiency of 10%. A precise determination of this latter parameter would require a dedicated study of the growth and accretion history of this SMBH, which is beyond the scope of this work. Keeping in mind these systematics, in the following we discuss our results based on the best-fitting values for $M_{\rm BH}$, $M_{\rm dyn}$ and SFR (reported in Tab. 5.1).

We evaluated the evolutionary state of the other QSOs in our sample. Fig. 5.2 presents our results, where HYPERION QSOs in our sample are shown as a star with green contours, and the other QSOs in our sample as a star with red contours. In Tripodi et al. (2022); Tripodi et al. (2023a), the evolutionary path of J2310+1855 and J0100+2802 were investigated in detail. Stars are color-coded as a function of $G_{\rm gal}$. The slope of the arrows associated to each star corresponds to the angle reported in Tab. 5.1, i.e., to the proportionality factor of the $G_{\rm BH} - G_{\rm gal}$ relation. Given the large systematics quoted above, we did not draw the uncertainty of the arrows to make the plot clearer. Overall, we see that the growth of the QSOs in our sample is mainly dominated by the galaxy or symbiotic (see also Tab. 5.1). In particular, looking at the color-code of the stars, we observe that -on average- the closer a QSO is to the local relation the slower is the growth of the galaxy.

The majority of QSOs lie above the local relation in the BH dominance regime (M. Volonteri, 2012). However, this tension can be partially softened if accounting for the uncertainties on the dynamical mass estimates and/or if BH masses are overestimated (see Sect. 1.1.3). Noteworthy, dynamical masses are computed within the size of observed [CII] emission that depends on both the resolution and the sensitivity of the observations. In principle, this makes the comparison among different QSOs challenging. In our case, the majority of dynamical masses in our sample have been derived from observations with similar resolution and sensitivity. Therefore, we are confident of tracing a similar portion of the galaxy among the studied QSOs. In addition, uncertainties on dynamical masses strongly depend on the determination of the disk inclination and can be significantly high for some QSOs (Valiante et al., 2014; Pensabene et al., 2020). This is also the case of J0100+2802, whose $M_{\rm dyn}$ can be in principle as high as 10^{12} $M_\odot$. As a word of caution, one should remember that the sample of high-z QSOs studied in this work is biased towards high luminosities and BH masses, and therefore represents the tail of the whole population of high-z QSOs, part of which is in agreement with the local relation in the $M_{\rm BH} - M_{\rm dyn}$ plane.

For J0100+2802, we found $G_{\rm BH} > G_{\rm gal}$, suggesting that the BH is still dominating the process of BH-galaxy growing in this QSO at $z = 6.327$. This result is still valid if considering lower SFR (adopting the correction by Fabio Di Mascia et al. 2023) and/or higher $M_{\rm dyn}$ (i.e. higher $M_{\rm gal}$ at fixed BH mass), since the galaxy growth factor would be even smaller. Our results do not consider the gas inflow. However, we expect this term to contribute on average to both SFR and $M_{\rm gal}$, leaving their ratio mostly unaffected. On the other hand, in QSO J2310+1855 at $z \sim 6$ AGN feedback might be slowing down the accretion onto the SMBH, while the host galaxy grows fast (Tripodi et al., 2022; Bischetti et al., 2022). One of the likely

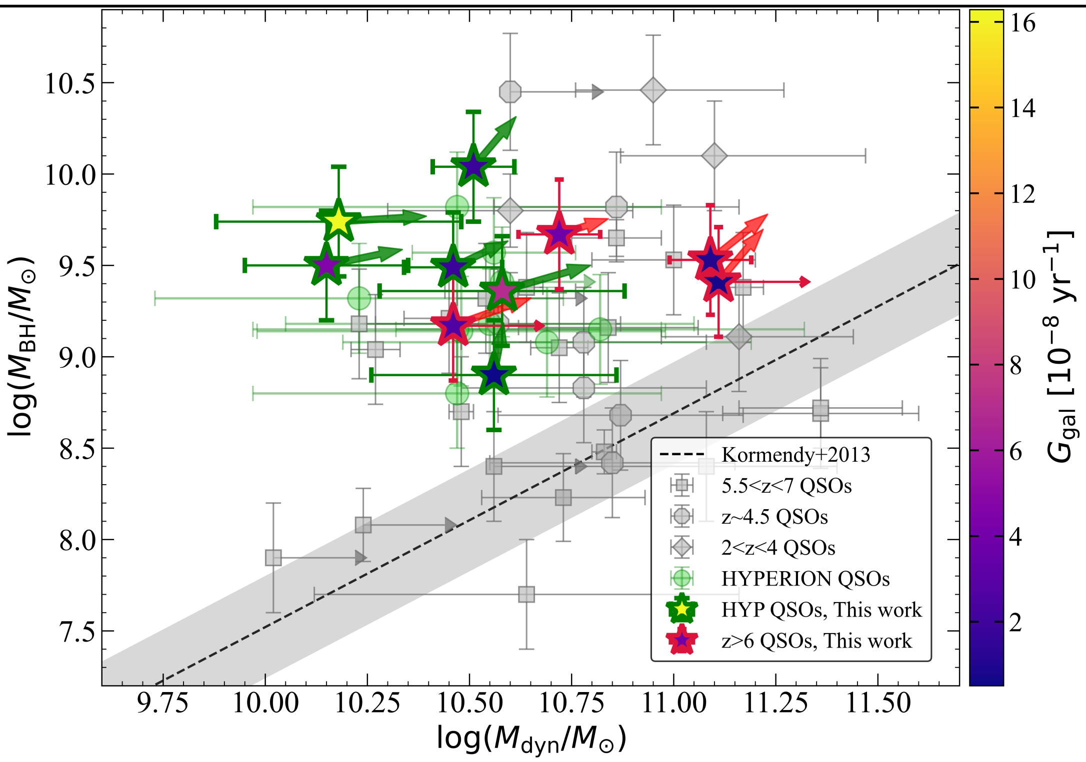

Figure 5.2: *BH mass vs dynamical mass for our sample (stars with green contours for HYPERION QSOs, red contours otherwise), WISSH QSOs at* $z \sim 2-4$ *(grey diamonds, Bischetti et al. 2021), and luminous* $z \sim 4-7$ *QSOs (grey dots and grey squares, B. P. Venemans et al. 2016; B. P. Venemans et al. 2017; Willott, Alain Omont, and Bergeron 2013; Willott, Bergeron, and Alain Omont 2015; Willott, Bergeron, and Alain Omont 2017; Kimball et al. 2015; Trakhtenbrot et al. 2017; Feruglio et al. 2018; Mortlock et al. 2011; De Rosa et al. 2014; Kashikawa et al. 2015; Neeleman et al. 2021). Black dashed line (and shaded area) is the local relation from Kormendy and Ho (2013). Light green dots are the remaining HYPERION QSOs for which we were not yet able to perform a detailed study of dust properties due to lack of observations in sub-mm regime. Stars are color-coded based on the value of* G_{gal}*. The thin red arrows indicate upper limits on the dynamical mass.*

causes of the slow-down of the SMBH accretion are radiatively driven AGN winds that impact on the accreting matter, providing enough momentum to stop further accretion, and which can further propagate outwards on the scale of the host galaxy. In J2310+1855, the SMBH accretion may be limited by the ionised wind traced by a CIV broad absorption line (BAL) system with velocity $v_{BAL} = 26900$ km s^{-1} and balnicity index $BI = 600$ (Bischetti et al., 2022). J2310+18655 also shows evidence of a [CII] outflow approximately located in the central kpc, with an outflow mass $M_{out} = 3.5 \times 10^8$ M$_\odot$. This is about 5% of the neutral gas mass in the disk, consistent with expectations of recent zoom-in hydrodynamical simulations presented by Valentini, Simona Gallerani, and Ferrara (2021). Additionally, Shao et al. (2022); Butler et al. (2023) detected molecular outflows traced by OH and OH+. The different evolutionary state of J0100+2802 and J2310+1855, separated by only $\sim$ 60 Myr (i.e. $\Delta z \sim 0.3$), arise mainly from the difference in their BH mass (i.e., $M_{BH,J0100+2802} \sim 2\times\ M_{BH,J2310+1855}$) and in SFR (i.e., SFR$_{J0100+2802} \sim 0.2 \times$ SFR$_{J2310+1855}$).

Moreover, we observe that -on average- the closer a QSO is to the local relation the slower is the growth of the galaxy. J2310+1855 and J231-20, which show a similar galaxy growth, are both BAL QSOs (Bischetti et al., 2022). Additionally, evidences of high-velocity [CII] emission wings and/or OH absorption wings indicating powerful and fast outflows are found in J2310+1855 (Tripodi et al., 2022; Shao et al., 2022; Butler et al., 2023), J2054-0005 (Salak et al., 2023), J1148+5251 (Maiolino et al., 2012; Cicone et al., 2015), and tentatively in J1319+0950 (Herrera-Camus et al., 2019). Therefore, the onset of the symbiotic or galaxy dominated regime may be linked to a phase of strong feedback hampering the BH growth. Three QSOs are still experiencing a BH dominated growth: J0100+2802, J1342+0928, and J183+05. J0100+2802 and J1342+0928, both belonging to the HYPERION sample, have the biggest and smallest BH mass in our sample, respectively. Given that SMBHs' masses observed locally do not exceed 10^{11} $M_{\odot}$ and that J0100+2802's BH is the most massive observed at $z > 6$ with already 10^{10} $M_{\odot}$, a substantial BH growth is a unlikely prospect. This is the reason why BH dominated growth is indeed a peculiar scenario for J0100+2802. On the contrary, it is likely that J1342+0928 is in the process of strong BH growth given its 'small' BH mass. Interestingly, J183+05 has almost finished building its galaxy mass, being the closest to the local relation. Both in J0100+2802 and J183+05, high-velocity wings were detected in [CII] and OH, respectively (Tripodi et al., 2023c; Butler et al., 2023). Also in this case the presence of outflows is possibly related to the fact that both QSOs may be approaching a phase of symbiotic growth.

We compared our results with 'zoom-in' simulations of QSOs using the moving-mesh code AREPO, following BH growth and feedback via energy-driven outflows (Costa et al., 2014; Costa, Sijacki, and Haehnelt, 2015). We found that simulations reproduce BHs only up to masses $\sim 10^{9}$ $M_{\odot}$ that have host galaxies with dynamical masses $\sim 10^{11}$ $M_{\odot}$. These are considerably more massive than the average host-galaxy in our sample, also considering that $M_{\rm dyn}$ from simulations are derived within average observed radius $>$ 1 kpc, which is the radius commonly observed for QSO's hosts. The growth of the system is characterised by intermittent phases, where the BH and galaxy-dominated growth phases change on short timescales. Hence, we plan to investigate the diagnostic power of the relation $G_{\rm BH} - G_{\rm gal}$ in a forthcoming work.

Summarizing, our study suggest that QSOs at $z \gtrsim 6$ are experiencing a phase of intense galaxy growth. This may be connected to the emergence of strong outflows that are able to regulate the BH growth. On the $M_{\rm BH} - M_{\rm dyn}$ plane high-z QSOs appear to be converging towards the massive end of the local relation. This suggests that they are viable and plausible candidates as progenitors of massive galaxies found in the local universe.

CHAPTER 6

CONCLUSION AND FUTURE PERSPECTIVES

Over the last decades, high-redshift QSOs have been proven to be an invaluable resource to investigate the mechanisms that drive the formation and evolution of the first massive galaxies, and that regulate the interaction between the SMBHs and their host galaxies. Even though important advances have been made in understanding the nature of high-z QSOs both from theory and observations, there are still significant uncertainties and systematics affecting the knowledge of the properties of QSOs' ISM.
My PhD project originates from the exploration of two crucial questions:

1. *Is the SMBHs growth coupled to the evolution of their host galaxies, and how?*
2. *Are QSO's hosts at high-z the progenitors of the massive galaxies observed in the local Universe?*

This Thesis aims to tackle these questions providing new observational constraints on the properties of QSOs' host galaxies at $z \gtrsim 6$. In particular, I employed ALMA and NOEMA observations, both proprietary and archival, to perform a comprehensive analysis of the molecular and multi-phase gas and the cold dust in a statistically sound sample of 12 QSOs at $z \gtrsim 6$. In Chap. 1, I provided an overview of the field of high-z QSOs, focusing on the properties of the ISM, on the open questions crucial to our investigation, and on our motivations. In Chap. 2, I presented the general properties of the studied sample of QSOs. Our sample of QSOs is mainly drawn from the HYPerluminous QSOs at the Epoch of ReionizatION (HYPERION) Survey, targeting the titans among $z > 6$ QSOs that are powered by the most massive SMBHs at their epoch (Zappacosta et al., 2023). Among $\sim$ 300 QSOs known at EoR, the HYPERION sample comprises the 18 QSOs which experienced the most rapid SMBH mass growth. Therefore, studying the properties of HYPERION QSOs host galaxies can inform about the concurrent growth of BH and galaxies in this extreme regime. This makes them ideal targets for our study.

Here I summarize the main results we have achieved in this Thesis. Conclusions are divided according to the main topic investigated in each chapter, namely i) the properties of cold gas in QSOs' hosts; ii) the properties of the cold dust and SFR derived from the modelling of cold dust SED; iii) the evolutionary path of high-z QSOs and their host galaxies at $z \gtrsim 6$.

Cold gas properties

In Chap. 3, I presented our investigation on the cold gas in the QSOs J2310+1855, J0100+2802, J1007+2115, J1319+0950, J2054-0005 and J0129-0035 based on ALMA and/or NOEMA observations of the [CII], H_2O, CO(6-5) and/or CO(7-6) emission lines of these sources. Here I summarize our main results.

- We conducted an analysis of the CO(6-5) emission line in the QSOs J1007+2115, J1319+0950, J2054-0005, J0129-0035, and the CO(7-6) emission in J0224-4711. Notably, our detection of CO(6-5) and CO(7-6) in J1007+2115 represents the highest-redshift measurement of cold and dense molecular gas to date. Our primary objective was to estimate the molecular gas mass of these QSOs with the smallest statistical errors. On average, our analysis revealed molecular gas masses of approximately 10^{10} $M_\odot$, consistent with the typical gas masses observed in other high-redshift QSOs. Our findings support the picture in which high-z QSO's host galaxies have large gas reservoirs that constitute the fuel for star-formation. Combining this information with the SFR and dust masses estimated from the analysis of the SEDs can provide crucial insights on the galaxy assembly and evolution (see next sections).
- Recent ALMA observations in Bands 6 and 3 of the QSO J0100+2802 have unveiled a compelling new perspective on the most luminous QSO at $z > 6$. This investigation has revealed an interacting companion and a high-velocity cold outflow, which were previously undetected both in higher-resolution observations and in JWST-NIRCam imaging. Notably, the [CII] emission and its underlying continuum exhibit a structure elongated in the East-West direction with multiple peaks. The [CII] channel maps provide further clarity, resolving a clumpy morphology and a tidal tail. The enhanced [CII] velocity dispersion along the axis of elongation supports the scenario in which the companion is in the process of merging with the QSO host. Moreover, we interpreted the broad component in the [CII] spectrum as an indication of an outflow, which is resolved with a size of $\sim 5.4 \times 4.0$ kpc^2. Our assessment of the outflow energetics led to the conclusion that the outflow may not be highly efficient in removing gas from the galaxy. These findings highlight the importance of deep low-resolution ALMA observations in advancing our understanding of QSOs at the EoR, in particular concerning the complex nature of high-z QSOs. Indeed, whether they are caught in merging processes, or with a large number of close companions, directly influence the way in which galaxies assemble their mass and the relation between the BH and the galaxy growth. As seen in Chap. 5, J0100+2802 has the most massive BH at $z > 6$, similar to the most massive BHs observed in the local Universe, therefore a substantial growth of the galaxy is a likely prospect.

- We reported results from a deep ALMA observation of the sub-mm continuum, [CII], and H_2O emission lines with sub-kpc resolution, targeting the $z \sim 6$ QSO J2310+1855. The 900 pc resolution of this dataset allowed us to perform a detailed study of the cold gas kinematics and dynamics. SDSS J2310+18655 showed evidence of a [CII] outflow approximately located in the central kpc, whose energetics agree with the scaling for ionised winds and with expectations for momentum-conserving winds. For the first time, we successfully mapped a spatially resolved H_2O v=0 $3_{(2,2)} - 3_{(1,3)}$ emission line at $\nu_{\rm obs} = 274.074$ GHz at a statistical significance of 10σ. Its emission is consistent with a water vapour disk whose kinematics agrees with that of the [CII] disk. Additionally, this observation allowed us to study the environment of J2310+1855, scanning the data cube for line and continuum emitters. No line emitter was detected down to a 3σ upper limit of SFR < 2.5 $M_\odot yr^{-1}$. We also note that the proximate DLA J2310+1855 did not show any line-emitting counterpart down to this limit, and therefore we propose that the line emitter reported in V. D'Odorico et al. (2018), called Serenity-18, is most likely a lower-z interloper. These findings collectively indicate that J2310+1855 does not exhibit any compelling evidence of companions, interactions, or mergers, particularly at scales exceeding $\sim$ 50 kpc. Interestingly, this observation is not consistent with the current scenario, where about 20-50% of QSOs display evidence of mergers or close companions, regardless of their luminosity. It is also different from the scenario found in J0100+2802, which is caught in a merging process. Either J2310+1855 already experienced an intense merging phase, or it has fainter companions that remained undetected by our observations. This latter implies that powerful mechanisms, such as strong feedback, may be responsible for the suppression of SF activity in the companions.

- We performed a refined kinematic and dynamical modeling of the [CII] emission of J2310+1855, that allowed us to detect a central compact mass component in J2310+1855, which is composed by a SMBH and a stellar bulge having similar masses of the order of $\sim 1.7 \times 10^{10}$ $M_\odot$. This is the first time that a compact bulge component is detected at this high redshift. We discussed different mechanisms of bulge formation (disc instabilities, major mergers, SF in AGN driven outflows, direct dissipative collapse), also comparing with galaxy simulations. For J2310+1855, disc instabilities can be likely ruled out because such secular processes occur on long timescales (~3-5 Gyr) while the age of the Universe at $z \simeq 6$ is only ~900 Myr in the adopted cosmology. All the other mechanisms, instead, appear viable. To end up on the local $M_{\rm SMBH} - M_{\rm bulge}$ relation, the bulge mass should increase by a factor of ~40 from $z = 6$ to 0, while the SMBH mass should grow at most by a factor of 4, pointing to asynchronous galaxy-BH co-evolution. A robust interpretation of our results is strongly dependent on the accuracy of the determination of the physical quantities at play. This is why higher resolution observations are required to validate our scenario. The employed methodology hold the keys to reveal compact stellar components at very high redshift, and has the potential to provide independent measurements of the BH mass based on dynamical modeling. This is particularly important given that virial estimates of the BH masses may be strongly affected by systematic errors.

Cold dust properties and SFR

We exploited newly acquired and archival ALMA observations in Band 9 and/or Band 8 for 5 QSOs at $z \gtrsim 6$ (J0100+2802, J036+03, J0224-4711, J231-20, J2054-0005) to derive their dust properties and SFR with the smallest statistical uncertainty. This has been achieved through the study of the cold dust SED of the targeted QSOs. In Chap. 4, I explained the cold dust SED modelling in detail. Here I recall that the cold dust SED depends on the dust temperature, $T_{\rm dust}$, dust mass, $M_{\rm dust}$ and dust emissivity index, β, and is related to the SFR since the SFR is proportional to the total infrared luminosity, $L_{\rm TIR}$, derived from the integration of the SED from 8μm to 1000μm. To convert $L_{\rm TIR}$ to SFR we assumed a Kroupa IMF (Kroupa and Weidner, 2003).

In Sect. 4.3.1, I presented a state-of-the-art modelling of the SED of J2310+1855 including the contribution of both the large-scale dust in the ISM and the dusty torus emission. The accurate sampling of the QSO's SED, especially at lower wavelengths ($\lambda \sim 10 - 100$ μm), allowed us to constrain $T_{\rm dust}$ with an uncertainty $\Delta < 6\%$, $M_{\rm dust}$ with $\Delta \sim 15\%$, and β with $\Delta \sim 6\%$. In principle, one should consider also a warmer dust that is mainly heated by the central AGN. The resolution of the available observations for J2310+1855 (as well as for the other QSOs in our sample) did not allow us to perform a spatially resolved study of the dust emission, and therefore to isolate the warmer central dust component. That is why we modelled the dust emission with a single temperature BB, hence mixing the dust emission heated by the stellar distribution with the dust heated by the central AGN. We discussed the systematics arising by not including this warm component and what is needed to determine the AGN contribution to the dust heating, in terms of radiative transfer modelling and high-resolution observations. In our work, we assumed an average AGN contribution of $\sim 50\%$ to the total FIR luminosity, which also accounts for the uncertainties in the radiative transfer model and which is in line with the results found in R. Schneider et al. (2015); Duras et al. (2017). This assumption implied a SFR = 1855^{+464}_{-389} $\mathrm{M_{\odot} yr^{-1}}$ for J2310+1855.

Since we aimed at performing a statistically sound investigation of the dust properties in a sample of $z > 6$ QSOs, we included other 4 QSOs (J1319+0950, J1148+5251, J1342+0928, J183+05) in our analysis that had multiple-frequency observations sampling the Rayleigh-Jeans part and of the peak of the cold dust SED. This selection allowed us to define a final sample of 10 QSOs at $z \gtrsim 10$ for which the dust properties have been accurately determined. It is the first time that this kind of analysis is done on a sample of $z > 6$ QSOs. Our results are crucial for tackling the aforementioned questions, since the SFR is directly connected with the growth of the galaxy. Here I summarize the main findings.

- We conducted an analysis of the redshift distribution of dust temperatures within our sample, comparing it to other samples of local and high-redshift QSOs and galaxies. Our investigation revealed a large scatter in dust temperature between QSOs and typical star-forming galaxies at fixed redshift, though indicating a general trend of increasing $T_{\rm dust}$ with redshift as theoretically expected. Considering the whole population of galaxies at $0 < z < 7$, our best-fitting $T_{\rm dust} - z$ relation is of the form $T_{\rm dust} \propto (1 + z)^{0.7\pm0.1}$, which is steeper than expected from theory ($T_{\rm dust} \propto (1 + z)^{0.4}$, see Sommovigo et al. 2022). This implies that the variation of $T_{\rm dust}$ in different sources has non-negligible dependencies from other physical properties, such us optical depth and metallicity.

- Investigating the variation of the dust emissivity index β with redshift, we found that it is approximately constant with z, indicating that all sources share similar dust properties. Two QSOs, J0100+2802 and J036+03, show $\beta > 2$, suggesting that they may have peculiar dust properties. The analysis of the dust extinction curves in the rest-frame UV-optical could provide complementary information on the properties of dust in these QSOs.

- Overall, the SFR is higher in the highest-z samples by $\sim$ 2 order of magnitudes on average, ranging from few hundreds to thousands $\rm M_\odot\ yr^{-1}$. This supports the well-known concept that high-z QSOs are hosted in highly star-forming galaxies. The dust masses are higher at high-z as well, by $\lesssim$ 2 order of magnitudes on average. As a preliminary result, HYPERION QSOs in our sample have -on average- smaller dust mass ($\sim$ 1 order of magnitude) than the other QSOs in our sample.

- Finally, we found a large scatter of the GDR in our sample, from 30 to 250. The lowest measured GDRs are due to massive reservoirs of dust, $M_{\rm dust} \sim (5 - 6) \times 10^8\ \rm M_\odot$, which pose challenges to theoretical modelling of dust formation. Interestingly, HYPERION QSOs show the highest GDRs in our sample, owing to their lower dust masses, $M_{\rm dust} \sim (2 - 9) \times 10^7\ \rm M_\odot$, whereas their H_2 gas reservoirs are in line with those of the general sample ($M(H_2) \sim 10^{10}\ \rm M_\odot$).

Evolutionary paths of high-z QSOs

Combining the results achieved in Chaps. 3 and 4, we were able to investigate and discuss the evolutionary path of our sample of 10 QSOs with accurate determination of dust properties and SFR. Our study suggests that QSOs at $z \gtrsim 6$ are experiencing a phase of rapid galaxy growth. This may be connected to the emergence of strong outflows that are able to regulate the BH growth. Indeed BALs were detected in J2310+1855 and J231-20 (Bischetti et al., 2022), and evidences of powerful and fast outflows were found in J2310+1855 (Tripodi et al., 2022; Shao et al., 2022; Butler et al., 2023), J2054-0005 (Salak et al., 2023), J1148+5251 (Maiolino et al., 2012; Cicone et al., 2015), and tentatively in J1319+0950 (Herrera-Camus et al., 2019). On the $M_{\mathrm{BH}} - M_{\mathrm{dyn}}$ plane, high-z QSOs appear to be converging towards the massive end of the local relation. This makes high-z QSOs viable and plausible candidates as progenitors of massive galaxies found in the local universe. Interestingly, the average pathway pursued by high-z QSOs to end-up as local massive galaxies involves an intense BH growth, which is supported by the up-ward offset from the local $M_{\mathrm{BH}} - M_{\mathrm{dyn}}$ relation, followed by a substantial growth of the galaxy. This is in contrast with a picture of formation of massive local galaxies via symbiotic growth. Our scenario is further supported by the evidence of a stellar bulge in J2310+1855, which indicates that the structure of QSOs at $z \sim 6$ is surprisingly akin to that typical of local massive galaxies. We plan to further explore and strengthen our findings about the evolutionary scenario connecting high-z QSOs to local galaxies in future works.

Perspectives for future research

Throughout the course of this work, numerous prospects for forthcoming projects have emerged. In this section, I briefly outline the research lines that I plan to follow-up.

Dynamical estimates of BH mass and observation of the stellar distribution in high-z QSOs. As outlined above, dynamical modelling with high angular resolution is a promising tool to detect compact mass components and measure BH masses out to the highest redshifts. In this context, I am the PI of a ALMA+JWST joint proposal approved with A priority in ALMA cycle 10 call for proposals, named ‘Dissecting the kinematics of the central region of a $z \sim 6$ QSO with ALMA and JWST’ (ID: 2023.1.00452.S). The goal of this ALMA-JWST joint proposal is to investigate the innermost region of the host galaxy of the $z \sim 6$ QSO SDSS J2310+1855, in order to unveil the stellar distribution in the host galaxy, determining the possible presence and characteristics of a bulge-like component, and to put tighter constraints on its BH mass. As pointed out in Chap. 1, the most accurate estimates of BH masses at high-z are usually obtained via sensitive NIR spectroscopy through the analysis of MgII emission lines (Shen et al., 2019; J. Yang et al., 2019; Farina et al., 2022; Mazzucchelli et al., 2023) or Hβ emission lines (Madeline A. Marshall et al., 2023), based on the still unverified assumption that the local calibrations of the single epoch methods to measure the BH mass are also valid in the early Universe. These estimates intrinsically suffer of high systematic uncertainties, that can be as high as a factor of 3-5 (Shen et al., 2013). To overcome these uncertainties we proposed to determine the BH mass from dynamical modelling of the rotation curve. QSO SDSS J2310+1855 was the best scientific case to demonstrate this methodology, since it had a well-studied rotation curve, with 0.1-0.15 arcsec resolution ALMA observation (Shao et al., 2022; Tripodi et al., 2023b), its BH mass was estimated through MgII emission line analysis ($M_{\mathrm{BH,J2310}} = 5 \times 10^9$ M$_\odot$, Tripodi et al. 2022) with 0.5 dex uncertainty, and the properties of the molecular gas and dust are accurately determined (Feruglio et al., 2018; Tripodi et al., 2022; Shao et al., 2022). The results of Shao et al. (2022) and Tripodi et al. (2023b) clearly

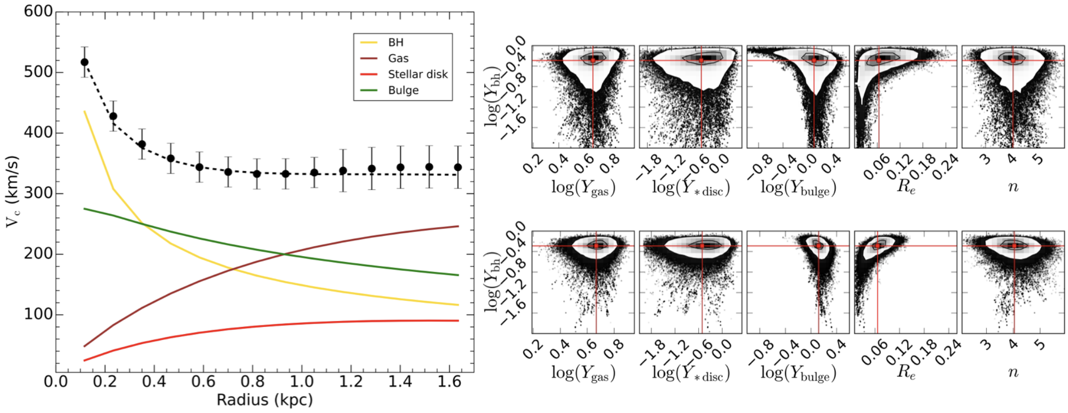

Figure 6.1: *Left panel: Simulated rotation curve of J2310+1855 for ALMA-alone observation based on the results of Tripodi et al. (2023b). In this case,* $r_{\rm SOI} \sim 300$ *pc, at the crossing of green and yellow line. Top right panel: zoom-in of the contour plot, highlighting the degeneracy between the BH mass and the other parameters for the ALMA-alone observation. Bottom right panel: same as top right but for the joint ALMA-JWST observations. Note that* $Y_i = M_i/10^{10}M_\odot$*, where* $i = \text{gas}, *\text{disk}, \text{bulge}, \text{bh}$.

demonstrate how the current observations are not able to distinguish among various scenarios with different dynamical modelling. The resolution that will be achieved by the new ALMA observations is guaranteed to probe the BH sphere of influence of this object even in the most conservative case (i.e., $M_{\rm BH,low} = 2.5\times10^9$ M$_\odot$, based on an uncertainty of 0.3 dex for $M_{\rm BH,J2310}$) and to resolve it in the case of higher BH mass. For BH masses lower than $\sim 10^{10}$ M$_\odot$ (that is the upper bound value for $M_{\rm BH,J2310}$), Tripodi et al. (2023b) show that the innermost part of the rotation curve cannot be explained without the presence of an additional central component in the form of a bulge.

Remarkably, JWST-NIRCam photometry will enables us to image the stellar distribution in the host-galaxy directly (as done by Ding et al. 2022 for two high-z QSOs). We will observe in two filters (F150W and F410M), that bracket the rest-frame 4000 Angstrom break, in order to constrain the stellar mass density on sub-kpc scales. Therefore, we will gain crucial information on the stellar properties, assessing whether the stellar component is in the form of a disk or a bulge or both, and obtaining estimates on the size, radial profile distribution, and mass of these components. This will allow us to put tighter priors on the stellar properties (i.e, $R_e, n, M_{\rm bulge}, M_{*\rm disk}$). Thanks to the ALMA high resolution and to the JWST-NIRCam observation, we will be able to provide additional constraints on the stellar contribution to the rotation curve, increasing the number of free parameters in our dynamical analysis (e.g., effective radius, Sérsic index). We will be able to unveil the presence of a bulge for the first time at $z > 6$ and determine its properties with 20% accuracy, that in turn will lead to an accuracy of $\sim 15\%$ in the BH mass estimate. This pilot project will open the way to the accurate study of rotation curves in high-z QSO host galaxies, allowing the dynamical estimates of the BH masses and the potential discovery of massive stellar bulges. We indeed plan to exploit the results of this pilot study to design future ALMA observations for a statistically significant sample of

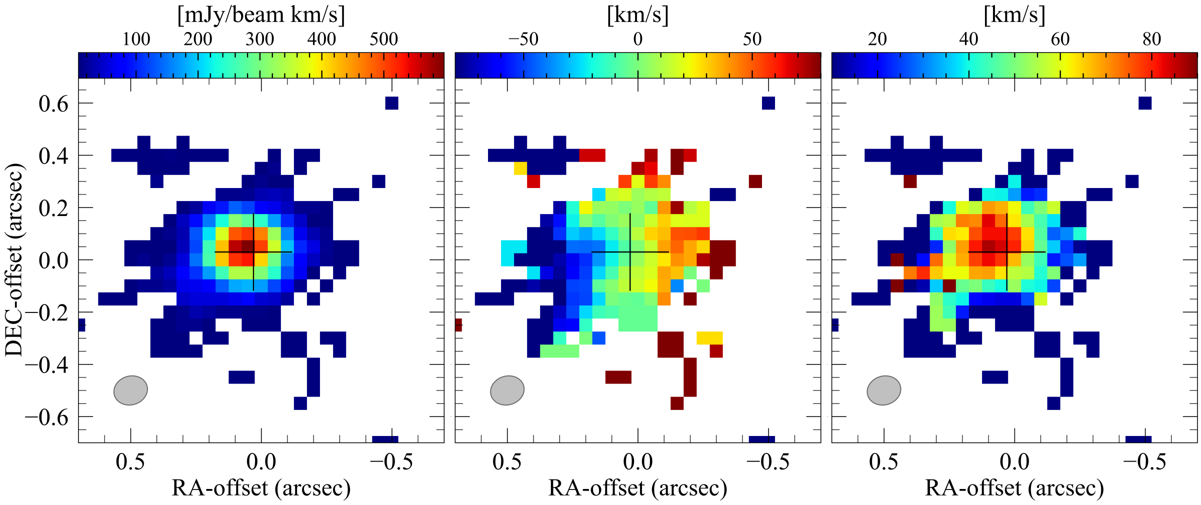

Figure 6.2: *Moment maps the [CII] emission line of QSO J0224-4711. From left to right: integrated flux, mean velocity map, and velocity dispersion map. The clean beam is plotted in the left corner of the moment maps. The cross indicates the peak position of the integrated flux for each line.*

$\sim$ 20 QSOs between $5 < z < 8$ that show clear rotation disks and very bright [CII] emission. This will shed light onto the mechanisms of bulge formation that are still poorly understood, allowing the comparison between observations of high-z QSOs and simulations.

Dynamical studies of the velocity rotation curves in J036+03 and J0224-4711. During the investigation the continuum emissions of QSOs J036+03 and J0224-4711 at different frequencies, we found high-resolution (< 0.05 arcsec) ALMA observations targeting the [CII] emission of these two QSOs. Both sources showed interesting and clear velocity gradient in the moment-1 map, indicating a rotating disk. While this was already known for J036+03 thanks to a lower resolution observation Neeleman et al. (2021), it is a new discovery for J0224-4711 (see Fig. 6.2). We plan to perform dynamical modelling with 3D BAROLO, as done for J2310+1855, that will improve the estimate of the dynamical mass for J036+03 and will give a first precise estimate for J0224-4711. Given the results of 3D BAROLO, we will try a dynamical decomposition of their rotation curves using the methodology employed successfully in J2310+1855. We may be able to find additional evidence of stellar bulges.

Assessing the contribution of the AGN to the dust heating through refined radiative transfer modelling. I plan to investigate the role of AGN in the dust heating in J2310+1855, for which I already studied its SED modelling both the dust and torus emissions (see Sect. 4.3.1, Tripodi et al., 2022), by performing radiative transfer modelling with SKIRT. SKIRT is a state-of-the-art software for simulating radiation transfer in astrophysical systems (Maarten Baes et al., 2003; Maarten Baes et al., 2011; Camps and M. Baes, 2015; Camps and M. Baes, 2020), and it is well suited to model QSO host galaxies (e.g., Fabio Di Mascia et al., 2023). I will adopt SKIRT to reproduce the observed SED accounting for both the dusty torus and the AGN contribution to the dust heating (similarly as in R. Schneider et al. 2015). I will take advantage

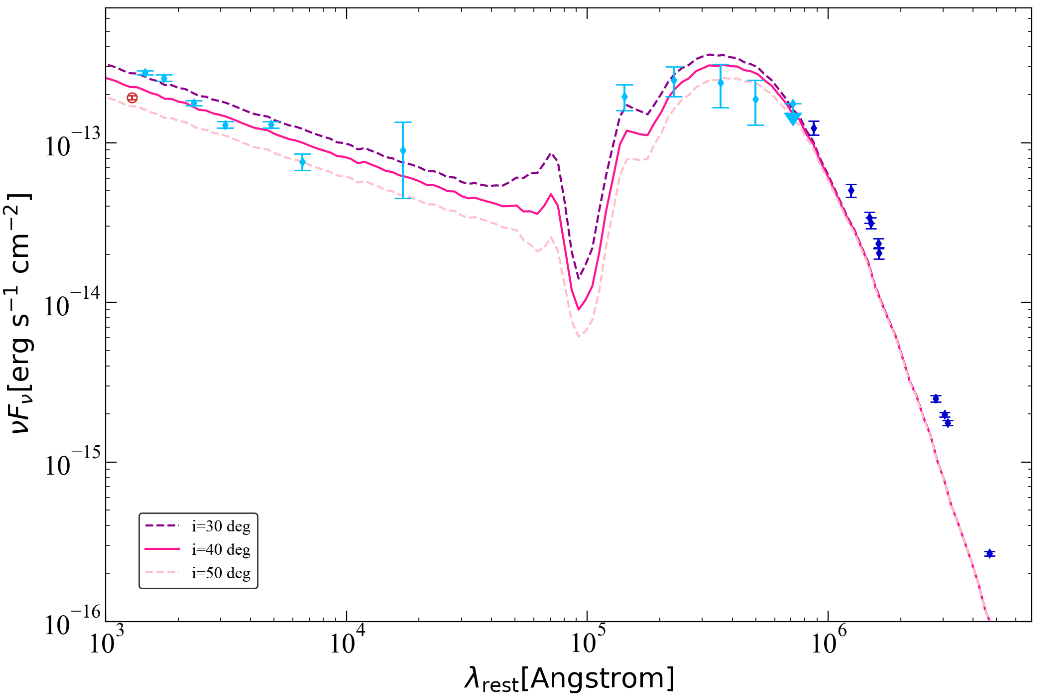

Figure 6.3: *Observed SED of QSO J2310+1855 (cyan and blue diamonds) fitted by the model obtained by the radiative transfer calculation for different values of inclination of the galaxy. Blue diamonds are ALMA observations presented in Tripodi et al. (2022), while cyan diamonds are Herschel observations, WISE and SDSS photometry.*

of the high quality, high resolution images available today for this QSOs, which were not available for, e.g., R. Schneider et al. 2015. Fig. 6.3 shows the full observed SED of J2310+1855 fitted by the model produced by radiative transfer calculation with SKIRT accounting for the dusty torus emission and the dust heated by the AGN. Specifics on the radiative transfer modelling are beyond the purposes of these conclusions, since the work is just at the first stages. Here we show three output models obtained fixing different values for the inclination of the galaxy. I also plan to perform similar modelling to other 3 QSOs that have at least 4 detections in the sub-mm regime, probed by ALMA, and at least two Herschel detections in the MIR. As outlined in throughout this Thesis, the reliability of kind of analysis is greatly improved if high spatial resolution, multi-frequency imaging is available.

Comparison with zoom-in simulations of high-z galaxies. As mentioned at the end of Chap. 5, we compared our results about the evolutionary paths of QSOs in our sample with ‘zoom-in’ simulations of QSOs using the moving-mesh code AREPO (Costa et al., 2014; Costa, Sijacki, and Haehnelt, 2015). We plan to explore how the relation between $G_{\rm gal}$ and $G_{\rm BH}$ varies with the radius used to extract the galaxies properties, and if using the stellar mass instead of the galaxy mass at the denominator of $G_{\rm gal}$. We also aim at exploring other diagnostics to determine the evolutionary paths of QSOs as, for instance, exploring the plane $\dot{M}_{\rm BH} - {\rm SFR}$.

“I advocate wholehearted devotion to the study of nature (physics),
and it is through this principle that I lead a satisfied life”

Epicuro, Letter to Erodoto

BIBLIOGRAPHY

Aalto, S. et al. “Detection of HCN, HCO^+, and HNC in the Mrk 231 molecular outflow. Dense molecular gas in the AGN wind”. *A&A* 537, A44 (Jan. 2012), A44. doi: 10.1051/0004-6361/201117919. arXiv: 1111.6762 [astro-ph.CO].

Aalto, S. et al. “High resolution observations of HCN and $HCO^+ J = 3$-2 in the disk and outflow of Mrk 231. Detection of vibrationally excited HCN in the warped nucleus”. *A&A* 574, A85 (Feb. 2015), A85. doi: 10.1051/0004-6361/201423987. arXiv: 1411.2474 [astro-ph.GA].

Abel, Tom et al. “Modeling primordial gas in numerical cosmology”. *New Astronomy* 2.3 (Aug. 1997), 181–207. doi: 10.1016/S1384-1076(97)00010-9. arXiv: astro-ph/9608040 [astro-ph].

Accurso, G. et al. “Deriving a multivariate α_{CO} conversion function using the [C II]/CO (1-0) ratio and its application to molecular gas scaling relations”. *MNRAS* 470.4 (Oct. 2017), 4750–4766. doi: 10.1093/mnras/stx1556. arXiv: 1702.03888 [astro-ph.GA].

Aihara, Hiroaki et al. “The Hyper Suprime-Cam SSP Survey: Overview and survey design”. *PASJ* 70, S4 (Jan. 2018), S4. doi: 10.1093/pasj/psx066. arXiv: 1704.05858 [astro-ph.IM].

Algera, Hiddo S. B. et al. “Cold Dust and Low [O III]/[C II] Ratios: an Evolved Star-forming Population at Redshift 7”. *MNRAS* (Oct. 2023). doi: 10.1093/mnras/stad3111. arXiv: 2301.09659 [astro-ph.GA].

Alton, P. B. et al. “The emissivity of dust grains in spiral galaxies”. *A&A* 425 (Oct. 2004), 109–120. doi: 10.1051/0004-6361:20040438. arXiv: astro-ph/0406389 [astro-ph].

Aumer, Michael et al. “The Structure of Gravitationally Unstable Gas-rich Disk Galaxies”. *ApJ* 719.2 (Aug. 2010), 1230–1243. doi: 10.1088/0004-637X/719/2/1230. arXiv: 1007.0169 [astro-ph.GA].

Baes, Maarten et al. “Radiative transfer in disc galaxies - III. The observed kinematics of dusty disc galaxies”. *MNRAS* 343.4 (Aug. 2003), 1081–1094. doi: 10.1046/j.1365-8711.2003.06770.x. arXiv: astro-ph/0304501 [astro-ph].

Baes, Maarten et al. “Efficient Three-dimensional NLTE Dust Radiative Transfer with SKIRT”. *ApJS* 196.2, 22 (Oct. 2011), 22. doi: `10.1088/0067-0049/196/2/22`. arXiv: `1108.5056 [astro-ph.CO]`.

Bakx, Tom J. L. C. et al. “ALMA uncovers the [C II] emission and warm dust continuum in a z = 8.31 Lyman break galaxy”. *MNRAS* 493.3 (Apr. 2020), 4294–4307. doi: `10.1093/mnras/staa509`. arXiv: `2001.02812 [astro-ph.GA]`.

Bakx, Tom J. L. C. et al. “Accurate dust temperature determination in a z = 7.13 galaxy”. *MNRAS* 508.1 (Nov. 2021), L58–L63. doi: `10.1093/mnrasl/slab104`. arXiv: `2108.13479 [astro-ph.GA]`.

Bañados, Eduardo et al. “An 800-million-solar-mass black hole in a significantly neutral Universe at a redshift of 7.5”. *Nature* 553.7689 (Jan. 2018), 473–476. doi: `10.1038/nature25180`. arXiv: `1712.01860 [astro-ph.GA]`.

Banerji, Manda et al. “The interstellar medium properties of heavily reddened quasarsand companions at z ~2.5 with ALMA and JVLA”. *Monthly Notices of the Royal Astronomical Society* 479.1 (June 2018), 1154–1169. issn: 0035-8711. doi: `10.1093/mnras/sty1443`. eprint: `https://academic.oup.com/mnras/article-pdf/479/1/1154/25129078/sty1443.pdf`. url: `https://doi.org/10.1093/mnras/sty1443`.

Barth, Aaron J. et al. “The Lick AGN Monitoring Project 2011: Spectroscopic Campaign and Emission-line Light Curves”. *ApJS* 217.2, 26 (Apr. 2015), 26. doi: `10.1088/0067-0049/217/2/26`. arXiv: `1503.01146 [astro-ph.GA]`.

Beelen, Alexandre et al. “350 μm Dust Emission from High-Redshift Quasars”. *ApJ* 642.2 (May 2006), 694–701. doi: `10.1086/500636`. arXiv: `astro-ph/0603121 [astro-ph]`.

Beeston, R. A. et al. “GAMA/H-ATLAS: the local dust mass function and cosmic density as a function of galaxy type - a benchmark for models of galaxy evolution”. *MNRAS* 479.1 (June 2018), 1077–1099. doi: `10.1093/mnras/sty1460`. arXiv: `1712.07261 [astro-ph.GA]`.

Behrens, C. et al. “Dusty galaxies in the Epoch of Reionization: simulations”. *MNRAS* 477.1 (June 2018), 552–565. doi: `10.1093/mnras/sty552`. arXiv: `1802.07772 [astro-ph.GA]`.

Bentz, Misty C. et al. “The Low-luminosity End of the Radius-Luminosity Relationship for Active Galactic Nuclei”. *ApJ* 767.2, 149 (Apr. 2013), 149. doi: `10.1088/0004-637X/767/2/149`. arXiv: `1303.1742 [astro-ph.CO]`.

Bershady, Matthew A. et al. “The DiskMass Survey. I. Overview”. *ApJ* 716.1 (June 2010), 198–233. doi: `10.1088/0004-637X/716/1/198`. arXiv: `1004.4816 [astro-ph.CO]`.

Berta, S. et al. “Molecular gas mass functions of normal star-forming galaxies since z ~3”. *A&A* 555, L8 (July 2013), L8. doi: `10.1051/0004-6361/201321776`. arXiv: `1304.7771 [astro-ph.CO]`.

Bertoldi, F. et al. “Dust emission from the most distant quasars”. *A&A* 406 (July 2003), L55–L58. doi: `10.1051/0004-6361:20030710`. arXiv: `astro-ph/0305116 [astro-ph]`.

Bertoldi, F. et al. “High-excitation CO in a quasar host galaxy at z =6.42”. *A&A* 409 (Oct. 2003), L47–L50. doi: `10.1051/0004-6361:20031345`. arXiv: `astro-ph/0307408 [astro-ph]`.

Béthermin, M. et al. “The ALPINE-ALMA [CII] survey: Data processing, catalogs, and statistical source properties”. *A&A* 643, A2 (Nov. 2020), A2. doi: `10.1051/0004-6361/202037649`. arXiv: `2002.00962 [astro-ph.GA]`.

Bianchi, Simone and Raffaella Schneider. “Dust formation and survival in supernova ejecta”. *MNRAS* 378.3 (July 2007), 973–982. doi: `10.1111/j.1365-2966.2007.11829.x`. arXiv: `0704.0586 [astro-ph]`.

Bigiel, F. et al. “The Star Formation Law in Nearby Galaxies on Sub-Kpc Scales”. *AJ* 136.6 (Dec. 2008), 2846–2871. doi: `10.1088/0004-6256/136/6/2846`. arXiv: `0810.2541 [astro-ph]`.

Bischetti, M., C. Feruglio, V. D’Odorico, et al. *Nature in prep* (2022).

Bischetti, M. et al. “The gentle monster PDS 456. Kiloparsec-scale molecular outflow and its implications for QSO feedback”. *A&A* 628, A118 (Aug. 2019), A118. doi: `10.1051/0004-6361/201935524`. arXiv: `1903.10528 [astro-ph.GA]`.

Bischetti, M. et al. “Widespread QSO-driven outflows in the early Universe”. *A&A* 630, A59 (Oct. 2019), A59. doi: `10.1051/0004-6361/201833557`. arXiv: `1806.00786 [astro-ph.GA]`.

Bischetti, M. et al. “The WISSH quasars project. IX. Cold gas content and environment of luminous QSOs at z ∼ 2.4-4.7”. *A&A* 645, A33 (Jan. 2021), A33. doi: `10.1051/0004-6361/202039057`. arXiv: `2009.01112 [astro-ph.GA]`.

Bischetti, M. et al. “Suppression of black-hole growth by strong outflows at redshifts 5.8-6.6”. *Nature* 605.7909 (May 2022), 244–247. doi: `10.1038/s41586-022-04608-1`. arXiv: `2205.00021 [astro-ph.GA]`.

Bogdán, Ákos et al. “Evidence for heavy-seed origin of early supermassive black holes from a z ≈ 10 X-ray quasar”. *Nature Astronomy* (Nov. 2023). doi: `10.1038/s41550-023-02111-9`. arXiv: `2305.15458 [astro-ph.GA]`.

Bolatto, Alberto D., Mark Wolfire, and Adam K. Leroy. “The CO-to-H_2 Conversion Factor”. *ARA&A* 51.1 (Aug. 2013), 207–268. doi: `10.1146/annurev-astro-082812-140944`. arXiv: `1301.3498 [astro-ph.GA]`.

Bournaud, Frédéric, Bruce G. Elmegreen, and Debra Meloy Elmegreen. “Rapid Formation of Exponential Disks and Bulges at High Redshift from the Dynamical Evolution of Clump-Cluster and Chain Galaxies”. *ApJ* 670.1 (Nov. 2007), 237–248. doi: `10.1086/522077`. arXiv: `0708.0306 [astro-ph]`.

Bourne, Martin A., Kastytis Zubovas, and Sergei Nayakshin. “The resolution bias: low-resolution feedback simulations are better at destroying galaxies”. *MNRAS* 453.2 (Oct. 2015), 1829–1842. doi: `10.1093/mnras/stv1730`. arXiv: `1507.08283 [astro-ph.GA]`.

Bouwens, R. J. et al. “Reionization Era Bright Emission Line Survey: Selection and Characterization of Luminous Interstellar Medium Reservoirs in the z ¿ 6.5 Universe”. *ApJ*

931.2, 160 (June 2022), 160. doi: 10.3847/1538-4357/ac5a4a. arXiv: 2106.13719 [astro-ph.GA].

Bradford, C. M. et al. “The Warm Molecular Gas around the Cloverleaf Quasar”. *ApJ* 705.1 (Nov. 2009), 112–122. doi: 10.1088/0004-637X/705/1/112. arXiv: 0908.1818 [astro-ph.CO].

Burtscher, L. et al. “A diversity of dusty AGN tori. Data release for the VLTI/MIDI AGN Large Program and first results for 23 galaxies”. *A&A* 558, A149 (Oct. 2013), A149. doi: 10.1051/0004-6361/201321890. arXiv: 1307.2068 [astro-ph.CO].

Butler, Kirsty M. et al. “Molecular Outflows in z ¿ 6 Unobscured QSO Hosts Driven by Star Formation”. *ApJ* 944.2, 134 (Feb. 2023), 134. doi: 10.3847/1538-4357/acad03. arXiv: 2212.09675 [astro-ph.GA].

Calura, F. et al. “The dust content of QSO hosts at high redshift”. *MNRAS* 438.4 (Mar. 2014), 2765–2783. doi: 10.1093/mnras/stt2329. arXiv: 1312.1087 [astro-ph.GA].

Camps, P. and M. Baes. “SKIRT: An advanced dust radiative transfer code with a user-friendly architecture”. *Astronomy and Computing* 9 (Mar. 2015), 20–33. doi: 10.1016/j.ascom.2014.10.004. arXiv: 1410.1629 [astro-ph.IM].

— “SKIRT 9: Redesigning an advanced dust radiative transfer code to allow kinematics, line transfer and polarization by aligned dust grains”. *Astronomy and Computing* 31, 100381 (Apr. 2020), 100381. doi: 10.1016/j.ascom.2020.100381. arXiv: 2003.00721 [astro-ph.GA].

Carilli, C. L., R. J. Ivison, and D. A. Frail. “Variability of Submillijansky Radio Sources”. *ApJ* 590.1 (June 2003), 192–196. doi: 10.1086/375005. arXiv: astro-ph/0302528 [astro-ph].

Carilli, C. L. and F. Walter. “Cool Gas in High-Redshift Galaxies”. *ARA&A* 51.1 (Aug. 2013), 105–161. doi: 10.1146/annurev-astro-082812-140953. arXiv: 1301.0371 [astro-ph.CO].

Carniani, S. et al. “Extended ionised and clumpy gas in a normal galaxy at z = 7.1 revealed by ALMA”. *A&A* 605, A42 (Sept. 2017), A42. doi: 10.1051/0004-6361/201630366. arXiv: 1701.03468 [astro-ph.GA].

Carniani, S. et al. “Kiloparsec-scale gaseous clumps and star formation at z = 5-7”. *MNRAS* 478.1 (July 2018), 1170–1184. doi: 10.1093/mnras/sty1088. arXiv: 1712.03985 [astro-ph.GA].

Carniani, S. et al. “Constraints on high-J CO emission lines in z ∼ 6 quasars”. *MNRAS* 489.3 (Nov. 2019), 3939–3952. doi: 10.1093/mnras/stz2410. arXiv: 1902.01413 [astro-ph.GA].

Casertano, S. “Rotation curve of the edge-on spiral galaxy NGC 5907 : disc and halo masses.” *MNRAS* 203 (May 1983), 735–747. doi: 10.1093/mnras/203.3.735.

Chabrier, Gilles. “Galactic Stellar and Substellar Initial Mass Function”. *PASP* 115.809 (July 2003), 763–795. doi: 10.1086/376392. arXiv: astro-ph/0304382 [astro-ph].

Chambers, K. C. et al. “The Pan-STARRS1 Surveys”. *arXiv e-prints*, arXiv:1612.05560 (Dec. 2016), arXiv:1612.05560. DOI: `10.48550/arXiv.1612.05560`. arXiv: `1612.05560 [astro-ph.IM]`.

Cicone, C. et al. “Very extended cold gas, star formation and outflows in the halo of a bright quasar at $z > 6$”. *A&A* 574, A14 (Feb. 2015), A14. DOI: `10.1051/0004-6361/201424980`. arXiv: `1409.4418 [astro-ph.GA]`.

Clements, D. L. et al. “HERUS: the far-IR/submm spectral energy distributions of local ULIRGs and photometric atlas”. *MNRAS* 475.2 (Apr. 2018), 2097–2121. DOI: `10.1093/mnras/stx3227`. arXiv: `1712.04843 [astro-ph.GA]`.

Coatman, Liam et al. “Correcting C IV-based virial black hole masses”. *MNRAS* 465.2 (Feb. 2017), 2120–2142. DOI: `10.1093/mnras/stw2797`. arXiv: `1610.08977 [astro-ph.GA]`.

Combes, F. and R. H. Sanders. “Formation and properties of persisting stellar bars.” *A&A* 96 (Mar. 1981), 164–173.

Combes, F. et al. “A bright $z = 5.2$ lensed submillimeter galaxy in the field of Abell 773. HLSJ091828.6+514223”. *A&A* 538, L4 (Feb. 2012), L4. DOI: `10.1051/0004-6361/201118750`. arXiv: `1201.2908 [astro-ph.CO]`.

Combes, F. et al. “ALMA observations of molecular tori around massive black holes”. *A&A* 623, A79 (Mar. 2019), A79. DOI: `10.1051/0004-6361/201834560`. arXiv: `1811.00984 [astro-ph.GA]`.

Combes, Françoise. “Molecular gas in distant galaxies from ALMA studies”. *A&A Rev.* 26.1, 5 (Aug. 2018), 5. DOI: `10.1007/s00159-018-0110-4`. arXiv: `1806.06712 [astro-ph.GA]`.

Compiègne, M. et al. “The global dust SED: tracing the nature and evolution of dust with DustEM”. *A&A* 525, A103 (Jan. 2011), A103. DOI: `10.1051/0004-6361/201015292`. arXiv: `1010.2769 [astro-ph.GA]`.

Cormier, D. et al. “The Herschel Dwarf Galaxy Survey. I. Properties of the low-metallicity ISM from PACS spectroscopy”. *A&A* 578, A53 (June 2015), A53. DOI: `10.1051/0004-6361/201425207`. arXiv: `1502.03131 [astro-ph.GA]`.

Costa, T., Joakim Rosdahl, and Taysun Kimm. “The hidden satellites of massive galaxies and quasars at high redshift”. *MNRAS* 489.4 (Nov. 2019), 5181–5186. DOI: `10.1093/mnras/stz2471`. arXiv: `1909.01360 [astro-ph.GA]`.

Costa, T., D. Sijacki, and M. G. Haehnelt. “Fast cold gas in hot AGN outflows.” *MNRAS* 448 (Mar. 2015), L30–L34. DOI: `10.1093/mnrasl/slu193`. arXiv: `1411.0678 [astro-ph.GA]`.

Costa, T. et al. “The environment of bright QSOs at $z \sim 6$: star-forming galaxies and X-ray emission”. *MNRAS* 439.2 (Apr. 2014), 2146–2174. DOI: `10.1093/mnras/stu101`. arXiv: `1307.5854 [astro-ph.CO]`.

Costa, T. et al. “Quenching star formation with quasar outflows launched by trapped IR radiation”. *MNRAS* 479.2 (Sept. 2018), 2079–2111. DOI: `10.1093/mnras/sty1514`. arXiv: `1709.08638 [astro-ph.GA]`.

Costa, T. et al. “AGN-driven outflows and the formation of Lyα nebulae around high-z quasars”. *MNRAS* 517.2 (Dec. 2022), 1767–1790. DOI: 10.1093/mnras/stac2432. arXiv: 2203.11232 [astro-ph.GA].

D’Amato, Q. et al. “Discovery of molecular gas fueling galaxy growth in a protocluster at z = 1.7”. *A&A* 641, L6 (Sept. 2020), L6. DOI: 10.1051/0004-6361/202038711. arXiv: 2008.13665 [astro-ph.GA].

D’Odorico, V. et al. “Witnessing Galaxy Assembly at the Edge of the Reionization Epoch”. *ApJL* 863.2, L29 (Aug. 2018), L29. DOI: 10.3847/2041-8213/aad7b7. arXiv: 1808.01146 [astro-ph.GA].

D’Odorico, Valentina et al. “XQR-30: The ultimate XSHOOTER quasar sample at the reionization epoch”. *MNRAS* 523.1 (July 2023), 1399–1420. DOI: 10.1093/mnras/stad1468. arXiv: 2305.05053 [astro-ph.GA].

da Cunha, Elisabete et al. “New insight into the relation between star formation activity and dust content in galaxies”. *MNRAS* 403.4 (Apr. 2010), 1894–1908. DOI: 10.1111/j.1365-2966.2010.16344.x. arXiv: 1001.2309 [astro-ph.CO].

da Cunha, Elisabete et al. “On the Effect of the Cosmic Microwave Background in High-redshift (Sub-)millimeter Observations”. *ApJ* 766.1, 13 (Mar. 2013), 13. DOI: 10.1088/0004-637X/766/1/13. arXiv: 1302.0844 [astro-ph.CO].

Davies, Frederick B. et al. “Constraining the Gravitational Lensing of z $\gtrsim$ 6 Quasars from Their Proximity Zones”. *ApJL* 904.2, L32 (Dec. 2020), L32. DOI: 10.3847/2041-8213/abc61f. arXiv: 2007.15657 [astro-ph.GA].

Davies, R. et al. “How Well Can We Measure the Intrinsic Velocity Dispersion of Distant Disk Galaxies?” *ApJ* 741.2, 69 (Nov. 2011), 69. DOI: 10.1088/0004-637X/741/2/69. arXiv: 1108.0285 [astro-ph.CO].

De Looze, Ilse et al. “The applicability of far-infrared fine-structure lines as star formation rate tracers over wide ranges of metallicities and galaxy types”. *A&A* 568, A62 (Aug. 2014), A62. DOI: 10.1051/0004-6361/201322489. arXiv: 1402.4075 [astro-ph.GA].

De Lucia, Gabriella et al. “Times, environments and channels of bulge formation in a Lambda cold dark matter cosmology”. *MNRAS* 414.2 (June 2011), 1439–1454. DOI: 10.1111/j.1365-2966.2011.18475.x. arXiv: 1102.3186 [astro-ph.CO].

de Nicola, Stefano, A. Marconi, and Giuseppe Longo. “The fundamental relation between supermassive black holes and their host galaxies”. *MNRAS* 490.1 (Nov. 2019), 600–612. DOI: 10.1093/mnras/stz2472. arXiv: 1909.01749 [astro-ph.GA].

De Rosa, Gisella et al. “Black Hole Mass Estimates and Emission-line Properties of a Sample of Redshift z > 6.5 Quasars”. *ApJ* 790.2, 145 (Aug. 2014), 145. DOI: 10.1088/0004-637X/790/2/145. arXiv: 1311.3260 [astro-ph.CO].

De Vis, P. et al. “A systematic metallicity study of DustPedia galaxies reveals evolution in the dust-to-metal ratios”. *A&A* 623, A5 (Mar. 2019), A5. DOI: 10.1051/0004-6361/201834444. arXiv: 1901.09040 [astro-ph.GA].

Decarli, R. et al. “Varying [C II]/[N II] Line Ratios in the Interacting System BR1202-0725 at z = 4.7”. *ApJL* 782.2, L17 (Feb. 2014), L17. DOI: 10.1088/2041-8205/782/2/L17. arXiv: 1401.5076 [astro-ph.GA].

Decarli, R. et al. “Rapidly star-forming galaxies adjacent to quasars at redshifts exceeding 6”. *Nature* 545.7655 (May 2017), 457–461. DOI: 10.1038/nature22358. arXiv: 1705.08662 [astro-ph.GA].

Decarli, R. et al. “An ALMA [C II] Survey of 27 Quasars at z ¿ 5.94”. *ApJ* 854.2, 97 (Feb. 2018), 97. DOI: 10.3847/1538-4357/aaa5aa. arXiv: 1801.02641 [astro-ph.GA].

Decarli, R. et al. “The ALMA Spectroscopic Survey in the Hubble Ultra Deep Field: Multiband Constraints on Line-luminosity Functions and the Cosmic Density of Molecular Gas”. *ApJ* 902.2, 110 (Oct. 2020), 110. DOI: 10.3847/1538-4357/abaa3b. arXiv: 2009.10744 [astro-ph.GA].

Decarli, R. et al. “Molecular gas in $z \sim 6$ quasar host galaxies”. *A&A* 662, A60 (June 2022), A60. DOI: 10.1051/0004-6361/202142871. arXiv: 2203.03658 [astro-ph.GA].

Decarli, R. et al. “A comprehensive view of the interstellar medium in a quasar host galaxy at $z \approx 6.4$”. *A&A* 673, A157 (May 2023), A157. DOI: 10.1051/0004-6361/202245674. arXiv: 2302.04312 [astro-ph.GA].

Di Mascia, F. et al. “Infrared emission of $z \sim 6$ galaxies: AGN imprints”. *MNRAS* 503.2 (May 2021), 2349–2368. DOI: 10.1093/mnras/stab528. arXiv: 2102.08956 [astro-ph.GA].

Di Mascia, Fabio et al. “Is the star-formation rate in z 6 quasars overestimated?” *MNRAS* 518.3 (Jan. 2023), 3667–3674. DOI: 10.1093/mnras/stac3306. arXiv: 2211.05790 [astro-ph.GA].

Di Teodoro, E. M. and F. Fraternali. “^{3D} BAROLO: a new 3D algorithm to derive rotation curves of galaxies”. *MNRAS* 451.3 (Aug. 2015), 3021–3033. DOI: 10.1093/mnras/stv1213. arXiv: 1505.07834 [astro-ph.GA].

Ding, Xuheng et al. “Detection of stellar light from quasar host galaxies at redshifts above 6”. *arXiv e-prints*, arXiv:2211.14329 (Nov. 2022), arXiv:2211.14329. DOI: 10.48550/arXiv.2211.14329. arXiv: 2211.14329 [astro-ph.GA].

Downes, D. and P. M. Solomon. “Rotating Nuclear Rings and Extreme Starbursts in Ultraluminous Galaxies”. *ApJ* 507.2 (Nov. 1998), 615–654. DOI: 10.1086/306339. arXiv: astro-ph/9806377 [astro-ph].

Draine, B. T. et al. “Dust Masses, PAH Abundances, and Starlight Intensities in the SINGS Galaxy Sample”. *ApJ* 663.2 (July 2007), 866–894. DOI: 10.1086/518306. arXiv: astro-ph/0703213 [astro-ph].

Driver, Simon P. et al. “GAMA/G10-COSMOS/3D-HST: the 0 ¡ z ¡ 5 cosmic star formation history, stellar-mass, and dust-mass densities”. *MNRAS* 475.3 (Apr. 2018), 2891–2935. DOI: 10.1093/mnras/stx2728. arXiv: 1710.06628 [astro-ph.GA].

Dunne, L. et al. “Herschel-ATLAS: rapid evolution of dust in galaxies over the last 5 billion years”. *MNRAS* 417.2 (Oct. 2011), 1510–1533. DOI: `10.1111/j.1365-2966.2011.19363.x`. arXiv: `1012.5186 [astro-ph.CO]`.

Dunne, L. et al. “Dust continuum, CO, and [C I] 1 - 0 lines: self-consistent H_2 mass estimates and the possibility of globally CO-’dark’ galaxies at z = 0.35”. *MNRAS* 501.2 (Feb. 2021), 2573–2607. DOI: `10.1093/mnras/staa3526`. arXiv: `2111.09067 [astro-ph.GA]`.

Duras, F. et al. “The WISSH quasars project. II. Giant star nurseries in hyper-luminous quasars”. *A&A* 604, A67 (Aug. 2017), A67. DOI: `10.1051/0004-6361/201731052`. arXiv: `1706.04214 [astro-ph.GA]`.

Dyson, J. E. and D. A. Williams. *Physics of the interstellar medium*. 1980.

Eilers, Anna-Christina et al. “Implications of z ~ 6 Quasar Proximity Zones for the Epoch of Reionization and Quasar Lifetimes”. *ApJ* 840.1, 24 (May 2017), 24. DOI: `10.3847/1538-4357/aa6c60`. arXiv: `1703.02539 [astro-ph.GA]`.

Eilers, Anna-Christina et al. “EIGER III. JWST/NIRCam observations of the ultra-luminous high-redshift quasar J0100+2802”. *arXiv e-prints*, arXiv:2211.16261 (Nov. 2022), arXiv:2211.16261. DOI: `10.48550/arXiv.2211.16261`. arXiv: `2211.16261 [astro-ph.GA]`.

Elbaz, D. et al. “ISOCAM mid-infrared detection of HR 10: A distant clone of Arp 220 at z = 1.44”. *A&A* 381 (Jan. 2002), L1–L4. DOI: `10.1051/0004-6361:20011520`. arXiv: `astro-ph/0111243 [astro-ph]`.

Elmegreen, Bruce G., Frédéric Bournaud, and Debra Meloy Elmegreen. “Bulge Formation by the Coalescence of Giant Clumps in Primordial Disk Galaxies”. *ApJ* 688.1 (Nov. 2008), 67–77. DOI: `10.1086/592190`. arXiv: `0808.0716 [astro-ph]`.

Euclid Collaboration et al. “Euclid preparation. V. Predicted yield of redshift 7 ¡ z ¡ 9 quasars from the wide survey”. *A&A* 631, A85 (Nov. 2019), A85. DOI: `10.1051/0004-6361/201936427`. arXiv: `1908.04310 [astro-ph.GA]`.

Faisst, Andreas L. et al. “Are High-redshift Galaxies Hot? Temperature of z ¿ 5 Galaxies and Implications for Their Dust Properties”. *ApJ* 847.1, 21 (Sept. 2017), 21. DOI: `10.3847/1538-4357/aa886c`. arXiv: `1708.07842 [astro-ph.GA]`.

Faisst, Andreas L. et al. “ALMA characterizes the dust temperature of z ~ 5.5 star-forming galaxies”. *MNRAS* 498.3 (Nov. 2020), 4192–4204. DOI: `10.1093/mnras/staa2545`. arXiv: `2005.07716 [astro-ph.GA]`.

Fan, Xiaohui, Eduardo Banados, and Robert A. Simcoe. “Quasars and the Intergalactic Medium at Cosmic Dawn”. *arXiv e-prints*, arXiv:2212.06907 (Dec. 2022), arXiv:2212.06907. DOI: `10.48550/arXiv.2212.06907`. arXiv: `2212.06907 [astro-ph.GA]`.

Fan, Xiaohui et al. “High-Redshift Quasars Found in Sloan Digital Sky Survey Commissioning Data”. *AJ* 118.1 (July 1999), 1–13. DOI: `10.1086/300944`. arXiv: `astro-ph/9903237 [astro-ph]`.

Fan, Xiaohui et al. “A Survey of z¿5.8 Quasars in the Sloan Digital Sky Survey. I. Discovery of Three New Quasars and the Spatial Density of Luminous Quasars at z~6”. *AJ* 122.6 (Dec. 2001), 2833–2849. DOI: `10.1086/324111`. arXiv: `astro-ph/0108063 [astro-ph]`.

Fan, Xiaohui et al. “A Survey of z¿5.7 Quasars in the Sloan Digital Sky Survey. II. Discovery of Three Additional Quasars at z¿6”. *AJ* 125.4 (Apr. 2003), 1649–1659. DOI: `10.1086/368246`. arXiv: `astro-ph/0301135 [astro-ph]`.

Farina, Emanuele Paolo et al. “The REQUIEM Survey. I. A Search for Extended Lyα Nebular Emission Around 31 z > 5.7 Quasars”. *ApJ* 887.2, 196 (Dec. 2019), 196. DOI: `10.3847/1538-4357/ab5847`. arXiv: `1911.08498 [astro-ph.GA]`.

Farina, Emanuele Paolo et al. “The X-shooter/ALMA Sample of Quasars in the Epoch of Reionization. II. Black Hole Masses, Eddington Ratios, and the Formation of the First Quasars”. *ApJ* 941.2, 106 (Dec. 2022), 106. DOI: `10.3847/1538-4357/ac9626`. arXiv: `2207.05113 [astro-ph.GA]`.

Faucher-Giguère, Claude-André and Eliot Quataert. “The physics of galactic winds driven by active galactic nuclei”. *MNRAS* 425.1 (Sept. 2012), 605–622. DOI: `10.1111/j.1365-2966.2012.21512.x`. arXiv: `1204.2547 [astro-ph.CO]`.

Ferrarese, Laura and Holland Ford. “Supermassive Black Holes in Galactic Nuclei: Past, Present and Future Research”. *Space Science Reviews* 116.3-4 (Feb. 2005), 523–624. DOI: `10.1007/s11214-005-3947-6`. arXiv: `astro-ph/0411247 [astro-ph]`.

Feruglio, C. et al. “Quasar feedback revealed by giant molecular outflows”. *A&A* 518, L155 (July 2010), L155. DOI: `10.1051/0004-6361/201015164`. arXiv: `1006.1655 [astro-ph.CO]`.

Feruglio, C. et al. “The dense molecular gas in the z ~ 6 QSO SDSS J231038.88+185519.7 resolved by ALMA”. *A&A* 619, A39 (Nov. 2018), A39. DOI: `10.1051/0004-6361/201833174`. arXiv: `1804.05566 [astro-ph.GA]`.

Feruglio, C. et al. “First Constraints on Dense Molecular Gas at z = 7.5149 from the Quasar Pōniuā’ena”. *ApJL* 954.1, L10 (Sept. 2023), L10. DOI: `10.3847/2041-8213/ace0c8`. arXiv: `2304.09129 [astro-ph.GA]`.

Fiore, F. et al. “AGN wind scaling relations and the co-evolution of black holes and galaxies”. *A&A* 601, A143 (May 2017), A143. DOI: `10.1051/0004-6361/201629478`. arXiv: `1702.04507 [astro-ph.GA]`.

Flores Velázquez, José A. et al. “The time-scales probed by star formation rate indicators for realistic, bursty star formation histories from the FIRE simulations”. *MNRAS* 501.4 (Mar. 2021), 4812–4824. DOI: `10.1093/mnras/staa3893`. arXiv: `2008.08582 [astro-ph.GA]`.

Fluetsch, A. et al. “Cold molecular outflows in the local Universe and their feedback effect on galaxies”. *MNRAS* 483.4 (Mar. 2019), 4586–4614. DOI: `10.1093/mnras/sty3449`. arXiv: `1805.05352 [astro-ph.GA]`.

Fontanot, Fabio et al. “The rise of active galactic nuclei in the galaxy evolution and assembly semi-analytic model”. *MNRAS* 496.3 (Aug. 2020), 3943–3960. DOI: `10.1093/mnras/staa1716`. arXiv: `2002.10576 [astro-ph.CO]`.

Foreman-Mackey, Daniel et al. “emcee: The MCMC Hammer”. *PASP* 125.925 (Mar. 2013), 306. DOI: `10.1086/670067`. arXiv: `1202.3665 [astro-ph.IM]`.

Gabor, J. M. and Frédéric Bournaud. “Active galactic nuclei-driven outflows without immediate quenching in simulations of high-redshift disc galaxies”. *MNRAS* 441.2 (June 2014), 1615–1627. DOI: `10.1093/mnras/stu677`. arXiv: `1402.4482 [astro-ph.GA]`.

Gallerani, S. et al. “First CO(17-16) emission line detected in a z ¿ 6 quasar”. *MNRAS* 445.3 (Dec. 2014), 2848–2853. DOI: `10.1093/mnras/stu2031`. arXiv: `1409.4413 [astro-ph.GA]`.

Galliano, Frédéric, Maud Galametz, and Anthony P. Jones. “The Interstellar Dust Properties of Nearby Galaxies”. *ARA&A* 56 (Sept. 2018), 673–713. DOI: `10.1146/annurev-astro-081817-051900`. arXiv: `1711.07434 [astro-ph.GA]`.

Garratt, T. K. et al. “Cosmic Evolution of the H_2 Mass Density and the Epoch of Molecular Gas”. *ApJ* 912.1, 62 (May 2021), 62. DOI: `10.3847/1538-4357/abec81`. arXiv: `2103.08613 [astro-ph.GA]`.

Genzel, R. et al. “The SINS/zC-SINF Survey of z ~2 Galaxy Kinematics: Evidence for Gravitational Quenching”. *ApJ* 785.1, 75 (Apr. 2014), 75. DOI: `10.1088/0004-637X/785/1/75`. arXiv: `1310.3838 [astro-ph.CO]`.

Genzel, R. et al. “Rotation Curves in z $\sim$ 1-2 Star-forming Disks: Evidence for Cored Dark Matter Distributions”. *ApJ* 902.2, 98 (Oct. 2020), 98. DOI: `10.3847/1538-4357/abb0ea`. arXiv: `2006.03046 [astro-ph.GA]`.

Genzel, Reinhard. “The Early Evolution of Galactic Disks: Structure, Dynamics and Feedback”. *Disk Instabilities Across Cosmic Scales*. July 2017, 5, 5.

Glikman, Eilat et al. “MAJOR MERGERS HOST THE MOST-LUMINOUS RED QUASARS AT z $\sim$ 2: A HUBBLE SPACE TELESCOPE WFC3/IR STUDY*”. *The Astrophysical Journal* 806.2 (June 2015), 218. DOI: `10.1088/0004-637X/806/2/218`. URL: `https://dx.doi.org/10.1088/0004-637X/806/2/218`.

Greiner, J. et al. “Quasar clustering at redshift 6”. *A&A* 654, A79 (Oct. 2021), A79. DOI: `10.1051/0004-6361/202140790`. arXiv: `2107.09739 [astro-ph.GA]`.

Grier, C. J. et al. “The Sloan Digital Sky Survey Reverberation Mapping Project: Hα and Hβ Reverberation Measurements from First-year Spectroscopy and Photometry”. *ApJ* 851.1, 21 (Dec. 2017), 21. DOI: `10.3847/1538-4357/aa98dc`. arXiv: `1711.03114 [astro-ph.GA]`.

Gullberg, B. et al. “The nature of the [C II] emission in dusty star-forming galaxies from the SPT survey”. *MNRAS* 449.3 (May 2015), 2883–2900. DOI: `10.1093/mnras/stv372`. arXiv: `1501.06909 [astro-ph.GA]`.

Hailey-Dunsheath, S. et al. “Detection of the 158 μm [C II] Transition at z = 1.3: Evidence for a Galaxy-wide Starburst”. *ApJL* 714.1 (May 2010), L162–L166. DOI: `10.1088/2041-8205/714/1/L162`. arXiv: `1003.2174 [astro-ph.CO]`.

Hamanowicz, Aleksandra et al. “ALMACAL VIII: a pilot survey for untargeted extragalactic CO emission lines in deep ALMA calibration data”. *MNRAS* 519.1 (Feb. 2023), 34–49. DOI: `10.1093/mnras/stac3159`. arXiv: `2211.00066 [astro-ph.GA]`.

Harikane, Yuichi et al. “Large Population of ALMA Galaxies at z ¿ 6 with Very High [O III] 88 μm to [C II] 158 μm Flux Ratios: Evidence of Extremely High Ionization Parameter or PDR Deficit?” *ApJ* 896.2, 93 (June 2020), 93. doi: 10.3847/1538-4357/ab94bd. arXiv: 1910.10927 [astro-ph.GA].

Harikane, Yuichi et al. “JWST/NIRSpec First Census of Broad-Line AGNs at z=4-7: Detection of 10 Faint AGNs with M_BH~106̂-107̂ M_sun and Their Host Galaxy Properties”. *arXiv e-prints*, arXiv:2303.11946 (Mar. 2023), arXiv:2303.11946. doi: 10.48550/arXiv.2303.11946. arXiv: 2303.11946 [astro-ph.GA].

Hashimoto, Takuya et al. “Detections of [O III] 88 μm in two quasars in the reionization epoch”. *PASJ* 71.6, 109 (Dec. 2019), 109. doi: 10.1093/pasj/psz094. arXiv: 1811.00030 [astro-ph.GA].

Hernquist, Lars and Joshua E. Barnes. “Origin of kinematic subsystems in elliptical galaxies”. *Nature* 354.6350 (Nov. 1991), 210–212. doi: 10.1038/354210a0.

Herrera-Camus, R. et al. “[C II] 158 μm Emission as a Star Formation Tracer”. *ApJ* 800.1, 1 (Feb. 2015), 1. doi: 10.1088/0004-637X/800/1/1. arXiv: 1409.7123 [astro-ph.GA].

Herrera-Camus, R. et al. “SHINING, A Survey of Far-infrared Lines in Nearby Galaxies. II. Line-deficit Models, AGN Impact, [C II]-SFR Scaling Relations, and Mass-Metallicity Relation in (U)LIRGs”. *ApJ* 861.2, 95 (July 2018), 95. doi: 10.3847/1538-4357/aac0f9. arXiv: 1803.04422 [astro-ph.GA].

Herrera-Camus, R. et al. “Molecular and Ionized Gas Phases of an AGN-driven Outflow in a Typical Massive Galaxy at z $\approx$ 2”. *ApJ* 871.1, 37 (Jan. 2019), 37. doi: 10.3847/1538-4357/aaf6a7. arXiv: 1807.07074 [astro-ph.GA].

Herrera-Camus, R. et al. “Molecular gas inflows and outflows in ultraluminous infrared galaxies at z ~ 0.2 and one QSO at z = 6.1”. *A&A* 633, L4 (Jan. 2020), L4. doi: 10.1051/0004-6361/201937109. arXiv: 1912.05548 [astro-ph.GA].

Hines, Dean C. et al. “Spitzer Observations of High-Redshift QSOs”. *ApJL* 641.2 (Apr. 2006), L85–L88. doi: 10.1086/504109. arXiv: astro-ph/0604347 [astro-ph].

Hjorth, Jens, Christa Gall, and Michał J. Michałowski. “Shaping the Dust Mass-Star-formation Rate Relation”. *ApJL* 782.2, L23 (Feb. 2014), L23. doi: 10.1088/2041-8205/782/2/L23. arXiv: 1401.5578 [astro-ph.GA].

Hollenbach, D. J. and A. G. G. M. Tielens. “Photodissociation regions in the interstellar medium of galaxies”. *Reviews of Modern Physics* 71.1 (Jan. 1999), 173–230. doi: 10.1103/RevModPhys.71.173.

Hollenbach, David et al. “Water, O_2, and Ice in Molecular Clouds”. *ApJ* 690.2 (Jan. 2009), 1497–1521. doi: 10.1088/0004-637X/690/2/1497. arXiv: 0809.1642 [astro-ph].

Homayouni, Y. et al. “The Sloan Digital Sky Survey Reverberation Mapping Project: Mg II Lag Results from Four Years of Monitoring”. *ApJ* 901.1, 55 (Sept. 2020), 55. doi: 10.3847/1538-4357/ababa9. arXiv: 2005.03663 [astro-ph.GA].

Hopkins, Philip F. et al. “A Physical Model for the Origin of Quasar Lifetimes”. *ApJL* 625.2 (June 2005), L71–L74. DOI: `10.1086/431146`. arXiv: `astro-ph/0502241 [astro-ph]`.

Hu, Haojie et al. “Supercritical Growth Pathway to Overmassive Black Holes at Cosmic Dawn: Coevolution with Massive Quasar Hosts”. *ApJ* 935.2, 140 (Aug. 2022), 140. DOI: `10.3847/1538-4357/ac7daa`. arXiv: `2204.12513 [astro-ph.GA]`.

Inayoshi, Kohei et al. “Rapid Growth of Seed Black Holes during Early Bulge Formation”. *ApJ* 927.2, 237 (Mar. 2022), 237. DOI: `10.3847/1538-4357/ac4751`. arXiv: `2110.10693 [astro-ph.GA]`.

Ishibashi, W. and A. C. Fabian. “How the central black hole may shape its host galaxy through AGN feedback”. *MNRAS* 441.2 (June 2014), 1474–1478. DOI: `10.1093/mnras/stu672`. arXiv: `1404.0908 [astro-ph.GA]`.

Ishibashi, W., A. C. Fabian, and R. Maiolino. “The energetics of AGN radiation pressure-driven outflows”. *MNRAS* 476.1 (May 2018), 512–519. DOI: `10.1093/mnras/sty236`. arXiv: `1801.09700 [astro-ph.GA]`.

Iwamuro, Fumihide et al. “Fe II/Mg II Emission-Line Ratios of QSOs. II. z ¿ 6 Objects”. *ApJ* 614.1 (Oct. 2004), 69–74. DOI: `10.1086/423610`. arXiv: `astro-ph/0408517 [astro-ph]`.

Izumi, Takuma et al. “Subaru High-z Exploration of Low-Luminosity Quasars (SHELLQs). III. Star formation properties of the host galaxies at z $\gtrsim$ 6 studied with ALMA”. *PASJ* 70.3, 36 (June 2018), 36. DOI: `10.1093/pasj/psy026`. arXiv: `1802.05742 [astro-ph.GA]`.

Izumi, Takuma et al. “Subaru High-z Exploration of Low-Luminosity Quasars (SHELLQs). VIII. A less biased view of the early co-evolution of black holes and host galaxies”. *PASJ* 71.6, 111 (Dec. 2019), 111. DOI: `10.1093/pasj/psz096`. arXiv: `1904.07345 [astro-ph.GA]`.

Izumi, Takuma et al. “Subaru High-z Exploration of Low-luminosity Quasars (SHELLQs). XII. Extended [C II] Structure (Merger or Outflow) in a z = 6.72 Red Quasar”. *ApJ* 908.2, 235 (Feb. 2021), 235. DOI: `10.3847/1538-4357/abd7ef`. arXiv: `2101.01199 [astro-ph.GA]`.

Izumi, Takuma et al. “Subaru High-z Exploration of Low-luminosity Quasars (SHELLQs). XIII. Large-scale Feedback and Star Formation in a Low-luminosity Quasar at z = 7.07 on the Local Black Hole to Host Mass Relation”. *ApJ* 914.1, 36 (June 2021), 36. DOI: `10.3847/1538-4357/abf6dc`. arXiv: `2104.05738 [astro-ph.GA]`.

Jaffe, W. et al. “The central dusty torus in the active nucleus of NGC 1068”. *Nature* 429.6987 (May 2004), 47–49. DOI: `10.1038/nature02531`.

Jiang, Linhua et al. “Probing the Evolution of Infrared Properties of z ~6 Quasars: Spitzer Observations”. *AJ* 132.5 (Nov. 2006), 2127–2134. DOI: `10.1086/508209`. arXiv: `astro-ph/0608006 [astro-ph]`.

Jiang, Linhua et al. “A Survey of z ~6 Quasars in the Sloan Digital Sky Survey Deep Stripe. I. A Flux-Limited Sample at z$_{AB}$ ¡ 21”. *AJ* 135.3 (Mar. 2008), 1057–1066. doi: 10.1088/0004-6256/135/3/1057. arXiv: 0708.2578 [astro-ph].

Jiang, Linhua et al. “A Survey of z ~6 Quasars in the Sloan Digital Sky Survey Deep Stripe. II. Discovery of Six Quasars at z $_{AB}$¿21”. *AJ* 138.1 (July 2009), 305–311. doi: 10.1088/0004-6256/138/1/305. arXiv: 0905.4126 [astro-ph.CO].

Jiang, Linhua et al. “The Final SDSS High-redshift Quasar Sample of 52 Quasars at z¿5.7”. *ApJ* 833.2, 222 (Dec. 2016), 222. doi: 10.3847/1538-4357/833/2/222. arXiv: 1610.05369 [astro-ph.GA].

Johnson, Jarrett L. and Francesco Haardt. “The Early Growth of the First Black Holes”. *PASA* 33, e007 (Mar. 2016), e007. doi: 10.1017/pasa.2016.4. arXiv: 1601.05473 [astro-ph.GA].

Jones, A. P. et al. “The evolution of amorphous hydrocarbons in the ISM: dust modelling from a new vantage point”. *A&A* 558, A62 (Oct. 2013), A62. doi: 10.1051/0004-6361/201321686. arXiv: 1411.6293 [astro-ph.GA].

Jones, A. P. et al. “The global dust modelling framework THEMIS”. *A&A* 602, A46 (June 2017), A46. doi: 10.1051/0004-6361/201630225. arXiv: 1703.00775 [astro-ph.GA].

Kapala, M. J. et al. “The Survey of Lines in M31 (SLIM): Investigating the Origins of [C II] Emission”. *ApJ* 798.1, 24 (Jan. 2015), 24. doi: 10.1088/0004-637X/798/1/24. arXiv: 1410.6158 [astro-ph.GA].

Kashikawa, Nobunari et al. “The Subaru High-z Quasar Survey: Discovery of Faint z ~6 Quasars”. *ApJ* 798.1, 28 (Jan. 2015), 28. doi: 10.1088/0004-637X/798/1/28. arXiv: 1410.7401 [astro-ph.GA].

Kashino, Daichi et al. “EIGER I. a large sample of [OIII]-emitting galaxies at $5.3 < z < 6.9$ and direct evidence for local reionization by galaxies”. *arXiv e-prints*, arXiv:2211.08254 (Nov. 2022), arXiv:2211.08254. doi: 10.48550/arXiv.2211.08254. arXiv: 2211.08254 [astro-ph.GA].

Kennicutt, Robert C. and Neal J. Evans. “Star Formation in the Milky Way and Nearby Galaxies”. *ARA&A* 50 (Sept. 2012), 531–608. doi: 10.1146/annurev-astro-081811-125610. arXiv: 1204.3552 [astro-ph.GA].

Kimball, Amy E. et al. “ALMA detection of a disc-dominated [C II] emission line at z=4.6 in the luminous QSO J1554+1937”. *MNRAS* 452.1 (Sept. 2015), 88–98. doi: 10.1093/mnras/stv1160. arXiv: 1505.05262 [astro-ph.GA].

Klitsch, Anne et al. “ALMACAL - VI. Molecular gas mass density across cosmic time via a blind search for intervening molecular absorbers”. *MNRAS* 490.1 (Nov. 2019), 1220–1230. doi: 10.1093/mnras/stz2660. arXiv: 1909.08624 [astro-ph.GA].

Kocevski, Dale D. et al. “CEERS Key Paper. II. A First Look at the Resolved Host Properties of AGN at $3 < z < 5$ with JWST”. *ApJL* 946.1, L14 (Mar. 2023), L14. doi: 10.3847/2041-8213/acad00. arXiv: 2208.14480 [astro-ph.GA].

Kormendy, John and Luis C. Ho. "Coevolution (Or Not) of Supermassive Black Holes and Host Galaxies". *Annual Review of Astronomy and Astrophysics* 51.1 (2013), 511–653. DOI: `10.1146/annurev-astro-082708-101811`. eprint: `https://doi.org/10.1146/annurev-astro-082708-101811`. URL: `https://doi.org/10.1146/annurev-astro-082708-101811`.

Kroupa, Pavel and Carsten Weidner. "Galactic-Field Initial Mass Functions of Massive Stars". *ApJ* 598.2 (Dec. 2003), 1076–1078. DOI: `10.1086/379105`. arXiv: `astro-ph/0308356 [astro-ph]`.

La Franca, F. et al. "The HELLAS2XMM Survey. VII. The Hard X-Ray Luminosity Function of AGNs up to z = 4: More Absorbed AGNs at Low Luminosities and High Redshifts". *ApJ* 635.2 (Dec. 2005), 864–879. DOI: `10.1086/497586`. arXiv: `astro-ph/0509081 [astro-ph]`.

La Franca, F. et al. "Extending virial black hole mass estimates to low-luminosity or obscured AGN: the cases of NGC 4395 and MCG -01-24-012". *MNRAS* 449.2 (May 2015), 1526–1535. DOI: `10.1093/mnras/stv368`. arXiv: `1502.07234 [astro-ph.GA]`.

La Franca, Fabio et al. "Detection of faint BLR components in the starburst/Seyfert galaxy NGC 6221 and measure of the central BH mass". *Frontiers in Astronomy and Space Sciences* 3, 12 (Apr. 2016), 12. DOI: `10.3389/fspas.2016.00012`. arXiv: `1605.06253 [astro-ph.GA]`.

Lagache, G., M. Cousin, and M. Chatzikos. "The [CII] 158 μm line emission in high-redshift galaxies". *A&A* 609, A130 (Jan. 2018), A130. DOI: `10.1051/0004-6361/201732019`. arXiv: `1711.00798 [astro-ph.GA]`.

Lamperti, Isabella et al. "JINGLE - V. Dust properties of nearby galaxies derived from hierarchical Bayesian SED fitting". *MNRAS* 489.3 (Nov. 2019), 4389–4417. DOI: `10.1093/mnras/stz2311`. arXiv: `1909.05266 [astro-ph.GA]`.

Laporte, N. et al. "Dust in the Reionization Era: ALMA Observations of a z = 8.38 Gravitationally Lensed Galaxy". *ApJL* 837.2, L21 (Mar. 2017), L21. DOI: `10.3847/2041-8213/aa62aa`. arXiv: `1703.02039 [astro-ph.GA]`.

Larson, Rebecca L. et al. "A CEERS Discovery of an Accreting Supermassive Black Hole 570 Myr after the Big Bang: Identifying a Progenitor of Massive z ¿ 6 Quasars". *ApJL* 953.2, L29 (Aug. 2023), L29. DOI: `10.3847/2041-8213/ace619`. arXiv: `2303.08918 [astro-ph.GA]`.

Lehnert, M. D. et al. "Etching glass in the early Universe: Luminous HF and H_2O emission in a QSO-SMG pair at z = 4.7". *A&A* 641, A124 (Sept. 2020), A124. DOI: `10.1051/0004-6361/201935755`. arXiv: `2004.04176 [astro-ph.GA]`.

Leipski, C. et al. "Complete Infrared Spectral Energy Distributions of Millimeter Detected Quasars at z ¿ 5". *ApJ* 772.2, 103 (Aug. 2013), 103. DOI: `10.1088/0004-637X/772/2/103`. arXiv: `1305.3999 [astro-ph.CO]`.

Leipski, C. et al. “Spectral Energy Distributions of QSOs at z ¿ 5: Common Active Galactic Nucleus-heated Dust and Occasionally Strong Star-formation”. *ApJ* 785.2, 154 (Apr. 2014), 154. doi: `10.1088/0004-637X/785/2/154`. arXiv: `1402.5976 [astro-ph.GA]`.

Lelli, Federico et al. “A massive stellar bulge in a regularly rotating galaxy 1.2 billion years after the Big Bang”. *Science* 371.6530 (Feb. 2021), 713–716. doi: `10.1126/science.abc1893`. arXiv: `2102.05957 [astro-ph.GA]`.

Lelli, Federico et al. “WISDOM Project - XIII. Feeding molecular gas to the supermassive black hole in the starburst AGN-host galaxy Fairall 49”. *MNRAS* 516.3 (Nov. 2022), 4066–4083. doi: `10.1093/mnras/stac2493`. arXiv: `2209.00363 [astro-ph.GA]`.

Lenkić, Laura et al. “Plateau de Bure High-z Blue Sequence Survey 2 (PHIBSS2): Search for Secondary Sources, CO Luminosity Functions in the Field, and the Evolution of Molecular Gas Density through Cosmic Time”. *AJ* 159.5, 190 (May 2020), 190. doi: `10.3847/1538-3881/ab7458`. arXiv: `1908.01791 [astro-ph.GA]`.

Lequeux, James. *The Interstellar Medium*. 2005. doi: `10.1007/b137959`.

Leroy, Adam K. et al. “The Star Formation Efficiency in Nearby Galaxies: Measuring Where Gas Forms Stars Effectively”. *AJ* 136.6 (Dec. 2008), 2782–2845. doi: `10.1088/0004-6256/136/6/2782`. arXiv: `0810.2556 [astro-ph]`.

Leroy, Adam K. et al. “The CO-to-H_2 Conversion Factor from Infrared Dust Emission across the Local Group”. *ApJ* 737.1, 12 (Aug. 2011), 12. doi: `10.1088/0004-637X/737/1/12`. arXiv: `1102.4618 [astro-ph.CO]`.

Li, Jianan et al. “Probing the Full CO Spectral Line Energy Distribution (SLED) in the Nuclear Region of a Quasar-starburst System at z = 6.003”. *ApJ* 889.2, 162 (Feb. 2020), 162. doi: `10.3847/1538-4357/ab65fa`. arXiv: `1912.12813 [astro-ph.GA]`.

Li, Jianan et al. “Spatially Resolved Molecular Interstellar Medium in a z = 6.6 Quasar Host Galaxy”. *ApJ* 930.1, 27 (May 2022), 27. doi: `10.3847/1538-4357/ac61d7`. arXiv: `2204.00793 [astro-ph.GA]`.

Lima Neto, G. B., D. Gerbal, and I. Márquez. “The specific entropy of elliptical galaxies: an explanation for profile-shape distance indicators?” *MNRAS* 309.2 (Oct. 1999), 481–495. doi: `10.1046/j.1365-8711.1999.02849.x`. arXiv: `astro-ph/9905048 [astro-ph]`.

Liu, L. et al. “HIFI Spectroscopy of H_2O Submillimeter Lines in Nuclei of Actively Star-forming Galaxies”. *ApJ* 846.1, 5 (Sept. 2017), 5. doi: `10.3847/1538-4357/aa81b4`. arXiv: `1707.04914 [astro-ph.GA]`.

Liu, Yuanqi et al. “Exploring the Radio Spectral Energy Distribution of the Ultraluminous Radio-quiet Quasar SDSS J0100+2802 at Redshift 6.3”. *ApJ* 929.1, 69 (Apr. 2022), 69. doi: `10.3847/1538-4357/ac5c50`. arXiv: `2203.02922 [astro-ph.GA]`.

Madden, S. C. et al. “Tracing the total molecular gas in galaxies: [CII] and the CO-dark gas”. *A&A* 643, A141 (Nov. 2020), A141. doi: `10.1051/0004-6361/202038860`. arXiv: `2009.00649 [astro-ph.GA]`.

Maio, U., Céline Péroux, and Benedetta Ciardi. "Atomic and molecular gas from the epoch of reionisation down to redshift 2". *A&A* 657, A47 (Jan. 2022), A47. DOI: `10.1051/0004-6361/202142264`. arXiv: `2111.13701 [astro-ph.GA]`.

Maio, U. et al. "Metal and molecule cooling in simulations of structure formation". *MNRAS* 379.3 (Aug. 2007), 963–973. DOI: `10.1111/j.1365-2966.2007.12016.x`. arXiv: `0704.2182 [astro-ph]`.

Maiolino, R. and G. Risaliti. "X-ray Absorption in Active Galactic Nuclei". *The Central Engine of Active Galactic Nuclei*. Ed. by L. C. Ho and J. -W. Wang. Vol. 373. Astronomical Society of the Pacific Conference Series. Oct. 2007, 447. DOI: `10.48550/arXiv.astro-ph/0701109`. arXiv: `astro-ph/0701109 [astro-ph]`.

Maiolino, R. et al. "First detection of [CII]158 μm at high redshift: vigorous star formation in the early universe". *A&A* 440.2 (Sept. 2005), L51–L54. DOI: `10.1051/0004-6361:200500165`. arXiv: `astro-ph/0508064 [astro-ph]`.

Maiolino, R. et al. "Evidence of strong quasar feedback in the early Universe". *MNRAS* 425.1 (Sept. 2012), L66–L70. DOI: `10.1111/j.1745-3933.2012.01303.x`. arXiv: `1204.2904 [astro-ph.CO]`.

Maiolino, R. et al. "Star formation inside a galactic outflow". *Nature* 544.7649 (Mar. 2017), 202–206. DOI: `10.1038/nature21677`. arXiv: `1703.08587 [astro-ph.GA]`.

Maiolino, R. et al. "A small and vigorous black hole in the early Universe". *arXiv e-prints*, arXiv:2305.12492 (May 2023), arXiv:2305.12492. DOI: `10.48550/arXiv.2305.12492`. arXiv: `2305.12492 [astro-ph.GA]`.

Malhotra, Sangeeta et al. "Herschel Extreme Lensing Line Observations: [CII] Variations in Galaxies at Redshifts z=1-3". *ApJ* 835.1, 110 (Jan. 2017), 110. DOI: `10.3847/1538-4357/835/1/110`.

Malik, U. et al. "OzDES Reverberation Mapping Program: Hβ lags from the 6-yr survey". *MNRAS* 520.2 (Apr. 2023), 2009–2023. DOI: `10.1093/mnras/stad145`. arXiv: `2210.03977 [astro-ph.GA]`.

Mancuso, C. et al. "The Main Sequences of Star-forming Galaxies and Active Galactic Nuclei at High Redshift". *ApJ* 833.2, 152 (Dec. 2016), 152. DOI: `10.3847/1538-4357/833/2/152`. arXiv: `1610.05910 [astro-ph.GA]`.

Marconi, A. et al. "Local supermassive black holes, relics of active galactic nuclei and the X-ray background". *MNRAS* 351.1 (June 2004), 169–185. DOI: `10.1111/j.1365-2966.2004.07765.x`. arXiv: `astro-ph/0311619 [astro-ph]`.

Marshall, M. A. et al. "Limits to Rest-frame Ultraviolet Emission from Far-infrared-luminous $z \simeq 6$ Quasar Hosts". *ApJ* 900.1, 21 (Sept. 2020), 21. DOI: `10.3847/1538-4357/abaa4c`. arXiv: `2007.13859 [astro-ph.GA]`.

Marshall, Madeline A. et al. "GA-NIFS: Black hole and host galaxy properties of two z≃6.8 quasars from the NIRSpec IFU". *arXiv e-prints*, arXiv:2302.04795 (Feb. 2023), arXiv:2302.04795. DOI: `10.48550/arXiv.2302.04795`. arXiv: `2302.04795 [astro-ph.GA]`.

Mathis, J. S., W. Rumpl, and K. H. Nordsieck. “The size distribution of interstellar grains.” *ApJ* 217 (Oct. 1977), 425–433. DOI: 10.1086/155591.

Matsuoka, Yoshiki et al. “Subaru High-z Exploration of Low-luminosity Quasars (SHELLQs). XVI. 69 New Quasars at 5.8 ¡ z ¡ 7.0”. *ApJS* 259.1, 18 (Mar. 2022), 18. DOI: 10.3847/1538-4365/ac3d31. arXiv: 2111.12766 [astro-ph.GA].

Matthews, James H. et al. “A disc wind model for blueshifts in quasar broad emission lines”. *MNRAS* 526.3 (Dec. 2023), 3967–3986. DOI: 10.1093/mnras/stad2895. arXiv: 2309.14434 [astro-ph.GA].

Mazzucchelli, C. et al. “Physical Properties of 15 Quasars at $z \gtrsim 6.5$”. *ApJ* 849.2, 91 (Nov. 2017), 91. DOI: 10.3847/1538-4357/aa9185. arXiv: 1710.01251 [astro-ph.GA].

Mazzucchelli, C. et al. “XQR-30: Black Hole Masses and Accretion Rates of 42 z¿6 Quasars”. *arXiv e-prints*, arXiv:2306.16474 (June 2023), arXiv:2306.16474. DOI: 10.48550/arXiv.2306.16474. arXiv: 2306.16474 [astro-ph.GA].

McMullin, J. P. et al. “CASA Architecture and Applications”. *Astronomical Data Analysis Software and Systems XVI*. Ed. by R. A. Shaw, F. Hill, and D. J. Bell. Vol. 376. Astronomical Society of the Pacific Conference Series. Oct. 2007, 127.

Mechtley, M. et al. “Near-infrared Imaging of a z = 6.42 Quasar Host Galaxy with the Hubble Space Telescope Wide Field Camera 3”. *ApJL* 756.2, L38 (Sept. 2012), L38. DOI: 10.1088/2041-8205/756/2/L38. arXiv: 1207.3283 [astro-ph.CO].

Mejıéa-Restrepo, J. E. et al. “Can we improve C IV-based single-epoch black hole mass estimations?” *MNRAS* 478.2 (Aug. 2018), 1929–1941. DOI: 10.1093/mnras/sty1086. arXiv: 1805.00942 [astro-ph.GA].

Meyer, Romain A., Sarah E. I. Bosman, and Richard S. Ellis. “New constraints on quasar evolution: broad-line velocity shifts over $1.5 \lesssim z \lesssim 7.5$”. *MNRAS* 487.3 (Aug. 2019), 3305–3323. DOI: 10.1093/mnras/stz1504. arXiv: 1902.04558 [astro-ph.GA].

Miettinen, O. et al. “An ALMA survey of submillimetre galaxies in the COSMOS field: Physical properties derived from energy balance spectral energy distribution modelling”. *A&A* 606, A17 (Sept. 2017), A17. DOI: 10.1051/0004-6361/201730762. arXiv: 1707.00637 [astro-ph.GA].

Mortlock, Daniel J. et al. “The UKIRT Infrared Deep Sky Survey and the search for the most distant quasars”. *arXiv e-prints*, arXiv:0810.3859 (Oct. 2008), arXiv:0810.3859. DOI: 10.48550/arXiv.0810.3859. arXiv: 0810.3859 [astro-ph].

Mortlock, Daniel J. et al. “A luminous quasar at a redshift of z = 7.085”. *Nature* 474.7353 (June 2011), 616–619. DOI: 10.1038/nature10159. arXiv: 1106.6088 [astro-ph.CO].

Murray, N. et al. “Accretion Disk Winds from Active Galactic Nuclei”. *ApJ* 451 (Oct. 1995), 498. DOI: 10.1086/176238.

Neeleman, Marcel et al. “Resolved [C II] Emission from z ¿ 6 Quasar Host-Companion Galaxy Pairs”. *ApJ* 882.1, 10 (Sept. 2019), 10. DOI: 10.3847/1538-4357/ab2ed3. arXiv: 1907.02536 [astro-ph.GA].

Neeleman, Marcel et al. “The Kinematics of $z \gtrsim 6$ Quasar Host Galaxies”. *ApJ* 911.2, 141 (Apr. 2021), 141. DOI: 10.3847/1538-4357/abe70f. arXiv: 2102.05679 [astro-ph.GA].

Neri, R. et al. “High-resolution C^+ imaging of HDF850.1 reveals a merging galaxy at $z = 5.185$”. *A&A* 562, A35 (Feb. 2014), A35. DOI: 10.1051/0004-6361/201322528. arXiv: 1401.2396 [astro-ph.GA].

Netzer, Hagai. *The Physics and Evolution of Active Galactic Nuclei*. 2013.

Neufeld, David A. and Michael J. Kaufman. “Radiative Cooling of Warm Molecular Gas”. *ApJ* 418 (Nov. 1993), 263. DOI: 10.1086/173388.

Neufeld, David A., Stephen Lepp, and Gary J. Melnick. “Thermal Balance in Dense Molecular Clouds: Radiative Cooling Rates and Emission-Line Luminosities”. *ApJS* 100 (Sept. 1995), 132. DOI: 10.1086/192211.

Novak, Mladen et al. “An ALMA Multiline Survey of the Interstellar Medium of the Redshift 7.5 Quasar Host Galaxy J1342+0928”. *ApJ* 881.1, 63 (Aug. 2019), 63. DOI: 10.3847/1538-4357/ab2beb. arXiv: 1906.08569 [astro-ph.GA].

Oesch, P. A. et al. “A Remarkably Luminous Galaxy at z=11.1 Measured with Hubble Space Telescope Grism Spectroscopy”. *ApJ* 819.2, 129 (Mar. 2016), 129. DOI: 10.3847/0004-637X/819/2/129. arXiv: 1603.00461 [astro-ph.GA].

Olsen, Karen et al. “Challenges and Techniques for Simulating Line Emission”. *Galaxies* 6.4 (Sept. 2018), 100. DOI: 10.3390/galaxies6040100. arXiv: 1808.08251 [astro-ph.GA].

Omont, A. et al. “H_2O emission in high-z ultra-luminous infrared galaxies”. *A&A* 551, A115 (Mar. 2013), A115. DOI: 10.1051/0004-6361/201220811. arXiv: 1301.6618 [astro-ph.CO].

Onori, F. et al. “Detection of faint broad emission lines in type 2 AGN - II. On the measurement of the black hole mass of type 2 AGN and the unified model”. *MNRAS* 468.1 (June 2017), L97–L102. DOI: 10.1093/mnrasl/slx032. arXiv: 1703.05167 [astro-ph.GA].

Orr, Matthew E. et al. “What FIREs up star formation: the emergence of the Kennicutt-Schmidt law from feedback”. *MNRAS* 478.3 (Aug. 2018), 3653–3673. DOI: 10.1093/mnras/sty1241. arXiv: 1701.01788 [astro-ph.GA].

Pallottini, A. et al. “A survey of high-z galaxies: SERRA simulations”. *MNRAS* 513.4 (July 2022), 5621–5641. DOI: 10.1093/mnras/stac1281. arXiv: 2201.02636 [astro-ph.GA].

Papadopoulos, Padeli et al. “A massive reservoir of low-excitation molecular gas at high redshift”. *Nature* 409.6816 (Jan. 2001), 58–60. DOI: 10.1038/35051029. arXiv: astro-ph/0101028 [astro-ph].

Papadopoulos, Padeli P. et al. “CO Spectral Line Energy Distributions of Infrared-Luminous Galaxies and Active Galactic Nuclei”. *ApJ* 715.2 (June 2010), 775–792. DOI: 10.1088/0004-637X/715/2/775. arXiv: 1003.5889 [astro-ph.CO].

Parente, Massimiliano et al. “The $z \lesssim 1$ drop of cosmic dust abundance in a semi-analytic framework”. *MNRAS* 521.4 (June 2023), 6105–6123. DOI: 10.1093/mnras/stad907. arXiv: 2302.03058 [astro-ph.GA].

Park, Daeseong et al. “Extending the Calibration of C IV-based Single-epoch Black Hole Mass Estimators for Active Galactic Nuclei”. *ApJ* 839.2, 93 (Apr. 2017), 93. DOI: `10.3847/1538-4357/aa6a53`. arXiv: `1703.09867 [astro-ph.GA]`.

Pearson, W. J. et al. “Main sequence of star forming galaxies beyond the Herschel confusion limit”. *A&A* 615, A146 (July 2018), A146. DOI: `10.1051/0004-6361/201832821`. arXiv: `1804.03482 [astro-ph.GA]`.

Peng, Chien Y. et al. “Probing the Coevolution of Supermassive Black Holes and Galaxies Using Gravitationally Lensed Quasar Hosts”. *ApJ* 649.2 (Oct. 2006), 616–634. DOI: `10.1086/506266`. arXiv: `astro-ph/0603248 [astro-ph]`.

Pensabene, A. et al. “The ALMA view of the high-redshift relation between supermassive black holes and their host galaxies”. *A&A* 637, A84 (May 2020), A84. DOI: `10.1051/0004-6361/201936634`. arXiv: `2002.00958 [astro-ph.GA]`.

Pensabene, A. et al. “ALMA multiline survey of the ISM in two quasar host-companion galaxy pairs at $z > 6$”. *A&A* 652, A66 (Aug. 2021), A66. DOI: `10.1051/0004-6361/202039696`. arXiv: `2105.09958 [astro-ph.GA]`.

Petric, Andreea O. et al. “Herschel Survey of the Palomar-Green QSOs at Low Redshift”. *ApJS* 219.2, 22 (Aug. 2015), 22. DOI: `10.1088/0067-0049/219/2/22`. arXiv: `1505.05273 [astro-ph.GA]`.

Pons, E. et al. “X-ray properties of $z \gtrsim 6.5$ quasars”. *MNRAS* 491.3 (Jan. 2020), 3884–3890. DOI: `10.1093/mnras/stz3275`. arXiv: `1910.04122 [astro-ph.GA]`.

Pozzi, F. et al. “The dust mass function from z ~0 to z ~2.5”. *MNRAS* 491.4 (Feb. 2020), 5073–5082. DOI: `10.1093/mnras/stz2724`. arXiv: `1909.11333 [astro-ph.GA]`.

Reed, S. L. et al. “Eight new luminous $z \geq 6$ quasars discovered via SED model fitting of VISTA, WISE and Dark Energy Survey Year 1 observations”. *MNRAS* 468.4 (July 2017), 4702–4718. DOI: `10.1093/mnras/stx728`. arXiv: `1701.04852 [astro-ph.GA]`.

Reed, S. L. et al. “Three new VHS-DES quasars at 6.7 ¡ z ¡ 6.9 and emission line properties at z ¿ 6.5”. *MNRAS* 487.2 (Aug. 2019), 1874–1885. DOI: `10.1093/mnras/stz1341`. arXiv: `1901.07456 [astro-ph.GA]`.

Reines, Amy E. and M. Volonteri. “Relations between Central Black Hole Mass and Total Galaxy Stellar Mass in the Local Universe”. *ApJ* 813.2, 82 (Nov. 2015), 82. DOI: `10.1088/0004-637X/813/2/82`. arXiv: `1508.06274 [astro-ph.GA]`.

Reuter, C. et al. “The Complete Redshift Distribution of Dusty Star-forming Galaxies from the SPT-SZ Survey”. *ApJ* 902.1, 78 (Oct. 2020), 78. DOI: `10.3847/1538-4357/abb599`. arXiv: `2006.14060 [astro-ph.GA]`.

Ricci, F. et al. “Detection of faint broad emission lines in type 2 AGNs - III. On the M_{BH}-$\sigma_\star$ relation of type 2 AGNs”. *MNRAS* 471.1 (Oct. 2017), L41–L46. DOI: `10.1093/mnrasl/slx103`. arXiv: `1706.06110 [astro-ph.GA]`.

Riechers, Dominik A. et al. “Imaging The Molecular Gas in a z = 3.9 Quasar Host Galaxy at 0farcs3 Resolution: A Central, Sub-Kiloparsec Scale Star Formation Reservoir in APM

08279+5255”. *ApJ* 690.1 (Jan. 2009), 463–485. doi: 10.1088/0004-637X/690/1/463. arXiv: 0809.0754 [astro-ph].

Riechers, Dominik A. et al. “A dust-obscured massive maximum-starburst galaxy at a redshift of 6.34”. *Nature* 496.7445 (Apr. 2013), 329–333. doi: 10.1038/nature12050. arXiv: 1304.4256 [astro-ph.CO].

Riechers, Dominik A. et al. “COLDz: A High Space Density of Massive Dusty Starburst Galaxies $\sim$1 Billion Years after the Big Bang”. *ApJ* 895.2, 81 (June 2020), 81. doi: 10.3847/1538-4357/ab8c48. arXiv: 2004.10204 [astro-ph.GA].

Riechers, Dominik A. et al. “VLA-ALMA Spectroscopic Survey in the Hubble Ultra Deep Field (VLASPECS): Total Cold Gas Masses and CO Line Ratios for $z = 2$-3 Main-sequence Galaxies”. *ApJL* 896.2, L21 (June 2020), L21. doi: 10.3847/2041-8213/ab9595. arXiv: 2005.09653 [astro-ph.GA].

Rizzo, F. et al. “A dynamically cold disk galaxy in the early Universe”. *Nature* 584.7820 (Aug. 2020), 201–204. doi: 10.1038/s41586-020-2572-6. arXiv: 2009.01251 [astro-ph.GA].

Rizzo, F. et al. “Dynamical properties of z 4.5 dusty star-forming galaxies and their connection with local early-type galaxies”. *MNRAS* 507.3 (Nov. 2021), 3952–3984. doi: 10.1093/mnras/stab2295. arXiv: 2102.05671 [astro-ph.GA].

Rizzo, F. et al. “Dynamical characterization of galaxies up to $z \sim 7$”. *A&A* 667, A5 (Nov. 2022), A5. doi: 10.1051/0004-6361/202243582. arXiv: 2204.05325 [astro-ph.GA].

Roos, Orianne et al. “Thermal and Radiative Active Galactic Nucleus Feedback have a Limited Impact on Star Formation in High-redshift Galaxies”. *ApJ* 800.1, 19 (Feb. 2015), 19. doi: 10.1088/0004-637X/800/1/19. arXiv: 1405.7971 [astro-ph.GA].

Runnoe, Jessie C., Michael S. Brotherton, and Zhaohui Shang. “Updating quasar bolometric luminosity corrections”. *MNRAS* 422.1 (May 2012), 478–493. doi: 10.1111/j.1365-2966.2012.20620.x. arXiv: 1201.5155 [astro-ph.CO].

Rupke, David S., Sylvain Veilleux, and D. B. Sanders. “Outflows in Infrared-Luminous Starbursts at $z < 0.5$. II. Analysis and Discussion”. *ApJS* 160.1 (Sept. 2005), 115–148. doi: 10.1086/432889. arXiv: astro-ph/0506611 [astro-ph].

Sahu, Nandini, Alister W. Graham, and Benjamin L. Davis. “Black Hole Mass Scaling Relations for Early-type Galaxies. I. M_{BH}-$M_{*,\ sph}$ and M_{BH}-$M_{*,gal}$”. *ApJ* 876.2, 155 (May 2019), 155. doi: 10.3847/1538-4357/ab0f32. arXiv: 1903.04738 [astro-ph.GA].

Saintonge, Amélie et al. “Validation of the Equilibrium Model for Galaxy Evolution to z ~3 through Molecular Gas and Dust Observations of Lensed Star-forming Galaxies”. *ApJ* 778.1, 2 (Nov. 2013), 2. doi: 10.1088/0004-637X/778/1/2. arXiv: 1309.3281 [astro-ph.CO].

Salak, Dragan et al. “Molecular outflow in the reionization-epoch quasar J2054-0005 revealed by OH 119 μm observations”. *arXiv e-prints*, arXiv:2307.02104 (July 2023), arXiv:2307.02104. doi: 10.48550/arXiv.2307.02104. arXiv: 2307.02104 [astro-ph.GA].

Salpeter, Edwin E. “The Luminosity Function and Stellar Evolution.” *ApJ* 121 (Jan. 1955), 161. DOI: 10.1086/145971.

Sanders, D. B. et al. “The IRAS Revised Bright Galaxy Sample”. *AJ* 126.4 (Oct. 2003), 1607–1664. DOI: 10.1086/376841. arXiv: astro-ph/0306263 [astro-ph].

Santini, P. et al. “The evolution of the dust and gas content in galaxies”. *A&A* 562, A30 (Feb. 2014), A30. DOI: 10.1051/0004-6361/201322835. arXiv: 1311.3670 [astro-ph.CO].

Santini, P. et al. “Early Results from GLASS-JWST. XI. Stellar Masses and Mass-to-light Ratio of z ¿ 7 Galaxies”. *ApJL* 942.2, L27 (Jan. 2023), L27. DOI: 10.3847/2041-8213/ac9586. arXiv: 2207.11379 [astro-ph.GA].

Sbarrato, T. et al. “Jetted radio-quiet quasars at z > 5”. *A&A* 655, A95 (Nov. 2021), A95. DOI: 10.1051/0004-6361/202141827. arXiv: 2109.08156 [astro-ph.HE].

Schindler, Jan-Torge et al. “The X-SHOOTER/ALMA Sample of Quasars in the Epoch of Reionization. I. NIR Spectral Modeling, Iron Enrichment, and Broad Emission Line Properties”. *ApJ* 905.1, 51 (Dec. 2020), 51. DOI: 10.3847/1538-4357/abc2d7. arXiv: 2010.06902 [astro-ph.GA].

Schneider, P. *Extragalactic Astronomy and Cosmology: An Introduction*. 2015. DOI: 10.1007/978-3-642-54083-7.

Schneider, R. et al. “The origin of the far-infrared continuum of z ~6 quasars. A radiative transfer model for SDSS J1148+5251”. *A&A* 579, A60 (July 2015), A60. DOI: 10.1051/0004-6361/201526105. arXiv: 1402.2279 [astro-ph.GA].

Schreiber, C. et al. “Dust temperature and mid-to-total infrared color distributions for star-forming galaxies at 0 ¡ z ¡ 4”. *A&A* 609, A30 (Jan. 2018), A30. DOI: 10.1051/0004-6361/201731506. arXiv: 1710.10276 [astro-ph.GA].

Schruba, Andreas et al. “A Molecular Star Formation Law in the Atomic-gas-dominated Regime in Nearby Galaxies”. *AJ* 142.2, 37 (Aug. 2011), 37. DOI: 10.1088/0004-6256/142/2/37. arXiv: 1105.4605 [astro-ph.CO].

Shakura, N. I. and R. A. Sunyaev. “Black holes in binary systems. Observational appearance.” *A&A* 24 (Jan. 1973), 337–355.

Shao, Yali et al. “Gas Dynamics of a Luminous z = 6.13 Quasar ULAS J1319+0950 Revealed by ALMA High-resolution Observations”. *ApJ* 845.2, 138 (Aug. 2017), 138. DOI: 10.3847/1538-4357/aa826c. arXiv: 1707.03078 [astro-ph.GA].

Shao, Yali et al. “Star Formation and ISM Properties in the Host Galaxies of Three Far-infrared Luminous Quasars at z ∼ 6”. *ApJ* 876.2, 99 (May 2019), 99. DOI: 10.3847/1538-4357/ab133d. arXiv: 1903.01105 [astro-ph.GA].

Shao, Yali et al. “The interstellar medium distribution, gas kinematics, and system dynamics of the far-infrared luminous quasar SDSS J2310+1855 at z = 6.0”. *A&A* 668, A121 (Dec. 2022), A121. DOI: 10.1051/0004-6361/202244610. arXiv: 2210.11926 [astro-ph.GA].

Shen, Yue and Brandon C. Kelly. "The Demographics of Broad-line Quasars in the Mass-Luminosity Plane. I. Testing FWHM-based Virial Black Hole Masses". *ApJ* 746.2, 169 (Feb. 2012), 169. doi: 10.1088/0004-637X/746/2/169. arXiv: 1107.4372 [astro-ph.CO].

Shen, Yue and Xin Liu. "Comparing Single-epoch Virial Black Hole Mass Estimators for Luminous Quasars". *ApJ* 753.2, 125 (July 2012), 125. doi: 10.1088/0004-637X/753/2/125. arXiv: 1203.0601 [astro-ph.CO].

Shen, Yue et al. "Biases in Virial Black Hole Masses: An SDSS Perspective". *ApJ* 680.1 (June 2008), 169–190. doi: 10.1086/587475. arXiv: 0709.3098 [astro-ph].

Shen, Yue et al. "A Catalog of Quasar Properties from Sloan Digital Sky Survey Data Release 7". *ApJS* 194.2, 45 (June 2011), 45. doi: 10.1088/0067-0049/194/2/45. arXiv: 1006.5178 [astro-ph.CO].

Shen, Yue et al. "Constraining Sub-parsec Binary Supermassive Black Holes in Quasars with Multi-epoch Spectroscopy. I. The General Quasar Population". *ApJ* 775.1, 49 (Sept. 2013), 49. doi: 10.1088/0004-637X/775/1/49. arXiv: 1306.4330 [astro-ph.CO].

Shen, Yue et al. "Gemini GNIRS Near-infrared Spectroscopy of 50 Quasars at z $\gtrsim$ 5.7". *ApJ* 873.1, 35 (Mar. 2019), 35. doi: 10.3847/1538-4357/ab03d9. arXiv: 1809.05584 [astro-ph.GA].

Solomon, P. M. and P. A. Vanden Bout. "Molecular Gas at High Redshift". *ARA&A* 43.1 (Sept. 2005), 677–725. doi: 10.1146/annurev.astro.43.051804.102221. arXiv: astro-ph/0508481 [astro-ph].

Sommovigo, L. et al. "Warm dust in high-z galaxies: origin and implications". *MNRAS* 497.1 (Sept. 2020), 956–968. doi: 10.1093/mnras/staa1959. arXiv: 2004.09528 [astro-ph.GA].

Sommovigo, L. et al. "Dust temperature in ALMA [C II]-detected high-z galaxies". *MNRAS* 503.4 (May 2021), 4878–4891. doi: 10.1093/mnras/stab720. arXiv: 2102.08950 [astro-ph.GA].

Sommovigo, L. et al. "The ALMA REBELS Survey: cosmic dust temperature evolution out to z 7". *MNRAS* 513.3 (July 2022), 3122–3135. doi: 10.1093/mnras/stac302. arXiv: 2202.01227 [astro-ph.GA].

Stacey, G. J. et al. "A 158 μm [C II] Line Survey of Galaxies at z ~1-2: An Indicator of Star Formation in the Early Universe". *ApJ* 724.2 (Dec. 2010), 957–974. doi: 10.1088/0004-637X/724/2/957. arXiv: 1009.4216 [astro-ph.CO].

Stalevski, Marko et al. "The dust covering factor in active galactic nuclei". *MNRAS* 458.3 (May 2016), 2288–2302. doi: 10.1093/mnras/stw444. arXiv: 1602.06954 [astro-ph.GA].

Stanley, F. et al. "A spectral stacking analysis to search for faint outflow signatures in z $\sim$ 6 quasars". *A&A* 631, A78 (Nov. 2019), A78. doi: 10.1051/0004-6361/201834530. arXiv: 1908.11395 [astro-ph.GA].

Stefan, Irina I. et al. "Imaging the cold molecular gas in SDSS J1148 + 5251 at z = 6.4". *Monthly Notices of the Royal Astronomical Society* 451.2 (June 2015), 1713–1718. issn: 0035-8711. doi: 10.1093/mnras/stv1108. eprint: https://academic.oup.com/

mnras/article-pdf/451/2/1713/5728562/stv1108.pdf. URL: https://doi.org/10.1093/mnras/stv1108.

Tacconi, L. J. et al. “High molecular gas fractions in normal massive star-forming galaxies in the young Universe”. *Nature* 463.7282 (Feb. 2010), 781–784. DOI: 10.1038/nature08773. arXiv: 1002.2149 [astro-ph.CO].

Terzić, Balša and Alister W. Graham. “Density-potential pairs for spherical stellar systems with Sérsic light profiles and (optional) power-law cores”. *MNRAS* 362.1 (Sept. 2005), 197–212. DOI: 10.1111/j.1365-2966.2005.09269.x. arXiv: astro-ph/0506192 [astro-ph].

Tielens, A. G. G. M., L. B. F. M. Waters, and T. J. Bernatowicz. “Origin and Evolution of Dust in Circumstellar and Interstellar Environments”. *Chondrites and the Protoplanetary Disk*. Ed. by A. N. Krot, E. R. D. Scott, and B. Reipurth. Vol. 341. Astronomical Society of the Pacific Conference Series. Dec. 2005, 605.

Tielens, A. G. G. M. et al. “Interstellar Solid CO: Polar and Nonpolar Interstellar Ices”. *ApJ* 381 (Nov. 1991), 181. DOI: 10.1086/170640.

Toyouchi, Daisuke et al. “Super-Eddington Mass Growth of Intermediate-mass Black Holes Embedded in Dusty Circumnuclear Disks”. *ApJ* 907.2, 74 (Feb. 2021), 74. DOI: 10.3847/1538-4357/abcfc2. arXiv: 2009.14673 [astro-ph.GA].

Trakhtenbrot, Benny et al. “ALMA Observations Show Major Mergers Among the Host Galaxies of Fast-growing, High-redshift Supermassive Black Holes”. *ApJ* 836.1, 8 (Feb. 2017), 8. DOI: 10.3847/1538-4357/836/1/8. arXiv: 1612.00010 [astro-ph.GA].

Tremaine, Scott et al. “The Slope of the Black Hole Mass versus Velocity Dispersion Correlation”. *ApJ* 574.2 (Aug. 2002), 740–753. DOI: 10.1086/341002. arXiv: astro-ph/0203468 [astro-ph].

Trinca, Alessandro et al. “The low-end of the black hole mass function at cosmic dawn”. *MNRAS* 511.1 (Mar. 2022), 616–640. DOI: 10.1093/mnras/stac062. arXiv: 2201.02630 [astro-ph.GA].

Tripodi, R. et al. “Black hole and host galaxy growth in an isolated zSO observed with ALMA”. *A&A* 665 (2022), A107. DOI: 10.1051/0004-6361/202243920. URL: https://doi.org/10.1051/0004-6361/202243920.

Tripodi, R. et al. “Accurate Dust Temperature and Star Formation Rate in the Most Luminous z > 6 Quasar in the Hyperluminous Quasars at the Epoch of Reionization (HYPERION) Sample”. *ApJL* 946.2, L45 (Apr. 2023), L45. DOI: 10.3847/2041-8213/acc58d. arXiv: 2303.11961 [astro-ph.GA].

Tripodi, R. et al. “Dynamical signature of a stellar bulge in a quasar-host galaxy at $z \simeq 6$”. *A&A* 671, A44 (Mar. 2023), A44. DOI: 10.1051/0004-6361/202245202. arXiv: 2301.07023 [astro-ph.GA].

Tripodi, R. et al. “HYPERION. Merger and outflow in the most luminous $z > 6$ quasar”. *accepted by A&A*, arXiv:2306.01644 (June 2023), arXiv:2306.01644. DOI: `10.48550/arXiv.2306.01644`. arXiv: `2306.01644 [astro-ph.GA]`.

Tsukui, Takafumi et al. “Spatially resolved dust properties and quasar-galaxy decomposition of a hyper-luminous infrared galaxy at z = 4.4”. *MNRAS* 523.3 (Aug. 2023), 4654–4679. DOI: `10.1093/mnras/stad1464`. arXiv: `2302.07272 [astro-ph.GA]`.

Übler, Hannah et al. “GA-NIFS: A massive black hole in a low-metallicity AGN at z ∼ 5.55 revealed by JWST/NIRSpec IFS”. *A&A* 677, A145 (Sept. 2023), A145. DOI: `10.1051/0004-6361/202346137`. arXiv: `2302.06647 [astro-ph.GA]`.

Urry, C. Megan and Paolo Padovani. “Unified Schemes for Radio-Loud Active Galactic Nuclei”. *PASP* 107 (Sept. 1995), 803. DOI: `10.1086/133630`. arXiv: `astro-ph/9506063 [astro-ph]`.

Uzgil, Bade D. et al. “Constraining the ISM Properties of the Cloverleaf Quasar Host Galaxy with Herschel Spectroscopy”. *ApJ* 832.2, 209 (Dec. 2016), 209. DOI: `10.3847/0004-637X/832/2/209`. arXiv: `1610.00347 [astro-ph.GA]`.

Valentini, Milena, Simona Gallerani, and Andrea Ferrara. “Host galaxies of high-redshift quasars: SMBH growth and feedback”. *MNRAS* 507.1 (Oct. 2021), 1–26. DOI: `10.1093/mnras/stab1992`. arXiv: `2107.05638 [astro-ph.GA]`.

Valiante, Rosa et al. “The origin of the dust in high-redshift quasars: the case of SDSS J1148+5251”. *MNRAS* 416.3 (Sept. 2011), 1916–1935. DOI: `10.1111/j.1365-2966.2011.19168.x`. arXiv: `1106.1418 [astro-ph.CO]`.

Valiante, Rosa et al. “High-redshift quasars host galaxies: is there a stellar mass crisis?” *MNRAS* 444.3 (Nov. 2014), 2442–2455. DOI: `10.1093/mnras/stu1613`. arXiv: `1409.2873 [astro-ph.GA]`.

Vallini, L. et al. “CO line emission from galaxies in the Epoch of Reionization”. *MNRAS* 473.1 (Jan. 2018), 271–285. DOI: `10.1093/mnras/stx2376`. arXiv: `1709.03993 [astro-ph.GA]`.

Vallini, L. et al. “High [O III]/[C II] surface brightness ratios trace early starburst galaxies”. *MNRAS* 505.4 (Aug. 2021), 5543–5553. DOI: `10.1093/mnras/stab1674`. arXiv: `2106.05279 [astro-ph.GA]`.

van der Werf, P. P. et al. “Black hole accretion and star formation as drivers of gas excitation and chemistry in Markarian 231”. *A&A* 518, L42 (July 2010), L42. DOI: `10.1051/0004-6361/201014682`. arXiv: `1005.2877 [astro-ph.GA]`.

van der Werf, Paul P. et al. “Water Vapor Emission Reveals a Highly Obscured, Star-forming Nuclear Region in the QSO Host Galaxy APM 08279+5255 at z = 3.9”. *ApJL* 741.2, L38 (Nov. 2011), L38. DOI: `10.1088/2041-8205/741/2/L38`. arXiv: `1106.4825 [astro-ph.CO]`.

Vanden Berk, Daniel E. et al. “Composite Quasar Spectra from the Sloan Digital Sky Survey”. *AJ* 122.2 (Aug. 2001), 549–564. DOI: `10.1086/321167`. arXiv: `astro-ph/0105231 [astro-ph]`.

Venemans, B. P. et al. “Bright [C II] and Dust Emission in Three z > 6.6 Quasar Host Galaxies Observed by ALMA”. *ApJ* 816.1, 37 (Jan. 2016), 37. DOI: `10.3847/0004-637X/816/1/37`. arXiv: `1511.07432 [astro-ph.GA]`.

Venemans, B. P. et al. “The Compact, ∼1 kpc Host Galaxy of a Quasar at a Redshift of 7.1”. *ApJ* 837.2, 146 (Mar. 2017), 146. DOI: `10.3847/1538-4357/aa62ac`. arXiv: `1702.03852 [astro-ph.GA]`.

Venemans, B. P. et al. “Dust Emission in an Accretion-rate-limited Sample of z $\gtrsim$ 6 Quasars”. *ApJ* 866.2, 159 (Oct. 2018), 159. DOI: `10.3847/1538-4357/aadf35`. arXiv: `1809.01662 [astro-ph.GA]`.

Venemans, B. P. et al. “Kiloparsec-scale ALMA Imaging of [C II] and Dust Continuum Emission of 27 Quasar Host Galaxies at z ∼ 6”. *ApJ* 904.2, 130 (Dec. 2020), 130. DOI: `10.3847/1538-4357/abc563`. arXiv: `2010.14874 [astro-ph.GA]`.

Venemans, B. P. et al. “The Identification of Z-dropouts in Pan-STARRS1: Three Quasars at 6.5¡ z¡ 6.7”. *ApJL* 801.1, L11 (Mar. 2015), L11. DOI: `10.1088/2041-8205/801/1/L11`. arXiv: `1502.01927 [astro-ph.GA]`.

Vestergaard, M. and Patrick S. Osmer. “Mass Functions of the Active Black Holes in Distant Quasars from the Large Bright Quasar Survey, the Bright Quasar Survey, and the Color-selected Sample of the SDSS Fall Equatorial Stripe”. *ApJ* 699.1 (July 2009), 800–816. DOI: `10.1088/0004-637X/699/1/800`. arXiv: `0904.3348 [astro-ph.CO]`.

— “Mass Functions of the Active Black Holes in Distant Quasars from the Large Bright Quasar Survey, the Bright Quasar Survey, and the Color-selected Sample of the SDSS Fall Equatorial Stripe”. *ApJ* 699.1 (July 2009), 800–816. DOI: `10.1088/0004-637X/699/1/800`. arXiv: `0904.3348 [astro-ph.CO]`.

Vestergaard, M. and Bradley M. Peterson. “Determining Central Black Hole Masses in Distant Active Galaxies and Quasars. II. Improved Optical and UV Scaling Relationships”. *ApJ* 641.2 (Apr. 2006), 689–709. DOI: `10.1086/500572`. arXiv: `astro-ph/0601303 [astro-ph]`.

Viero, Marco P. et al. “The early Universe was dust-rich and extremely hot”. *MNRAS* 516.1 (Oct. 2022), L30–L34. DOI: `10.1093/mnrasl/slac075`. arXiv: `2203.14312 [astro-ph.GA]`.

Vietri, G. et al. “The WISSH quasars project. IV. Broad line region versus kiloparsec-scale winds”. *A&A* 617, A81 (Sept. 2018), A81. DOI: `10.1051/0004-6361/201732335`. arXiv: `1802.03423 [astro-ph.GA]`.

Vogelaar, M. G. R. and J. P. Terlouw. “The Evolution of GIPSY—or the Survival of an Image Processing System”. *Astronomical Data Analysis Software and Systems X*. Ed. by Jr. Harnden F. R., Frances A. Primini, and Harry E. Payne. Vol. 238. Astronomical Society of the Pacific Conference Series. Jan. 2001, 358.

Volonteri, M. “Formation of supermassive black holes”. *A&A Rev.* 18.3 (July 2010), 279–315. DOI: `10.1007/s00159-010-0029-x`. arXiv: `1003.4404 [astro-ph.CO]`.

Volonteri, M. “The Formation and Evolution of Massive Black Holes”. *Science* 337.6094 (Aug. 2012), 544. DOI: 10.1126/science.1220843. arXiv: 1208.1106 [astro-ph.CO].

Volonteri, Marta and Priyamvada Natarajan. “Journey to the M_{BH}-σ relation: the fate of low-mass black holes in the Universe”. *MNRAS* 400.4 (Dec. 2009), 1911–1918. DOI: 10.1111/j.1365-2966.2009.15577.x. arXiv: 0903.2262 [astro-ph.CO].

Walter, F. et al. “Molecular gas in the host galaxy of a quasar at redshift z = 6.42”. *Nature* 424.6947 (July 2003), 406–408. DOI: 10.1038/nature01821. arXiv: astro-ph/0307410 [astro-ph].

Walter, F. et al. “Resolved Molecular Gas in a Quasar Host Galaxy at Redshift z=6.42”. *ApJL* 615.1 (Nov. 2004), L17–L20. DOI: 10.1086/426017. arXiv: astro-ph/0410229 [astro-ph].

Walter, F. et al. “ALMA 200 pc Imaging of a z 7 Quasar Reveals a Compact, Disk-like Host Galaxy”. *ApJ* 927.1, 21 (Mar. 2022), 21. DOI: 10.3847/1538-4357/ac49e8. arXiv: 2201.06396 [astro-ph.GA].

Wang, F. et al. “A Survey of Luminous High-redshift Quasars with SDSS and WISE. I. Target Selection and Optical Spectroscopy”. *ApJ* 819.1, 24 (Mar. 2016), 24. DOI: 10.3847/0004-637X/819/1/24. arXiv: 1602.04659 [astro-ph.GA].

Wang, F. et al. “Spatially Resolved Interstellar Medium and Highly Excited Dense Molecular Gas in the Most Luminous Quasar at z = 6.327”. *ApJ* 880.1, 2 (July 2019), 2. DOI: 10.3847/1538-4357/ab2717. arXiv: 1906.06801 [astro-ph.GA].

Wang, F. et al. “A Luminous Quasar at Redshift 7.642”. *ApJL* 907.1, L1 (Jan. 2021), L1. DOI: 10.3847/2041-8213/abd8c6. arXiv: 2101.03179 [astro-ph.GA].

Wang, R. et al. “Star Formation and Gas Kinematics of Quasar Host Galaxies at z ~6: New Insights from ALMA”. *ApJ* 773.1, 44 (Aug. 2013), 44. DOI: 10.1088/0004-637X/773/1/44. arXiv: 1302.4154 [astro-ph.CO].

Wang, Ran et al. “Far-infrared and Molecular CO Emission from the Host Galaxies of Faint Quasars at z ~6”. *AJ* 142.4, 101 (Oct. 2011), 101. DOI: 10.1088/0004-6256/142/4/101. arXiv: 1107.5065 [astro-ph.CO].

Warner, P. J., M. C. H. Wright, and J. E. Baldwin. “High resolution observations of neutral hydrogen in M33 - II. The velocity field.” *MNRAS* 163 (Jan. 1973), 163. DOI: 10.1093/mnras/163.2.163.

Warren, S. J. et al. “First observation of a quasar with a redshift of 4”. *Nature* 325.6100 (Jan. 1987), 131–133. DOI: 10.1038/325131a0.

Weiß, A. et al. “Highly-excited CO emission in APM 08279+5255 at z = 3.9”. *A&A* 467.3 (June 2007), 955–969. DOI: 10.1051/0004-6361:20066117. arXiv: astro-ph/0702669 [astro-ph].

Willott, Chris J., Jacqueline Bergeron, and Alain Omont. “Star Formation Rate and Dynamical Mass of 10^8 Solar Mass Black Hole Host Galaxies At Redshift 6”. *ApJ* 801.2, 123 (Mar. 2015), 123. DOI: 10.1088/0004-637X/801/2/123. arXiv: 1501.07538 [astro-ph.GA].

— "A Wide Dispersion in Star Formation Rate and Dynamical Mass of 10^8 Solar Mass Black Hole Host Galaxies at Redshift 6". *ApJ* 850.1, 108 (Nov. 2017), 108. DOI: `10.3847/1538-4357/aa921b`. arXiv: `1710.02212 [astro-ph.GA]`.

Willott, Chris J., Alain Omont, and Jacqueline Bergeron. "Redshift 6.4 Host Galaxies of 10^8 Solar Mass Black Holes: Low Star Formation Rate and Dynamical Mass". *ApJ* 770.1, 13 (June 2013), 13. DOI: `10.1088/0004-637X/770/1/13`. arXiv: `1302.1587 [astro-ph.CO]`.

Witstok, Joris et al. "Dual constraints with ALMA: new [O III] 88-μm and dust-continuum observations reveal the ISM conditions of luminous LBGs at z 7". *MNRAS* 515.2 (Sept. 2022), 1751–1773. DOI: `10.1093/mnras/stac1905`. arXiv: `2207.00022 [astro-ph.GA]`.

Witstok, Joris et al. "An empirical study of dust properties at the earliest epochs". *MNRAS* 523.2 (Aug. 2023), 3119–3132. DOI: `10.1093/mnras/stad1470`. arXiv: `2305.09714 [astro-ph.GA]`.

Wolfe, Arthur M., Eric Gawiser, and Jason X. Prochaska. "Damped Ly α Systems". *ARA&A* 43.1 (Sept. 2005), 861–918. DOI: `10.1146/annurev.astro.42.053102.133950`. arXiv: `astro-ph/0509481 [astro-ph]`.

Wolfire, Mark G., Livia Vallini, and Mélanie Chevance. "Photodissociation and X-Ray Dominated Regions". *arXiv e-prints*, arXiv:2202.05867 (Feb. 2022), arXiv:2202.05867. arXiv: `2202.05867 [astro-ph.GA]`.

Wu, Xue-Bing et al. "An ultraluminous quasar with a twelve-billion-solar-mass black hole at redshift 6.30". *Nature* 518.7540 (Feb. 2015), 512–515. DOI: `10.1038/nature14241`. arXiv: `1502.07418 [astro-ph.GA]`.

Yang, C. et al. "Water Vapor in nearby Infrared Galaxies as Probed by Herschel". *ApJL* 771.2, L24 (July 2013), L24. DOI: `10.1088/2041-8205/771/2/L24`. arXiv: `1305.6351 [astro-ph.GA]`.

Yang, C. et al. "Submillimeter H_2O and H_2O^+emission in lensed ultra- and hyper-luminous infrared galaxies at z 2-4". *A&A* 595, A80 (Nov. 2016), A80. DOI: `10.1051/0004-6361/201628160`. arXiv: `1607.06220 [astro-ph.GA]`.

Yang, J. et al. "Far-infrared Properties of the Bright, Gravitationally Lensed Quasar J0439+1634 at z = 6.5". *ApJ* 880.2, 153 (Aug. 2019), 153. DOI: `10.3847/1538-4357/ab2a02`. arXiv: `1907.00385 [astro-ph.GA]`.

Yang, J. et al. "Pōniuā'ena: A Luminous z = 7.5 Quasar Hosting a 1.5 Billion Solar Mass Black Hole". *ApJL* 897.1, L14 (July 2020), L14. DOI: `10.3847/2041-8213/ab9c26`. arXiv: `2006.13452 [astro-ph.GA]`.

Yang, J. et al. "A SPectroscopic Survey of Biased Halos in the Reionization Era (ASPIRE): A First Look at the Rest-frame Optical Spectra of z ¿ 6.5 Quasars Using JWST". *ApJL* 951.1, L5 (July 2023), L5. DOI: `10.3847/2041-8213/acc9c8`. arXiv: `2304.09888 [astro-ph.GA]`.

Yong, Suk Yee, Rachel L. Webster, and Anthea L. King. “Black Hole Mass Estimation: How Good is the Virial Estimate?” *PASA* 33, e009 (Mar. 2016), e009. doi: `10.1017/pasa.2016.8`. arXiv: `1602.04672 [astro-ph.GA]`.

Yong, Suk Yee et al. “The Kinematics of Quasar Broad Emission Line Regions Using a Disk-Wind Model”. *PASA* 34, e042 (Sept. 2017), e042. doi: `10.1017/pasa.2017.37`. arXiv: `1708.07237 [astro-ph.GA]`.

Yu, Zhefu et al. “OzDES Reverberation Mapping Programme: Mg II lags and R-L relation”. *MNRAS* 522.3 (July 2023), 4132–4147. doi: `10.1093/mnras/stad1224`. arXiv: `2208.05491 [astro-ph.GA]`.

Yue, Minghao et al. “ALMA Observations of the Sub-kpc Structure of the Host Galaxy of a z = 6.5 Lensed Quasar: A Rotationally Supported Hyper-Starburst System at the Epoch of Reionization”. *ApJ* 917.2, 99 (Aug. 2021), 99. doi: `10.3847/1538-4357/ac0af4`. arXiv: `2106.07429 [astro-ph.GA]`.

Zana, Tommaso et al. “Enhanced star formation in z 6 quasar companions”. *MNRAS* 513.2 (June 2022), 2118–2135. doi: `10.1093/mnras/stac978`. arXiv: `2204.03658 [astro-ph.GA]`.

Zanella, A. et al. “The [C II] emission as a molecular gas mass tracer in galaxies at low and high redshifts”. *MNRAS* 481.2 (Dec. 2018), 1976–1999. doi: `10.1093/mnras/sty2394`. arXiv: `1808.10331 [astro-ph.GA]`.

Zappacosta, L. et al. “HYPerluminous quasars at the Epoch of ReionizatION (HYPERION). A new regime for the X-ray nuclear properties of the first quasars”. *arXiv e-prints*, arXiv:2305.02347 (May 2023), arXiv:2305.02347. doi: `10.48550/arXiv.2305.02347`. arXiv: `2305.02347 [astro-ph.GA]`.

Zhang, Haowen et al. “TRINITY II: The luminosity-dependent bias of the supermassive black hole mass-galaxy mass relation for bright quasars at z = 6”. *MNRAS* 523.1 (July 2023), L69–L74. doi: `10.1093/mnrasl/slad060`. arXiv: `2303.08150 [astro-ph.GA]`.

Zhang, Yechi et al. “The Stellar Mass-Black Hole Mass Relation at z 2 down to $M_{\mathrm{BH}} \sim 10^7\ \mathrm{M}_\odot$ Determined by HETDEX”. *ApJ* 948.2, 103 (May 2023), 103. doi: `10.3847/1538-4357/acc2c2`. arXiv: `2303.02929 [astro-ph.GA]`.

Zubko, Viktor, Eli Dwek, and Richard G. Arendt. “Interstellar Dust Models Consistent with Extinction, Emission, and Abundance Constraints”. *ApJS* 152.2 (June 2004), 211–249. doi: `10.1086/382351`. arXiv: `astro-ph/0312641 [astro-ph]`.

Zubovas, Kastytis and Andrew King. “Clearing Out a Galaxy”. *ApJL* 745.2, L34 (Feb. 2012), L34. doi: `10.1088/2041-8205/745/2/L34`. arXiv: `1201.0866 [astro-ph.GA]`.